Modeling the surface-atmosphere coupling in the Moroccan semi-arid plains in the context of climate change

Khadija Arjdal

INSTITUT POLYTECHNIQUE DE PARIS

NNT : 2023IPPAX104

Thèse de doctorat

UM6P College of Agriculture & Environmental Sciences

ÉCOLE POLYTECHNIQUE

IP PARIS

Modeling the surface-atmosphere coupling in the Moroccan semi-arid plains in the context of climate change

Thèse de doctorat de l'Institut Polytechnique de Paris
préparée à l'École Polytechnique, et à l'Université Mohammed VI Polytechnique

École doctorale n°626 : Ecole Doctorale de l'Institut Polytechnique de Paris (ED IP Paris)
Spécialité de doctorat: Sciences de l'environnement

Thèse présentée et soutenue à Benguerir, Maroc, le 20/12/2023, par

Khadija Arjdal

Thèse encadrée par :

Fatima Driouech
Professeure, UM6P/CAES
Étienne Vignon
Chargé de recherche CNRS, LMD

Composition du Jury :

Wahid Mellouki Professeur, UM6P/CSAES/ACAQCC	Président du jury
Fabienne Lohou Professeure, U. Paul Sabatier Toulouse III	Rapporteure
Marina Baldi Professeure, Istituto per la BioEconomia–CNR	Rapporteure
Rafiq Hamdi Chargé de recherche, IRM de Belgique	Rapporteure
Romain Roehrig Chargé de recherche, Météo-France/CNRM	Examinateur
Philippe Drobinski Directeur de recherche CNRS, LMD	Co-directeur de thèse
Abdelghani Chehbouni Professeur, UM6P/CAES	Co-directeur de thèse
Fatima Driouech Professeure, UM6P/CAES	Invitée
Étienne Vignon Chargé de recherche CNRS, LMD	Invité

Summary

Moroccan plains play a major role in the agricultural production of the country, accounting for a third of utilized agricultural land and two thirds of the irrigated areas of the country. However, the increasing droughts and water shortage risks raise a real challenge for sustainable water management in such vulnerable regions. An accurate modeling of the near surface climate is critical to understand and anticipate the climate change in the plains and their potential impacts on the region's water cycle and resources.

The aim of this thesis is two fold: i) to evaluate and improve the modeling of the physical processes governing the surface climate and the water and energy budgets over the Moroccan agricultural plains, and ii) to conduct a critical assessment of future climate projections over the North African region and more particularly over the Moroccan plains. To this purpose, we use the LMDZ-ORCHIDEE model, the atmosphere-land surface component of IPSL-CM (The Institut de Pierre Simon Laplace Coupled Model). An original configuration has been set-up - leveraging the 'zooming capability' of LMDZ - with a global grid locally refined over the Haouz plain in Marrakech region and with the large-scale dynamics nudged to follow reanalysis outside of the zoomed area.

The first part of this work consists of performing a thorough evaluation of LMDZ-ORCHIDEE in representing the surface-atmosphere interactions using in situ measurements collected over the Haouz plain. Sensitivity experiments are performed with adapted land cover to make more robust model-observation comparison. Results show that LMDZ-ORCHIDEE - with the CMIP6 version of its physics - reasonably represents the plain's near surface climate. However, a nocturnal warm bias associated with underestimated sensible heating and wind speed has been identified and partly corrected by prescribing more realistic roughness heights. An underestimation of the evapotranspiration and soil moisture along with overly warm diurnal temperatures remain in our simulations. A first-order irrigation parameterisation has then been implemented in ORCHIDEE to mimic the drip irrigation process extensively used in the plain. Comparison with observations show that the evapotranspiration flux and the daytime temperature biases are reduced, suggesting that irrigation plays a significant role in determining the local climate in the agricultural fields.

In the second part, we assessed the response of the different terms of the surface water budget to climate change over the Mediterranean basin and North-Africa. An in-depth analysis using selected CMIP6 models is carried out, and suggests a statistically robust amplification of the drying over the Mediterranean and an increasing precipitation pattern over Sahara, counterbalanced by increasing evaporative flux. Compared to the CMIP5 exercise, CMIP6 models show qualitatively similar patterns but generally predict more intense changes in precipitation and evapotranspiration over the Mediterranean basin and South-Eastern Sahara, especially during winter. To refine the projections over the Moroccan agricultural plains, we then run a new simulation with LMDZ-ORCHIDEE configuration - with a "zoom" over the Haouz plain - in which wind and temperature fields outside Morocco are nudged towards a CMIP6 SSP5-8.5 Shared Socioeconomic Pathway. This simulation shows a warming of 4K by the end of the century over the plain with the high-end scenario, as well as a decrease in soil moisture and latent heat flux following the decrease in precipitation by 30%. Sensitivity studies

suggest that irrigation can potentially mitigate by 1K the climate change-induced warming and reduce the Bowen ratio as a result of enhanced soil moisture, emphasizing the importance of accounting for the irrigation in climate projections over the Moroccan agricultural areas.

Key words: General Circulation Model, Land-atmosphere interactions, Morocco, Climate change, Irrigation, In situ data.

Résumé

Les plaines Marocaines jouent un rôle majeur dans la production agricole du pays, représentant ainsi un tiers des terres agricoles et deux tiers des zones irriguées du pays. Cependant, la fréquence croissante des sécheresses constitue un défi majeur pour la gestion durable des ressources en eau, en particulier, dans ces régions vulnérables. Correctement représenter le climat de surface au Maroc dans les modèles de climat est fondamental pour prédire les effets du changement climatique sur les ressources en eau dans cette région.

L'objectif de cette thèse consiste en deux volets: i) évaluer et améliorer la représentation des processus physiques qui gouvernent le climat de surface et le bilan d'eau et d'énergie dans la plaine du Haouz, située à la région de Marrakech. ii) Mettre en place des projections futures fiables dans l'Afrique du Nord et plus particulièrement dans les plaines Marocaines. Ainsi, nous utilisons la composante LMDZ-ORCHIDEE du Modèle Couplé de l'Institut Pierre Simon Laplace (IPSL-CM), dont le modèle atmosphérique LMDZ est couplé au modèle de surface continentale ORCHIDEE. Une configuration originale a été mise en place, en bénéficiant de la "capacité du zoom" du LMDZ, avec une grille globale raffinée autour de la plaine du Haouz, et la dynamique à grande échelle forcée à suivre les réanalyses à l'extérieur de la zone zoomée.

La première partie de ce travail est consacrée à la mise en place d'une évaluation approfondie du modèle LMDZ-ORCHIDEE dans la représentation des interactions surface-atmosphère en utilisant des mesures sur site collectées dans la plaine du Haouz. Des expériences de sensibilité sont menées avec un couvert végétal adapté afin de permettre une comparaison modèle-observation plus robuste et concluante. Les résultats montrent que le modèle -avec sa physique standard du CMIP6- représente raisonnablement bien le climat de la surface dans la plaine. Cependant, un biais chaud de température nocturne, associé à une sous-estimation de la chaleur sensible et de la vitesse du vent a été identifié et partiellement corrigé en prescrivant des hauteurs de rugosité plus réalistes. Une sous-estimation de l'évapotranspiration et de l'humidité du sol, accompagnée des biais chauds de la température diurne ont été également identifiés dans nos simulations. Ainsi, une paramétrisation du premier ordre, visant à imiter l'irrigation dans la plaine, est développée en ORCHIDEE. Les résultats montrent une réduction des biais de l'évapotranspiration et de la température diurne. Par conséquent, cette étude de sensibilité souligne le rôle majeur qu'occupe l'irrigation dans la régulation du climat local dans les champs agricoles.

Dans la deuxième partie, nous avons étudié la réponse de l'hydrologie de surface au changement climatique dans le bassin Méditerranéen et l'Afrique du nord. Une analyse approfondie des modèles CMIP6 montre un assèchement intense à la Méditerranée et une augmentation des précipitations au Sahara, cependant, celles-ci sont compensées par l'augmentation de l'évapotranspiration. Une étude de comparaison à CMIP5 montre des résultats qualitativement similaires avec des changements moins intenses qu'en CMIP6, en particulier pendant l'hiver. Pour raffiner les projections sur les plaines agricoles Marocaines, nous avons mis en place une configuration LMDZ-ORCHIDEE zoomée sur la plaine du Haouz, dont les champs de vent et de température sont guidés à l'extérieur du Maroc vers une simulation globale CMIP6 bien choisie suivant un scénario SSP5-8.5. Les projections montrent

un réchauffement de 4K sur la plaine, ainsi qu'une diminution de l'humidité du sol et du flux latent suite à une diminution des précipitations par 30%. L'irrigation atténue le réchauffement induit par le changement climatique et réduit le rapport de Bowen suite à l'augmentation de l'humidité du sol, soulignant ainsi l'importance de la prise en compte de l'irrigation dans les simulations climatiques sur les zones agricoles Marocaines.

Mots clés: Modèle de circulation générale, Intéractions surface-atmosphère, Maroc, Changement Climatique, Irrigation, Données in situ.

Merci ...

Tout d'abord, un immense merci à Fatima Driouech et Étienne Vignon pour avoir encadré mon travail de thèse. Merci pour toutes ces discussions et transmission de connaissances sur le climat et la modélisation durant ces années. Et également pour toutes les corrections apportées à ce manuscrit.

Je remercie Fatima, sans qui cette thèse n'aurait pas vu le jour, pour sa patience, sa confiance et l'interêt toujours grandissant qu'elle a porté à mon travail, et surtout, pour ses discussions rassurantes quand ça marchait pas. Je remercie Étienne pour l'accueil chaleureux au LMD où chaque jour était une nouvelle opportunité de croissance personnelle et intellectuelle. Merci pour la passion que tu m'as transmise, la motivation et surtout pour ta bonne humeur grace à laquelle j'ai fini cette thèse en souriant.

Je remercie aussi Frédérique Chéruy d'avoir été très présente et très impliquée dans ma thèse, je la remercie pour ses explications et questionnements qui ont alimenté mes réflexions. Je remercie aussi Abdelghani Chehbouni et Philippe Drobinski pour la co-direction de cette thèse, les discussions pertinentes et pour avoir facilité les démarches administratives nécessaires pour le bon déroulement de cette thèse.

J'adresse mes sincères remerciements à Fabienne Lohou, Marina Baldi et Rafiq Hamdi qui ont eu la patience d'évaluer mon travail et dont les commentaires ont renforcé considérablement le manuscrit, et je remercie aussi Romain Roehrig et Wahid Mellouki d'avoir accepté d'examiner cette thèse. Je tiens aussi à exprimer ma gratitude envers les membres de mon comité de thèse: Catherine Rio et Florian Raymond.

Je ne saurai oublier l'aide précieuse de l'ensemble des personnes du LMD/Jussieu, chercheurs, ingénieurs et personnels administratifs pour leur accueil et soutien pendant la thèse, je pense en particulier à Adriana Sima, Abderrahmane Idelkadi, Frédéric Hourdin, Laurent Fairhead, Ehouarn Millour et Laurent Li. Je remercie également l'ensemble des chercheurs, ingénieurs et personnels de l'IWRI et CRSA, en particulier Salah Er-Raki, Jamal Ezzahar, Mohamed Kharrou et l'ensemble des collègue du LMI-TREMA, en particulier Vincent Simonnaux, pour l'accès aux données in-situ et la facilité de leur traitement, aussi bien que les discussions pertinentes autour des sites de mesure. Je remercie aussi Agnès Ducharne, Pedro Arboleda, Lucia Rinchiuso et Pierre Tiengou pour les

discussions pertinentes autour du module d'irrigation.

J'ai une pensée particulière pour saloua, avec qui j'ai partagé les bons et les "moins bons" moments tout au long de ces quatres ans, merci beaucoup pour l'aide technique, et les discussions scientifiques qui ont alimenté mes recherches. Il me sera impossible d'oublier l'ensemble mes co-bureaux et toutes les personnes qui ont rempli ma vie au LMD, et avec qui j'ai partagé des moments de joie, des blagues, des café et des discussions scientifiques aussi, je remercie infiniment Maelle, Valentin, Antony, Antoine, Nicolas, Lea et tous les autres. Sans oublier tous les doctorants de l'IWRI.

Pour finir je tiens à remercier chaleureusement mes parents et mes soeurs pour le soutien et la bienveillance tout au long de mes années d'études. Sans oublier toutes les personnes qui m'ont aidé pendant la thèse au niveau de la conception, l'accomplissement et la finition de la thèse et qui m'ont soutenue moralement, spécialement ceux que je n' ai pas cité mais qui se reconnaîtront.

Note to the reader

This manuscript is organized around two published articles (chapters 4 and 5) of the thesis. The published papers have been reported in their accepted versions and have been inserted as a whole. Consequently, repetitions between chapters can be noticed while reading but they are necessary for the self-consistency of each article. Each paper is introduced with a chapter introduction that explains how the article fits in the structure of the whole manuscript.

Note that, unless otherwise indicated in the text, the data processing and analysis, the run and analysis of model simulations as well as the code development in the model have been made by the author.

Contents

1 Introduction **11**

1.1 Climatological and socio-economical context of a changing Morocco 12
1.2 Anticipating a projected extreme water stress 16
1.3 The *Modélisation Climatique* project 18
1.4 The importance and challenge of developing and evaluating surface-atmosphere coupling parameterizations over semi-arid plains 19
1.5 Thesis objectives and outline of the manuscript 22

2 Observational dataset and climate of the Haouz Plain **23**

2.1 The Haouz plain 24
2.2 The LMI-TREMA observatory and the meteorological dataset 26
2.2.1 Agdal 26
2.2.2 Agafay 26
2.2.3 R3 27
2.2.4 Meteorological measurements 28
2.3 Characterizing the near-surface climate of the Haouz Plain 30

3 Modeling tools and simulations **34**

3.1 Preface 35
3.2 CMIP6 models 35
3.3 Surface layer and coupling of the LMDZ atmospheric component 36
3.4 ORCHIDEE land surface model 40
3.5 LMDZ-ORCHIDEE coupled model 42
3.6 Simulations set-up 43

4 Modeling the surface climate and the surface-atmosphere interactions over the Haouz plain **45**
4.1 Introduction to the chapter 46
4.2 Article. Modeling land-atmosphere interactions over semi-arid plains in Morocco: in-depth assessment of GCM stretched-grid simulations using in situ data 47
4.2.1 Introduction 47
4.2.2 Data, model and methods 49
4.2.3 Results and discussion 57
4.2.4 Summary and conclusions 67
4.3 Investigation of the impact of irrigation upon near surface climate: further analysis . 70
4.3.1 A more detailed description of the implemented irrigation parametrization . . 70
4.3.2 Diurnal cycle 72
4.3.3 Seasonal aspects 78
4.4 Chapter conclusions 81

5 Climate projections over Morocco: from global scenarios down to local assessment over the Haouz plain **82**
5.1 Introduction to the chapter 83
5.2 Article. Future of land surface water availability over the Mediterranean basin and North Africa: analysis and synthesis from the CMIP6 exercise 84
5.2.1 Introduction 84
5.2.2 Data and methods 86
5.2.3 Results and discussion 88
5.2.4 Summary and conclusions 96
5.3 Changing climate in the Haouz plain as simulated by LMDZ-ORCHIDEE 99
5.3.1 Numerical design 99
5.3.2 Projected near surface climate over the Haouz plain 101
5.3.3 Influence of the irrigation parametrization on climate change projections . . . 106
5.4 Chapter conclusions 112

6 Conclusions and prospects **114**
6.1 General conclusions on the representation of land-surface atmosphere interaction in semi-arid agricultural plains in Morocco 115
6.2 Prospects 117

Appendix A: ***Supporting information for "Modeling surface-atmosphere interactions over semi-arid plains in Morocco: in-depth assessment of GCM stretched-grid simulations using in situ data"*** **119**
A. Introduction 119
B. Supplementary Figures 120
C. Model evaluation at Graoua and Chichaoua stations 131

Appendix B: ***Supporting information for "Future of land surface water availability over the Mediterranean basin and North Africa: analysis and synthesis from the CMIP6 exercise"*** **134**
A. Introduction 134
B. Supplementary tables and figures 134
C. Model selection procedure 142

List of figures **151**

List of tables **152**

List of abbreviations **153**

Bibliography **180**

CHAPTER 1

Introduction

Contents

1.1 Climatological and socio-economical context of a changing Morocco 12

1.2 Anticipating a projected extreme water stress 16

1.3 The *Modélisation Climatique* project 18

1.4 The importance and challenge of developing and evaluating surface-atmosphere coupling parameterizations over semi-arid plains 19

1.5 Thesis objectives and outline of the manuscript 22

"We are drowning in information but starved for knowledge."
- John Naisbitt

1.1 Climatological and socio-economical context of a changing Morocco

Since the middle of the 20th century, there have been noticeable and continuous warming trends over the Middle East and North Africa (MENA), with more warm days and nights, and higher extreme temperature values (Donat et al. (2014)). Figure 1.1, from the last Intergovernmental Panel on Climate Change (IPCC) report (IPCC (2021)), shows significant rising trends in observed annual mean surface temperature over Africa from 1961 to 2015 and over 0.1 °C per decade over Northern Africa and the Mediterranean basin according to the Berkeley Earth and CRU TS datasets (Gutiérrez et al. (2021)). During the 1961–2015 period, the rate of surface temperature increase over northern Africa has been faster by more than 0.1°C compared with the global average, mainly explained by anthropogenic climate forcing (Gutiérrez et al. (2021)).

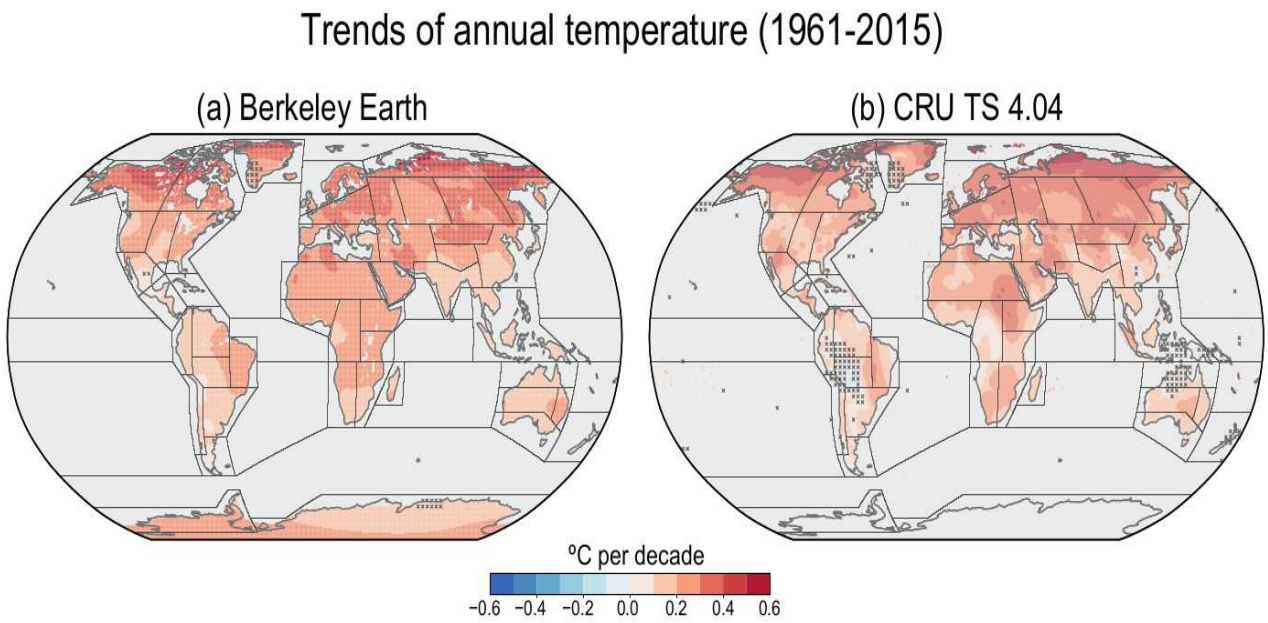

Figure 1.1: Figure Atlas 11 in IPCC (2021). Observed linear trends of signals in annual mean surface air temperature in the Berkeley Earth (**a**) and CRU TS dataset (**b**). Trends (°C per decade) correspond to 1961–2015 mean with respect to climatological period. Regions with non-significant trends (at a 0.1 significance level) are marked with crosses. The black outlines delimit the reference regions defined in Atlas.1.

Morocco, with its geographic position, has a climate influenced by the north Atlantic large-scale circulation, the Sahara desert, the Mediterranean Sea and the Atlas and Rif mountains (Knippertz (2004); Driouech et al. (2009); Filahi et al. (2017); Driouech et al. (2021)). The latter block sea breezes from moving across the continent while preventing hot and dry winds from the south and east from reaching the coast (Filahi et al. (2017)). Consequently, a wide range of climate patterns characterize the country's climate, from humid and sub-humid climate on the northern part of the

High Atlas to semi-arid and dry climates south of the Atlas (Born et al. (2008); D.G.M (2023)) (Figure 1.2), with northern and western areas of the Atlas Mountains dominated by winter precipitation, while the southern areas receive substantial contributions to their yearly precipitation from summertime rain frequently linked to the development of deep moist convection over the High Atlas Mountains (Knippertz et al. (2002, 2003); Born et al. (2010)). Precipitation occurs mainly from October to March with significant spatio-temporal variability (Figure 1.3.a) (Driouech (2010); Xoplaki (2002)), with higher total amounts localized mainly in the north and highlands (>700 mm yr^{-1}) compared to southern and south-eastern areas (< 100 mm yr^{-1}) (Driouech et al. (2021)). Rainfall in Morocco is characterized by recurrent droughts, with a series of dry years since the late 1970s (Knippertz et al. (2002)). Below average periods ranging from 1 to 4 consecutive years have characterised the 80s, with the 1999–2002 being the largest deficit period, followed by the 1992–1994 (Driouech et al. (2021)), and by 2019-2022 according to the last report from the Moroccan General Directorate for Meteorology[1] (Figure 1.3.c). The Atlas Mountains, considered as the Haouz region's 'water tower' (Chehbouni et al. (2008); Zkhiri et al. (2019)), registered a substantial reduction in the amount of rainfall and snowfall from 1990 to 2007 with a reduction of about 200 mm (Figure 1.4).

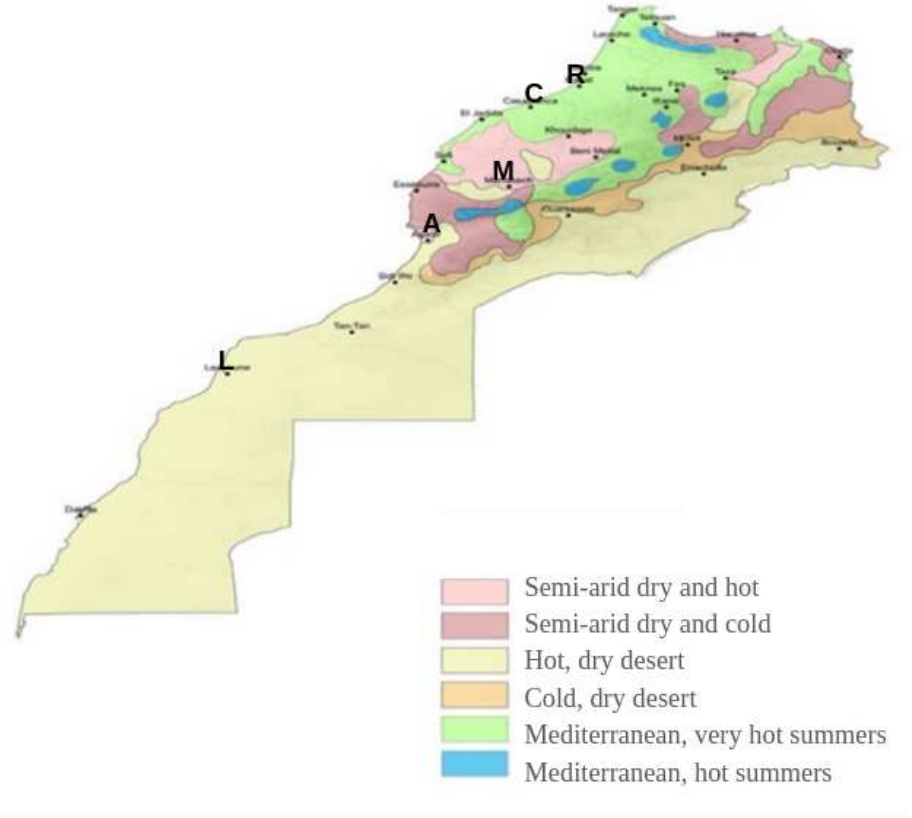

Figure 1.2: Moroccan climate types according to the Koeppen-Geiger classification based on in-situ parameters covering the period 1981-2010. As the name of cities is barely visible, we indicate the location of Marrakech, Casablanca, Rabat, Agadir and Laayoune with the letters M, C, R, A and L respectively. (Adapted from D.G.M (2023))

[1]https://www.marocmeteo.ma

The annual mean temperature in Morocco varies generally between about 11 and 21 °C, with the minima recorded in mountainous regions and the maxima in the southern zone (Driouech et al. (2021)). Morocco has already experienced warming patterns over the past century, Driouech et al. (2021) found that daily temperatures hold a trend of 0.33°C/decade for the period 1984-2016, resulting in more frequent and intense heatwaves. Filahi et al. (2016) showed that the past 4 decades (1970-2012) hold significant increase in the number of warm days and nights, and a significant decrease in the number of cold days and nights with the last two decades being the top 10 warmest years (Driouech et al. (2021)). The 2022 year was the hottest year on record in Moroccan history (Figure 1.3.b), it registered an annual mean anomaly of +1.63°C above the 1981-2010 average and 80% of the days of the year were above normal (D.G.M (2023)).

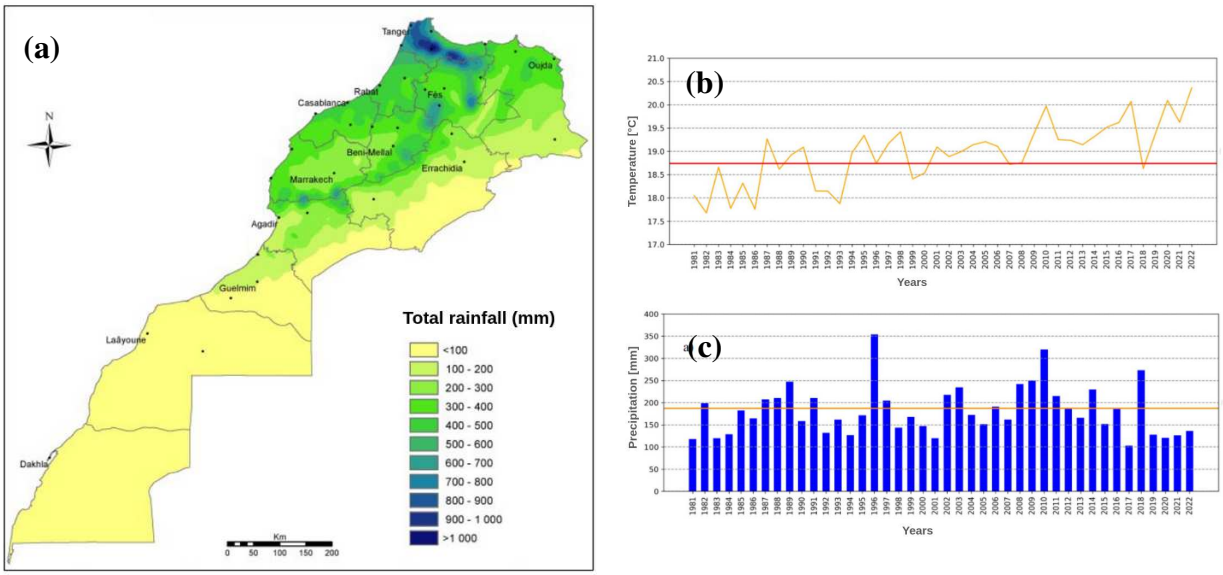

Figure 1.3: **a)** Spatially distributed average annual rainfall totals during the period 1991-2020. Time evolution of observed annual temperature (**b**) and precipitation (**c**) in Morocco. The red line represents the 1981-2010 average. (Adapted from D.G.M (2023)))

According to previous studies (Hurrell and Van Loon (1997); Nicholson and Kim (1997); Ward et al. (1999); Knippertz et al. (2002)), the observed droughts since 1970s in Morocco are attributed to the North Atlantic Oscillation (NAO) positive phase, as well as the El Nino-Southern Oscillation (ENSO) pattern. The NAO is a large-scale shift in the pressure difference between the Azores high surface pressure and the Icelandic subpolar-low surface pressure (Lamb and Peppier (1987)). Morocco's winter precipitation is inversely related to the NAO such that negative values of the NAO result in a strong westerly flow over Morocco that leads to to milder and wetter winters (Lamb and Peppier (1987); Hurrell and Van Loon (1997)). Besides, it is shown that the ENSO variability, by its impact on tropical convection, may affect the Moroccan climate (Born et al. (2010)). Indeed, high SSTs with increased tropical convection in the central and eastern Pacific, induce a reorganization of the atmospheric, tropical, east-west Walker circulation, therefore, impacting the tropical Indian and the Atlantic Oceans. Thus, extratropical teleconnections can shift as a result of the ENSO's influence

on tropical convection, and then affect Moroccan climate (Born et al. (2010)).

The increased aridity, defined as the balance between the water supply (precipitation) and the potential evapotranspiration (ET) (Berg et al. (2016)), in Morocco threatens the agricultural productivity and alters the planting seasons. Morocco, as most of African and Mediterranean countries, largely rely on agriculture for food and income (Waha et al. (2017)). This sector accounts for 14-20% of Morocco's Gross Domestic Product (GDP) and employs about 40% of its workforce with 78% of employment in rural areas (Saidi and Diouri (2017)). The agriculture in Morocco is the largest sector using water, with over 85% consumed annually (Srairi (2017); CESE (2021)). In fact, the renewable water volumes in several of the country's water basins are already fully utilized (Agoumi and DEBBARH (2006)). To overcome the growing water demand and its over-exploitation risks, Moroccan authorities started encouraging the adoption of drip irrigation instead of farrow systems (Srairi (2017)). However, the financial capacity of farmers can limit their access to necessary irrigation materials, thus, the access to deeper boreholes which increases in depth with recurrent droughts (Ameur et al. (2017)).

General Circulation Models (GCMs) are essential tools in characterizing the climate variability and identifying interactions between the atmospheric circulation, the land surface processes and the ocean currents (Forster et al. (2021)). They have a key role in detecting the associated risks of climate patterns such as the intensification of heatwaves, thunderstorms and precipitation extremes. Therefore, GCMs serve as a prevention tool for characterizing and predicting climate drivers and then, assessing the climate projections.

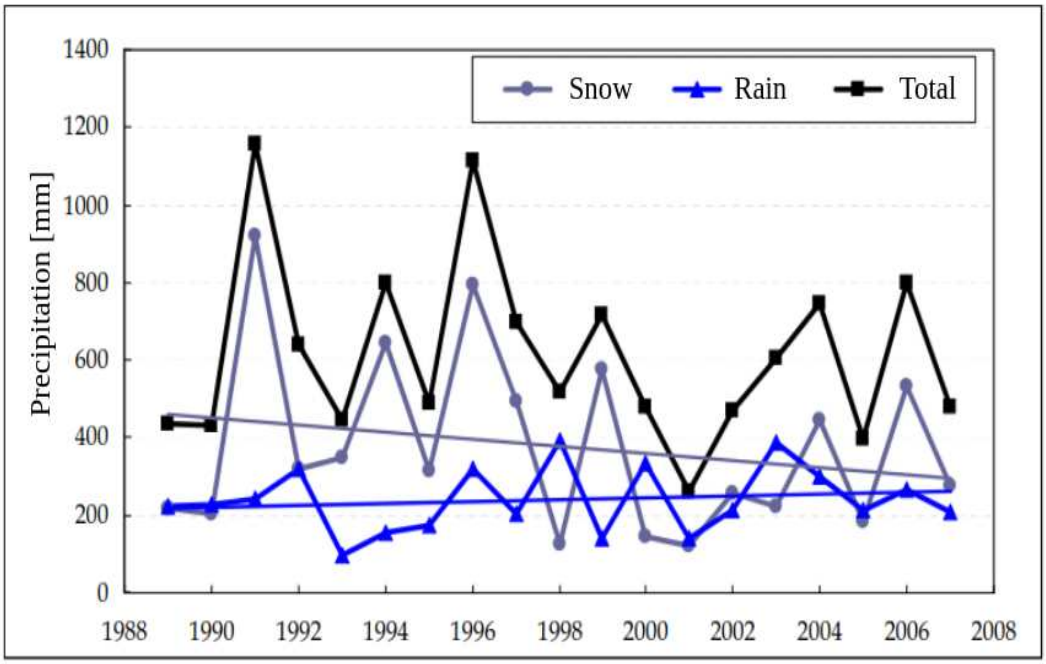

Figure 1.4: Variations in annual rainfall (blue curve), snowfall (grey) and total (black) measured at the Oukaimden station (3239m altitude) in the High Atlas between 1988 and 2008. (Figure adapted from Boudhar (2010)).

1.2 Anticipating a projected extreme water stress

The atmosphere's composition has been altered due to human activity since the mid of the 20th century, consequently, the Earth's energy balance has been modified and resulted in increasing surface temperature that is projected to intensify by the end of the 21st century (IPCC (2021)).

Scenarios realized in the framework of the Coupled Model Intercomparison Project (CMIP) exercises have emphasized that North Africa, and notably Morocco, are considered a global hot spots for drought by the end of the twenty-first century (Dai (2013); Orlowsky and Seneviratne (2013); Sillmann et al. (2013); Prudhomme et al. (2014); Waha et al. (2017); Schilling et al. (2020)). Models from the CMIP5 and CMIP6 project continued warming over African continent, with median projected regional warming of between 1°C and 2°C by 2080–2100 with reference to 1995–2014 under the SSP1-2.6/RCP2.6 scenarios (IPCC (2021)). In particular, summer mean temperatures are projected to exceed 6°C shift by the end of the tweny-first century with respect to the period 1970–2000 according to CMIP6, CMIP5 and the Coordinate Regional Downscaling EXperiment (CORDEX) climate models (Schilling et al. (2012); Ozturk et al. (2017); Almazroui et al. (2020)). In the Mediterranean basin, temperature increase over land will range to about 0.9 to 1.5°C and about 3.7 to 5.6°C under the RCP2.6 and the RCP8.5 respectively by the end of the 21st century, exceeding the global average by 20% (Figure 1.5) (MedECC (2020)). Driouech et al. (2020) showed increasing heat waves number, duration and magnitude with a projected warming ranging from 0.2°C to 0.5°C per decade over land in western MENA region along the Mediterranean. The average maximum temperature during the hottest days is expected to increase from 46 °C by the middle of the century to about 50 °C by the end of the century over the MENA under the RCP8.5 (Lelieveld et al. (2016)). According to CMIP6 projections, Morocco's annual near surface temperature could increase to reach up to 6°C of increase by the end of the century (2070–2099) with respect to the historical period (1980–2009) under the SSP5-8.5 and around 3°C of increase under the SSP2-4.5, with increased warmest annual temperatures mainly concentrated over the Southern and the Eastern parts of the country (Filahi et al. (2017); Bouramdane (2022)).

Both IPCC Assessment Reports AR5 and AR6 project future intensification of the global water cycle, which manifests in increasing global and continental precipitation, P–E and runoff, with the increasing magnitude of change as the radiative forcing increases (Douville and John (2021)). Despite the higher uncertainties and variations between climate models, northern Africa, the Mediterranean and the Middle East are a hotspot for droughts due to Greenhouse Gas (GHG) forcing (Douville and John (2021); IPCC (2021)). The Mediterranean region's annual precipitation over land is projected to decrease by about 4% per degree of global warming by the end of the twenty-first century (relative to the reference period 1980–1999) given a range of global warming of 0.9–5.6°C (Cherif et al. (2020)). Prudhomme et al. (2014) projected more than 50% rise in the frequency of drought by 2070–2099 relative to 1976–2005 and Orlowsky and Seneviratne (2013) reported that the moderate drought conditions are likely to occur at least six months per year in 2080–2100 under the RCP8.5 scenario in the same region.

Consistently with the whole region, total annual precipitation amounts in Morocco are also projected to decrease by up to 20% in the major part of the country with a slight increases in the Sahara, where total rainfall per year is is extremely low (Driouech and ElRhaz (2017)). Tramblay et al. (2018) showed that potential evapotranspiration is projected to increase by up to +11% for the 2036–2065 period and up to +14% for the 2066–2095 period relative to the historical period (1976–2005) under the RCP4.5 scenario over the Maghreb region as a response to temperature increase. Nevertheless, the projected changes in actual evapotranspiration follow the precipitation signal and vary between -10 to -35% in the same region (Tramblay et al. (2018)). Then, the surface runoff hold significant projected decrease from about 9% at 1.5K warming level to 17% at 2K (Schleussner et al. (2016); Donnelly et al. (2017)). Soil moisture has declined since the 20th century and is projected to decrease under all emission scenarios (IPCC (2021)). MedECC (2020) reported a soil moisture drought with up to 16.3% over the Mediterranean region. Therefore, projected dry soils can intensify the aridity, due to feedbacks with land surface temperature, relative humidity and precipitation (Berg et al. (2016)). Climate change and desertification have been linked to water shortage (Bayram and Öztürk (2014); Schwilch et al. (2014); Mohamed et al. (2016)), particularly in regions with extensive dryland areas such as Morocco (IPCC (2022)). Resulting in excessive use of surface and groundwater resources for irrigation and industry (Rochdane et al. (2012); Bahir et al. (2020); Choukri et al. (2020); Behnassi et al. (2021)). The Economic, Social and Environmental Council (CESE) stresses that the resource potential of natural water in Morocco has fallen from 2600 m^3/inhabitant in 1960 to 700 m^3/inhabitant in 2010 and is likely to drop below 500 m^3/inhabitant by 2030 (CESE (2014); Behnassi et al. (2021)), which endangers the food security, nutrition and human health.

In this context, the *Modélisation Climatique* project is among the growing efforts in Morocco that aim at advancing the African climate science and particularly the climate modeling branch.

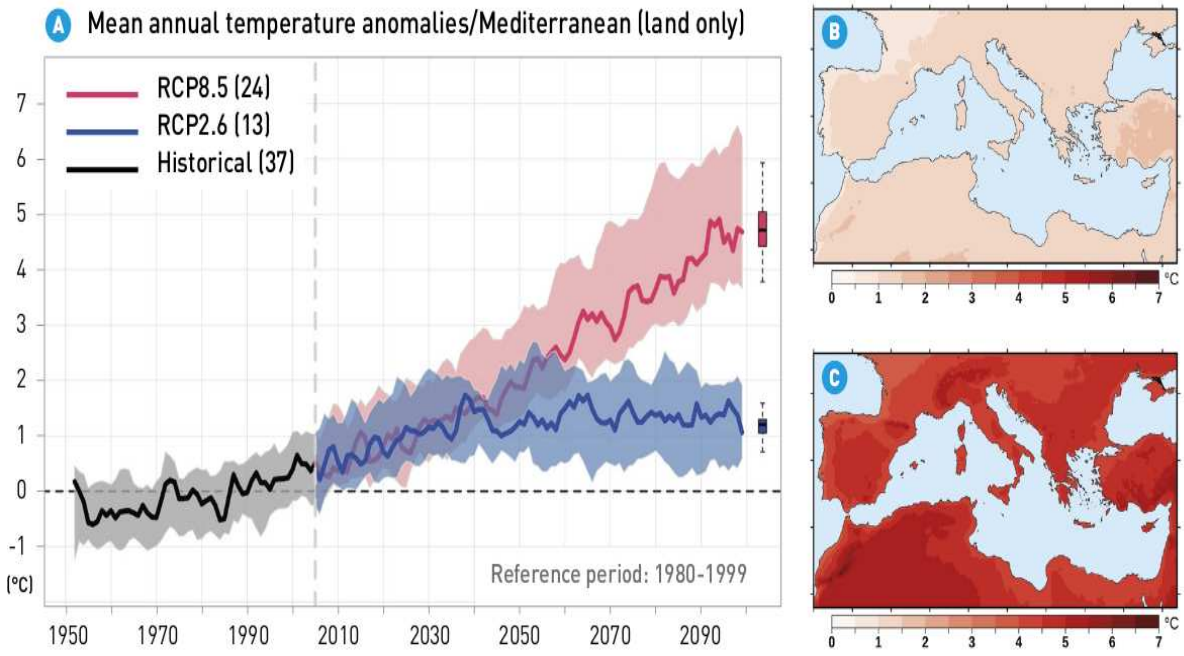

Figure 1.5: Projected warming in the Mediterranean basin over land. Projected changes in annual temperature relative to the recent past reference period (1980-1999), based on the EURO-CORDEX 0.11° ensemble mean, **A**: simulations for pathways RCP2.6 and RCP8.5, **B**: warming at the end of the 21st century (2080-2099) for RCP2.6, **C**: idem for RCP8.5. (Figure SPM.2 in MedECC (2020))

1.3 The *Modélisation Climatique* project

Moroccan climate has been subject of numerous relevant studies that advanced the comprehension of the country's climate patterns. For instance, Knippertz et al. (2002, 2003); Born et al. (2008, 2010) and Driouech et al. (2009, 2010) have explored the historical trends and variability of the Moroccan climate considering the role of large-scale climate drivers in modulating the seasonal and annual patterns. Future climate changes in Morocco has also been widely studied under different emission scenarios (Driouech et al. (2010, 2021); Schilling et al. (2012); Tramblay et al. (2012); Filahi et al. (2017)). However, most of the studies characterizing Moroccan past and future climate focus mainly on the atmospheric branch of the hydrological cycle but the complete water cycle remains incompletely understood. For instance, the soil moisture-climate feedbacks remain less investigated, mainly over agricultural regions. Despite the extensive use of irrigation in Morocco, the climate studies carried out have never been accounting for irrigation and the groundwater pumping feedbacks on the water and energy fluxes. Furthermore, there is an increasing need to assess the impact of the present and future land use changes on local and regional processes.

The *Modélisation Climatique* project is a collaboration project established in october 2020 between the *Mohammed VI Polytechnique University (UM6P)* in Morocco and *l'École Polytechnique de Paris (l'X)* in France, that aims to develop a climate model configuration with advanced capability to simulate the north African climate in order to set up a regional climate model to support management

and adaptation to climate change in Morocco and North Africa, and also, to set up a climate modeling research team within the *International Water Research Institute (IWRI)* of the *College of Agriculture and Environmental Sciences (CAES)* in the UM6P.

The project aims to improve the understanding of water cycle on the continent and assess its variability and changes using climate modelling. As a first step towards improving knowledge of the continent's water resources and so helping to decrease its vulnerability.
In particular, the *Modélisation Climatique* project aim at running LMDZ-ORCHIDEE, the land-surface atmosphere component of the Institut de Pierre Simon Laplace Coupled Model (IPSL-CM, Boucher et al. (2020)) that has been historically and actively involved in the 'CMIP' intercomparison projects, and whose simulations are analyzed by the Intergovernmental Panel on Climate Change (IPCC) to produce climate scenarios. Indeed, the project aims to adapting the LMDZ-ORCHIDEE model to characterize the Moroccan climate variability on the one hand, and to produce reliable future climate scenarios on the other hand, as a first step towards boosting the African climate science through the development of a Regional Climate Model (RCM) covering the whole of the African continent and generating reliable climate information to support decision-making and reduce risks.

1.4 The importance and challenge of developing and evaluating surface-atmosphere coupling parameterizations over semi-arid plains

The interactions between the land surface and the atmosphere is an important component affecting the surface climate, as it controls the exchange of energy, moisture and momentum, thus, it can impact the local weather as well as the climate patterns (Roy and Avissar (2002); Santanello et al. (2018); Gerken et al. (2019)). The land-atmosphere coupling can be defined as the degree to which one variable controls another one (Seneviratne et al. (2010)), for instance, as the solar forcing heats the soil and vegetation and drives turbulent fluxes between the land surface and the atmosphere, the atmospheric boundary-layer's (ABL) composition is altered by these energy fluxes that drive convective processes and deepen the ABL (see Figure 1.6) (Jacobs and De Bruin (1992); Jimenez et al. (2014); Gerken et al. (2019)). On the other hand, soil moisture, surface roughness, albedo, and other biophysical characteristics of the land surface that vary in response to atmospheric forcing (precipitation, solar radiation.. etc) modulate in turn the near surface characteristics (temperature, relative humidity and wind) (Ek and Mahrt (1994); Berg and Sheffield (2019)).

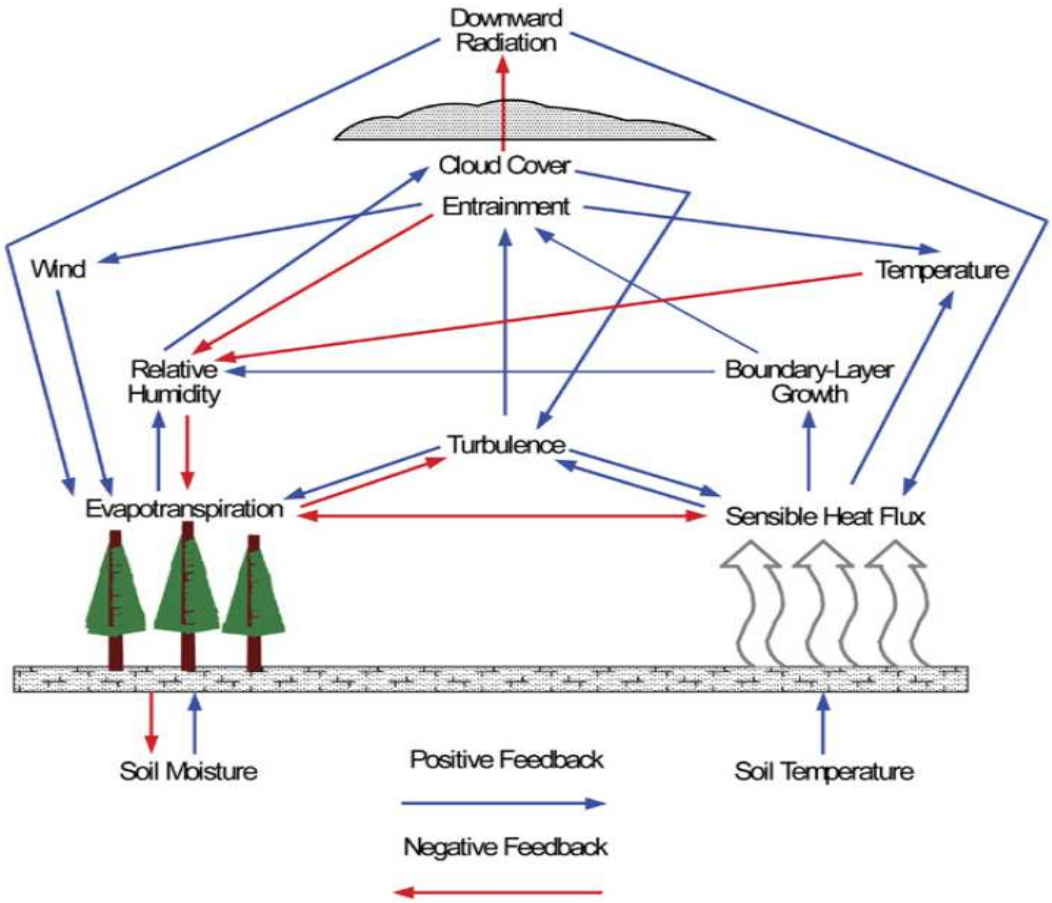

Figure 1.6: Schematic of land surface-atmosphere interactions. Blue arrows indicate a positive feedback that leads to an increase of the recipient variable, and red arrows indicate a negative one (Ochsner et al. (2013))

In recent years, the interactions between the hydrological system and the atmosphere have been subject of wide research (e.g., Seneviratne et al. (2010); Dirmeyer (2011); Berg et al. (2016); Dirmeyer et al. (2018); Berg and Sheffield (2019)). The soil moisture, defined as the amount of water stored in the unsaturated soil zone (Figure 1.7), is a key variable that controls the land energy and water balances through its impact on the energy partitioning at the surface especially over semi-arid regions that are characterized by limited water availability with moisture-limited evapotranspiration (Seneviratne et al. (2010)). Therefore, in the agricultural areas, irrigation increases the plant transpiration and reduces the Bowen ratio[2] due to the increased latent heat flux and decreased sensible flux which can influence directly soil and air temperature (Kueppers et al. (2007); Sacks et al. (2009); Cook et al. (2015)). Boucher et al. (2004) suggested that irrigation can also affect the regional and global radiative balance due to the increased atmosphere humidity that alters the longwave radiation uptake. The irrigation effect can also extend to the atmospheric circulation, Lo and Famiglietti (2013) demonstrated that the resulting water vapor convergence increases precipitation.

The land surface plays a crucial role in influencing extreme events like droughts and heatwaves

[2]The Bowen ratio is defined as the ratio of surface sensible heat flux to the surface latent heat flux: $\beta = \frac{H}{LE}$

(Roundy et al. (2013, 2014); Miralles et al. (2014); Wang et al. (2015); PaiMazumder and Done (2016)) particularly in a changing climate, where such feedback processes may intensify and impact the water availability and ecosystem resilience (Gerken et al. (2019)). For instance, Ferguson and Maxwell (2012) reported the critical impact of irrigation in amplifying the effects of climate change on groundwater storage and stream discharge in semi-arid basins. Hence, realistic representation of the land-atmosphere fluxes and their interaction within the climate system, taking into account the local water management practices in numerical climate models is a prerequisite for accurate climate predictability (Ferguson and Maxwell (2012); Dirmeyer et al. (2018); Santanello et al. (2018); Berg and Sheffield (2019)).

In the irrigated Moroccan plains, accurate parameterization of surface-atmosphere interactions is fundamental, however it faces several challenges, namely, the highly heterogeneous land surface. This latter may generate strong horizontal temperature and pressure gradients, due to the differences in radiative and thermal properties from a location to its surroundings limiting the generalization of measurements (Segal and rritt (1992); Roy and Avissar (2002); Santanello et al. (2018)). Furthermore, the horizontal pressure gradients produced by landscape heterogeneities generate strong mesoscale circulations that can modify the structure of the Planetary Boundary Layer (PBL) (Avissar and Liu (1996); Roy and Avissar (2002)). Additionally, the limited observational data sets add further complexity to the land surface-atmosphere parameterization efforts.

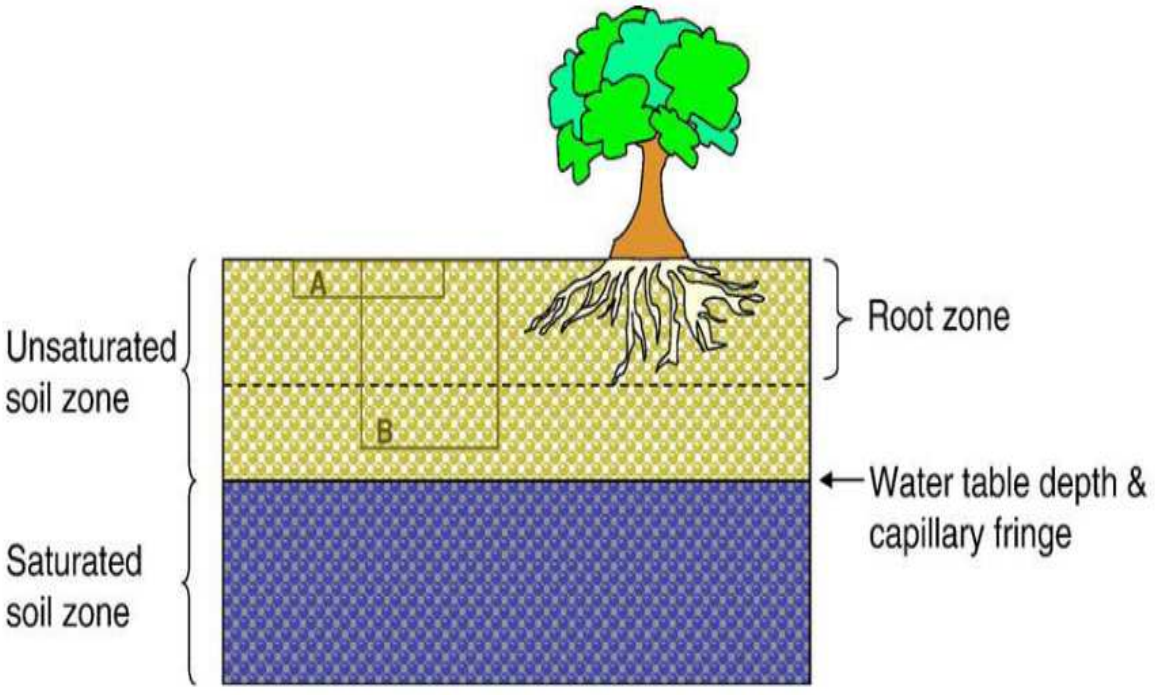

Figure 1.7: Overview of the Root zone with the saturated and unsaturated soil layers (Seneviratne et al. (2010))

1.5 Thesis objectives and outline of the manuscript

In this introduction chapter, we have outlined the Morocco and north Africa's vulnerability to climate change, and the challenging water shortage risks emphasizing the urgent need for adaptive measures. The latter depend closely on the understanding of the present and future climate processes. Indeed, a better knowledge of the land-atmosphere coupling and their representation in GCMs are extremely important to produce accurate future climate scenarios.

Through this thesis, we aim at enhancing our knowledge about the climate of Morocco, with a particular focus on the surface-atmosphere interactions in the Moroccan agricultural plains. We will more particularly focus on the Haouz plain in Marrakech region which stands as one of the key pillars of the country's agricultural sector and which was equipped with meteorological systems making process studies and model evaluations possible. Furthermore, we conduct a thorough analysis and synthesis of the future of surface water hydrology over the Mediterranean and Saharan region using the newly available CMIP6 GCMs. Through this study, we aim at updating the future projections documented above, prior to focusing on the Haouz plain to implement a future scenario with the IPSL-CM land-surface atmosphere components.

Hence, the main objective of the present work is to characterize the physical processes governing the surface climate and the water and energy balance over the Moroccan semi-arid agricultural plains, then, to evaluate and improve their representation in the IPSL-CM model and also to assess the climate future evolution and its sensitivity to the parametrization of key coupling processes.

More specifically, the present thesis aims to answer the following questions:

- **Question 1**: What is the ability of climate models - and more particularly that of IPSL - to simulate the near surface climate over the Moroccan semi-arid agricultural plain ?

- **Question 2**: Which processes control the surface energy and water budgets over the Moroccan semi-arid agricultural regions and how their parameterization in models are efficient and sensitive?

- **Question 3**: How surface climate over the Moroccan semi-arid agricultural plains will evolve in the future and what is the sensitivity of climate scenarios to the parameterization of local processes driving the surface-atmosphere coupling?

In this manuscript, we firstly present the Haouz plain geographic and climatic settings with the meteorological dataset used to evaluate the model (chapter 2). Then, we present the atmospheric model LMDZ coupled with the land surface model ORCHIDEE of the IPSL-CM Earth System Model in chapter 3, with the relevant model physics and a brief description of how LMDZ is coupled to ORCHIDEE. We also present the CMIP6 models and the scientific approach followed in characterizing the future projections over Morocco in the same chapter. Then, chapter 4 presents an in-depth LMDZ-ORCHIDEE evaluation using in-situ data collected over the Haouz plain. Finally, chapter 5 presents climate projections simulated by GCMs and LMDZ-ORCHIDEE.

CHAPTER 2

Observational dataset and climate of the Haouz Plain

Contents

2.1 The Haouz plain 24

2.2 The LMI-TREMA observatory and the meteorological dataset 26

2.2.1 Agdal 26

2.2.2 Agafay 26

2.2.3 R3 27

2.2.4 Meteorological measurements 28

2.3 Characterizing the near-surface climate of the Haouz Plain 30

"What we observe is not nature itself, but nature exposed to our method of questioning".
-Werner Heisenberg

2.1 The Haouz plain

The Haouz plain (8°4'W - 7°5'W; 31°2N - 31°8'N), located at Marrakech-Safi region (Figure 2.1), is a vast agricultural plain of the Tensift basin covering an area of 6000 km^2, stretching approximately 150 kilometers from east to west. The topography is almost flat with slopes not exceeding 5%, the elevation varies from 0 m to the north to about 900 m at the foothills of the Atlas (Ait Hssaine (2019); Rochdane et al. (2022)). Land use in the Haouz plain consists of a mosaic of various plant categories: uncultivated crops, farmed grasslands, and sporadic patches of forests (Figure 2.2), with separate buildings in the eastern and southern parts and around the city of Marrakech. Certainly, it is important to consider these surface heterogeneities in the analysis since they may skew the model-observations comparisons, thus, the model sensitivity to the land cover is one of the key points tackled in section 4.2.

The plain is crossed from south to north by several wadis[1], which are the main tributaries of two major rivers, the Tensift River and the Oum Er Rbia River (Diarra (2017)). There are three sources of water supply in the plain; the first one is the river flows from the High Atlas that receives high precipitation amounts as rain or snow (Boudhar et al. (2010); Le Page et al. (2012)), then, large dams are used to hold water that flows down from the mountains, especially during the rainy season, and it is mostly used to irrigate the plain (Simonneaux et al. (2008)). The second one is the water transfer from the 118 km long *Canal de Rocade* (Figure 2.1) conceived since late 70s to ensure water supply to the city of Marrakech and modern irrigation areas (Kabbaj et al. (1979)). The third one is the groundwater provided by an heterogeneous aquifer with thickness varying from 20 m at the north to 120 m at the south of the plain (Le Page et al. (2012)). The groundwater is extensively used for irrigation in the region, between 2003 and 2006, more than 24000 wells were pumped and the groundwater depth falls by up to 3 m/year in some areas (Abourida et al. (2009); Le Page et al. (2012)). The irrigated land counts over 3000 km^2, and about 38% of the irrigated lands are utilized for tree plantations (olive, citrus, and apricot) frequently mixed with an understory of other annuals (wheat or grass) (Simonneaux et al. (2008); Diarra (2017)).

[1]Wadi is a commonly used word in Arabic to mean "river". A wadi is a stream which only sometimes reaches its maximum capacity, usually during and after a thunderstorm (Sen (2008)).

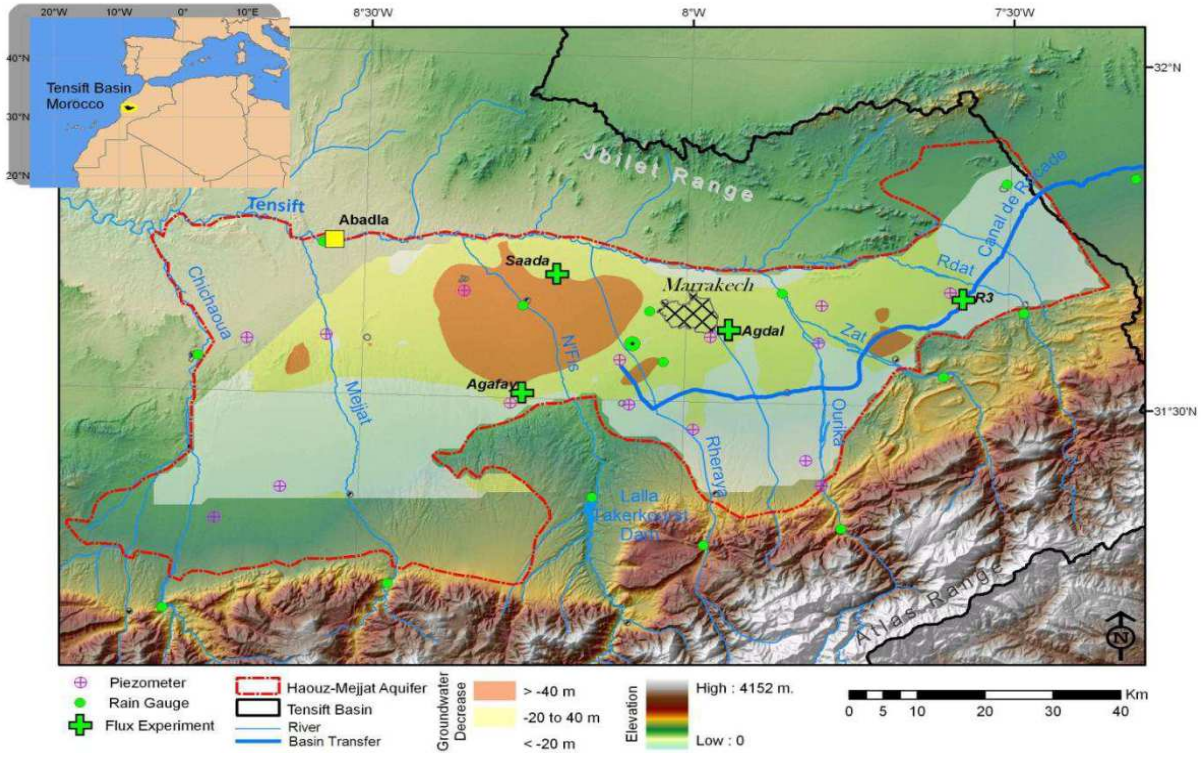

Figure 2.1: Topography of the Haouz plain (the red border) within Tensift basin (black border) with piezometer, rain gauge and tower fluxes superimposed together with a map showing the groundwater decrease between 1972 and 2008 calculated from piezometic levels. (Figure from Le Page et al. (2012))

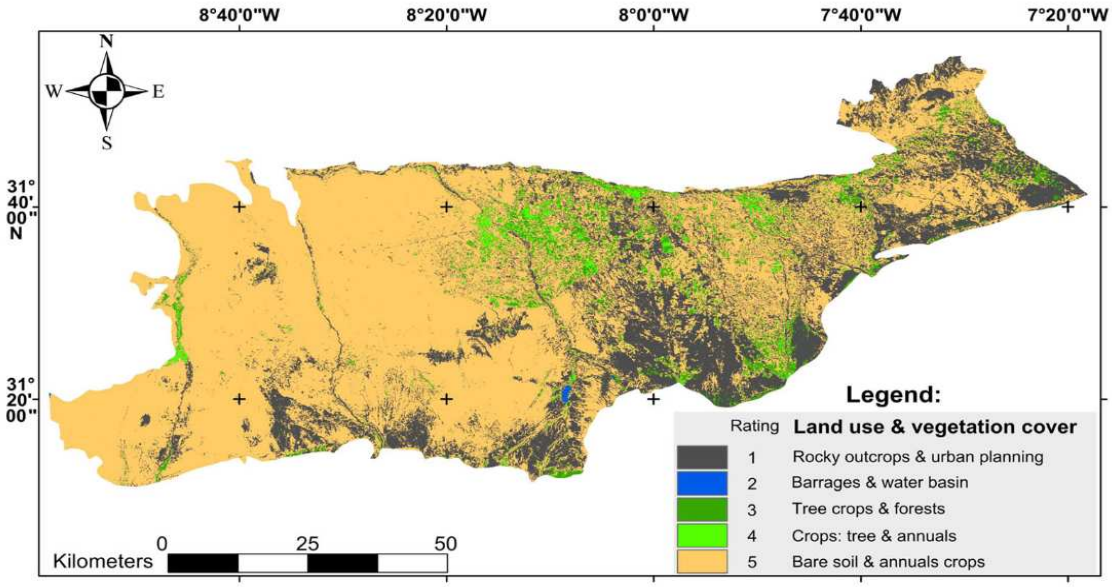

Figure 2.2: Land use and land cover map of the Haouz Plain on 2011 issued from Landsat-5 TM satellite image (Figure from Ait El Mekki and Laftouhi (2016))

2.2 The LMI-TREMA observatory and the meteorological dataset

The Tensift basin was equipped with a meteorological network in the framework of the *SUDMED* program (Chehbouni et al. (2003, 2008)). The SUDMED program was conceived in 2002 and intends to explore the integrated hydrological functioning of the Tensift semi-arid basin in Morocco and help for sustainable management of water resources in the basin (Chehbouni et al. (2008)). The Laboratoire Mixte International de Télédetection et Ressources en Eau en Méditerrannée semi Aride (LMI-TREMA[2]), based at the Cadi Ayyad University of Marrakech, Morocco, was created in 2011 based on a long-standing partnership between the CEnter for the Study of the Biosphere from Space (CESBIO) and actors from Marrakech region within the frame of the *SUDMED* program (Jarlan et al. (2015)). Several weather stations, rain gauges and flux measurements sites have been installed over the plain since 2002 (Figure 2.1) (Le Page et al. (2012)). Contributing to explore the weather conditions and the hydrological functionning of the region (e.g., Ezzahar et al. (2007); Abourida et al. (2009); Le Page et al. (2012); Marchane et al. (2017); Nassah et al. (2018); Zkhiri et al. (2019); Bell et al. (2022)). In order to construct the evaluation dataset, we conducted a rigorous preprocessing to sub-hourly observations provided by the LMI-TREMA observatory. Indeed, we quality controlled the dataset to eliminate the outliers and inconsistencies, identifying and extracting the time intervals where the data exhibited optimal quality for a maximum range of meteorological, energy budget and radiation data. This involved also regular interactions with the colleagues within the LMI who provided valuable insights into the data, facilitating the analysis and interpretation of results.Then, among the dataset we received, we will mostly focus on the following three sites: Agdal, Agafay, and R3 (Figures 2.3, 2.4) since they provide both meteorological data, energy and radiation fluxes. The in situ data from these sites will serve for the model evaluation work. Additional data set from neighbouring stations is briefly commented to characterize the region's climate (section 2.3).

2.2.1 Agdal

Agdal site is a 275 ha olive orchard site located to the south of Marrakech city (7.97390°W; 31.60137°N) (Ezzahar et al. (2007)). Measurements were collected between 2002 and 2004 at the southern area of Agdal within the olive fields of 6m high and an average coverage of 55% (Ezzahar et al. (2007)). For irrigation, each tree is encircled by a tiny earthen levy that collects irrigation water and directs it manually to each tree through a network of ditches. Approximately 80 mm of water was used for each irrigation event, starting from the southern part of the site, it takes around 12 days to move towards the site's northern edge (Ezzahar et al. (2007)).

2.2.2 Agafay

Agafay station is a 38 ha citrus orchards located at 44 km southwest of Marrakech (8.24662°W; 31.50395°N). Measurements were collected between 2006 and 2009 within a mandarin orchard planted in July 2000 (Nassah et al. (2018)). The trees height was about 3m covering around 35% of

[2]https://www.lmi-trema.ma/

the ground. Drip irrigation was used to sustain the crop under excessive watering, during irrigation events, farmers applied about 2 to 9 mm day^{-1} almost every day despite the rainfall events in order to eliminate the soil salinity from the root zone (0.6 m) (Nassah et al. (2018)).

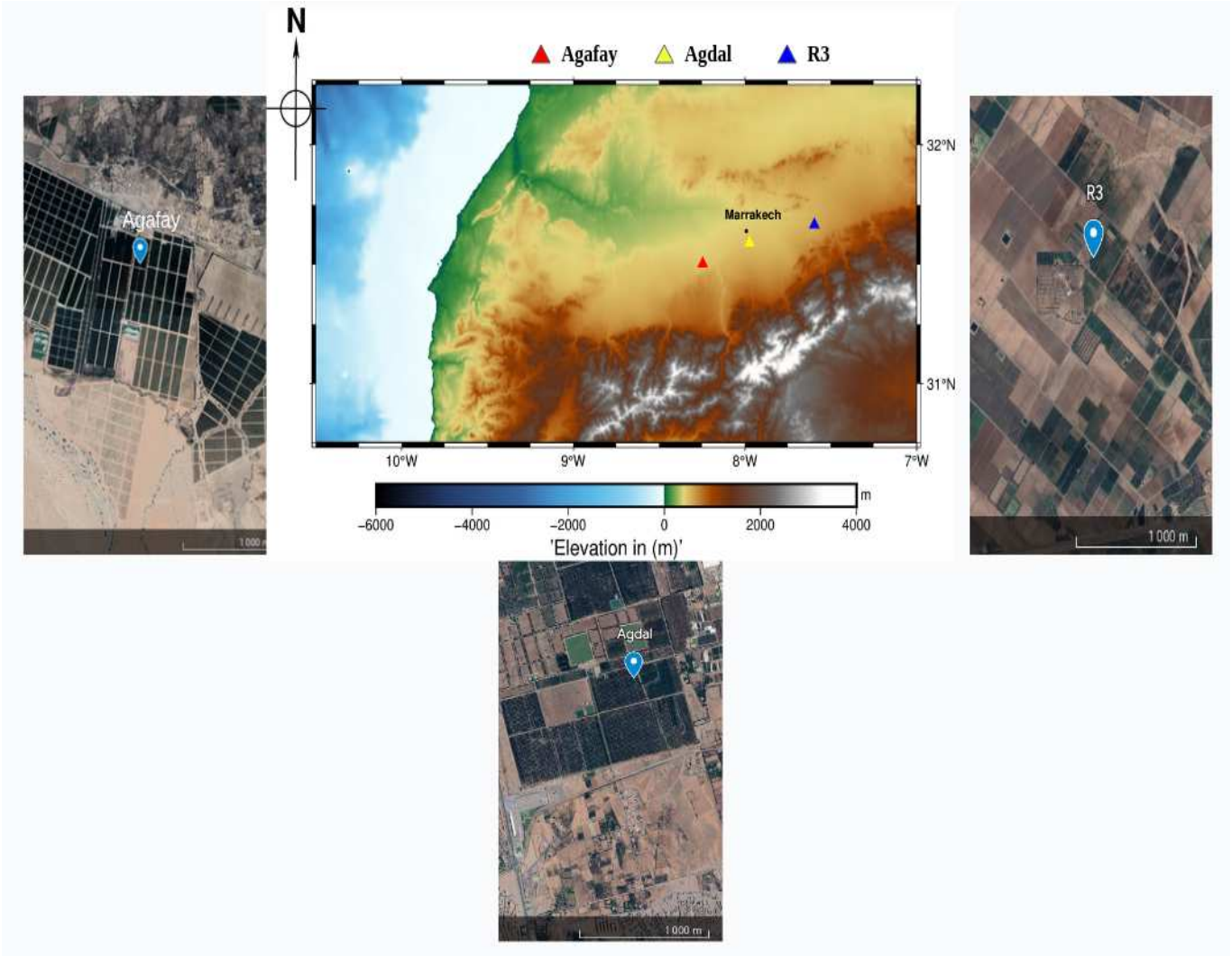

Figure 2.3: Overview of the studied in situ sites location with satellite maps showing their position with respect to the agricultural fields. (Satellite maps from Google Earth)

2.2.3 R3

R3 is an irrigated wheat crop located 40 km East of Marrakech (7.59583°W; 31.66722°N), managed by a regional public agency (Office Régional de Mise en Valeur Agricole du Haouz (ORMVAH)) since 1999. It covers around 2800 ha with the cereals being the main land cover (Duchemin et al. (2006); Er-Raki et al. (2021)). Measurements were collected during the wheat agricultural season (January to May 2003) during which a regularly distributed irrigation was applied; periodic flooding irrigation of about 30 mm per 4 ha was applied regardless of rain events (Er-Raki et al. (2007)).

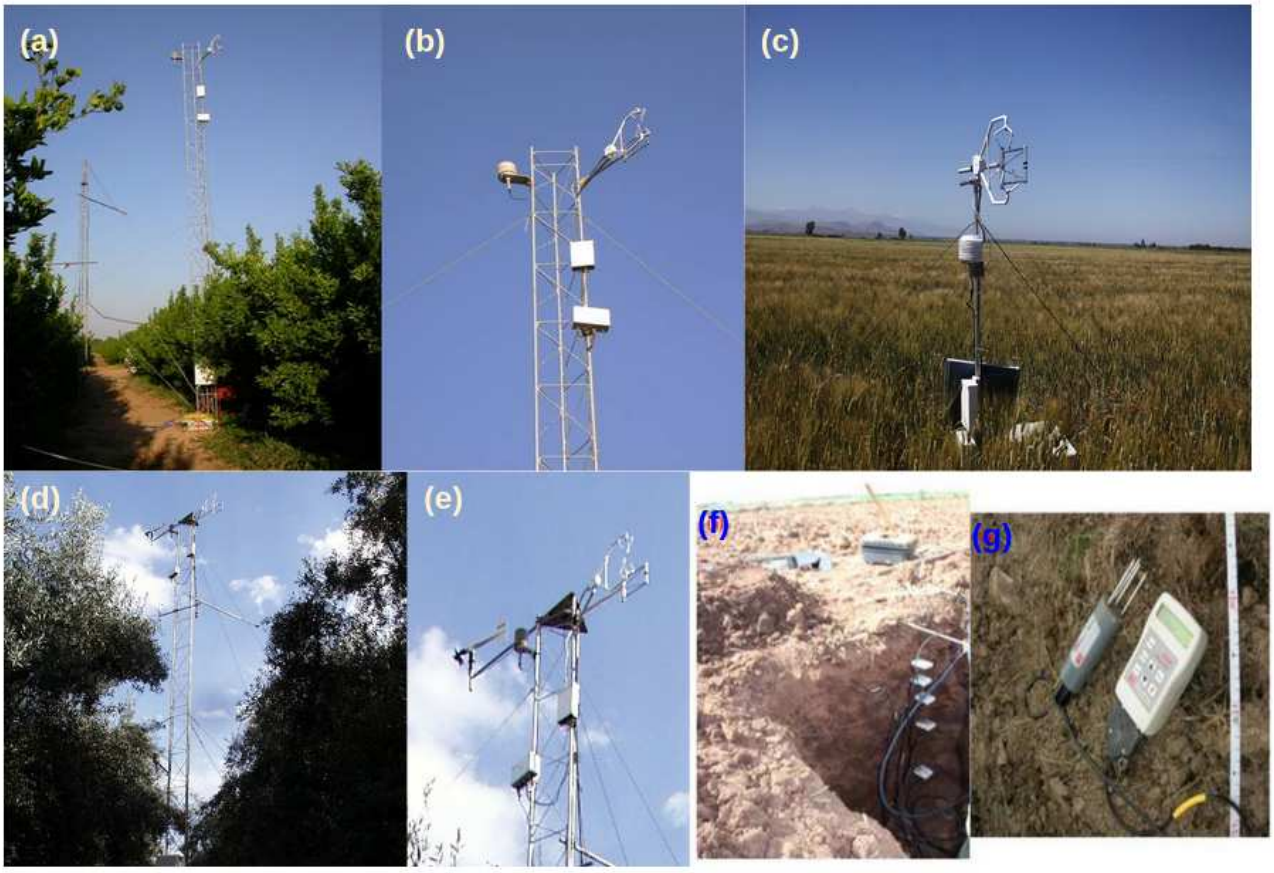

Figure 2.4: Photograph of the sonic anemometer in Agafay **(a,b)**, R3 **(c)** and Agdal site **(d,e)** with an example of the the Time Domain Reflectometry instrument **(g)** planted at different soil depths **(f)** over the three sites (Copyright: LMI-TREMA).

2.2.4 Meteorological measurements

Over each site, 30 min measurements of meteorological data were collected: air temperature and humidity were measured with a Campbell Scientific HMP45C probe. Wind speed and direction were measured using a Young Wp200 anemometer at 1.3m, 2m and 3.25m in R3, Agafay and Agdal respectively above the vegetation height, this latter ranges on average to 6m (Agdal) and 3m (Agafay). In R3 it reaches around 0.7m during the growing season (see table 2.1). Precipitation was collected with a Campbell FSS500 tipping bucket automatic rain gauge and the radiation components were measured with a Kipp and Zonen CNR1 radiometer (Er-Raki et al. (2021)). Surface temperature (Ts) was calculated based on the Stefan-Boltzman law, using a surface emissivity ϵ of 1:

$$Ts = \left(\frac{LW_{up} + (\epsilon - 1)LW_{dn}}{\epsilon\sigma}\right)^{1/4} \tag{2.1}$$

Where σ is the Stefan-Boltzman constant, LW_{dn} and LW_{up} are the downward and upward longwave radiative fluxes respectively.

The sensible and latent heat fluxes were measured using the Eddy Covariance system (EC) installed

over each station. Figure 2.5 shows the footprint for the prevailing wind direction of the EC system at Agdal station. EC systems over the three stations are made up of a 3D sonic anemometer (CSAT3, Campbell Scientific Ltd.) that measured temperature and wind velocity component fluctuations, with an open-path infrared gas analyzer (Li7500, Licor Inc.) that measured carbon dioxide and water vapor concentrations. Data were sampled at a rate of 20 Hz and were recorded using CR23X data loggers (Campbell Scientific Ltd.) (Er-Raki et al. (2007); Ezzahar et al. (2007); Nassah et al. (2018)). Soil moisture was recorded at different soil depths (from 5 to 80 cm) using CS-616 Time Domain Reflectometry (TDR) that draws a linear relationship between the dielectric constant of the soil ϵ and its volumetric water content $\theta[m^3m^{-3}]$ as follows:

$$\sqrt{\epsilon} = a_0 + a_1\theta \tag{2.2}$$

Detailed technical informations of the data are summarized in Table 2.1

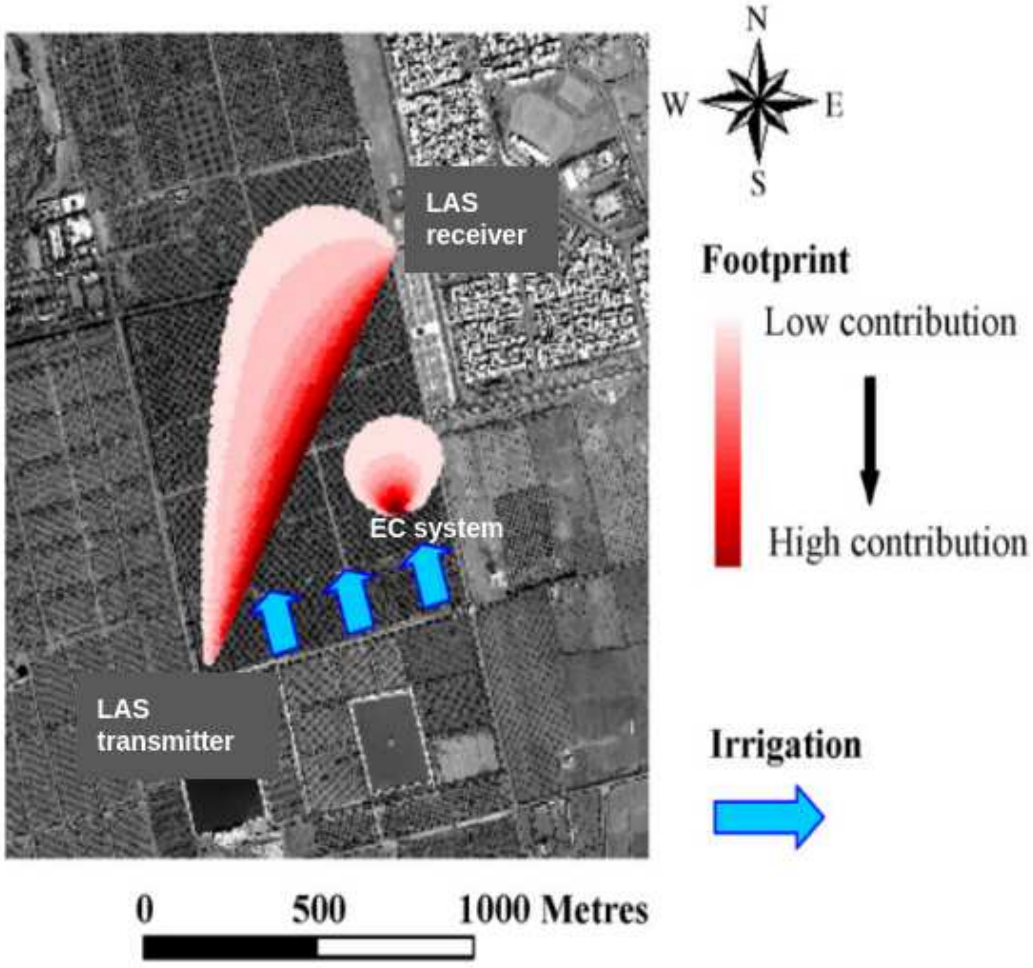

Figure 2.5: Location and footprint of the EC system installed at Agdal station (corresponding to 95% of the sensible heat flux), with irrigation orientation. (Figure adapted from Ezzahar et al. (2007))

Table 2.1: Characteristics of the in situ measurements in the three sites Agdal, Agafay and R3

Quantity	Instrument	Height from vegetation top
Air temperature (T)	Vaisala HMP45AC probe	2 m
Relative humidity (RH)	-	-
Wind direction / Wind speed (U)	Young Wp200 anemometer	3.25 m (Agdal) 2 m (Agafay) 1.3 m (R3)
Precipitation	TRP525M Rain gauge	1 m
Sensible heat flux (H)	20Hz 3D sonic thermo-anemometer (CSAT3) and open-path infrared gas analyzer (Li7500, Licor Inc)	3.25 m (Agdal) 5.5 m (Agafay) 1.3 m (R3)
Latent heat flux (Le)	-	-
Friction velocity (u*)	-	-
Downward shortwave radiation (SWdn)	CNR1 radiometer	2 m
Upward shortwave radiation (SWup)	-	-
Downward longwave radiation (LWdn)	-	-
Upward longwave radiation (LWup)	-	-
Skin surface Temperature (Ts)	-	-
Soil moisture	CS616 water content reflectometer	5 cm depth

2.3 Characterizing the near-surface climate of the Haouz Plain

The regional climate in the Haouz plain is arid to semi-arid with temperature varying from -7.2 °C to 48.2 °C with an annual average of 27.8 °C, and low and irregular rainfall, characterised by episodic dry spells and high temporal and spatial heterogeneity reflecting that of the topography (Figure 2.6) (HAJHOUJI (2018)). From 1962 to 2015, average precipitation recorded in the High Atlas is around 530 mm yr^{-1} whereas it is less than 200 mm yr^{-1} in Marrakech site (HAJHOUJI (2018)), with evaporative demand of up to 1600 mm yr^{-1} (Er-Raki et al. (2010)).

We leveraged the LMI-TREMA dataset to make a short updated climatology of the Haouz plain, Figure 2.8 represents the 2004-2020 seasonal cycle of temperature and precipitation of four selected sites in the Haouz plain (Figure 2.7): Chichaoua (8.65°W;31.42°N) wheat irrigated field located 70 km western Marrakech city, Graoua (7.91°W;31.58) located 10km southern Marrakech , Agafay (8.24662°W; 31.50395°N) and Aremd (7.92°W;31.12°N). This latter is located 70km southern Marrakech at the Atlas mountain. These four sites have been carefully selected as they provide a relatively

long time series of the meteorological data.

From January to December, the cycle begins with relatively lower temperatures during winter (< 20°C), gradually increasing through spring and summer to reach their peaks during the summer months with up to 28°C in Chichawa, Grawa and Agafay and around 23°C in Aremd, reflecting the region's typical arid conditions. Aremd Station, situated in highland (2058m altitude), shows cooler temperatures throughout the year aligned with higher amounts of rainfall compared to surrounding lowland areas, due to a possible orographic effects. Indeed, summer rainfall is very low at the lowland stations, but it reaches up to 50mm in Aremd. In winter, the monthly total rainfall varies between 20 and 50 mm in Chichaoua, Graoua and Agafay stations and exceeds 80 mm at Aremd.

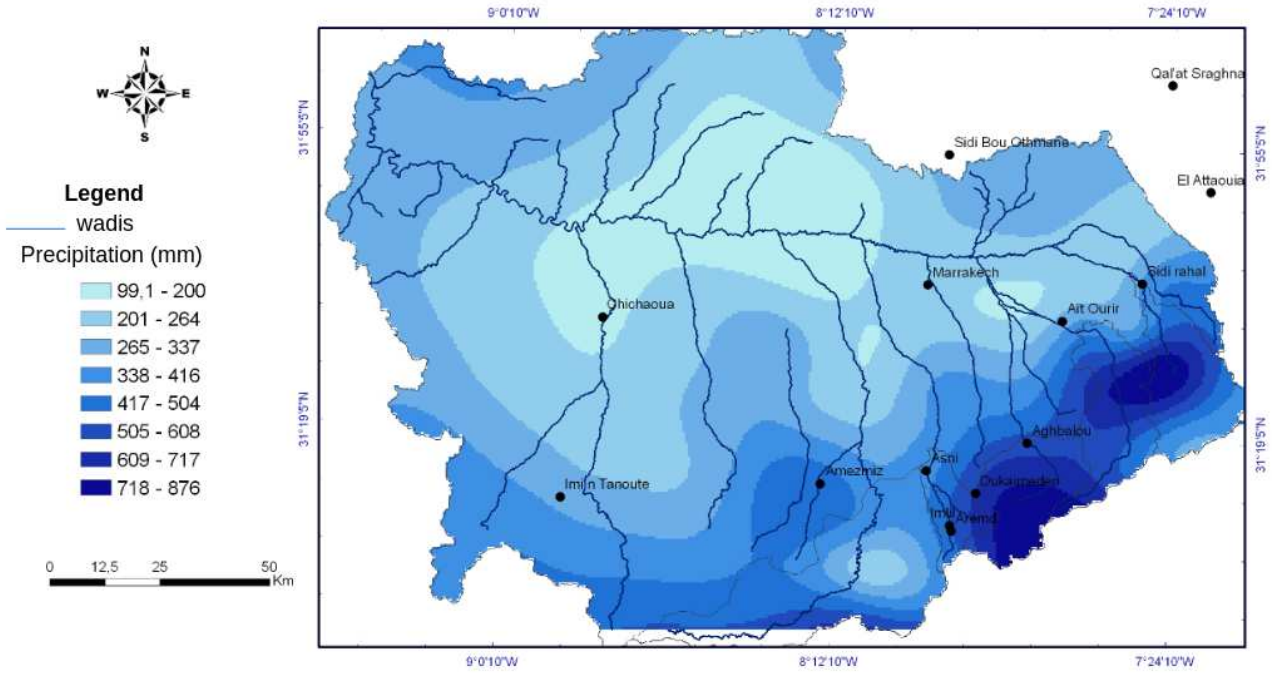

Figure 2.6: Annual rainfall distribution in the catchments of Tensift basin between 1972 and 2000 (adapted from Boudhar (2010))

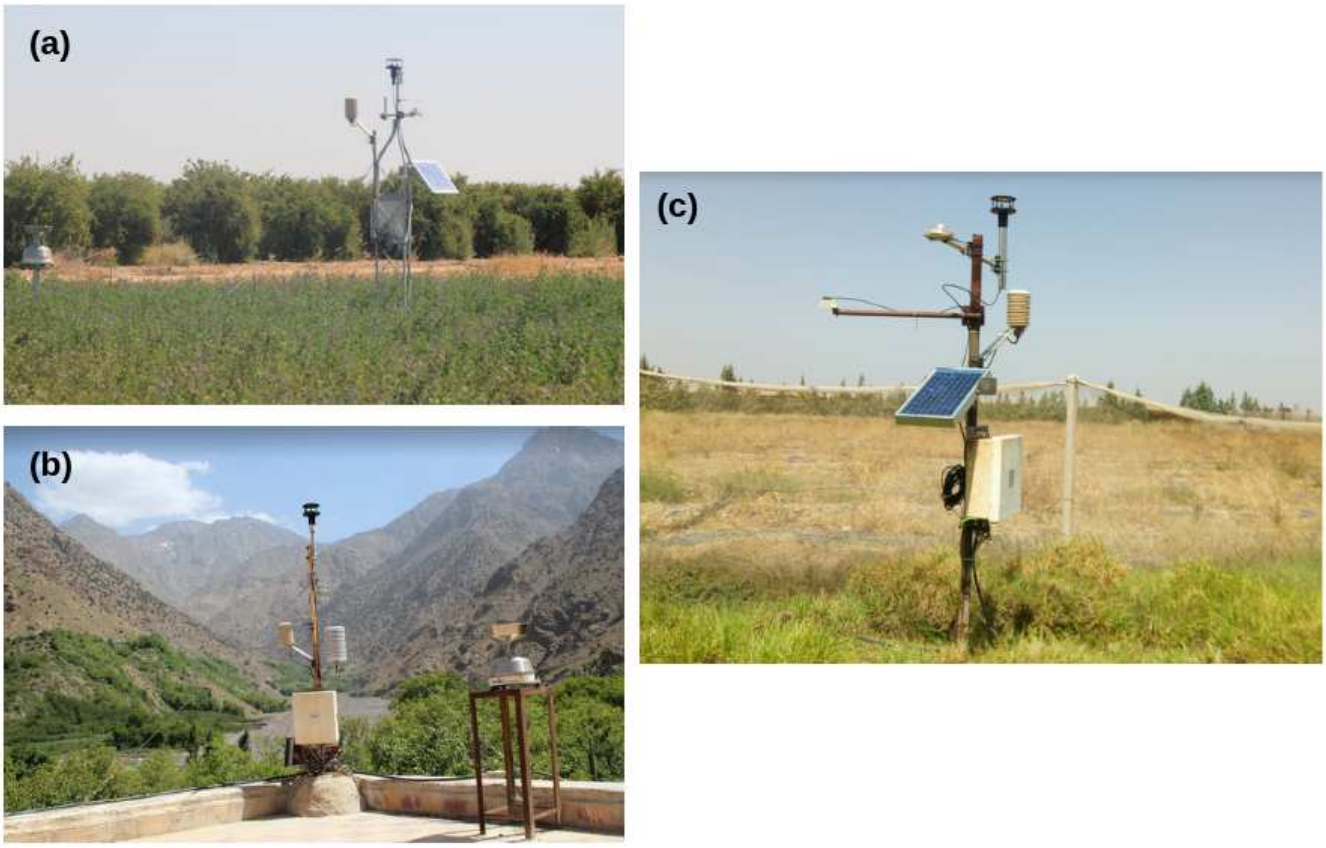

Figure 2.7: Overview of the instrumented stations Chichawa (a), Aremd (b) and Grawa (c) (Figures from http://trema.ucam.ac.ma/Obs_TREMA)

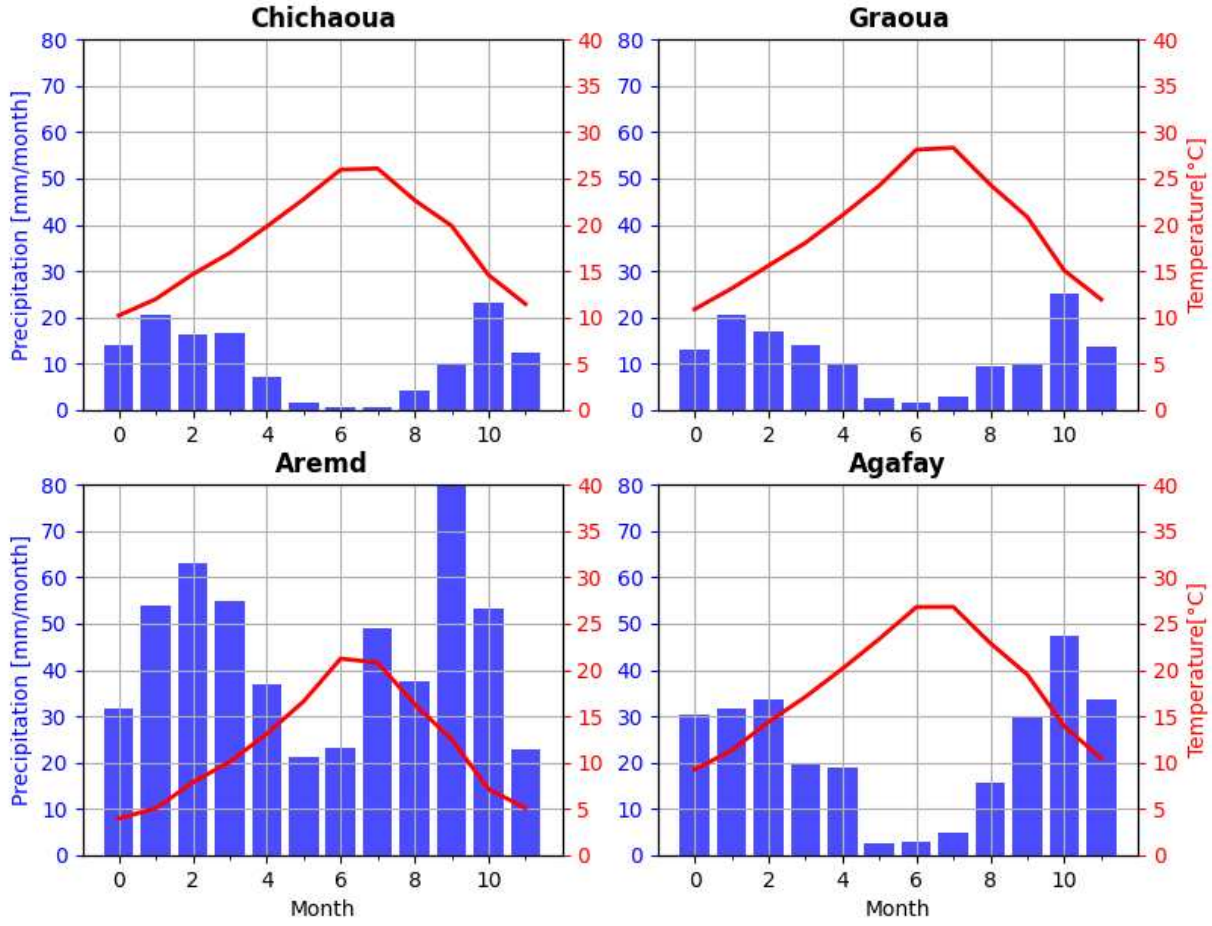

Figure 2.8: Seasonal cycles of mean temperatures (curves) and cumulative rainfall (bars) at Chichaoua, Graoua, Aremd and Agafay stations between 2004 and 2020

CHAPTER 3

Modeling tools and simulations

Contents

3.1 Preface **35**

3.2 CMIP6 models **35**

3.3 Surface layer and coupling of the LMDZ atmospheric component **36**

3.4 ORCHIDEE land surface model **40**

3.5 LMDZ-ORCHIDEE coupled model **42**

3.6 Simulations set-up **43**

"Science is not only a disciple of reason but, also, one of romance and passion"
-Stephen Hawking

3.1 Preface

The Earth's climate is a complex ecosystem made up of a finite number of key elements: the atmosphere, the hydrosphere, the cryosphere, the geosphere and the biosphere.

Climate models are computer programs performed to produce numerical simulations of changes in the atmosphere's conditions (Hourdin and Guillemot (2021)). The General Circulation Models (GCMs) represent the dynamics of momentum, energy and water using the fundamental laws of physics, based on approximate forms of the equations which govern the circulation of the atmosphere above the earth's surface (the dynamical core), and of the other processes affecting the Earth's climate such as solar radiation, clouds, rain... etc (Hourdin and Guillemot (2021)). Since the mid-1950s, the evolution of computing technologies allowed scientists to develop models simulating the climate system as a whole, through coupling several models, each describing a specific component of the climate system. The models formed are referred to as the Global Climate Model (GCMs). They serve to predict the weather situation for a few days, but also, for longer time scales ranging from years to several decades or even millennia. Those models have been developed to include further processes such as the biogeochemical cycles, and they are called Earth System Models (ESMs).

3.2 CMIP6 models

In order to provide a comprehensive study of the surface water supply projections over the Mediterranean and Sahara as simulated by the most recent GCMs from the sixth CMIP exercise, we conducted an in-depth study analyzing how these models respond to climate change in the Mediterranean and North African region. We have used outputs from 17 GCMs included in the CMIP6 database (https://esgf-node.llnl.gov/search/cmip6/), for both the "historical" (1850–2014) simulations and the low and high-end forcing Shared Socio-economic Pathways "SSP2-4.5" and "SSP5-8.5" (2015–2100) from Scenario Model Intercomparison Project (ScenarioMIP) (O'Neill et al. (2016)). SSP2-4.5 (+4.5 W m^{-2}; 2015-2100) is the updated scenario of the so-called RCP4.5 used in CMIP5 with a moderate level of greenhouse gas emissions, SSP5-8.5 (+8.5 W m^{-2}; 2015-2100) is the updated scenario of the so-called RCP8.5 that considers a world with a strong reliance on fossil fuels (Gillett et al. (2016); Li et al. (2020)). The historical simulations are forced with a combination of natural (e.g., solar variability, volcanic aerosols) and anthropogenic (e.g., greenhouse gas emissions and aerosols) climate forcings (Eyring et al. (2016); Cook et al. (2020)).

CMIP5 models response to climate change is also assessed in our study, then, for the sake of fairness in our comparative study, we selected the available set of climate models from CMIP5 and its updated version of CMIP6 (Table 6.1). Selected models cover the period from 1850 to 2100 (historical + SSP) (Table 3.1) which provide the following output variables: precipitation rate, evapotranspiration and surface soil moisture. Although the scope of our study is limited to the surface water supply terms and the surface water evolution, we will also briefly comment on the behavior of the total soil moisture which provides further informations on the hydrological response of the deeper soil layer. Analyses are conducted over the Mediterranean (MED) and Sahara (SAH) subregions as defined for the IPCC's

sixth assessment (Iturbide et al. (2020)). Further details about the protocole followed are in chapter 5.

Table 3.1: List of the CMIP6 and CMIP5 models used in our study with the nominal resolution

CMIP6 models	lon x lat	CMIP5 models	lon x lat
BCC-CSM2-MR	1.1° x 1.1°	-	-
CAMS-CSM1-0	1.1° x 1.1°	-	-
CESM2	1.3° x 0.9°	-	-
CESM2-WACCM	1.3° x 0.9°	-	-
CMCC-CM2-SR5	0.9° x 1.2°	CMCC-CM	0.75° x 0.75°
MPI-ESM1-2-HR	0.9° x 0.9°	MPI-ESM-MR	1.8° x 1.8°
MRI-ESM2-0	1.1° x 1.1°	MRI-ESM1	1° x 0.5°
NorESM2-MM	1.2° x 0.9°	NorESM1-M	1° x 0.5°
TaiESM1	0.9° x 1.25°	-	-
CNRM-CM6-1	1.4° x 1.4°	CNRM-CM5	1.4° x 1.4°
CNRM-ESM2-1	1.4° x 1.4°	-	-
GISS-E2-1-G	2° x 2.5°	GISS-E2-R	2° x 2.5°
IPSL-CM6A-LR	2.5° x 1.3°	IPSL-CM5A-LR	2.5° x 1.3°
MIROC6	1.4° x 1.4°	MIROC5	1.4° x 1.4 °
MPI-ESM1-2-LR	1.9° x 1.9°	MPI-ESM-LR	1.8° x 1.8°
NorESM2-LM	2.5° x 1.9°	-	-
UKESM1-0-LL	1.9° x 1.3°	-	-

3.3 Surface layer and coupling of the LMDZ atmospheric component

In order to regionalize the climate over the Moroccan plains, we use the Laboratoire de Météorologie Dynamique model, with a stretchable horizontal grid (LMDZ, "Z" for the Zoom), the atmospheric component of the IPSL-CM, coupled with the land surface model ORCHIDEE (section 3.4). LMDZ has been developed since 80s by Sadourny and Laval (1984). The LMDZ dynamical core integrates the primitive equations of the atmospheric circulation over time and space on a rectangular horizontal grid in the longitude-latitude plane. The physical core computes the vertical radiative transfer and small-scale movements, convection and clouds within a grid-cell (Hourdin and Guillemot (2021)). In the vertical, the model discretization uses the so-called hybrid sigma-pressure coordinate (Boucher et al. (2020)). This thesis is based on the CMIP6 version of the atmospheric model LMDZ (LMDZ6A), where a “New Physics” package was improved relative to its CMIP5 version (Hourdin et al. (2013)). The LMDZ6A is based on a complete revision of the turbulence, convection, and clouds parameterizations (Boucher et al. (2020)).

LMDZ can be run solely or coupled to one or several components of IPSL-CM, each one corresponds to a sub-surface type of LMDZ as shown in Figure 3.1:

- The land surface model **ORCHIDEE**.
- The ocean model **NEMO**, or sea surface temperature forcing.
- The sea ice model **LIM**.
- The land ice model incorporating the land glaciers and ice sheets.

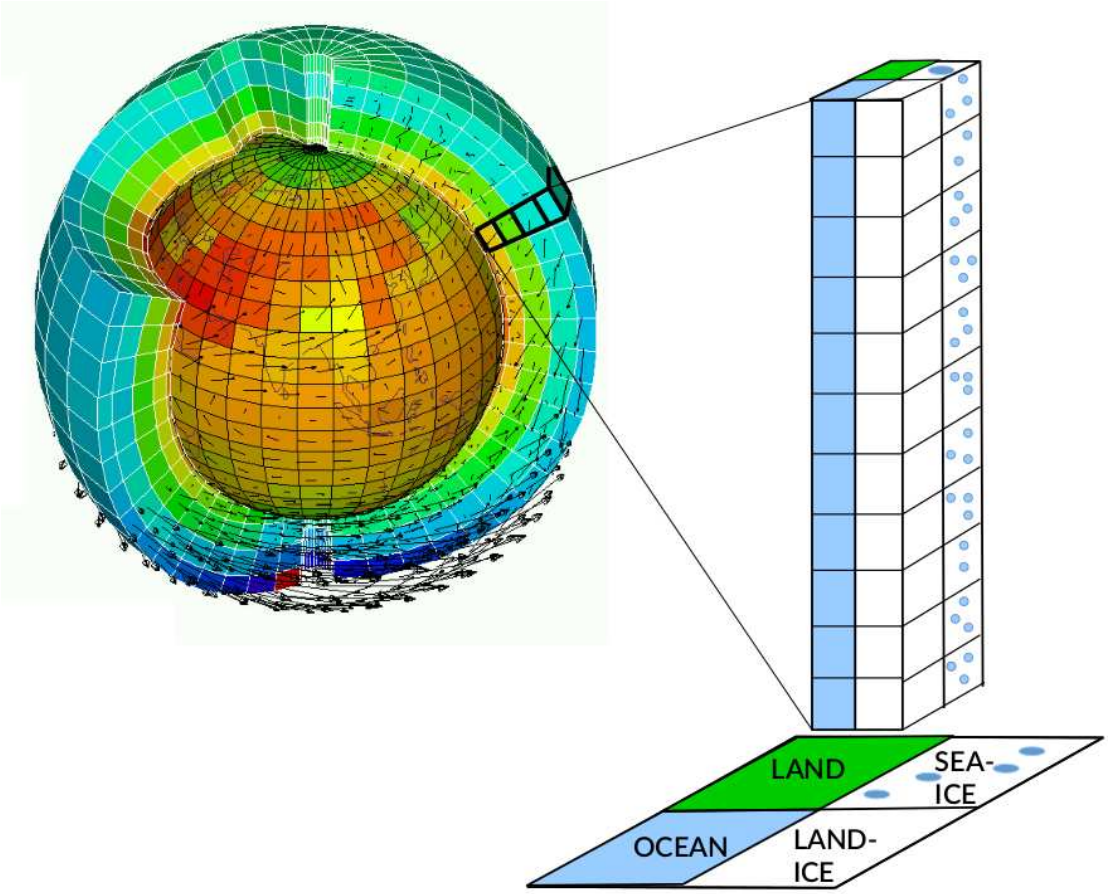

Figure 3.1: The sub-surfaces treatment in LMDZ. (Figure from Vignon (2017))

The boundary layer processes are handled for each sub-surface (Vignon (2017)) and then mixed at the first atmospheric level of the model (Cheruy (2018)). The vertical diffusion is treated independently for each one of the sub-surfaces (Cheruy (2018)). The time evolution of a state variable X (being T, U, V or Q) associated to turbulent diffusion equation reads:

$$\frac{\partial X}{\partial t} = -\frac{1}{\rho}\frac{\phi_X}{\partial z} \tag{3.1}$$

The parametrization of the vertical turbulent flux $\rho\overline{w'q'}$ of a scalar q (the wind components, the virtual potential temperature or the specific humidity) reads:

$$\rho\overline{w'q'} = \rho\hat{\alpha}\hat{w}(\hat{q} - q) - \rho K_q \frac{\partial q}{\partial z} \tag{3.2}$$

Where z is the height, ρ is the air density, $\hat{\alpha}$ is the fraction of the horizontal surface covered by ascending plumes, $\hat{w}$ is the turbulent vertical velocity in the thermals, $\hat{q}$ is the value of q in the plume and K_q is a local turbulent diffusion coefficient (Vignon et al. (2017)). The term $\rho\hat{\alpha}\hat{w}(\hat{q}-q)$ corresponds to the non-local mixing, parametrized with a mass flux representation called "Thermal Plume Model" (Hourdin et al. (2002); Rio et al. (2010); Jam et al. (2013); Hourdin et al. (2019)). The local turbulent diffusion term $(-\rho K_q \frac{\partial q}{\partial z})$ is parameterized using a 1.5 order closure K-gradient scheme based on Yamada (1983) revisited in Vignon et al. (2017).

The surface turbulence fluxes in LMDZ are based on the Monin-Obukhov (MO) similarity theory (Monin and Obukhov (1954)) (See the highlighted box at the end of this section). The sensible (H) and latent heat (Le) fluxes are calculated using a bulk formula between the surface and the first model level as follows:

$$H = \rho_1 c_p C_h U_1 (\theta_{v1} - \theta_s) \tag{3.3}$$

$$Le = \rho_1 \beta L_{vap} C_h U_1 (q_{v1} - q_{s,sat}) \tag{3.4}$$

with c_p is the specific heat of air at constant pressure, β is the aridity coefficient, L_{vap} is the latent heat of vaporization. ρ_1, U_1 ,q_{v1} and θ_{v1} are the air density, the wind speed, the specific humidity and the virtual potential temperature at the first model level respectively; θ_s and $q_{s,sat}$ are the virtual potential temperature and the saturation specific humidity at the surface; C_h is the drag coefficient for heat, and reads:

$$C_h = \frac{\kappa^2}{\ln(z_1/z_{0m})\ln(z_1/z_{0h})} \times f_h(Ri_b) \tag{3.5}$$

Where $z_1$is the first model level height, z_{0m} and z_{0h} are the roughness lengths for momentum and heat respectively, $\kappa = 0.41$ is the Von Kármán constant and f_h is the stability function of the bulk Richardson number Ri_b between the first model level and the surface (Vignon et al. (2017)). The stability function f_h in CMIP6 version is set to a more realistic "short-tail" version from King et al. (2001) shown to enhance modelled Antarctic surface climate, instead of the default one from Louis et al. (1982) (Cheruy et al. (2020)). It reads:

$$f_h(Ri_b) = \begin{cases} (1 - Ri_b/c_2)^2 & Ri_b < c_2/2 \\ c_3 * (c_2/Ri_b)^2 & Ri_b \geq c_2/2 \end{cases} \tag{3.6}$$

with $c_2 = 0.25$ and $c_3 = 0.0625$

In the coupled mode, the drag coefficient C_h is calculated in LMDZ, using the roughness heights computed by the land surface model ORCHIDEE at each time-step (section 3.4). The 'aridity coefficient' (β), also computed by ORCHIDEE, is a function of total soil moisture (θ_t) as follows:

$$\beta = \begin{cases} 1 & \theta_t > \theta_c \\ \frac{\theta_t}{\theta_c} & \theta_t \leq \theta_c \end{cases} \tag{3.7}$$

Where, $\theta_c = 0.5 \times \theta_{tmax}$, critical amount of soil moisture, above which evapotranspiration reaches the potential rate (E_p), this latter is a function of the gradient of specific humidity between the surface

and the overlying air (Coindreau et al. (2007); Fita (2013)):

$$E_p = \rho \frac{q_{sat}(T_g) - q_a}{r_a} \tag{3.8}$$

The radiative scheme in LMDZ is inherited from the ECMWF weather forecast model (Hourdin et al. (2020a)), where a k-correlated Rapid Radiative Tranfer Model (RRTM) model (Mlawer et al. (1997); Michael J Iacono (2011)) with 16 spectral bands was introduced in LMDZ for the longwave spectrum. A new radiative code (ECRAD) is currently being implemented in LMDZ. In particular, this code enables radiation-cloud interactions to be handled more physically.

A note on fundamentals of the Monin Obukhov's theory

The MO similarity theory uses dimensional analysis following the Buckingham's π-theorem[a] (Foken (2008)). The MO theory proposes that the mean gradients and other statistical parameters become a universal functions of z/L (Cheruy (2018)). L, the so-called 'Obukhov length', is a scaling parameter that can be interpreted in unstable situation as being proportional to the height above the surface at which the buoyancy effects dominate the mechanical effects (shear). It reads:

$$L = \frac{\bar{\theta_v}}{g} \frac{u*^2}{\kappa \theta_v *} \qquad with \qquad u* = (\frac{\tau}{\rho})^{1/2} \tag{3.9}$$

With κ is the Von Kármán constant, g is the acceleration of gravity and z is the height of the first model layer, τ is the surface stress and d is the displacement height taken equal to 2/3 of the canopy height. With U and θ having the following vertical gradients respectively:

$$\frac{\partial U}{\partial z} = \frac{u*}{\kappa z} \phi(\frac{z}{L}) \tag{3.10}$$

$$\frac{\partial \theta}{\partial z} = \frac{\theta*}{\kappa z} \phi(\frac{z}{L}) \tag{3.11}$$

With $\theta* = -(\bar{w}'\theta')/u*$, z_{0m} and z_{0h} are the so called aerodynamical roughness lengths for momentum and heat respectively, defined such as U ($z = z_{0m}$) = 0 and $\theta_v(z = z_{0h}) = \theta_{vs}$. U is the wind speed at z, θ_v is the virtual potential temperature at z and θ_{vs} is the virtual potential temperature at z_{0h}. ψ_m and ψ_h are the integrated form of the stability correction functions for momentum and sensible heat transfer, respectively:

$$\psi_{m,h}(x) = \int_0^x (1 - \phi_{m,h}(X))/X dX \tag{3.12}$$

Assuming that turbulent fluxes are constant and independent of the distance from the surface, the MO similarity theory predicts a pseudo-logarithmic form for the wind speed U and potential

temperature θ profiles as follows:

$$U(z) = \frac{u*}{\kappa}[\ln(\frac{z-d}{z_{0m}}) - \psi_m(\frac{z-d}{L}) + \psi_m(\frac{z_{0m}}{L})] \tag{3.13}$$

$$\theta_v - \theta_{vs} = \frac{\theta*}{\kappa}[\ln(\frac{z-d}{z_{0h}}) - \psi_h(\frac{z-d}{L}) + \psi_h(\frac{z_{0h}}{L})] \tag{3.14}$$

[a]Buckingham's π-theorem (Kantha and Clayson (2000)) states that for n+1 dependent parameters and k independent dimensions, there exist exactly n+1-k dimensionless parameters which characterize the process. For further details, we refer the reader to the supplement 2.3 of Foken (2008)

3.4 ORCHIDEE land surface model

ORCHIDEE (ORganizing Carbon and Hydrology In Dynamics EcosystEm) is a dynamical global vegetation model, developed by the IPSL, which represents the mass, momentum and energy fluxes between the surface and the atmosphere (Krinner et al. (2005)). It is based on two main models: 1) the SECHIBA (Schématisation des Échanges Hydriques à l'Interface Biosphère Atmosphère; Ducoudré et al. (1993)) hydrological model that computes the soil water content as well as the energy and water exchanges between the atmosphere and the surface. 2) the STOMATE (Saclay Toulouse Orsay Model for the Analysis of Terrestrial Ecosystems; Botta et al. (2000)) carbon cycle model that represents photosynthesis processes, carbon allocation, litter decomposition and phenology (Krinner et al. (2005)).

In ORCHIDEE, the soil hydrology is discretized into 11 layer for a 2m depth (panel b in Fig. 3.2) instead of the two-layer bucket model used previously in the CMIP5 IPSL-CM5 model version (Boucher et al. (2020)). In each single grid-cell, vegetation is described using 15 plant functional types (PFTs) classified into three soil tiles sharing the same physiological behavior (see panel a of Figure 3.2) (Boucher et al. (2020)): **bare soil**, **forests** (tropical broadleaf evergreen, tropical broadleaf raingreen, temperate needleleaf evergreen, temperate broadleaf evergreen, temperate broadleaf summergreen, boreal needleleaf evergreen, boreal broadleaf summergreen, boreal needleleaf deciduous) and **grasses** (temperate natural grassland (C3), natural grassland (C4), crops (C3), crops (C4), tropical natural grassland (C3) boreal natural grassland (C3))[1].

In a single mesh, the vegetation fraction of a given PFT is determined by its maximum fraction F_{PFT} prescribed by a map and the Leaf Area Index (LAI) parametrized with STOMATE following Monsi and Saeki (1953):

$$F_{PFT} = F_{maxPFT}(1 - e^{k*LAI}) \tag{3.15}$$

With k is the extinction coefficient set at 0.5 in ORCHIDEE. Within a grid cell, the three PFTs soil tiles share a unique energy and snow budget, however, the water budget is computed independently for each tile. For a finite soil layer, ORCHIDEE computes the total water stock W as a function of total precipitation P (rainfall and snowfall), surface runoff R, the drainage to groundwater D and evapotranspiration E (panel a of Fig. 3.2).

[1]https://orchidas.lsce.ipsl.fr/dev/lccci/orc_15pft.php

$$\frac{\partial W}{\partial t} = P - R - D - E \tag{3.16}$$

The surface roughness height (z_0) in ORCHIDEE was initially computed as constant values for each of the plant functional types (see Table 3.2). In the CMIP6 version, the surface roughness height is now parameterized as a function of the LAI and the vegetation height based on an internal canopy turbulence model developed by Massman (1999) and evaluated by Su et al. (2001). At the time of writing this manuscript, an ongoing discussion about the formulation of the roughness height in ORCHIDEE model is held within the ORCHIDEE team. Since the CMIP6 release, some studies (including our research, see section 4.2) have revealed biases in the simulated surface drag. Therefore, the calculation method of the surface roughness heights in ORCHIDEE is currently subject of discussion.

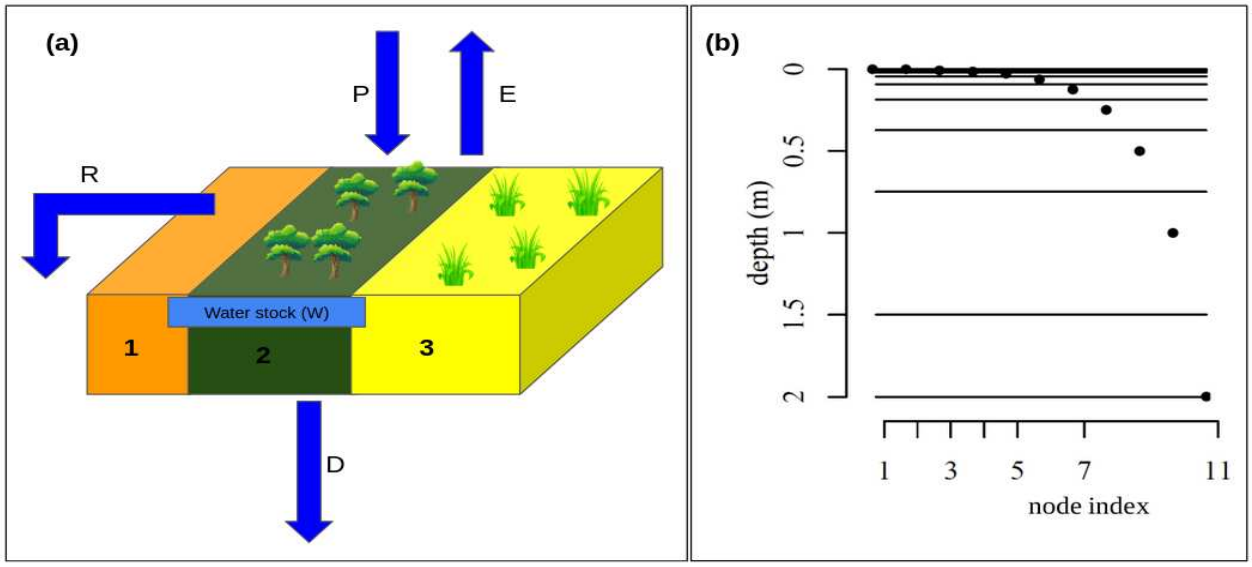

Figure 3.2: **a)**: Overview of the three soil tiles of the ORCHIDEE land surface model; 1: bare soil, 2: forests and 3: crops, the blue arrows indicate the main water balance fluxes in the surface. **b)**: the vertical discretization of the 2m soil into 11 layers with geometric distance between layers (from De Rosnay et al. (2002))

Table 3.2: Prescribed roughness lengths for momentum and for heat per PFT

PFT	z_{0m}	z_{0h}
Bare soil	0.01	0.0001
Tropical Broadleaf Evergreen	0.0625	0.0625
Tropical Broadleaf Raingreen	0.0625	0.0625
Temperate Needleleaf Evergreen	0.0625	0.0625
Temperate Broadleaf Evergreen	0.0625	0.0625
Temperate Broadleaf Summergreen	0.0625	0.0625
Boreal Needleleaf Evergreen	0.0625	0.0625
Boreal Broadleaf Summergreen	0.0625	0.0625
Boreal Needleleaf Deciduous	0.0625	0.0625
Temperate Natural Grassland (C3)	0.1	0.001
Natural Grassland (C4)	0.0833	0.000833
Crops (C3)	0.25	0.0025
Crops (C4)	0.25	0.0025
Tropical Natural Grassland (C3)	0.1	0.001
Boreal Natural Grassland (C3)	0.1	0.001

3.5 LMDZ-ORCHIDEE coupled model

In this thesis work, LMDZ is coupled with the ORCHIDEE v2.2 land surface model. Sea surface temperature and sea ice cover are prescribed in the simulations.

LMDZ and ORCHIDEE are coupled using an implicit scheme that ensures the continuity of exchanged fluxes and temperature. ORCHIDEE soil tiles are coupled to a unique atmosphere (the sub-surface land in Figure 3.1). The surface temperature is determined from the energy balance closure at the surface (Polcher et al. (1998); Cheruy (2018)):

$$C_s \frac{\partial \theta_s}{\partial t} = LW_{net} + SW_{net} + H + Le + G \tag{3.17}$$

Where θ_s is the surface temperature, C_s is the surface heat capacity per unit area, LW_{net} is the net longwave radiation at the surface, SW_{net} is the net shortwave radiation at the surface, Le is the latent heat flux, H is the sensible heat flux and G is the ground heat flux. All fluxes are positive downward. The turbulent diffusion coefficients are calculated from the summit of the atmosphere to the surface at each timestep using the K-gradient expressions. Then, the heat diffusion is also calculated using a coefficients and the temperature is updated, then, the main atmospheric quantities are calculated upward ensuring the surface and atmosphere consistency (for further details, we refer the reader to Dufresne and Ghattas (2009))

In the coupled mode, LMDZ computes the radiation calculations (net solar radiation, the zenith

angle and the downward longwave radiation) through the surface boundary conditions provided by ORCHIDEE (Albedo, emissivity and surface radiative temperature) (Polcher et al. (1998)).

3.6 Simulations set-up

General circulation models are the main tools for climate simulations (Giorgi and Mearns (1991)). However, the necessity to adequately representing the regional and subgrid-scale atmospheric processes within global runs is computationally demanding (Giorgi and Mearns (1991)). Global climate models with a zoom have the potential to study the regional climate with variable-resolution grids. They allow for the higher-resolution domain to be placed over the region of interest within the global models, and then, a well downscaled information from the large-scale to the regional scale compared to the other regionalization tools, despite the relatively higher demand on computer resources when the zoom limits are smooth (Déqué and Piedelievre (1995); Goubanova and Li (2007); Yang et al. (2016)). The LMDZ model was used with a zoom for the first time by Krinner et al. (1997) over the Antarctic region as an alternative to model nesting, where they reported a significant improvement in the simulated climate compared to the regular-grid version. Then, the zoomed and nudged LMDZ has been used in various regionalization studies and has shown significant improvements of the atmospheric circulation, surface air temperature, and precipitation (Gao et al. (2011)). Several applications have been held in different regions: The Mediterranean (e.g., Casado-Lopez and Li (2009); Chéruy and Aires (2009); Drobinski et al. (2016)); East Asia (e.g., Xin et al. (2008); Lee et al. (2012); Yang et al. (2016)) and West-Africa (e.g., Hourdin et al. (2014, 2015); Diallo et al. (2017)).

The simulations presented in this thesis all consist on a zoomed and nudged configuration with a 64x64 horizontal grid, and a 79 vertical levels of the coupled land surface-atmosphere model LMDZ-ORCHIDEE. The center of the zoom is fixed at the Haouz plain (7.5°W;31.5°N) where the horizontal resolution reaches about 25km over a 300 km perimeter (see Fig. 3.3). By default, LMDZ is set up in "climate mode" where variables are computed freely and the "trajectory" of the model only depends on the initial and the boundary conditions, such as the SST, albedo, aerosols... etc (Gueye (2015)). However, to reduce the model's internal variability and improve the model-observation comparisons, as demonstrated in several studies focusing on the surface-atmosphere coupling (Coindreau et al. (2007); Cheruy et al. (2013); Diallo et al. (2017)), we run our simulations in a "nudged" mode. This latter forces the large-scale dynamics to follow the real one, by relaxing meteorological variables towards reanalysis as follows:

$$\frac{\partial X}{\partial t} = \frac{\partial X}{\partial t}_{dyn} + \frac{\partial X}{\partial t}_{phys} + \frac{X^a - X}{\tau} \tag{3.18}$$

Where X is either the temperature T, the specific humidity Q, the zonal and meridional wind U,V. F is the operator characterizing the physical and dynamical processes that determine the evolution of X. X^a is the equivalent field from ERA5 and τ is the relaxation time that controls the nudging intensity (Coindreau et al. (2007); Vignon et al. (2018)).
Nudged variables in our simulations are temperature, wind speed and humidity. To ensure a model

simulation fully governed by the model's physics and dynamics within the zoom area, we varied the relaxation time τ from a small value ($\tau_{min} = 6h$) outside the zoom to a large value ($\tau_{min} = 240h$) inside the zoom.

The reference simulation consists of the configuration described above and is denoted **STD**. A series of test simulations were carried out to evaluate the model's performances (chapter 4).

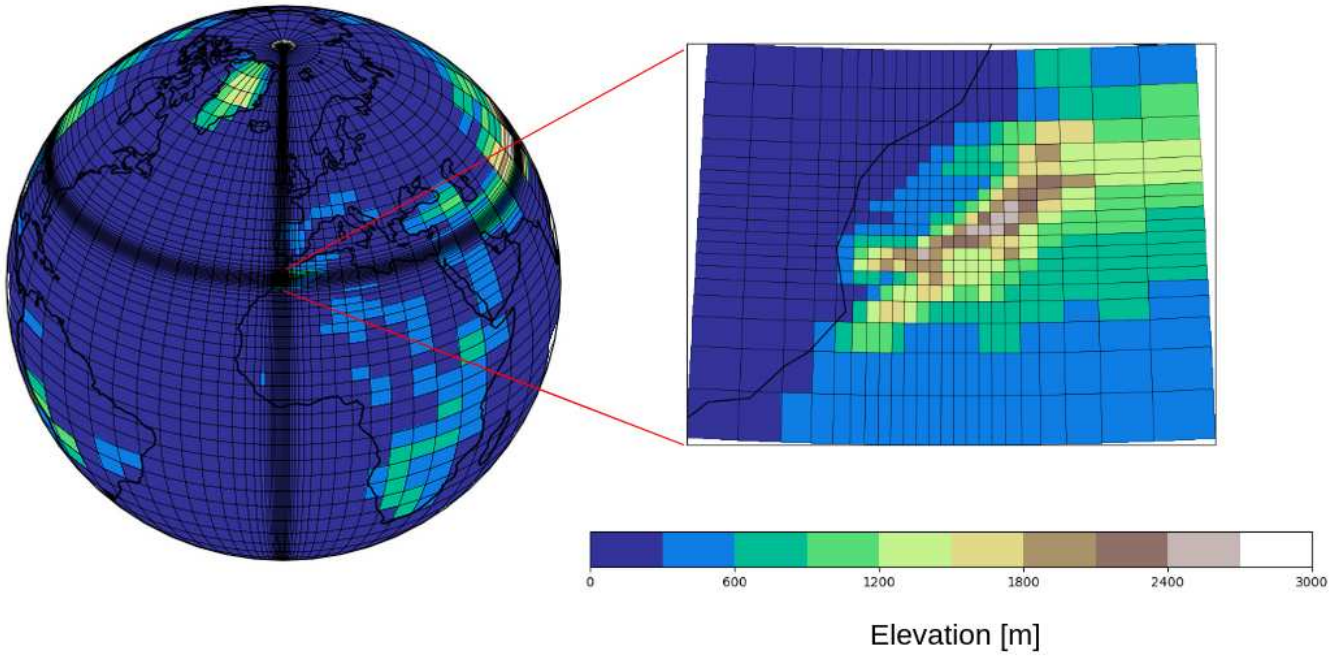

Figure 3.3: Overview of the implemented LMDZ grid with 64x64 horizontal resolution and the grid refinement over the Haouz plain (right panel)

CHAPTER 4

Modeling the surface climate and the surface-atmosphere interactions over the Haouz plain

Contents

4.1 Introduction to the chapter 46

4.2 Article. Modeling land-atmosphere interactions over semi-arid plains in Morocco: in-depth assessment of GCM stretched-grid simulations using in situ data 47

4.2.1 Introduction 47

4.2.2 Data, model and methods 49

4.2.3 Results and discussion 57

4.2.4 Summary and conclusions 67

4.3 Investigation of the impact of irrigation upon near surface climate: further analysis 70

4.3.1 A more detailed description of the implemented irrigation parametrization . 70

4.3.2 Diurnal cycle 72

4.3.3 Seasonal aspects 78

4.4 Chapter conclusions 81

"Research is to see what everybody else has seen, and to think what nobody else has thought."
- Albert Szent-Györgyi

4.1 Introduction to the chapter

The land-atmosphere interactions involve a variety of processes that modulate the regional climate (Seneviratne et al. (2010); Cheruy et al. (2020)), they rely on intricate land-atmosphere interactions, such as the impact of the surface physical and radiative properties on the atmosphere on the one hand, and the modulated surface properties by the atmosphere on the other hand (Betts et al. (1996); Schär et al. (1999); Berg and Sheffield (2019)). Encompassing a wide range of spatiotemporal scales, from diurnal to longer-term climate feedbacks (Berg and Sheffield (2019)).

Assessing the land-surface atmosphere interactions has been a central focus in the continuous development of LMDZ-ORCHIDEE model (e.g., Coindreau et al. (2007), Cheruy et al. (2013, 2017, 2020), Campoy et al. (2013), Aït-Mesbah et al. (2015), Wang et al. (2018) and Tang et al. (2023)). In particular, the Sahelian climate was subject of active research (e.g. Gueye (2015); Hourdin et al. (2015); Diallo et al. (2017)). For instance, Diallo et al. (2017) reported the substantial role of wind nudging in the improvement of the model comparison with station observations over West Africa. They also identified a persistent temperature, surface albedo and incoming solar radiation biases linked with the representation of the soil thermal inertia and the turbulent mixing efficiency.

Our understanding of the surface–atmosphere interactions in Morocco remains limited, due to the climate models ability to simulate surface-atmosphere interactions and also due to the scarcity of in-situ measurements, specifically over the agricultural areas.

The purpose of this chapter is to use in-situ precious measurements collected over the Haouz plain to evaluate and improve the simulated present-day climate over the plain, with a particular focus on the near surface climate. The first part of this chapter includes a paper accepted in the Journal of Applied Meteorology and Climatology, in which we evaluate the LMDZ-ORCHIDEE's ability to simulate the near-surface meteorology, and the different terms of the surface energy balance (sections 4.2.3.1, 4.2.3.2). Then, we conduct a series of sensitivity experiments to identify the sources of the observed warm and dry biases (sections 4.2.3.3, 4.2.3.4). The supplementary information of the paper is given in Appendix A.

Since Moroccan agricultural fields are extensively irrigated, we expand our analysis of a first-order parameterization (section 4.3) in the land-surface model ORCHIDEE to mimic the drip irrigation at the plain and we assessed its potential impact on the diurnal (section 4.3.2) and seasonal (section 4.3.3) near surface climate.

4.2 Article. Modeling land-atmosphere interactions over semi-arid plains in Morocco: in-depth assessment of GCM stretched-grid simulations using in situ data

Arjdal, K., Vignon, É., Driouech, F., Chéruy, F., Sima, A., Er-Raki, S., Chehbouni, A., Drobinski, P. (2023). Modeling land-atmosphere interactions over semi-arid plains in Morocco: in-depth assessment of GCM stretched-grid simulations using in situ data. *Journal of Applied Meteorology and Climatology*. https://doi.org/10.1175/JAMC-D-23-0099.1

Abstract *Land surface-atmosphere interactions are a key component of climate modeling. They are particularly critical to understand and anticipate the climate and the water resources over the semi-arid and arid North-African regions. This study uses in situ observations to assess the ability of the IPSL-CM global climate model to simulate the land-atmosphere interactions over Moroccan semi-arid plains. A specific configuration with a grid refinement over the Haouz plain, near Marrakech, and nudging outside Morocco has been performed to properly assess the model's performances. To ensure reliable model-observation comparisons despite the fact that stations measurements are not representative of a mesh-size area, we carried out experiments with adapted vegetation properties. Results show that the CMIP6 version of the model's physics represents the near surface climate over the Haouz plain reasonably well. Nonetheless, the simulation exhibits a nocturnal warm bias, and the wind speed is overestimated in tree-covered meshes and underestimated in the wheat-covered region. Further sensitivity experiments reveal that LAI-dependent parameterization of roughness length leads to a strong surface wind drag and to an underestimated thermal coupling between the land surface and the atmosphere. Setting the roughness heights to the observed values improves the wind speed and to a lesser extent the nocturnal temperature. A low-bias in latent heat flux and soil moisture coinciding with a pronounced diurnal warm bias at the surface is still present in our simulations. Including a first-order irrigation parametrization yields more realistic simulated evapotranspiration flux and daytime skin surface temperatures. This result raises the importance of accounting for the irrigation process in present and future climate simulations over Moroccan agricultural areas.*

4.2.1 Introduction

The Mediterranean basin is one of the most vulnerable climate change hotspots (Diffenbaugh and Giorgi (2012); Douville and John (2021); Ali et al. (2022)). Several parts of the region have registered a decrease in rainfall since 1960 with significant changes in the aridity and drought (Douville and John (2021); Gutiérrez et al. (2021); Driouech et al. (2020)). Soil moisture observations show that the Mediterranean region's aridity has been strongly influenced by rising temperatures and increased atmospheric demand (Vicente-Serrano et al. (2014); Gutiérrez et al. (2021)). Furthermore, the sixth Assessment Report (AR6) and the first MedECC Assessment Report (MAR1) show that climate

models agree on a future warming ranging from 3.5°C to 8.75°C over the Mediterranean under the high-end scenario by the end of the 21st century (Cherif et al. (2020); Douville and John (2021); Arjdal et al. (2023); Balhane et al. (2021)). Climate change is projected to intensify throughout the region generating several cascading impacts on socio-economic sectors, including agriculture (Vafeidis et al. (2020)).

Among the Mediterranean and North African countries, Morocco is considered as one of the most vulnerable countries to climate change (Schilling et al. (2020)). Moroccan rainy season extends from October to April with a strong interannual precipitation variability (Born et al. (2010); Driouech (2010)). During the second half of the 20th century, the country experienced several below-average rainfall periods, mostly in winter and spring (Schilling et al. (2012); Fink et al. (2010); Meddi et al. (2010); Raymond et al. (2016, 2018); Tramblay et al. (2018)) and is expected to experience more winter and spring dry spells in the future (Raymond et al. (2019)). The observed trend towards a drier and warmer climate strengthens in future scenarios (Born et al. (2008); Driouech et al. (2020); Drobinski et al. (2020)). A rising temperature by +1.4°C to +2.6°C is projected, while precipitation is projected to decrease by about 10% to more than 30% by 2065 (Marchane et al. (2017); Schilling et al. (2012); Tramblay et al. (2013); Arjdal et al. (2023)).

The Moroccan economy, as most African countries, is heavily sustained by rainfed agriculture. This later contributes to about 13.6 % of the Global National Product (GNP) with 59% of agricultural areas used for cereal crops (Harbouze et al. (2019)). During periodic droughts, groundwater remains the sole water resource. Combined effects of drought and water use, in particular owing to the spreading of urban and industrial regions, and an intensification of the use of irrigation for agriculture, led to a significant groundwater shortage in areas such as the Haouz Plain (31°30'0" N; 8°0'0" W), (Ait El Mekki and Laftouhi (2016); Chehbouni et al. (2008)). In fact, irrigated agriculture accounts for 85% of the total water use in the Haouz plain (Chehbouni et al. (2008)), the Tensift watershed extending from the High Atlas mountains being the major water source (Zkhiri et al. (2019)). Developing climate change adaptation strategies requires fine and accurate projections of the future climate which themselves rely on appropriate parameterization of the physical processes that govern the hydrological cycle and surface climate in climate models. In particular, the physical parameterizations of boundary layer processes and surface-atmosphere interactions play a fundamental role for the climate models performance and for determining their reliability to simulate and predict the surface climate (Betts (2007); Cheruy et al. (2013); Santanello et al. (2018)). Several studies evaluating climate models in the Mediterranean region have been carried out (e.g. Cavicchia et al. (2018); Drobinski et al. (2016); Panthou et al. (2018)). However, most of the evaluations conducted rely on gridded datasets such as E-OBS, which has only a limited sub-dataset over Morocco, as highlighted in Cornes et al. (2018).

Arjdal et al. (2023) evidenced large inter-model spread in projected surface hydrology over the North-African region by climate models involved in the latest CMIP exercise (CMIP6). This spread can be attributed either to differences in large scale circulation patterns or to discrepancies and uncertainties in simulating the parameterized atmospheric processes, the surface-atmosphere interactions as well as their responses to anthropogenic forcings. Regarding more specifically the Moroccan region, previous studies have assessed the dynamics and the variability of precipitation and characterized the water

cycle (e.g., Driouech et al. (2009); Driouech (2010); Tramblay et al. (2013, 2012)). However, the ability of models to properly simulate the surface-atmosphere interactions remain under-explored. The main objective of this study is to perform a thorough evaluation of of LMDZ-ORCHIDEE, the atmosphere-land surface component of IPSL-CM (The Institut de Pierre Simon Laplace Coupled Model, Boucher et al. (2020)) in representing the land-surface atmosphere interactions in semi-arid conditions using rare and precious meteorological observations that were acquired over the Haouz Plain in Morocco. The IPSL-CM model has been historically and is still actively involved in the Coupled Model Intercomparison Projects (CMIP). A particular attention to the land-surface atmosphere coupling has been paid during the development of the successive versions (e. g., Aït-Mesbah et al. (2015); Cheruy et al. (2017, 2020); Hourdin et al. (2013); Wang et al. (2018)) but never with a specific focus on the North-African or Mediterranean regions. We propose an approach to perform reliable model-observation comparisons and conclusive evaluation of the model's physics, leveraging the "zoom" capability of LMDZ to refine the grid over the plain and applying a nudging towards atmospheric reanalysis outside of the zoom area.

This manuscript is organized as follows: Sect. 4.2.2 presents the geographical setting, the observational datasets, the model simulations and the evaluation methodology. Results are presented and discussed in Sect. 4.2.3. Sect. 4.2.4 closes the paper with conclusions.

4.2.2 Data, model and methods

4.2.2.1 Geographical setting and in situ measurements

The Haouz plain is located 40 km east of Marrakech city (central Morocco) and spreads over 20 450 km^2 (Khabba et al. (2013)). It is delimited by the High-Atlas mountain to the south which represents the region's 'water tower' (Chehbouni et al. (2008)) and the northern hills or jbilets, that is mountains with moderate relief that consists of rocky plains and hills located about 8 km north of Marrakech (see Fig. 4.1). The climate of the region is semi-arid with annual average rainfall ranges to $\sim$250 mm, primarily concentrated from autumn to spring. Average annual reference evapotranspiration (ETo) is of about 1600 mm (Er-Raki et al. (2010); Kharrou et al. (2011)). Consequently, in order to maintain growth and productivity, constant irrigation is required in the fields (Chehbouni et al. (2008); Khabba et al. (2013)). Major cultivation types include oranges, wheat and olive (40% of national production) (Chehbouni et al. (2008); Khabba et al. (2013)).

From the beginning of the 21th century, the Tensift watershed has been equipped with a network of meteorological and hydrological stations within the framework of the SUDMED Program (Chehbouni et al. (2003, 2008)), the measurement network has been managed by the Joint International Laboratory (LMI-TREMA) since 2011 (Jarlan et al. (2015); Khabba et al. (2013)). Amongst the network (Figs. 4.2.6.1), three stations are equipped with eddy-covariance systems, radiometers and soil heat flux measurements allowing for a detailed characterization of the energy and water exchanges between the land surface and the atmosphere. Those three stations, namely Agdal, Agafay and R3, will be used to evaluate the model. Two additional standard meteorological stations Graoua and Chichaoua respectively deployed in wheat fields - and for which we have access to long and high-quality time

series - have been used. Their data help us assess whether the model performance - in terms of near surface wind, humidity and temperature - at the three main sites is comparable at two other sites in the plain (see details in Sect. B. of the Supplement).

Agafay site is located in an orange crop (38 ha), Agdal in an olive crop (275 ha) and R3 in a wheat crop field (2800 ha). The average height of trees is about 3 m in Agafay (Nassah et al. (2018)) and 6 m in Agdal (Ezzahar et al. (2007)). The R3 vegetation height can reach up to 0.74 m during the growing season. Meteorological measurements specifications are detailed in Table 4.1. Measurements were sampled at either 1 or 20 Hz (see details in Table 4.1) and stored at 30 min intervals (Ezzahar et al. (2007)). In the present study, 1-hour data averages are used in comparisons with model outputs. For each station, the selection of the time period considered to evaluate the model has been made by targeting the longest continuous time period for which the observational dataset has been consistent and thoroughly quality-checked. Thus, the periods (10/2002 - 11/2004), (01/2003 - 05/2003) and (09/2006 - 12/2009) have been considered respectively for Agdal, R3 and Agafay.

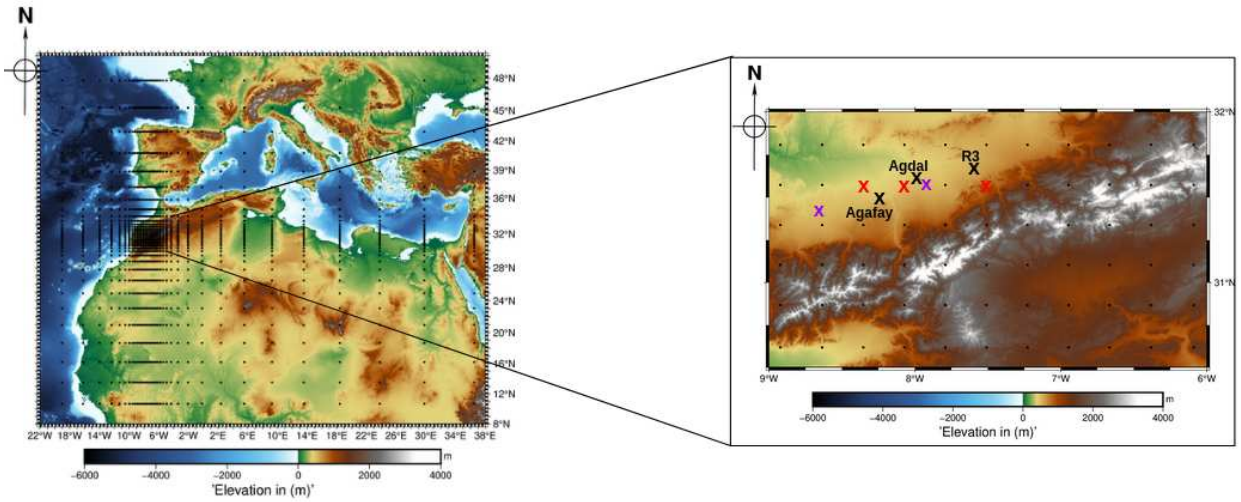

Figure 4.1: Map of the topography with a focus on the Haouz plain and the Atlas mountain range (inset). The black dots indicate the center of the model meshes. Black crosses show the location of the three main stations considered in this study, their corresponding model meshes are marked with red crosses. The location of the two additional stations Chichaoua and Graoua is indicated with purple crosses.

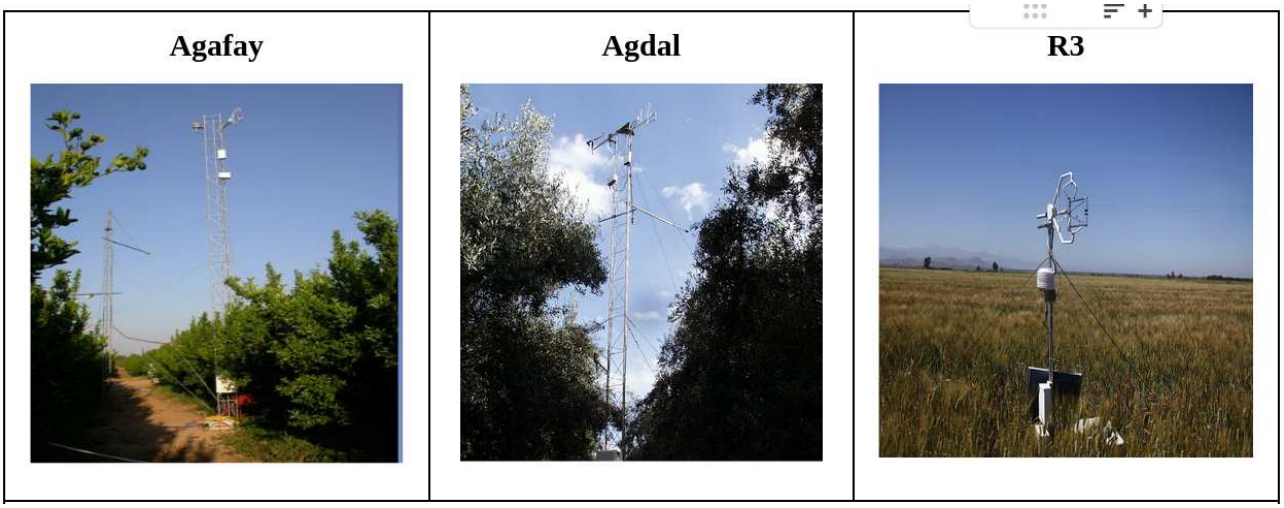

Figure 4.2: From left to right: Agafay, Agdal and R3 monitoring stations (Copyright: LMI-TREMA)

Table 4.1: Characteristics of the in situ measurements in the three stations Agdal, Agafay and R3

Quantity	Instrument	Height from vegetation top
Air temperature (T)	Vaisala HMP45AC probe	2 m
Relative humidity (RH)	-	-
Wind direction / Wind speed (U)	Young Wp200 anemometer	3.25 m (Agdal) 2 m (Agafay) 1.3 m (R3)
Precipitation	TRP525M Rain gauge	1 m
Sensible heat flux (H)	20Hz 3D sonic thermo-anemometer (CSAT3) and open-path infrared gas analyzer (Li7500, Licor Inc)	3.25 m (Agdal) 5.5 m (Agafay) 1.3 m (R3)
Latent heat flux (Le)	-	-
Friction velocity (u*)	-	-
Downward shortwave radiation (SWdn)	CNR1 radiometer	2 m
Upward shortwave radiation (SWup)	-	-
Downward longwave radiation (LWdn)	-	-
Upward longwave radiation (LWup)	-	-
Skin surface Temperature (Ts)	-	-
Soil moisture	CS616 water content reflectometer	5 cm depth

4.2.2.2 Model presentation, boundary layer and surface layer parameterizations

LMDZ is an atmospheric General Circulation Model (GCM) developed since the 80s (Sadourny and Laval (1984)) at Laboratoire de Météorologie Dynamique (LMD) and the atmospheric component of IPSL-CM. The "Z" in "LMDZ" refers to the zooming capability of its grid. LMDZ was intensively evaluated and developed for the tropical and equatorial regions (e.g., Diallo et al. (2017); Hourdin et al. (2015, 2020b)). Surface turbulent fluxes parameterization follows the Monin-Obukhov (MO) similarity theory and the details of the surface-layer scheme are given in Cheruy et al. (2020) and Vignon et al. (2017). The vertical turbulent diffusion follows a hybrid approach. First, the local mixing is parameterized using a TKE-l scheme based on the pioneering work of Yamada (1983) and revisited in Vignon et al. (2017). Second, the non-local mixing in the convective boundary layer is parameterized with a mass-flux scheme so-called the 'thermal plume model' (Hourdin et al. (2002, 2019); Jam et al. (2013); Rio et al. (2010)).

In LMDZ, the sensible (H) and latent heat (Le) fluxes are calculated using a bulk formula between the surface and the first model level as follows:

$$H = \rho_1 c_p C_h U_1 (\theta_{v1} - \theta_s) \tag{4.1}$$

$$Le = \rho_1 \beta L_{vap} C_h U_1 (q_{v1} - q_{s,sat}) \tag{4.2}$$

with c_p is the specific heat of air at constant pressure, β is the aridity coefficient, L_{vap} is the latent heat of vaporization. ρ_1, U_1 ,q_{v1} and $v1$ are the air density, the wind speed, the specific humidity and the virtual potential temperature at the first model level respectively; θ_s and $q_{s,sat}$ are the virtual potential temperature and the saturation specific humidity at the surface; C_h is the drag coefficient for heat, and reads:

$$C_h = \frac{\kappa^2}{\ln(z_1/z_{0m})\ln(z_1/z_{0h})} \times f_h \tag{4.3}$$

Where $z_1$is the first model level height, z_{0m} and z_{0h} are the roughness length for momentum and height respectively, $\kappa = 0.41$ is the Von Kármán constant and f_h is the stability function of the bulk Richardson number Ri_b between the first model level and the surface (Vignon et al. (2017)).
The surface energy balance reads:

$$R_n + H + Le + G = 0 \tag{4.4}$$

with H is the turbulent sensible heat flux, Le is the turbulent latent heat flux, G is the ground heat flux and R_n is the net radiative flux expressed as:

$$R_n = SW_{dn} - SW_{up} + LW_{dn} - LW_{up} \tag{4.5}$$

where SW_{dn} is the downward shortwave radiation, SW_{up} is the upward shortwave radiation,LW_{dn} is the downward longwave radiation and LW_{up} is the upward longwave radiation. All fluxes are defined as positive towards the surface.

In climate simulations, LMDZ is coupled to the land surface model ORCHIDEE (Organising Carbon and Hydrology In Dynamic EcosystEms; Cheruy et al. (2020)). ORCHIDEE consists in two sub-modules: i) SECHIBA (Schématisation des Échanges Hydriques à l'Interface Biosphère Atmosphère; Ducoudré et al. (1993)) that computes the energy and the hydrological budgets, ii) STOMATE (Saclay Toulouse Orsay Model for the Analysis of Terrestrial Ecosystems; Botta et al. (2000)) for phenology and carbon cycle. ORCHIDEE computes the exchanges between the soil and plant reservoirs. It provides to LMDZ the surface parameters needed to compute the energy and momentum fluxes at the interface with the atmosphere among which the roughness heights - which control the turbulent transfer of momentum (z_{0m}) , heat and humidity (z_{0h}) between the surface and the atmosphere - the albedo and the aridity coefficient β. When coupled to LMDZ, the roughness heights in ORCHIDEE are by default computed as a function of the leaf area index (LAI) for each Plant Functional Type (PFT), using the model proposed by Massman (1999) and tested by Su et al. (2001). The thermal roughness length (z_{0h}) is derived from z_{0m} as follows:

$$z_{0h} = \frac{z_{0m}}{\exp(\kappa B^{-1})} \tag{4.6}$$

where B^{-1} is the inverse Stanton number of heat transfer Su et al. (2001) and $\kappa = 0.41$ is the Von Kármán constant. z_{0m} is usually higher than z_{0h} due to the fact that heat and humidity transfer are dominated by molecular diffusion, while the momentum transfer is mostly controlled by pressure forces (Garratt and Hicks (1973); Su et al. (2001)).

4.2.2.3 Configuration of the simulations and introduction of a bulk parameterization of irrigation

In our simulations, we ran LMDZ with the 79-level vertical discretization used for CMIP6 and with a 64x64 horizontal grid centered on the Haouz plain (7.58 °W, 31.66 °N). The resolution at the center of the domain reaches 25 km x 25 km (Fig. 4.1). We apply nudging towards ERA5 reanalysis on the temperature, humidity and wind fields (as in Coindreau et al. (2007); Diallo et al. (2017); Vignon et al. (2018)) as follows:

$$\frac{\partial X}{\partial t} = F(X) - \frac{X - X^a}{\tau} \tag{4.7}$$

Where X is either the temperature T, the specific humidity Q, the zonal and meridional wind U,V. F(X) is the operator describing the dynamical and physical processes that determine the evolution of X. X^a is the equivalent field from ERA5 and is the relaxation time that controls the nudging intensity (Coindreau et al. (2007); Vignon et al. (2018)). We make the relaxation time vary from a small value ($\tau_{min} = 6h$) outside the zoom to a large value (($\tau_{min} = 240h$)) inside the zoom such that the simulated fields over the Haouz plain are fully governed by the model physics and dynamics. We use the exact same physics configuration as the one developed and calibrated for the CMIP6 exercise, i.e. the so-called 6A version (Cheruy et al. (2020); Hourdin et al. (2020b)).

Simulations are performed for the period of available in-situ data (2000–2009). The first 2 years

- which correspond to the spin-up time - are not included in the analysis. The vegetation in the land surface model ORCHIDEE is categorized into 15 Plant Functional Types (PFTs), including bare soil, which share similar structural properties (Lurton et al. (2020)). PFTs are classified into eight forest classes, six grass/crop classes and the bare soil, with a varying partitioning at each grid cell. The default partitioning of land cover in grid cells corresponding to each of the studied stations is shown in Fig. 4.3. It is worth noting that the Agdal and Agafay weather stations are set-up in olive and orange orchards whose surface area is smaller than our 25 km x 25 km grid mesh size. Therefore, we carefully designed a methodology enabling the model-observations comparison of the full corresponding grid mesh. Hence two simulation setups are considered: (i) the first one with the model's standard physics and land use map (STD); (ii) the second one with updated land use (CTRL) in which we set a unique PFT in each of the three grid cells corresponding to the 3 stations, the chosen PFT corresponding to the type of cultivation at the station (i.e Temperate Evergreen Broadleaf forests for Agdal and Agafay, and C3 crops for R3).

Note that in CTRL simulation, we only modify the vegetation cover in the mesh, not the soil texture, although soil properties also modulate the intensity of heat and water flux in the ground. In ORCHIDEE, the soil properties are taken from the prevailing soil texture (inferred from the Zobler (1986) map) within each mesh. At Agafay and Agdal, in situ observations show that the dominant soil texture is the "sandy class', which is consistent with the soil properties prescribed in ORCHIDEE for the corresponding meshes. At R3 close to the Atlas foothills, a dominant clay fraction is observed (Er-Raki et al. (2007)) which contrasts with the prevailing 'sand' category seen by ORCHIDEE. We have therefore run an additional simulation (CTRL-Txt, see Figs. 6.11, 6.12 and 6.13 in the supplement) in which we have changed both the vegetation cover (as in CTRL) and the soil texture (prescribing a prevailing clay texture at the R3 model grid point). This simulation is presented in the supplementary materials but the key message here is that the differences between CTRL and CTRL-Txt at R3 in terms of near surface climate are very weak and that all the main conclusions drawn from the CTRL simulations also hold from CTRL-Txt.

The three stations R3, Agdal and Agafay are located in croplands that are intensively irrigated all year long. One can question a possible modulation of the local meteorological fields by the irrigation process and therefore question the importance of accounting for irrigation in models to simulate the near-surface climate in the Haouz plain. Although parameterizations of irrigation have been developed for ORCHIDEE (e.g., De Rosnay et al. (2002); Arboleda-Obando (2023)), none is operational when ORCHIDEE is coupled to LMDZ and therefore applicable in our simulations.

To assess whether accounting for irrigation may improve the simulations, we implemented a coarse and first-order parameterization to roughly represent the effect of the drip irrigation on the soil moisture over the Haouz plain crops. It consists in nudging the soil moisture SM in the 10 cm below the surface towards the saturated value of SM_s when SM drops below a fraction x_1 of SM_s :

$$\frac{dSM}{dt} = -\frac{SM - SM_s}{\tau} \tag{4.8}$$

with τ is a typical time scale, dt is the surface model time scale. The nudging stops when SM becomes

greater than x_2 SM_s. x_1 and x_2 were set to 0.2 and 0.8 for our sensitivity experiments. We further set τ=6h since it is a reasonable time scale for the near-surface soil to be humidified during drip irrigation over the Haouz plain. Note that the nudging formulation of Eq. 4.8 does not enable us to capture the exact timing of irrigation events. Importantly, this parameterization does not intend to be an effective and elaborated irrigation parameterization, but a 1st order approach to assess 1st order effects.

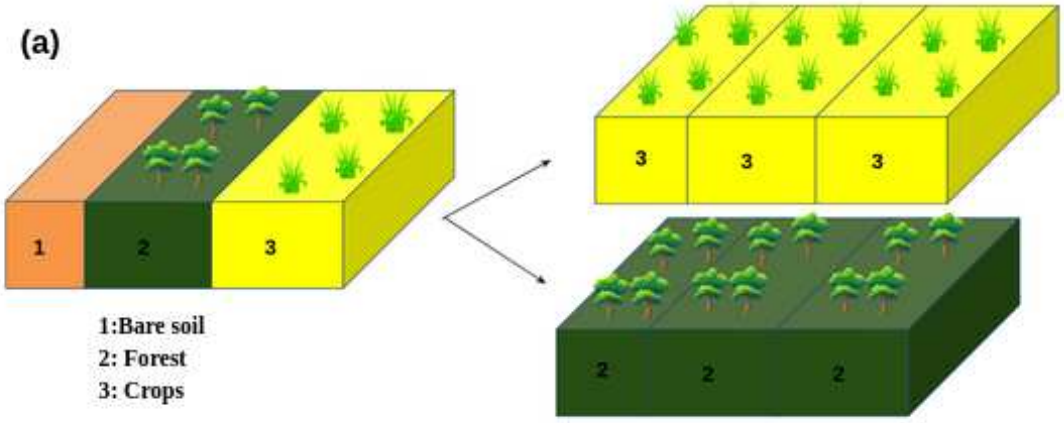

(b)

R3 (Wheat)	Bare soil: 12% Forest: 17% Crops: 71%
Agdal (Olive)	Bare soil: 25% Forest: 3% Crops: 72%
Agafay (Orange)	Bare soil: 33% Forest: 0.5% Crops: 66%

R3 (Wheat)	Wheat: 100%
Agdal (Olive)	Forest: 100%
Agafay (Orange)	Forest: 100%

Figure 4.3: Overview of the ORCHIDEE default grid cell land cover (a) and the updated one consisting of 100% of Forest in Agdal and Agafay and Crops in R3. The percentage of each type of land cover in each station grid cell is listed in the table (b) as simulated by the model (left panel) and the adapted one (right panel).

4.2.2.4 Observation-model comparison

Model evaluation is performed by comparing each station data to the nearest model grid point output (right panel in Fig 4.1). To take into consideration each station's elevation mismatch with its corresponding model grid box in model-observations comparisons, we use a moist lapse rate of 6.5 K K^{-1}. For wind speed, as the observation height is less than 10m (Table 4.1). We extrapolate the simulated 10-m wind speed assuming a logarithmic wind profile, based on the Monin-Obukhov Similarity theory in neutral conditions. The wind speed at a height h is given by:

$$U(h) = \frac{\log(h/z_{0m})}{\log(10/z_{0m})} \times U_{10} \tag{4.9}$$

Where z_{0m} is the aerodynamic roughness height, U is wind speed and U10 is the wind speed at 10 m height. In addition, the fifth generation of the ECMWF Reanalysis (ERA5, Hersbach et al. (2020)) is used to compare and discuss the model's performance with respect to a reanalysis product. Note that none of the LMI network data is assimilated by ERA5, but we include it in our analysis as it serves as a reference dataset frequently used for climate assessment in Morocco.
The observed surface albedo is calculated as the ratio of the upward radiation to the downward surface radiation above the canopy between 08h and 17h local time (LT). Reference observed skin surface temperature is calculated from downward and upward longwave radiative flux measurements above the canopy using the Stefan-Boltzman law and assuming a surface emissivity value of 1. Furthermore, an evaluation of the simulated aerodynamic roughness height z_{0m} is also conducted by comparing it with observations. These latter are estimated using sonic anemometer measurements of the wind speed and friction velocity u* and applying the MO similarity theory for wind speed profile:

$$U(z) = \frac{u*}{\kappa}[\ln((z-d)/z_{0m}) - \psi((z-d)/L)] \tag{4.10}$$

where z is the measurement height, d is the displacement height, assumed equal to $\frac{2}{3}$ of the canopy height (Foken (2008)). L is the MO length (Monin and Obukhov (1954)) and ψ is the integral of the stability function for momentum (Foken (2008)). Note that the evaluation of the roughness height is challenging, since the measured z_0 may include contributions from upstream areas advected at the measurement site, which is not accounted for in the model (Fesquet et al. (2009)). As MO theory is strictly valid in stationary and near-neutral conditions, a pre-selection of the wind data has been performed following Vignon et al. (2017) (see their Appendix A). In Agdal, given the station's position within the orchards (Ezzahar et al. (2007)), we considered the measurements corresponding only to northerly and north-westerly winds.
Unfortunately, no observational values for z_{0h} could be properly estimated. In fact, determining reliable z_{0h} from single sonic anemometer measurements is delicate since on one hand, the estimation errors in near-neutral conditions are large and on the other hand, z_{0h} values estimated far from neutrality are strongly dependent on the choice of the stability functions (Vignon et al. (2017)).

4.2.3 Results and discussion

In this section, we firstly evaluate the model outputs from the STD simulation and then discuss the model-observation comparison with updated land cover before running different sensitivity tests to explore the main identified biases.

4.2.3.1 Near surface meteorological fields

A. Overview analysis of the STD simulation

Observed and simulated mean diurnal cycles of averaged near-surface temperature (T), relative humidity (RH) and wind speed (U) are compared at the three stations: Agdal, R3 and Agafay (Fig. 4.4). The ERA5 reanalysis is also plotted as an indication. In this paragraph, the analysis will focus on the model STD simulation (orange curves in Fig. 4.4).

The observed minimum temperature occurs around 5:30 (LT) – 7:30 LT and the maximum around 15:30 LT. The average diurnal temperature range is around 12°C in R3 (Fig. 4.4.d) and reaches 15°C in Agdal and Agafay (Figs. 4.4.a, 4.4.g). The lower diurnal temperature in R3 when compared to the other stations is explained by the considered season at this station (winter and spring). Let's recall that the time periods considered for each station are different (Sect. 2.1). The daytime temperature is well captured by the model while ERA5 reanalysis exhibits a cold bias that reaches 4 K in the afternoon in Agdal. Saouabe et al. (2022) also reported a similar bias in air temperature in a 53-year study period from 1967 to 2020 over Tensift basin. Nighttime temperature is well simulated in Agdal with differences less than 0.5 K. However, the model shows a pronounced warm (+2 K) nocturnal bias in R3 and Agafay, which leads to an underestimated diurnal temperature range.

The relative humidity signal reflects that of the temperature and LMDZ-ORCHIDEE exhibits a pronounced low bias during night-time. Differences with observations range from -12 to - 20%. ERA5 fits well the observed RH during nights in Agdal and R3, however, an underestimation emerges during daytime at R3 and Agafay.

The average diurnal cycles show also that the STD simulation overestimates wind speed during day and night in Agdal and Agafay (Figs 4.4.c, 4.4.i) with positive differences reaching 1.5 to 2.5 ms^{-1}. Daytime differences are strongest during summer (Fig. 4.5) and the maximum occurs around 19:00 LT. An opposite behavior is noticeable at R3 station (Fig. 4.4.f) with a wind speed that is underestimated by up to -1.5 ms^{-1} in the afternoon. Note that the land cover varies between the studied sites, with wheat in R3 and trees in Agafay and Agdal (oranges and olive orchards). Note that the model-observation differences evidenced at R3 in terms of temperature, relative humidity and wind speed are qualitatively similar at the two other wheat-covered stations Graoua and Chichaoua. At this stage, it is difficult to know whether the model-observation differences are due to model physics shortcomings or to the representativeness of station observations with respect to the size of the corresponding mesh. Hence, we will now analyze the CTRL simulation in which the land cover is modified in the whole grid cell to better represent the vegetation type surrounding the corresponding station.

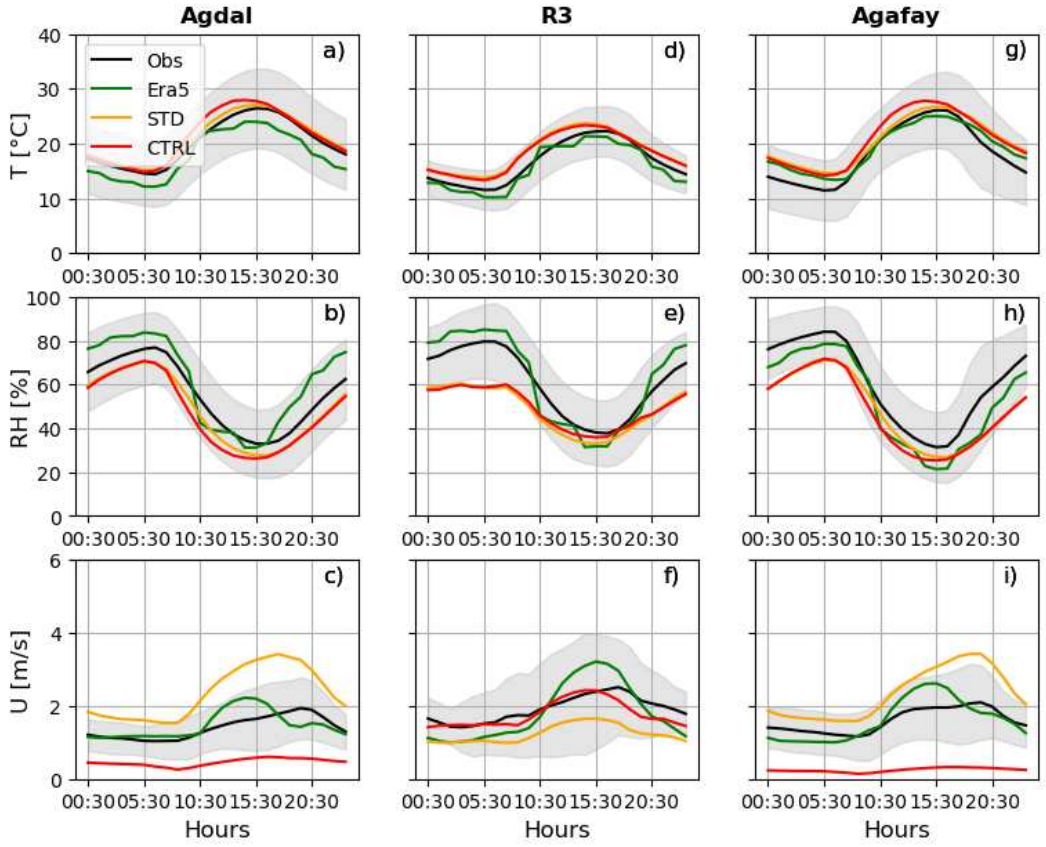

Figure 4.4: Mean diurnal cycle of T, RH and U over Agdal, R3 and Agafay stations. The black line shows observations, the orange line the standard simulation (STD), the red line the control simulation (CTRL) and the green one represents ERA5. Shadings denote the variability over the measurement period for each station ($\pm\sigma$). Note that the mean and standard deviation are calculated for each hour over the full measurement period for each station.

B. Analysis of the CTRL simulation with adapted land use for more consistent model-observation comparison

The comparison of the most relevant surface parameters for the surface-atmosphere coupling -namely the albedo and the roughness height - between the CTRL and STD simulations is given in Table 4.2. Overall a better agreement with observation in the CTRL set-up is noticeable for the two quantities. In particular, the CTRL simulation shows a closer-to-observation surface albedo value at the three sites owing to the removed bare soil fraction in the station grid cells, mainly in Agdal and Agafay where it was initially around 30% and then decreased by 50%.

The average diurnal cycle of T, RH and U of the updated land use simulation (CTRL) in Agdal, R3 and Agafay grid cells are shown in Fig. 4.4 (red curves). Overall, temperature and relative humidity show no significant change in the CTRL simulation wrt to STD at the three stations. Fig. 4.5 further shows the mean diurnal cycles separately for summer (JJA) and winter (DJF) seasons at Agafay station (similar Figures for Agdal and R3 are provided in the supplementary material: Figs. 6.1,6.2). While T and RH show no substantial differences with the STD simulation, the wind speed in the CTRL simulation is significantly weaker and even underestimated at Agdal and Agafay stations. This is

consistent with the much lower z_{0m} values in the CTRL configuration at these two stations. In the STD configuration, as the forest percentage only equals 3% and 1% in the Agdal and Agafay grid cells respectively, the mesh-averaged roughness height is much lower than the measured local one (Table 4.2). Conversely, the wind speed in CTRL is stronger at R3, where z_{0m} is higher than in the STD simulation for which the mesh-averaged roughness height is significantly higher than the observed one owing to a substantial forest percentage (17%) in the mesh. Overall the mean diurnal cycles of wind speed in CTRL are in better agreement with the local observations at R3 station than in STD (Fig. 4.4 and Fig 4.6). Although the CTRL set-up has improved the model-observation comparison, substantial biases in the simulation of the near-surface temperature, humidity and wind remain. A comprehensive analysis of the surface energy budget is necessary to decipher the remaining model-observation differences.

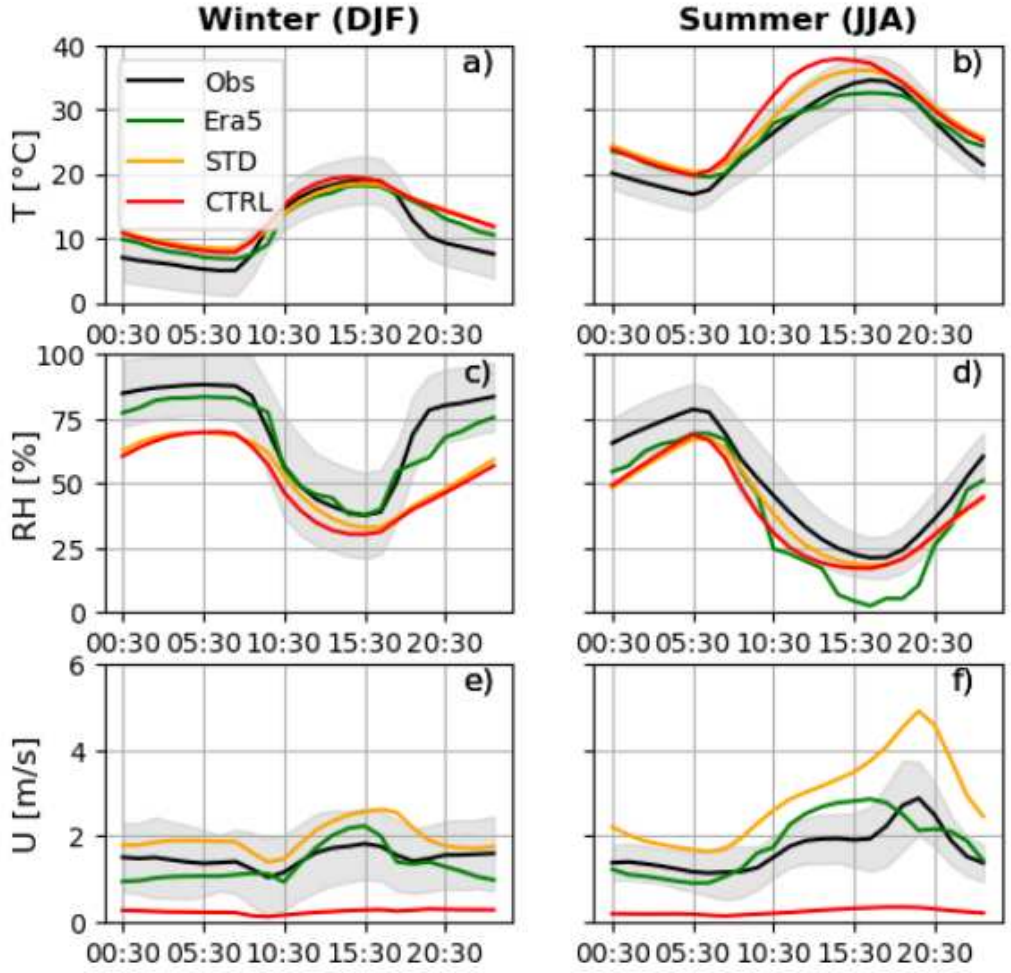

Figure 4.5: Mean diurnal cycle of T, RH and U during winter (DJF) and summer (JJA) for 2006-2009 period at Agafay station. The black line shows observations, the orange line the standard simulation (STD), the red line the control simulation (CTRL) and the green one represents ERA5. Shadings denote the variability over the measurement period for each station ($\pm\sigma$). Note that the mean and standard deviation are calculated for each hour over the full measurement period for each station.

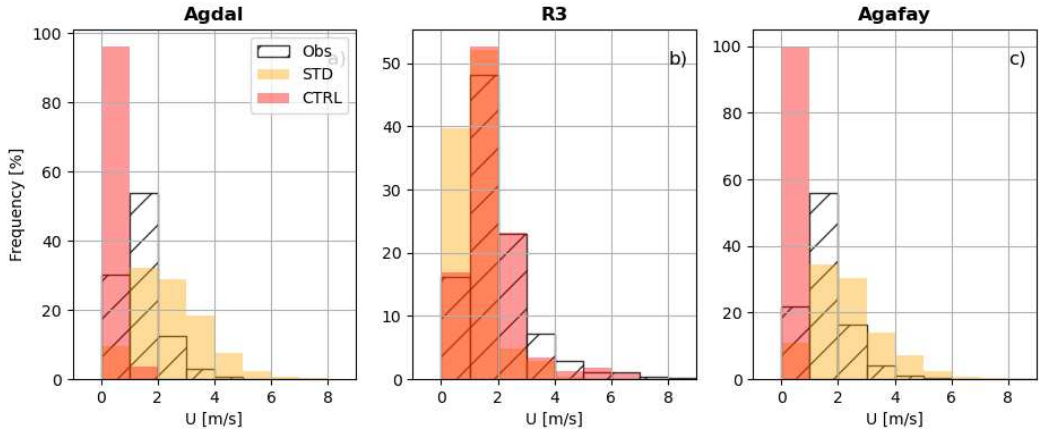

Figure 4.6: Wind speed distribution in observations (black hatches), STD (orange) and CTRL (red) simulations over Agdal (a), R3 (b) and Agafay (c) stations.

Table 4.2: Observed and simulated albedo and roughness height (median value and interquartile range in brackets). As z_{0m} spans several orders of magnitude, the median of z_{0m} is calculated as the median of the distribution of the logarithmic values i.e. the exponential of the median of $\log(z_{0m})$.

	z_{0m}[m]			Albedo		
Station	Obs	STD	CTRL	Obs	STD	CTRL
Agdal	1.29 (0.76)	0.01 (0.02)	1.42 (1.10^{-3})	0.11 (0.02)	0.26 (0.01)	0.11 (4.10^{-3})
R3	0.03 (0.07)	0.34 (0.01)	0.10 (1.10^{-4})	0.19 (0.04)	0.17 (3.10^{-3})	0.17 (3.10^{-3})
Agafay	0.16 (0.28)	0.01 (6.10^{-3})	1.40 (1.10^{-3})	0.15 (0.03)	0.29 (7.10^{-3})	0.14 (0.01)

4.2.3.2 Analysis of the surface energy balance and surface temperature

The diurnal cycles of the observed (Obs) and simulated (CTRL) surface energy balance over the studied stations are shown in Fig. 4.7. Results from the STD simulation are presented in the supplementary material (Fig 6.6). During daytime, incoming solar radiation reaches a maximum value of 800 to 900 W m^{-2} in the model. These values are higher than those observed suggesting a possible underestimated cloud cover in the simulation. Longwave radiative fluxes are well represented overall the studied sites, although, an overestimated daytime LW_{up} is noticeable, following the skin surface temperature (Ts) signal. Fig. 4.8 evidences a strong overestimation of Ts during daytime with differences wrt observations exceeding 5°C. During nighttime, Ts is reasonably well simulated at the two tree-filled sites Agafay and Agdal, but it is overestimated at R3 by nearly 2°C. At Agdal and Agafay, the simulated latent heat flux is underestimated by more than 100 W m^{-2} during daytime compared with observations. Conversely, the daytime sensible heat flux is overestimated in amplitude, with a bias exceeding 100 W m^{-2} at Agdal and Agafay at noon. At R3, a similar pattern is noticeable but the amplitude of the biases are reduced compared to the two other stations. Overall, the strong overestimation of the Bowen ratio - i.e. the ratio between the sensible and latent heat fluxes -associated

with too warm day time temperatures at the three sites may suggest an underestimation of the soil moisture leading to a deficit in evapotranspiration. This aspect will be further discussed in Sect. 4.2.3.4.

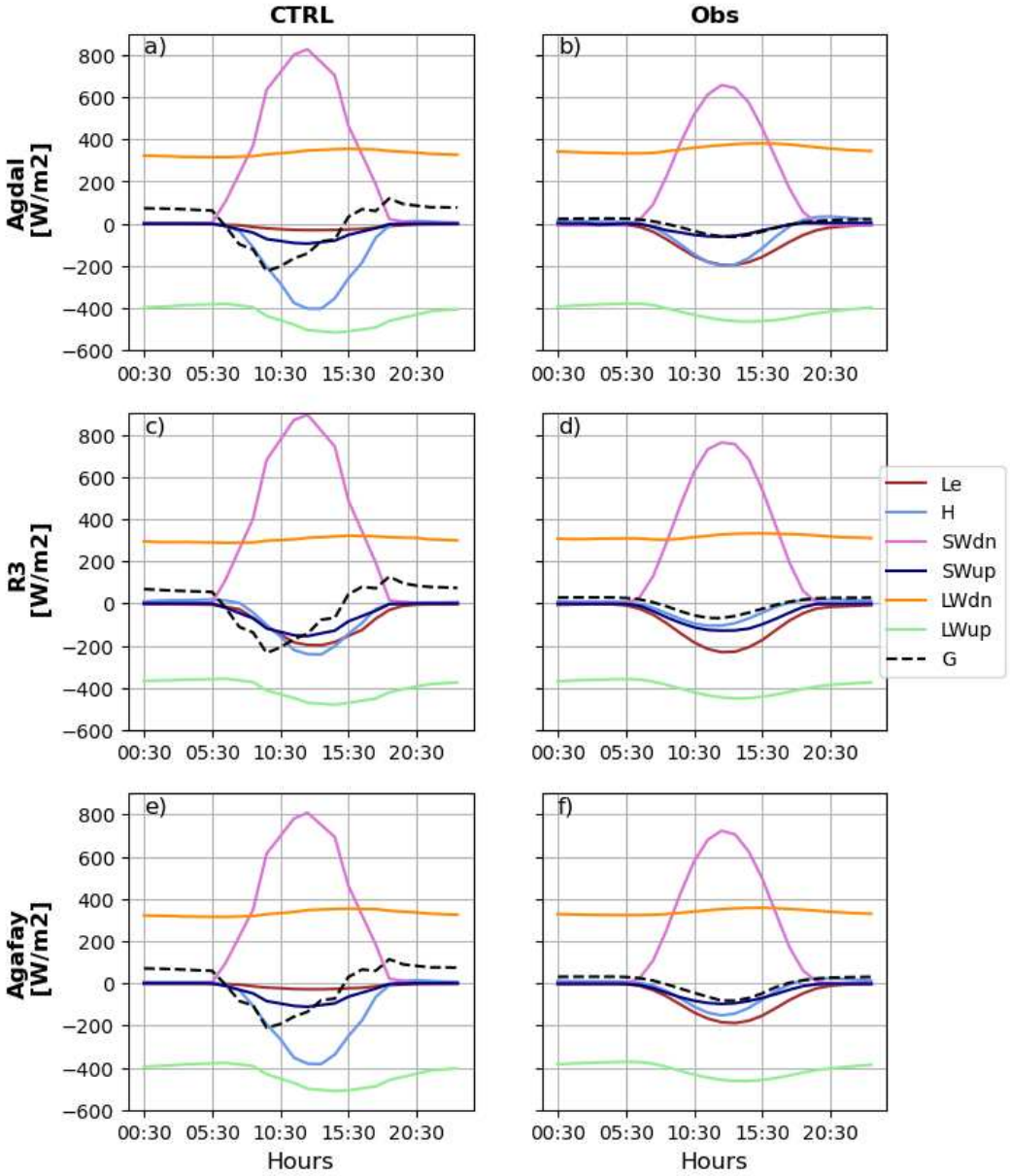

Figure 4.7: Average diurnal cycle of downward (SWdn) and upward (SWup) shortwave radiative fluxes, downward (LWdn) and upward (LWup) longwave radiation, the sensible (H) and latent heat fluxes (Le) and the ground heat flux (G) at Agdal (upper panel), R3 (middle panel) and Agafay (lower panel) stations. The left panel represents CTRL simulation and the right one represents observations. Fluxes are defined positive towards the surface.

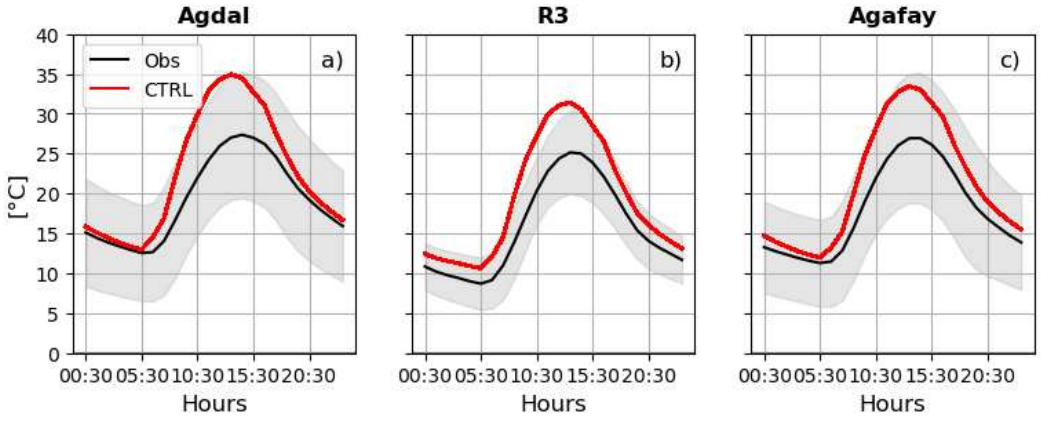

Figure 4.8: Observed (black curves) and simulated (red curves) skin surface temperature (solid lines) in Agdal, R3 and Agafay stations. Shadings denote the variability over the measurement period for each station ($\pm\sigma$). Note that the mean and standard deviation are calculated for each hour over the full measurement period for each station.

4.2.3.3 Investigation of the near-surface warm and dry nocturnal biases at R3 and Agafay

Amongst the remaining biases in the CTRL simulation, a warm bias at 2 m coinciding with an underestimation of the relative humidity is noticeable at R3 and Agafay stations (Fig 4.4).

At R3, the overestimated nocturnal air temperature is associated with an overestimated skin surface temperature (Fig. 4.8.b) which is mostly attributed to an overestimation of the nighttime ground heat flux (Fig 4.7.c). The latter can be explained by the strong overestimation of the daytime surface temperature and ground heat flux and to the subsequent excess in heat storage in the soil. This aspect is further investigated in the next section.

The explanation of the nocturnal warm bias at R3 also holds for Agafay station (see Fig 4.7.e.f and 8.c). However, a strong overestimation of the surface-based temperature inversion (Ta - Ts) is also noticeable at the latter station (see red line in Fig 4.9.c) thereby questioning the representation of the surface-atmosphere thermal coupling. The thermal coupling is controlled by the intensity of the surface turbulent sensible heat flux whose amplitude is underestimated during nighttime in the CTRL simulation at Agafay (Table 4.3). Such an underestimation can be - at least partly - explained by the underestimation of the near surface wind speed at Agafay in the CTRL simulation (Fig. 4.4.i) and linked to an overestimation of the surface wind drag. The latter strongly depends on the roughness of the terrain which is parameterized with the momentum (z_{0m}) and thermal roughness heights (z_{0h}), see Eq. 5. Table 4.2 shows that the z_{0m} in the CTRL simulation - which depends on the LAI following Eq. 1 - is significantly overestimated at Agafay compared to observations. We have therefore performed a sensitivity test (CTRL-z0 simulations) in which we prescribe the z_0 values. We set z_{0m} to the mean observed value (Table 4.2) for each station grid point and prescribe z_{0h}=z_{0m}/10 ratio that is commonly used for uniformly vegetated surfaces (e.g., Sandu et al. (2012)). The new values of z_{0m} and z_{0h} are shown in Table 4.3. In this new simulation (CTRL-z0), we obtained a more realistic wind speed (see blue line in Fig. 4.9.c), albeit slightly underestimated during nighttime, with differences lower than 0.25 m s^{-1}. However, the biases in nighttime 2m temperature and relative humidity as well as the

amplitude of the surface-based temperature inversion are only slightly reduced (Fig. 4.9.a, b, d). It is worth noting that the skin surface temperature remains similar between CTRL-z0 and CTRL (not shown).

Increasing the value of z_{0h} (or the ratio z_{0h}/z_{0m}) may help further enhance the intensity of the thermal coupling and reduce the amplitude of the surface-based inversion but calibrating more precisely this parameter in our case is delicate since we do not have any reliable observational reference.

Table 4.3: Median and interquartile values of thermal roughness length and sensible heat flux at 01:30 LT as simulated by STD, CTRL and CTRL-z0 configurations in Agafay station. As z_{0m} and z_{0h} span several orders of magnitude, their median is calculated as the median of the distribution of the logarithmic values i.e. the exponential of the median of $\log(z_{0m})$.

	z_{0m}[m]			z_{0h}[m]		H [W m^{-2}]		
Station	Obs	CTRL	CTRL-z0	CTRL ($.10^{-4}$)	CTRL-z0	Obs	CTRL	CTRL-z0
Agafay	0.16	1.40	0.14	5.8	0.01	-5.84	-3.54	-3.16
	(0.39)	(0.01)	(0.03)	(0.6)	(0.003)	(5.59)	(7.01)	(6.07)

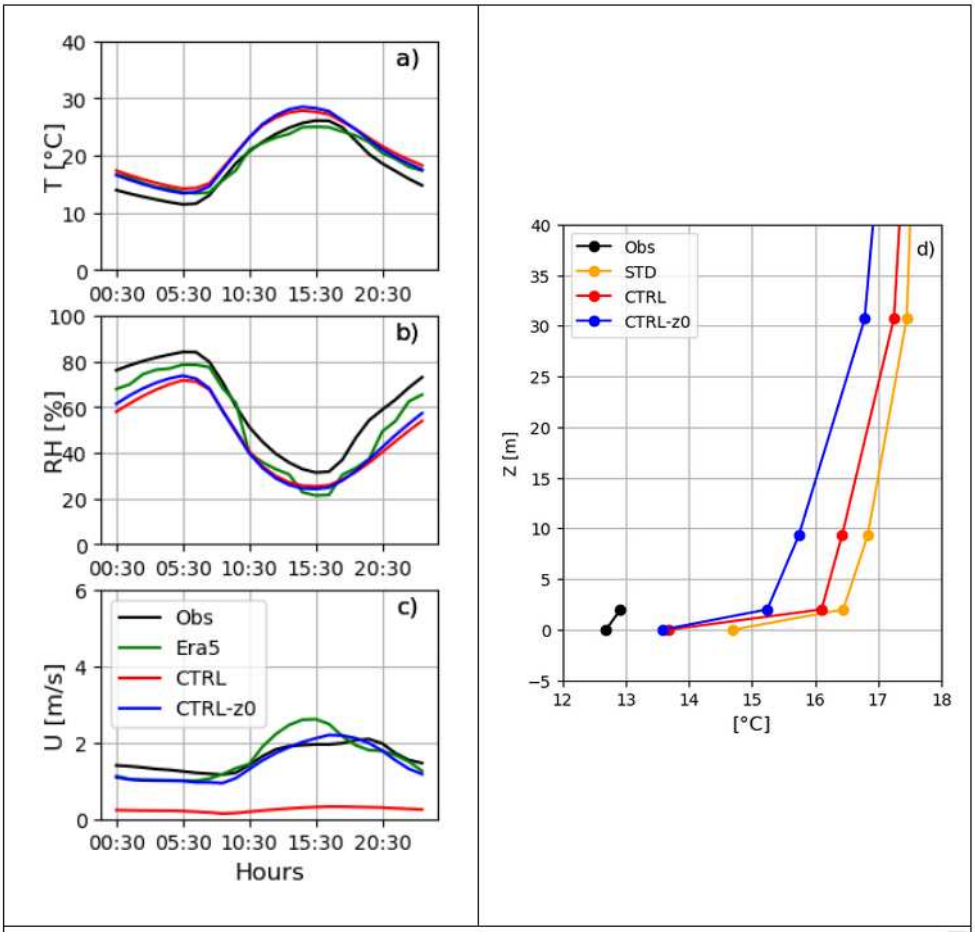

Figure 4.9: Mean diurnal cycle of T (panel a), RH (b) and U (c), with near-surface vertical profiles of temperature over Agafay station at 01:30 LT (d). The black line shows observations, the red line the control simulation (CTRL), the blue line the simulation with prescribed z_0 (CTRL-z0) and the green one shows ERA5.

4.2.3.4 Investigation of the surface dry bias and diurnal warm bias

The most pronounced biases that remains in the CTRL and CTRL-z0 simulations at the three stations is the low bias in RH and evaporation, the overestimation of the daytime surface temperature, as well as the overestimation of the Bowen ratio i.e. the ratio between the sensible heat flux (H) over latent heat flux (Le) during daytime. Such bias is associated with a deficit in soil moisture (Fig. 4.10), which itself may result from an underestimation of the input of soil water, namely precipitation and/or irrigation. Rainfall is relatively well captured near the Atlas piedmont at R3 but it is underestimated at Agafay and Agdal during the entire study period (Table 4.4). Differences in winter precipitation - which mostly originates from large-scale weather systems - exceed 0.7 mm day^{-1} at Agafay, and reach 0.3 mm day^{-1} at Agdal. Investigating the origin of the winter precipitation bias is beyond the scope of the present study and exploring the ability of LMDZ-ORCHIDEE to reproduce the main circulation patterns that drive precipitation in Morocco is tackled in Bahlane et al. (in revision). During summer, differences in precipitation vary from - 0.04 in Agafay to - 0.3 mm day^{-1} at Agdal. It is worth

mentioning that summer precipitation events in the Haouz plain are mostly related to the development of deep wet convective systems over the High Atlas Mountains (thunderstorms or showers) (Bell et al. (2022); Born et al. (2010)) that propagate over the plain in a second phase. The model simulates reasonable convective precipitation in summer but it remains localized over the high Atlas, particularly to the north of the Haouz plain (See Fig. 6.7). Despite an elaborated triggering scheme (Rio et al. (2013); Rochetin et al. (2014)), the deep convection parameterization in LMDZ does not allow for the horizontal propagation of deep convective systems from one mesh to its neighbor. This can be particularly detrimental for simulations with horizontal resolutions around a few tens of kms and may explain part of the lack of precipitation over the plain in our simulations. However, the deficit in precipitation cannot completely explain the underestimation of near-surface soil moisture throughout the year (see Fig. 4.10) which is noticeable at the three stations. Let's recall that the Haouz plain is an agricultural region with intensive use of irrigation. In a study based on simulations with the IPSL model, Mizuochi et al. (2021) show that irrigated zones are regions where the model biases in terms of near-surface climate and water cycle are amplified owing to the complex hydrometeorological regime. We therefore analyze a new simulation (CTRL-moist) which is similar to CTRL-z0 but in which we activate the first-order irrigation parameterization presented in Sect. 4.2.2.3.

Soil moisture at 5cm depth increases by up to 0.1 m^3 m^{-3} with respect to CTRL-z0 simulation (Fig. 6.7), and leads to an increase in latent heat flux by up to 70 W m^{-2} during daytime as well as decrease in sensible heat flux (Fig. 4.11). Similar results hold from R3 and Agafay stations (see Figs. 6.8, 6.9).

The increase in evaporation results in cooler daytime surface and 2 m temperatures as well as higher relative humidity by up to 10% and a decrease in specific humidity by 1. 10^{-3} kg kg^{-1}. However, it does not help reduce the overestimation of SW_{dn} which invites for a deeper evaluation of the model in the region in terms of convective boundary-layer dynamics and cloud parameterization. Further measurement systems giving access to vertical profiles of meteorological variables, such as radiosondes or remote-sensing instruments could help gain further insight into the thermo-dynamical structure of the boundary layer above the plain. Results also show an increase in local precipitation associated with the increase in evapo-transpiration which may suggest a local recycling of water as already noticed for other arid areas (Cheruy et al. (2013); Koster et al. (2004)). Overall, the results of this sensitivity test emphasize that the dry and warm bias at the surface and the underestimation of evapotranspiration at the station locations in our CTRL simulations is partly explained by a lack of an irrigation parameterization.

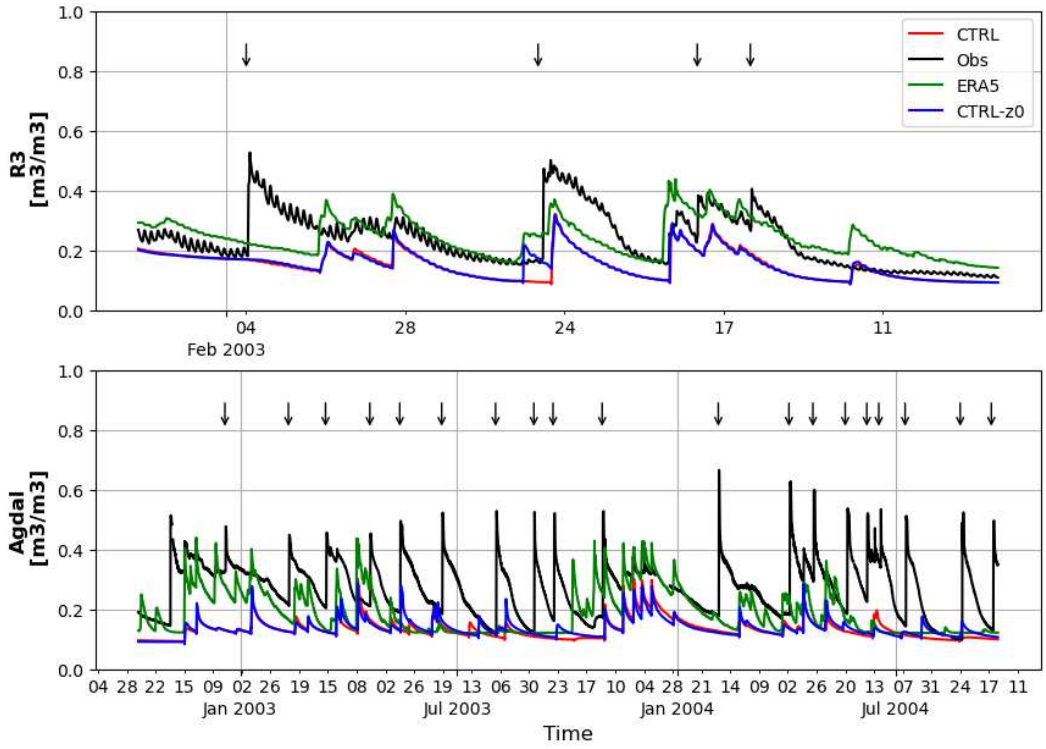

Figure 4.10: Soil moisture at 5 cm depth in R3 and Agafay stations grid cells for observations (black), ERA5 (green), CTRL (red) and CTRL-z0 (blue) simulation. The black arrows indicate the days with effective irrigation.

Table 4.4: Observed and simulated annual and seasonal averaged precipitation at the three stations during the study periods. Note that no measurements for the JJA period are available at R3.

Total average ($.10^{-1}$ mm day^{-1})		**Agdal** (10/2002 - 11/2004)	**Agafay** (09/2006 - 12/2009)	**R3** (01/2003 - 05/2003)
Year	**Obs**	5.48	5.60	6.08
	STD	1.38	1.78	5.17
	CTRL	1.94	2.14	6.36
	CTRL-z0	2.67	2.19	6.71
	Era5	4.15	3.02	5.38
DJF	**Obs**	4.16	9.42	5.42
	STD	1.76	2.15	5.93
	CTRL	1.76	2.02	6.78
	CTRL-z0	2.12	2.75	6.44
	Era5	2.71	3.02	3.56
JJA	**Obs**	4.27	1.51	-
	STD	0.51	1.31	-
	CTRL	1.40	1.09	-
	CTRL-z0	2.87	1.16	-
	Era5	0.28	0.65	-

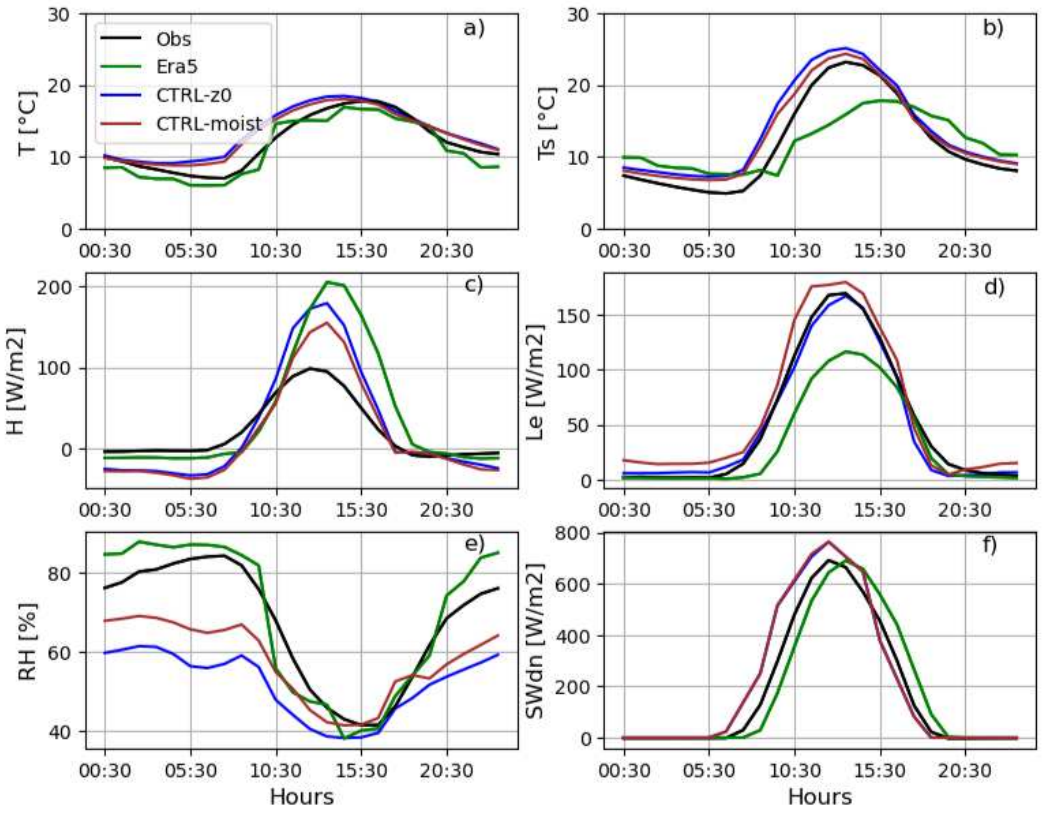

Figure 4.11: February 2003 evolution of Mean diurnal cycles of 2m temperature T, skin surface temperature Ts, Le, H, SWdn and RH in Agdal station from model simulations (CTRL-z0 in blue and CTRL-moist in brown), ERA5 (green) and observations (black). Note that the time in the Figures is in UTC time zone

4.2.4 Summary and conclusions

The ability of climate models to simulate the near-surface climate is generally insufficiently assessed over Africa, particularly owing to the scarcity of meteorological observatories. This can question to a certain extent the climate projections over the continent, especially over the Maghreb, a hotspot of the current climate change which is experiencing a pronounced drying trend. In this paper, we use an original dataset of in situ meteorological observations collected over the Haouz plain in Morocco to assess the ability of LMDZ-ORCHIDEE GCM - the atmospheric and land surface component of the IPSL Coupled Model actively involved in the CMIP exercises - to simulate the near-surface climate and the land-atmosphere coupling in semi-arid agricultural African plains. The model is run in a nudged and zoomed configuration which allows for a direct comparison between observations and simulations.

The analysis of the standard (STD) simulation revealed a 2 m nocturnal warm bias at R3 and Agafay, and a dry bias at all the stations as well as an overestimation (resp. underestimation) of the wind speed at the tree-covered (resp. wheat crop covered) stations. However, it is difficult to conclude from such an analysis if the model-observation differences are due to genuine model physics shortcomings or to the

non-representativeness of station observations with respect to the size of the corresponding mesh. Our control (CTRL) configuration, which incorporates specific land cover characteristics corresponding to each station's vegetation, exhibits similar 2 m nocturnal warm and dry biases over R3 and Agafay, but it shows a more realistic wind speed at R3 in the middle of wheat crop fields. At Agdal and Agafay - with olive and orange cultures respectively – the prescribed Evergreen Broadleaf forests PFT overcorrects the aerodynamic roughness heights and produces overly weak wind speeds.

The analysis of the surface energy budgets reveals i) an overestimation of the downward shortwave radiative flux pointing to a possible underestimation of cloud cover; ii) a strong underestimation of the turbulent latent heat flux coinciding with an overestimation of the sensible heat flux and too warm daytime skin surface temperatures.
Further sensitivity experiments made it possible to identify the causes of the major remaining biases in our simulations that can be summarized as follows:

- The 2m warm nocturnal bias at R3 station is attributed to the excess in daytime soil heating while a too strong nighttime thermal decoupling also explains part of the bias at Agafay. This point in fact questions the parameterization of the roughness height - and more generally of the surface drag - over Evergreen tree crops such as orange trees since neither parameters typical of low (C3 or C4) crops nor those of typical Evergreen high forest are appropriate.

- The overestimation of the daytime skin surface temperature and the lack of surface evapotranspiration are associated with a strong deficit in soil moisture over the three types of culture. The latter is partly explained by a lack of precipitation at Adgal and Agafay and by the absence of an effective irrigation parameterization in LMDZ-ORCHIDEE for the three sites. In fact, enhancing the model's surface moisture through a nudging method mimicking roughly an irrigation process helps simulate a more realistic evapotranspiration flux and daytime skin surface temperatures. Running reliable regional scenario simulations and carrying out impact studies over Morocco with LMDZ-ORCHIDEE would benefit from using a more sophisticated irrigation parameterization such as the one proposed in Arboleda-Obando et al. (2023).

This study has identified and highlighted the processes that should be correctly parameterized to realistically capture the main feature of the near-surface climate over the Moroccan agricultural plains. However, a comprehensive evaluation of the boundary layer dynamics in this region including an analysis of its vertical structure could not be performed, thereby raising the need to deploy observational systems such as radiosoundings or remote-sensing instruments. Note that the Moroccan weather services do not operate any routine radiosonde station over the Haouz plain, the nearest station is located at Casablanca, 220 km north of Marrakech.

In a Moroccan climate study perspective, it is also worth mentioning that our study has not assessed the performance of IPSL-CM to simulate the large-scale circulation patterns that drive the Moroccan climate and in particular the precipitation. This aspect has recently been tackled in Balhane et al. (in revision). Furthermore, our work has stressed the difficulty of evaluating numerical simulations from a model whose meshes are composed of heterogeneous vegetation cover with in situ station

data. Note that the ongoing MOSAI project (Modèles et Observations pour les Interactions entre la Surface et l'Atmopshère, https://anr.fr/Projet-ANR-20-CE01-0018) is tackling this issue, proposing original evaluation methods and revisiting the formulations of surface turbulent fluxes in heterogeneous meshes.

ACKNOWLEDGMENTS

This work is conducted in the context of Khadija Arjdal's doctoral program funded by Mohammed VI Polytechnic University (UM6P) in the framework of the UM6P and l'École Polytechnique de Paris (X) collaboration project on climate modeling.
We gratefully thank the Laboratoire Mixte Internationale (LMI-TREMA) for providing station data used for model evaluation. Vincent Simonneaux, Jamal Ezzahar and Mohamed Kharrou are thanked for their useful insights and discussions about the instrumented sites and also for the opportunity to visit these sites. Simulations were performed using HPC resources from the IDRIS (Institut du Développement et des Ressources en Informatique Scientifique, CNRS, France), projects RCES A0140100239 and RLMD AD010107632R1. We are grateful to Frédéric Hourdin, Abderrahmane Idelkadi, Florian Raymond, Catherine Rio, Maëlle Coulon Decorzons and Saloua Balhane for constructive insights. We also gratefully thank Agnès Ducharne, Pedro Arboleda Obando, Pierre Tiengou and Yann Meurdesoif for enriching and fruitful discussions about the irrigation process and its parameterization. We also acknowledge support from the DEPHY research group, funded by CNRS/INSU and Météo-France.

Data Availability Statement

Observation data is available on request from the joint international laboratory (LMI TREMA: https://www.lmi-trema.ma).
ERA5 data is available to download from the link https://cds.climate.copernicus.eu. The last version of the LMDZ source code can be downloaded freely from the LMDZ web site. The version used for the specific simulation runs for this paper is the "svn" release 3987 which can be downloaded and installed on a Linux computer by running the "installlmdz.sh" script available at this site (http://www.lmd.jussieu.fr/~/pub:./installlmdz.sh). The processing code used in this study is available from the authors on request (Khadija.Arjdal@um6p.ma).

Competing interest

The authors declare that they have no competing interests.

4.3 Investigation of the impact of irrigation upon near surface climate: further analysis

In section 4.2.3.4, we briefly analyzed the influence of irrigation parametrization on the near surface climate of the three studied stations Agdal, Agafay and R3 during the month of February 2003. In this section we will extend our analysis over the entire study period, with a more detailed analysis -at diurnal and seasonal scales- of the impact of irrigation on meteorological variables and the energy budget over the plain.

4.3.1 A more detailed description of the implemented irrigation parametrization

Irrigation schemes in climate modeling vary in terms of the added moisture as well as the frequency of its application (Zhang et al. (2017)). It may consist on maintaining constant soil moisture regardless of water demand (e.g. Harding and Snyder (2012)) or using realistic irrigation data set to define the model's irrigation locations and water amount (e.g. Sacks et al. (2009); Puma and Cook (2010); Arboleda-Obando et al. (2023)). Another type consists in using real-time climatic conditions to determine the irrigation frequency and moisture requirement (e.g., Tang et al. (2007); Pokhrel et al. (2012); Zhang et al. (2017)). Then, to assess the influence of the drip irrigation on the soil moisture across the Haouz plain, we developed a first order parameterization -derived from the latest category- that consists in nudging the volumetric soil moisture (SM, m^3 m^{-3}) in the 10 cm below the surface toward a saturated value (SM_s) when SM decreases below a fraction x_1 of SM_s (Figure 4.12):

$$\frac{dSM}{dt} = -\frac{SM - SM_s}{\tau} \tag{4.11}$$

with τ is a typical time scale, set equal to 6h, dt is the surface model time scale. The nudging stops when SM becomes greater than x_2 SM_s, such as x_1 and x_2 are set respectively to 0.2 and 0.8 for our experiment.

The irrigated domain is shown in Figure 4.13 (the red box), it includes the three stations grid points Agdal, Agafay and R3, with a unique PFT corresponding to the dominant vegetation cover on the stations (i.e Temperate Evergreen Broadleaf forests for Agdal and Agafay, and C3 crops for R3) and with prescribed aerodynamic roughness height (z_{0m}) (table 3.2). The simulations cover the period 2000-2011, with the first two years corresponding to the spin-up time. Here, the reference simulation is noted **PRSNT** and the one with activated irrigation is noted **PRSNT-Irr**.

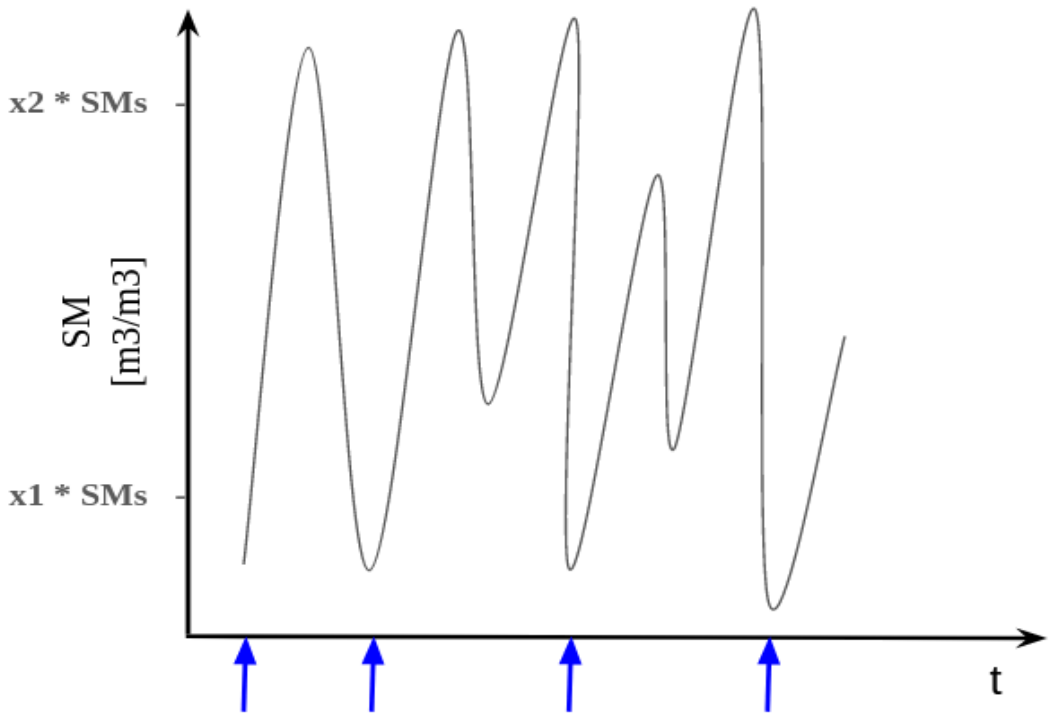

Figure 4.12: Simplified schematisation of the implemented nudging parameterization where soil moisture is forced to SMs (blue arrows) when it decreases below a fraction x_1 of SM_s

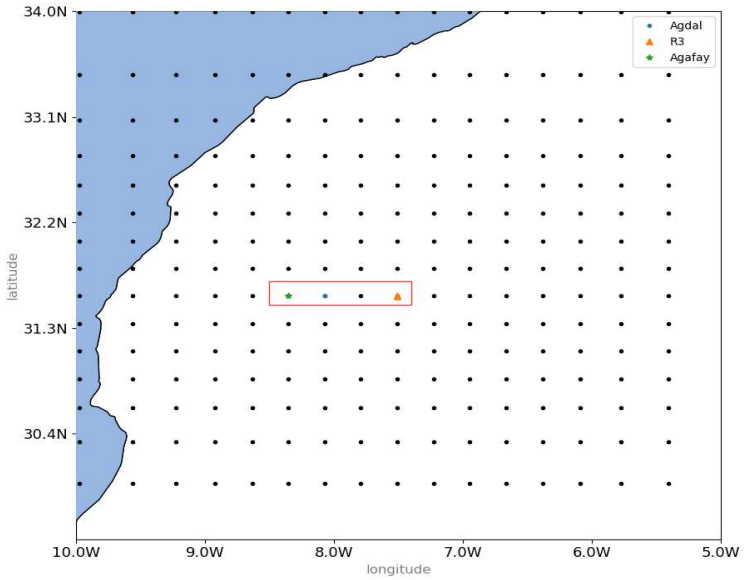

Figure 4.13: Overview of the irrigated longitude latitude box (red polygon), with the three stations location in colored symbols. Black points indicate the model grid.

4.3.2 Diurnal cycle

Over the three studied stations, surface energy budgets are significantly impacted by irrigation. As shown in panel a in Figures 4.14, 4.15 and 4.16, the magnitude of latent heat flux increases by 50 W m^{-2} during daytime, and by 5-10 W m^{-2} during nighttime. For sensible heat flux, the magnitude decreases by 15, 25 and 60 W m^{-2} in Agafay, Agdal and R3 respectively while nighttime changes are negligible, except for Agafay where it decreases by 1 to 10 W m^{-2}. Indeed, increased soil moisture is the main driver of the energy shift from the sensible heat towards the latent heat. Figure 4.17 shows the increased surface soil moisture by around 6% in Agdal and 13% in Agafay and R3 in PRSNT-Irr with respect to PRSNT which results in a dramatic increased evapotranspiration rates by +0.49 (+74%), +0.86 (+268%) and +0.77 (+44%) mm day^{-1} over Agdal, Agafay and R3 respectively (not shown). In fact, the soil moisture response to irrigation questions the soil characteristics in ORCHIDEE. The latter may have a weak saturated soil moisture, since peaks during nudging events are constantly less than 0.3 m^3 m^{-3} over the three stations. The relatively weaker change in soil moisture may also be explained by the possible effect of soil water retention, especially between the surface and 5 cm depth. For instance, an intense upward water transfer for evaporation may continuously dry-out the soil.

The enhanced evaporative flux leads to cooler skin surface temperatures, Figures 4.14.b, 4.15.b and 4.16.b show reduced daytime skin surface temperature by -1°C in Agdal and Agafay and by -2°C in R3. This latter is relatively higher, and is associated with a decrease in sensible heat flux and then the Bowen ratio. In contrast, nighttime skin surface temperature decreases very slightly over R3 (-0.1 °C) and holds inverse result over Agdal and Agafay where it increases slightly (+0.2°C), reducing the diurnal temperature range (DTR). This may be due to increased soil thermal inertia accompanying the soil moistening which reduces the nocturnal cooling as demonstrated in Aït-Mesbah et al. (2015) and Cheruy et al. (2017). Indeed, the ground heat flux (G) (panel g in Figures 4.14, 4.15 and 4.16) increases during daytime by around +10 W m^{-2} and decreases during nighttime by around -5 W m^{-2} in Agafay and Agdal, while it is almost unchanged with irrigation over R3. This could be linked with the increased soil thermal conductivity with irrigation in the tree-covered stations, that enhances the upward and downward heat fluxes in the soil resulting in warmer nighttime temperature that prevents the cooling effect of irrigation on skin surface temperature. A similar result was also shown in studies by Kanamaru and Kanamitsu (2008) and Wang et al. (2021).

The surface cooling results in cooler 2m temperatures, particularly during daytime, thus, the model warm biases are reduced by around 1°C over the plain. Correspondingly, the relative humidity increases by +5 to 10 % and it is maximal at noon over R3. The resulting colder air, supposed to emit less longwave radiation to the surface, is compensated by the enhanced greenhouse effect of the moist air. Thus, LW_{dn} changes with irrigation are smaller (<5 W m^{-2}). On the other hand, upward infrared radiation decreases by nearly -10 W m^{-2} as skin surface temperature decreases, resulting in decreased surface net longwave radiation.

Irrigation increases also vegetation transpiration as a direct response to the extra water in the soil. As shown in Figure 4.3.2, averaged vegetation transpiration increases by +0.15 (73%), 0.13 (82%) and 0.22 (58%) mm day^{-1} in Agdal, Agafay and R3 respectively from 2002 to 2011. We also noticed an increase in the LAI by up to +50% (not shown) in response of an enhanced photosynthesis and plant

development (Arboleda-Obando (2023)). Therefore, surface albedo is reduced by -0.02 (20%) and by -0.06 (50%) respectively in Agdal and Agafay with PRSNT-Irr, due to the darker effect of moist soil and also to the subsequent vegetation growth (Sacks et al. (2009); Jiang et al. (2014)). Thus, changes in reflected solar radiation range to -10 W m^{-2} and to -50 W m^{-2} respectively in Agdal and Agafay, reducing the net solar radiation given that incoming solar radiation has not changed with irrigation in our case. However, in R3 both solar radiation terms remain unchanged with irrigation due to the unchanged surface albedo. Suggesting that the cloud cover doesn't change locally.

The net surface radiation (Rn) increases by +60, 20 and 5 W m^{-2} over Agafay, Agdal and R3 respectively due to irrigation. The Rn excess, partly counterbalanced by the increased ground heat flux, is balanced by the evaporative flux at the expense of surface heating in the surface energy balance (see Eq. 4.4), particularly in Agafay where Le changes magnitude surpasses H. In Agdal and R3, the respective changes in turbulent fluxes are relatively equivalent in magnitude.

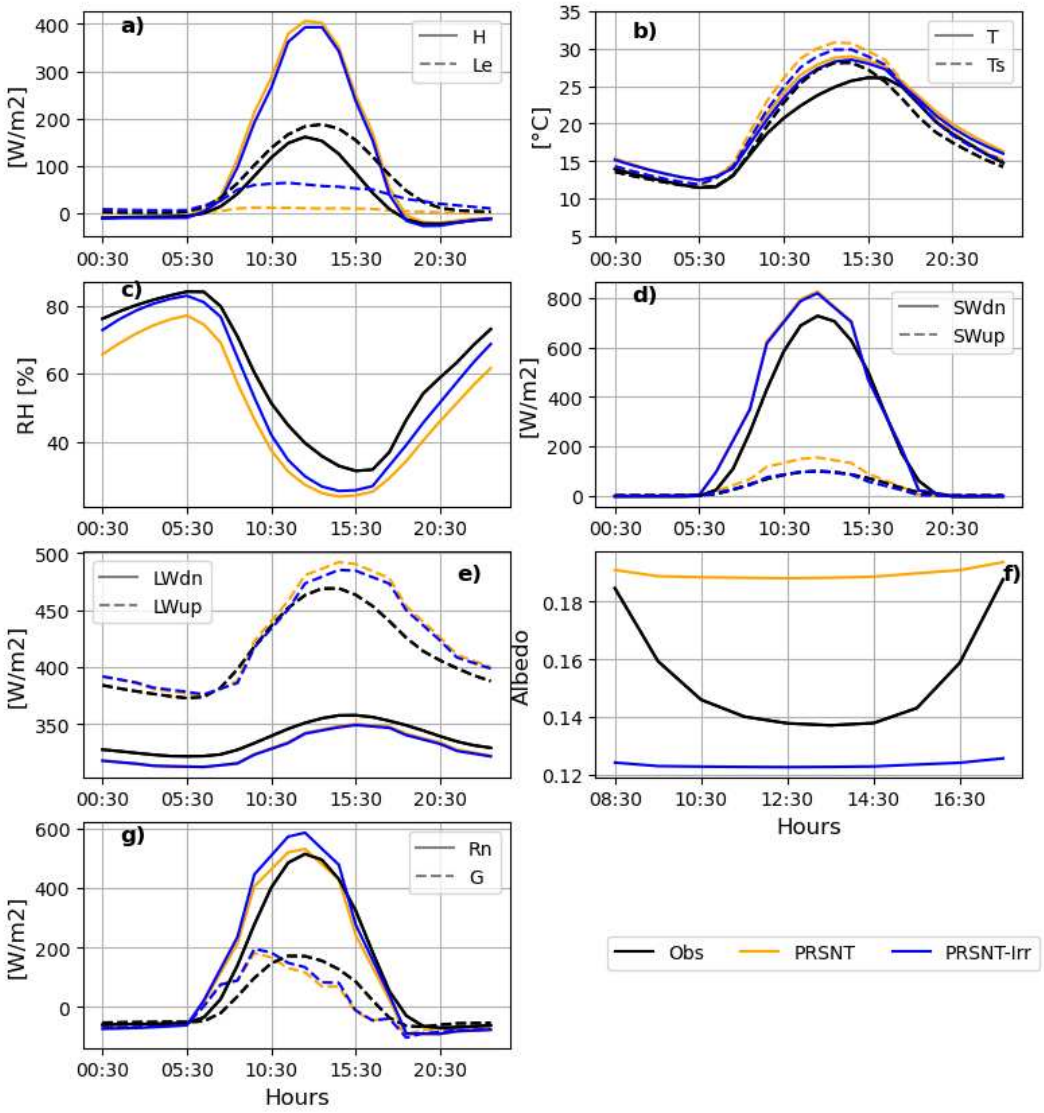

Figure 4.14: 2006-2009 diurnal cycle composite of (panel **a**): latent (Le) and sensible (H) heat fluxes, **b**): mean diurnal cycles of 2m temperature (T), skin surface temperature (Ts), **c**): relative humidity (RH), **d**): downward (SWdn) and upward solar radiation (SWup), **e**): downward (LWdn) and upward longwave radiation (LWup), **f**): albedo, **g**): surface net radiation (Rn) and the ground heat flux (G) in Agafay station from model simulations (PRSNT in orange and PRSNT-Irr in blue) and observations (black).

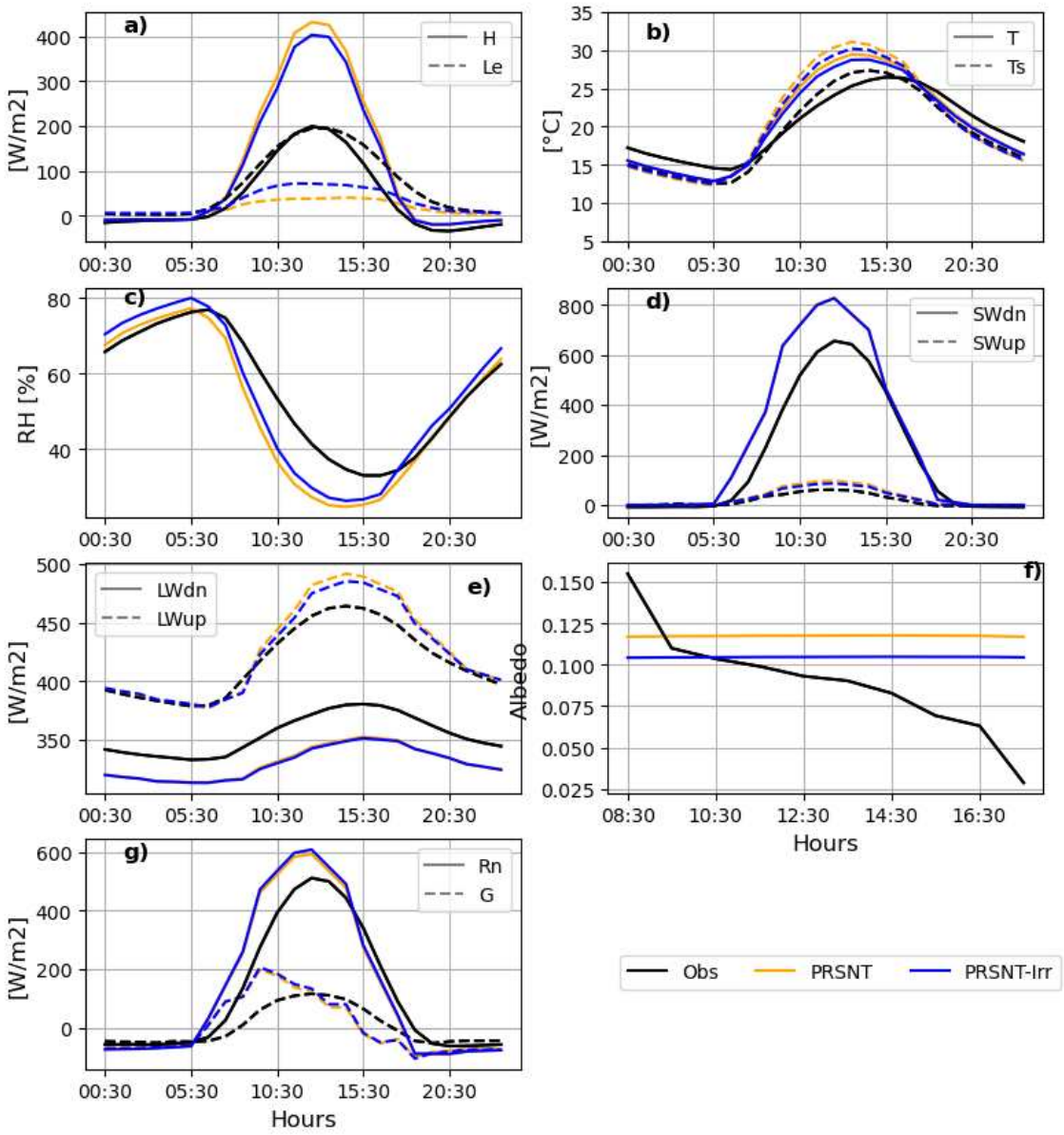

Figure 4.15: Similar as Figure 4.14 but for Agdal station during the study period 2002-2004

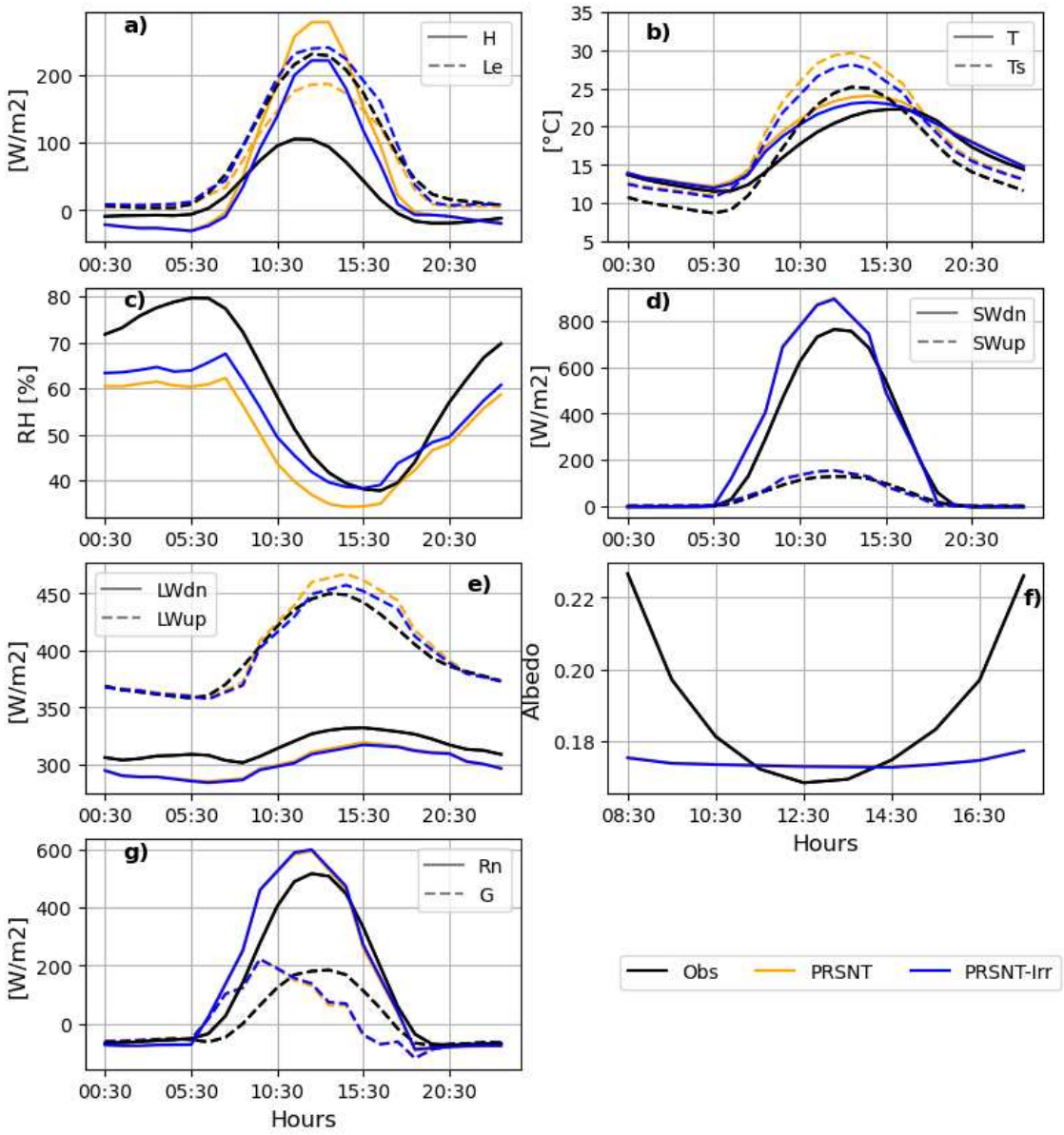

Figure 4.16: Similar as Figure 4.14 but for R3 station during the study period 01/2003 - 05/2003

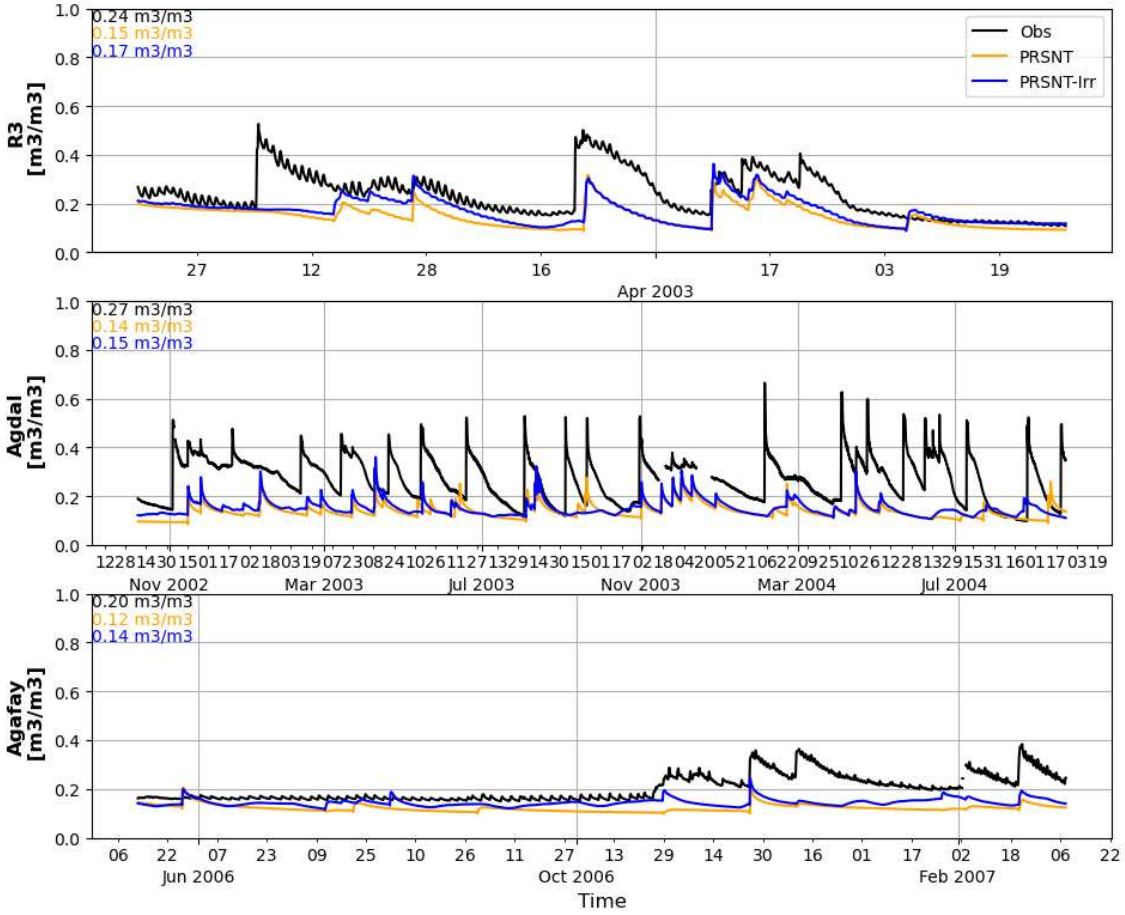

Figure 4.17: Soil moisture at 5 cm depth at R3, Agdal and Agafay stations grid cells for observations (black), PRSNT (blue) and PRSNT-Irr (orange) simulations. The average of each time series are shown at the top left of the Figure.

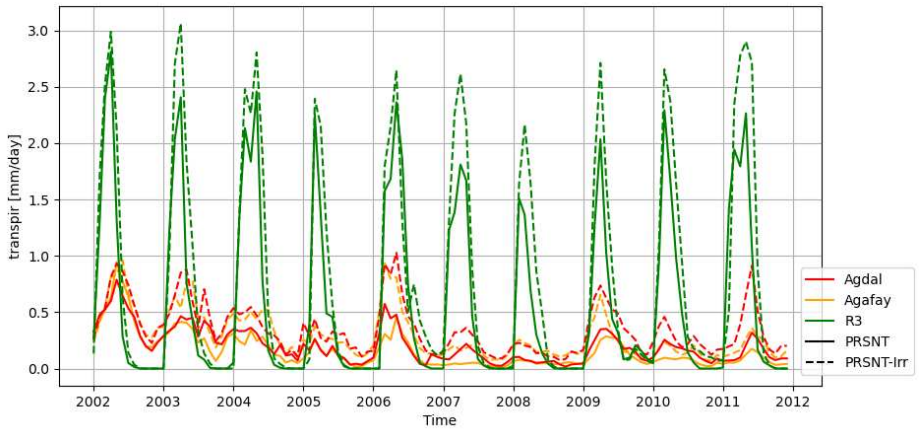

Figure 4.18: Monthly averaged transpiration (mm day^{-1}) over Agdal (red color), Agafay (orange) and R3 (green) during the 10-year simulaion 2002-2011. Solid lines correspond to the PRSNT configuration, dashed lines correspond to the PRSN-Irr.

4.3.3 Seasonal aspects

Figures 4.19 show the seasonal cycle of solar the meteorological variables (T, Ts, RH and Precip) over Agafay station during 2006-2009. In this section, the analysis is only focused on Agafay since the results are very similar at R3 and Agdal.

Simulated monthly averaged downward solar radiation is overestimated in the reference run (PRSNT) by +50 W m^{-2} during summer and by around +10 W m^{-2} during winter (not shown). In the irrigated configuration, no change was noted, whereas, the reflected surface solar radiation bias previously varying from +10 (in winter) to +25 W m^{-2} (in summer) in PRSNT is completely eliminated with PRSNT-Irr. Simulated SWup by this latter fits well the observed one from June to December, and it is 10 W m^{-2} lower than OBS in the first six months of the year following the surface albedo changes (not shown) associated with the darker effect of wetter soils on the one hand, and with the subsequent increased LAI on the other hand.

Latent heat flux increases with irrigation by +15 to 40 W m^{-2} from winter to summer, respectively (not shown). Reducing the model-observation differences from -100 to -60 W m^{-2} during summer, and from -25 to -10 W m^{-2} during winter. Thus, the PRSNT-Irr exhibits a clearer seasonality, in which the maximum flux rates occur in summer and the minimum in winter, following the temperature cycle. In fact, without irrigation there was not enough moisture supply to follow the potential evapotranspiration, as also reported by Zhang et al. (2017). Correspondingly, sensible heat flux decreases with irrigation, but not with the same rate as Le, nor with any particular seasonal pattern. H decreases by around 10 W m^{-2} throughout the year, maintaining the overestimated aspect and the very strong seasonal contrast (i.e. summer minus winter average) of +130 W m^{-2}. This latter is around +60 W m^{-2} in the observations.

Simulated monthly skin surface and near surface temperature are overestimated by around +1.5°C during winter (Figures 4.19.a, 4.19.b), and by up to +3°C during summer in the PRSNT. But when the irrigation is activated, and in accordance with the increased (respectively, decreased) latent heat flux (respectively, sensible heat flux), temperature is reduced at an almost constant rate of 1°C throughout the year, maintaining the model's seasonality and warm bias. PRSNT-Irr produces also a cooler surface air, as shown in Figure 4.19, relative humidity increases on average by +5 %.

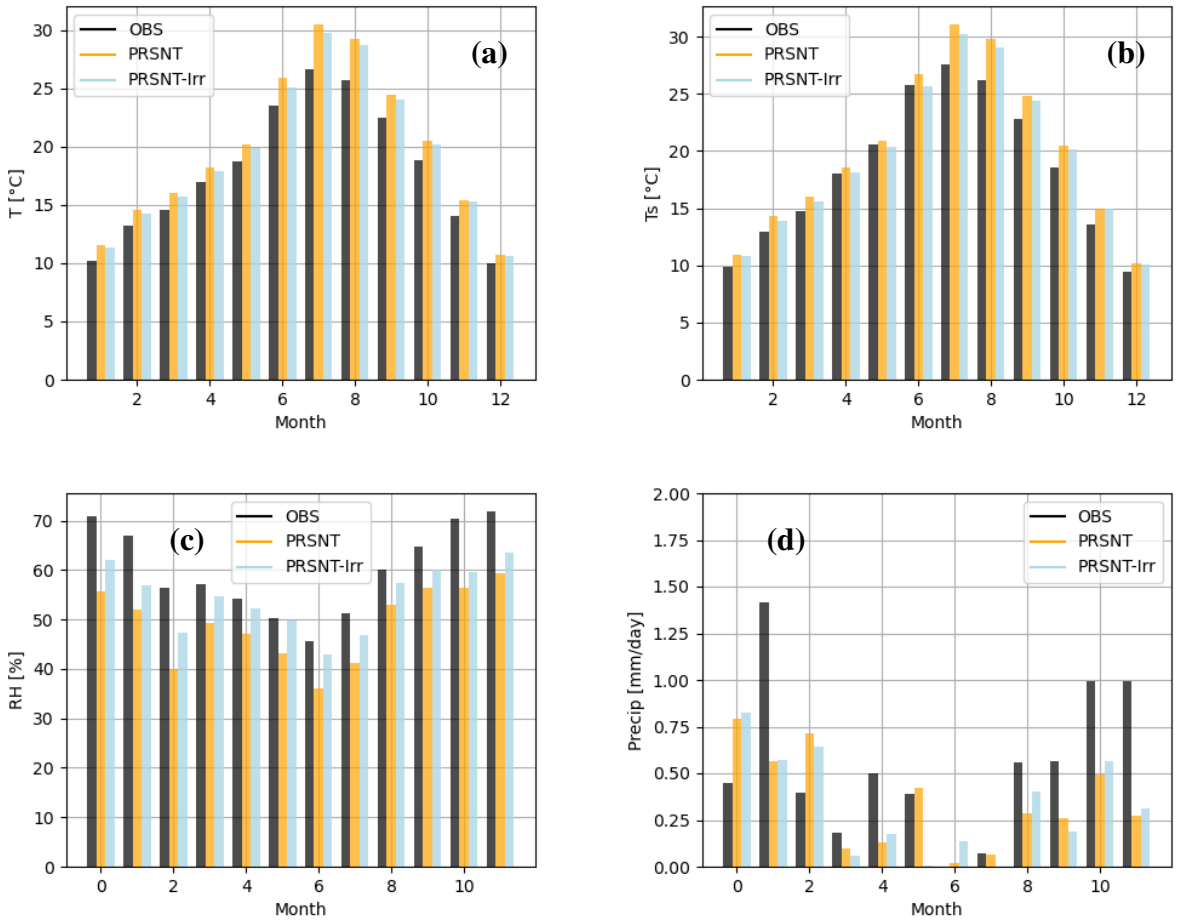

Figure 4.19: Observed and simulated (PRSNT and PRSNT-Irr) monthly surface and air temperature, relative humidity and precipitation rate during the period 2006-2009 over Agafay

Irrigation can potentially increase the local and the regional precipitation pattern by increasing relative humidity and latent heat flux that enhances the moist static energy within the convective boundary layer (DeAngelis et al. (2010); Zhang et al. (2017); Lo and Famiglietti (2013)), in our case, the change is negligible over the three stations and is even negative (-0.01 mm day^{-1}, -1%) in Agafay with a mixed seasonal behaviour (Figure 4.19.d). Over the 10-year simulation 2002-2011, it holds no significant change over the three stations (Figure 4.20). This suggests a possible competing effect of the surface cooling and the decreased sensible heat flux that prevent the PBL growing to trigger convection, as reported in Marcella and Eltahir (2014); Yang et al. (2016); Zhang et al. (2017).

Besides, a sensitivity analysis was also conducted for the adjacent cells to the irrigated zone to identify a possible remote effect of irrigation. Results suggest that there is not a significant effect on precipitation, radiative fluxes or meteorological variables.

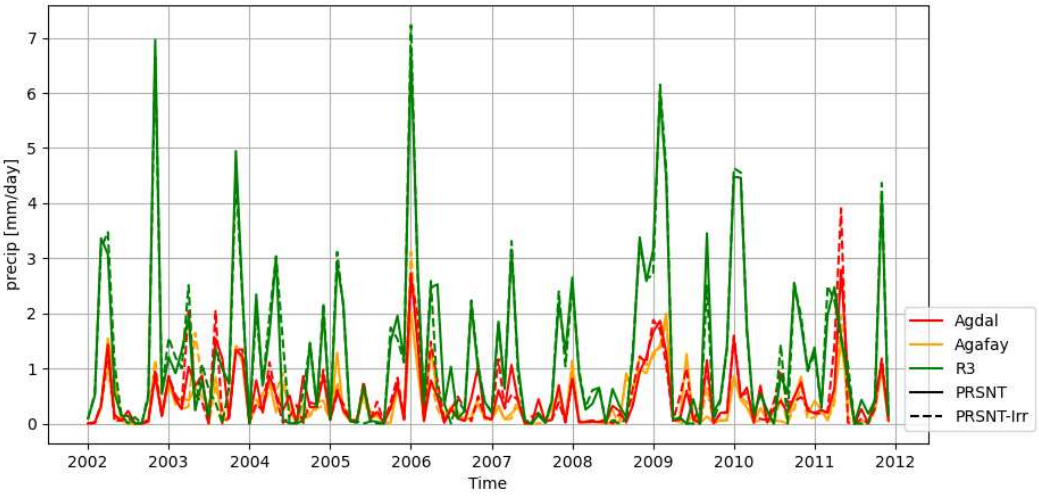

Figure 4.20: Monthly averaged precipitation rates (mm day^{-1}) over Agdal (red color), Agafay (orange) and R3 (green) during the 10-year simulaion 2002-2011. Solid lines correspond to the PRSNT configuration, dashed lines correspond to the PRSN-Irr.

4.4 Chapter conclusions

This chapter aims to evaluate the LMDZ-ORCHIDEE land-surface atmosphere model, in its CMIP6 version, over the Haouz plain using stations with different types of culture.

A standard simulation with a zoom centered over the plain and nudging outside of the zoom area was implemented, along with sensitivity tests that aimed at addressing the model robust biases. In fact, we carefully designed a methodology which allows the model-observations comparison despite the fact that the sites are not representative of the model grid cells. Then, we set a unique PFT in each mesh, compatible with the station's vegetation coverage, to disentangle the model biases. Based on the evaluation conducted, it can be concluded that LMDZ-ORCHIDEE provides a realistic representation of land-surface atmosphere interactions in the Haouz plain. It simulates reasonably the mean annual and seasonal patterns of meteorological variables and radiative fluxes over the plain. However, an in-depth analysis reveals some model-observation differences. On the one hand, an overestimated nighttime 2m temperature over R3 and Agafay is noticed, attributed to the excessive skin surface temperature exceeding 5K in R3, and to a higher thermal decoupling in Agafay, albeit partly. On the other hand, a negative evapotranspiration bias and an intense surface heating associated with a strong deficit in soil moisture are observed over the three stations. This latter may be partly explained by insufficient precipitation at Agdal and Agafay, and also by the absence of an irrigation module in ORCHIDEE for the three stations. Furthermore, the model holds a wind speed negative bias over the tree-covered stations, slightly reduced when deactivating the dynamical roughness height, questioning the parametrization of the surface drag in the model.

Incorporating an irrigation parametrization that mimics the drip irrigation in the plain, leads to substantial increase of daytime latent heat flux (+50 W day^{-1}) at the expense of sensible heating. This latter varies in magnitude between the stations, for instance, in the C3 crops-covered station (R3), where the surface albedo and the net surface radiation are almost unchanged with irrigation, H decreases with the same rate as Le. But in the tree-covered stations (Agdal, Agafay), where irrigation enhances the LAI and increases Rn, H decreases relatively less than Le. Irrigation also leads to a large cooling effect over the plain, the surface and 2m temperature biases are reduced by 2K and 1K respectively during daytime, in contrast to an opposing nighttime signal, albeit slight, attributed to increased soil thermal inertia accompanying the soil moistening. The irrigation's moistening and cooling effect mainly occurs during the day than night, and during summer than winter.

Although our irrigation parametrization is quite crude, with an artificial water supply which is not fed by surface or groundwater pumping, it has gathered first insights on the impact of irrigation on the surface climate of arid plains, using the coupled land-atmosphere model LMDZ-ORCHIDEE with a zoom. Therefore, our work has opened up new perspectives for developing a more advanced irrigation parameterization, such as the one proposed in Arboleda-Obando (2023), but on the coupled and zoomed configuration. Then, I am currently collaborating with P. Tiengou to implement the irrigation module on my configuration.

CHAPTER 5

Climate projections over Morocco: from global scenarios down to local assessment over the Haouz plain

Contents

5.1 Introduction to the chapter 83

5.2 Article. Future of land surface water availability over the Mediterranean basin and North Africa: analysis and synthesis from the CMIP6 exercise 84

5.2.1 Introduction 84

5.2.2 Data and methods 86

5.2.3 Results and discussion 88

5.2.4 Summary and conclusions 96

5.3 Changing climate in the Haouz plain as simulated by LMDZ-ORCHIDEE . . 99

5.3.1 Numerical design 99

5.3.2 Projected near surface climate over the Haouz plain 101

5.3.3 Influence of the irrigation parametrization on climate change projections . . 106

5.4 Chapter conclusions 112

"Science knows no country, because knowledge belongs to humanity, and is the torch which illuminates the world."
-Louis Pasteur

5.1 Introduction to the chapter

In the previous chapter we assessed the ability of LMDZ-ORCHIDEE to reproduce the present climate over the Moroccan plains, highlighting the critical roles of irrigation and key coupling parameters such as the surface drag. We will now focus on future climate projections over Morocco with a particular emphasis on the Haouz plain.

For this purpose, we will start by conducting a comprehensive analysis of the CMIP6 global scenarios over the Mediterranean and North Africa. Then, the first part of this chapter (section 5.2) includes a paper published in Atmospheric science letters (Arjdal et al. (2023)) that focuses on the future of land surface water availability over the Mediterranean basin and North Africa. The supplementary information of the paper is given in Appendix B. In its first sections (5.2.3.1, 5.2.3.2), we present the annual and seasonal patterns of future changes of precipitation, evapotranspiration, P-E, and surface moisture under the scenarios SSP2-4.5 and SSP5-8.5. Then, we analyze the time evolution of those patterns over three studied regions; northern and southern Mediterranean basin and Sahara, with a sensitivity study to the model horizontal resolution (section 5.2.3.3). Finally we make a comparative study to examine differences between CMIP5 and CMIP6 patterns of change (section 5.2.3.5).

Thereafter, we will regionalize the future scenarios to assess their impacts over the plain, using the nudged and zoomed configuration. we conduct an in-depth analysis of the projected near surface climate over the Haouz plain (section 5.3), using the land-surface atmosphere model LMDZ-ORCHIDEE with a grid refinement over the plain and nudging towards a CMIP6 SSP5-8.5 scenario outside of the zoom area. Section 5.3.1 represents the numerical design of the present and future simulations, then, section 5.3.2 explores the response of the LMDZ-ORCHIDEE to climate change over the studied sites Agdal, Agafay and R3. Finally we investigate how the irrigation practices may modulate the evolution of the local climate in Moroccan plains 5.3.3.

5.2 Article. Future of land surface water availability over the Mediterranean basin and North Africa: analysis and synthesis from the CMIP6 exercise

Arjdal, K., Driouech, F., Vignon, É., Chéruy, F., Manzanas, R., Drobinski, P., Chehbouni, A. and Idelkadi, A. (2023). Future of land surface water availability over the Mediterranean basin and North Africa: Analysis and synthesis from the CMIP6 exercise. Atmospheric Science Letters, e1180, https://doi.org/10.1002/asl.1180

Abstract

The Mediterranean basin and Northern Africa are projected to be among the most vulnerable areas to climate change. This research documents, analyzes, and synthesizes the projected changes in precipitation P, evapotranspiration E, net water supply from the atmosphere to the surface P–E, and surface soil moisture over these regions as simulated by 17 global climate models from the sixth exercise of the Coupled Model Intercomparison Project (CMIP6) under two Shared Socioeconomic Pathways, SSP2-4.5, and SSP5-8.5. It also explores the sensitivity of the results to the chosen climate scenario and model resolution and assesses how the projections have evolved from the fifth exercise (CMIP5). Models project a statistically robust drying over the entire Mediterranean and coastal North Africa. Over the Northern Mediterranean sector, a significant precipitation decrease reaching -0.4 $\pm$ 0.1 mm day^{-1} is projected during the 21st century under the SSP5-8.5 scenario. Conversely, a significant increase in precipitation of +0.05 to 0.3 $\pm$ 0.1 mm day^{-1} is projected over South-Eastern Sahara under the same scenario. Evapotranspiration and soil moisture exhibit decreasing trends over the Mediterranean basin and an increase over the Sahara for both SSPs, with a notable acceleration from the 2020s. As a result, P-E is projected to decrease at a rate of about -0.3 mm day^{-1} under the high-end scenario SSP5-8.5 over the Mediterranean whilst no significant changes are expected over the Sahara due to evapotranspiration compensation effects. CMIP6 and CMIP5 models project qualitatively similar patterns of changes but CMIP6 models exhibit more intense changes over the Mediterranean basin and South-Eastern Sahara, especially during winter.

5.2.1 Introduction

Climate projections indicate that the Mediterranean and adjacent Northern Africa are among the most vulnerable areas to global warming (Almazroui et al. (2020); Lee et al. (2020)), specifically regarding the hydrological cycle (Hanel et al. (2018)) and heat extremes (Seneviratne et al. (2021)). The intensity of climate change in the Mediterranean region and the associated high socio-economical risks raised the necessity of establishing the First Mediterranean Assessment Report (Cherif et al. (2020)).

Moreover, the recent sixth Assessment Report of the Intergovernmental Panel on Climate Change (IPCC) stresses that "there is high confidence that anthropogenic forcings are causing increased aridity and drought severity in the Mediterranean region" (Douville and John (2021)). Subsequently, potential stress on water resources are projected over the Southern Mediterranean region (Prudhomme et al. (2014)), consistently with a projected decrease in surface water resources in North Africa under various climatic scenarios owing to precipitation reduction and evapotranspiration increase (Balhane et al. (2021); Driouech et al. (2010); Tramblay et al. (2018)). Therefore, assessing the water cycle and surface hydrology response to global warming in water-stressed areas such as North Africa and the Southern Mediterranean region is crucial for anticipating consequences on water supplies, agriculture, and ecosystems (Marchane et al. (2017); Tramblay et al. (2018)).

Global climate models (GCMs), and in particular those included in the Coupled Model Intercomparison Projects (CMIP; IPCC (2021)), are commonly-used tools to assess the future effects of climate change on the water cycle and particularly on the different terms of the surface water budgets. In a CMIP5 (fifth CMIP phase)-based study, Mariotti et al. (2015) found a significant decrease in mean precipitation over southern areas of the Mediterranean during winter under a moderate greenhouse gas emission scenario. Lionello and Scarascia (2018) report a decrease of 4% per degree of warming in annual precipitation over the Mediterranean area according to CMIP5 models under the high-emission RCP8.5 scenario. Mariotti et al. (2015) found a precipitation reduction during summer over Spain, western Northern Africa, and Turkey along with a projected increase in winter evapotranspiration over Northern Mediterranean land by the end of the 21st-century relative to the 1980–2005 reference period.

Precipitation (P) minus evapotranspiration (E) (P–E hereafter) represents the net freshwater flux from the atmosphere to the surface as defined by Byrne and O'Gorman (2015), and is also called "water availability." P–E drives the water percolation and soil moisture (SM), the run-off, and ultimately the river flow and groundwater recharge. The climatological P–E is close to zero over Mediterranean (MED hereafter) lands except in Northern areas during winter where P surpasses E (Mariotti et al. (2015)). CMIP5 projections indicate a general decreasing trend for P–E across MED lands, specifically during summer due to the precipitation decrease over Northern areas (Mariotti et al. (2015)). Assessing future changes in surface SM is also critical to anticipate the impact of changes of the hydrological cycle on several socio-economical activities such as agriculture (Ruosteenoja et al. (2018); Seneviratne et al. (2010)), especially in arid and semi-arid areas. Over the Mediterranean basin, CMIP5 models simulate a continuous reduction in total soil moisture during the twentieth century, and it is expected to persist throughout the 21st-century (Mariotti et al. (2015)).

In addition to GCMs, regional climate models (RCMs) laterally forced with GCMs are also employed to provide scenarios at higher resolutions over a specific area. Climate change impacts across the MED area have been estimated from RCM simulations in the framework of the Coordinated Regional Climate Downscaling Experiment database (Drobinski et al. (2020); McSweeney et al. (2015); Tebaldi et al. (2005)). Tuel et al. (2021) underlined the necessity of carefully selecting the GCMs

used to force the RCM to properly project the climate over the MED region. Hence the need to select carefully and analyze the surface water projections and related uncertainties across the Mediterranean and North Africa from recent GCM simulations.

In this paper, we provide an in-depth analysis and synthesis of the surface water supply projections from the newly available CMIP6 GCMs—which show considerable improvements in terms of spatial resolution and physics with respect to CMIP5 (Eyring et al. (2016))—over MED and Saharan (SAH hereafter) subregions. For this purpose, we analyze the quantitative evolution of precipitation, evapotranspiration, P–E, and surface SM over those two regions for a carefully-selected set of simulations and thoroughly discuss the ensemble statistics. Note that evaluating RCM scenarios over MED and SAH is beyond the scope of the present paper, but our study will help better assess the suitability of future projections from the last generation global projections as boundary conditions for RCM runs.

5.2.2 Data and methods

We considered 17 GCMs involved in the CMIP6 database (https://esgf-node.llnl.gov/search/cmip6/) and analyzed the "historical" (1850–2014) simulations (Eyring et al. (2016)) and the low and high-end forcing Shared Socio-economic Pathways "SSP2-4.5" and "SSP5-8.5" (2015–2100) simulations from ScenarioMIP (O'Neill et al. (2016)). The models' selection was based on the availability of the following output variables at the time of the study: 2m temperature, precipitation rate, evapotranspiration, and surface SM content (top 10 cm) over the period 1850–2100 (historical + scenarios) (Table 5.1). Three models considering enclosed marginal seas as "land" have further been excluded to avoid inconsistencies in the multi-model land evapotranspiration statistics. Following Agosta et al. (2015) we have briefly assessed the performance of the selected model to simulate the large-scale climate patterns driving the MED and SAH climate (see Figure 6.23 in Section B of the supplement). None of the models considered here outperforms or lies outside the others but models with a higher horizontal resolution generally show better performance in terms of large-scale circulation metrics. For a thorough evaluation of CMIP6 models over the Mediterranean and African regions in terms of near-surface climate, we also refer the readers to Babaousmail et al. (2021); Bağçaci et al. (2021); Seker and Gumus (2022). For the sake of fairness in our comparative study, we selected the available set of climate models from CMIP5 and its updated version of CMIP6 (Table 6.1). We will also briefly comment on the behavior of the total SM content. SM contents will be expressed as relative rather than absolute quantities since the soil schemes of the different models and especially their depths vary (Cook et al. (2020)). Analyses are conducted over the MED and Sahara (SAH) subregions as defined for the IPCC's sixth assessment (Iturbide et al. (2020)), as shown in Figure 5.1.a.

Northern and Southern shores of the Mediterranean Sea are expected to exhibit quite different quantitative responses to climate change (Tuel et al. (2021)), We, therefore, subdivide the MED sector into two sub-regions for our analyses: the Northern (N_MED, northern than 35°N) and Southern (S_MED) Mediterranean (see Figure 5.1).

In order to assess uncertainties and identify robust signals in future model projections, we calculated the multimodel ensemble mean and variance across models. As the large-scale circulation fields over

the MED and SAH regions seem to be resolution dependent (Section B of the supplement), we will separately consider two groups of models depending on their resolution (Table 5.1): one group for which the native horizontal resolution is close to ∼100 km and another one for which it is close to ∼250 km. Given that our work focuses on land, we masked out grid boxes where the land area fraction is less than 90%. This later has been chosen as a trade-off to conserve the largest possible study area avoiding retaining meshes at the continent margins for which the evapotranspiration flux is not representative for land surfaces (Figures 6.16 and 6.17). For assessing the statistical robustness of future changes (or non-changes), we use the nonparametric Wilcoxon–Mann–Whitney test comparing future (2071–2100) and historical (1981–2010) data for each individual model. An increase or a decrease is deemed statistically robust if at least two-thirds of the models project significant (i.e., the p-value of the Wilcoxon–Mann–Whitney test <= 0.05) changes that agree on the sign. Unlike the robustness tests used in IPCC (2021), we also consider a constant response to be robust if at least two-thirds of the models exhibit a non-statistically significant change.

Table 5.1: List and characteristics of CMIP6 models used in this study.

CMIP6 models	Original horizontal resolution (lon×lat)	Run	References
BCC-CSM2-MR	1.1° x 1.1°	r1i1p1f1	Wu et al. (2019)
CAMS-CSM1-0	1.1° x 1.1°	r2i1p1f1	Rong et al. (2019)
CESM2	1.3° x 0.9°	r4i1p1f1	Lauritzen et al. (2018)
CESM2-WACCM	1.3° x 0.9°	r1i1p1f1	Li (2019)
CMCC-CM2-SR5	0.9° x 1.2°	r1i1p1f1	Cherchi et al. (2019)
MPI-ESM1-2-HR	0.9° x 0.9°	r1i1p1f1	Gutjahr et al. (2019)
MRI-ESM2-0	1.1° x 1.1°	r1i1p1f1	Yukimoto et al. (2019)
NorESM2-MM	1.2° x 0.9°	r1i1p1f1	Seland et al. (2020)
TaiESM1	0.9° x 1.25°	r1i1p1f1	Lee et al. (2020)
CNRM-CM6-1	1.4° x 1.4°	r1i1p1f2	Voldoire et al. (2019)
CNRM-ESM2-1	1.4° x 1.4°	r1i1p1f2	Séférian et al. (2019)
GISS-E2-1-G	2° x 2.5°	r1i1p1f2	Kelley et al. (2020)
IPSL-CM6A-LR	2.5° x 1.3°	r1i1p1f1	Boucher et al. (2020)
MIROC6	1.4° x 1.4°	r1i1p1f1	Tatebe et al. (2019)
MPI-ESM1-2-LR	1.9° x 1.9°	r1i1p1f1	Mauritsen et al. (2019)
NorESM2-LM	2.5° x 1.9°	r1i1p1f1	Seland et al. (2020)
UKESM1-0-LL	1.9° x 1.3°	r1i1p1f2	Sellar et al. (2019)

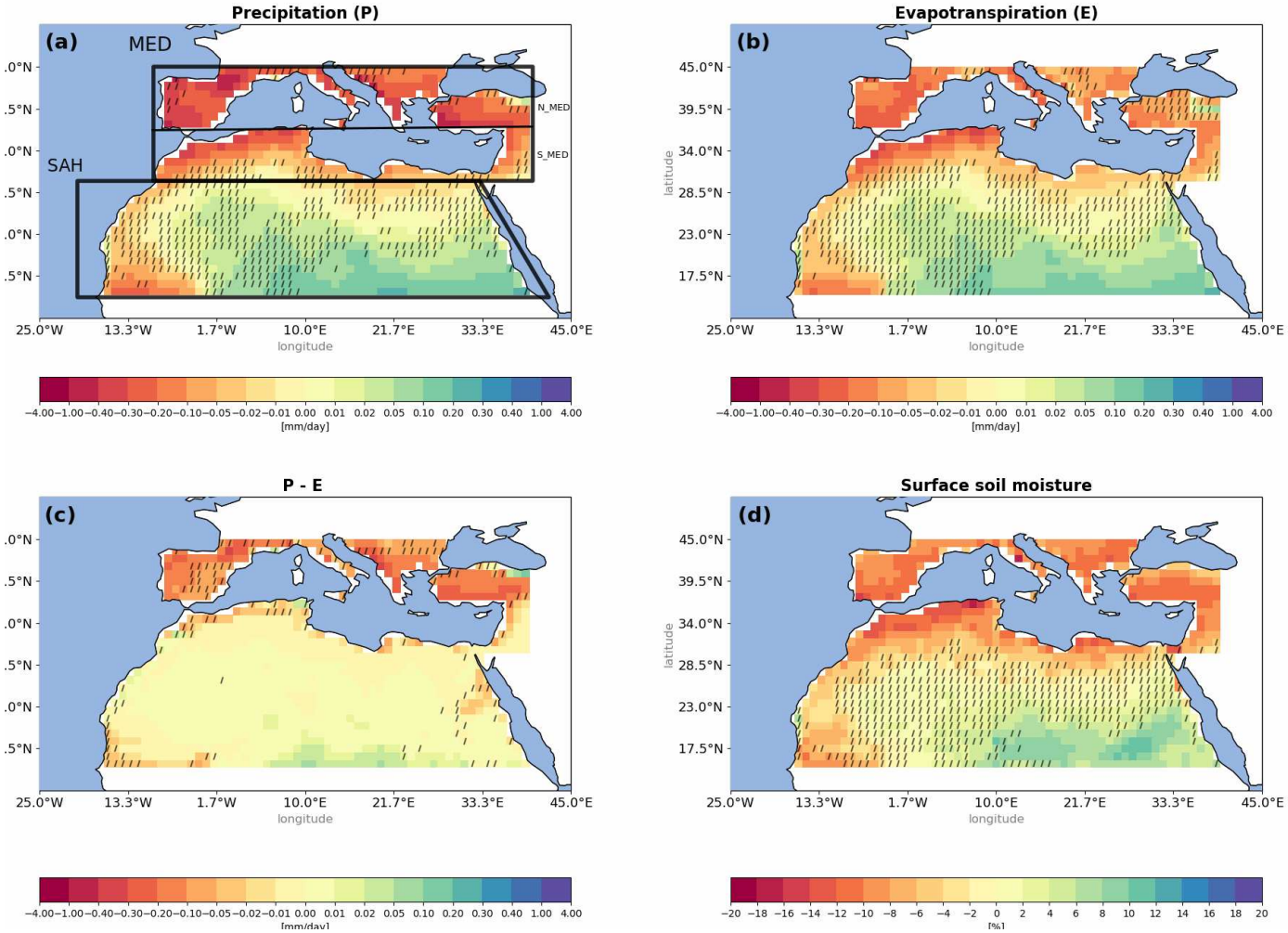

Figure 5.1: Future changes in the 100 km ensemble-mean annual precipitation (mm day^{-1}), evapotranspiration (mm day^{-1}), P–E (mm day^{-1}), and surface soil moisture (%) over the Mediterranean basin and the Sahara under the SSP5-8.5 scenario for 2071–2100 with respect to 1981–2010. The slashes correspond to grid boxes exhibiting nonrobust changes based on the nonparametric Wilcoxon–Mann–Whitney test with a 95% threshold.

5.2.3 Results and discussion

5.2.3.1 Spatial patterns of future changes of precipitation, evapotranspiration, P-E, and surface moisture for the SSP2-4.5 and SSP5-8.5 scenarios

Figures 5.1, 5.2 show the 100 km ensemble-mean annual changes under SSP5-8.5 and SSP2-4.5 scenarios respectively. The projected changes—calculated as the difference between the 2071–2100 and 1981–2010 periods—show reduced precipitation over MED and all along the Atlantic coasts of Morocco and Mauritania. Figures 5.1.a, 5.2a show a robust decrease of precipitation reaching -0.4 (-0.3) mm day^{-1} across the western part of MED and nearly -0.1 to -0.02 (respectively, -0.05 to -0.01) mm day^{-1} in the eastern part, mostly in Libya and Egypt for the SSP5-8.5 (respectively, SSP2-4.5) scenario ensembles. The increase in precipitation over the South-Eastern SAH ranges between

+0.05 to 0.3 (respectively, +0.01 to 0.3) mm day^{-1} by the end of the century for high (medium)-end scenario emission. This concurs with Waha et al. (2017) who showed that a projected northward shift of the inter-tropical convergence zone (ITCZ) will enhance moisture transfer to the Southern Middle East and North Africa. CMIP6 models also project a robust northward shift of the ITCZ over eastern Africa, mostly between May and October (Mamalakis et al. (2021)). Our results show that precipitation changes are more pronounced under the SSP5-8.5 scenario. Consistently, a statistically robust decrease in evapotranspiration is also projected over the whole Mediterranean region (Figures 5.1.b, 5.2.b), especially over the Iberian Peninsula (IP) and Northern Africa. The projected changes range from -0.05 to -0.3 (respectively, -0.01 to -0.2) mm day^{-1} over Spain, Northern Morocco, Algeria, and Tunisia, with less intense changes not exceeding $\sim$ -0.05 (respectively, -0.02) mm day^{-1} projected over Egypt, Syria, and Turkey for the SSP5-8.5 (respectively, SSP2-4.5) scenario, in addition to positive changes ($\sim$+0.02 mm day^{-1}) over Greece and Southern Black sea borders under the medium-end scenario. As shown in Mariotti et al. (2015), this decrease in evapotranspiration over the MED region can be mostly explained by the decrease in precipitation that reduces the SM content available for evapotranspiration. An increase in evapotranspiration (+0.02 to +0.20 mm day^{-1}), corresponding to a relative change of about +10% to 50%, is projected over SAH, in Southern Egypt, Libya, and Sudan, for both scenarios.

Regarding P–E (Figures 5.1.c, 5.2.c), there is an overall projected decrease over MED, more pronounced in the European part. The projected changes range between -0.05 and -0.3 (respectively, -0.02 and -0.2) mm day^{-1} over the IP, Italy, and Turkey under the SSP5-8.5 (respectively, SSP2-4.5) scenario, which corresponds to a relative evolution of approximately -20%. However, Northern Africa already characterized by a climatological P–E close to zero, exhibits weaker change signals ($\sim\pm0.01$) with a slight positive P–E in far south SAH.

Consistently with P and E responses, an overall decrease in SM (Figures 5.1.d, 5.2.d) is simulated. The projected changes in SM reach -12 (-8)% in parts of Spain, Northern Morocco, and Algeria for the SSP5-8.5 (SSP2-4.5) scenario. However, large parts of SAH show nonrobust changes especially under the SSP2-4.5 scenario, while about +10% changes can be pointed out in the far south of SAH under the SSP5-8.5 scenario. The total SM shows similar evolution (Figure 6.18), with changes from -6 to -12 (respectively, -4 and -8) % over MED, and from +6 to +20 (respectively, +4 to +14) % over Southern SAH under the SSP5-8.5 (respectively, SSP2-4.5) scenario, with the strongest change much more localized in the IP, Italy, Northern Morocco, and Algeria. While P–E is close to zero, the relative SM changes in North Africa are significant.

Our results thus show a robust decrease in future water availability over MED due to the decreasing precipitation over the region. However, despite the robust wetting signal for precipitation in South-Eastern Sahara, a near-zero change in the freshwater flux is projected owing to the response of evapotranspiration. Model ensembles exhibit a general south-to-north soil drying, and the inspection of the individual models behavior reveals that most models reproduce this general pattern (Figure 6.19), with the exception of the GISS-E2-1-G model that projects extensive drying over the entire study area.

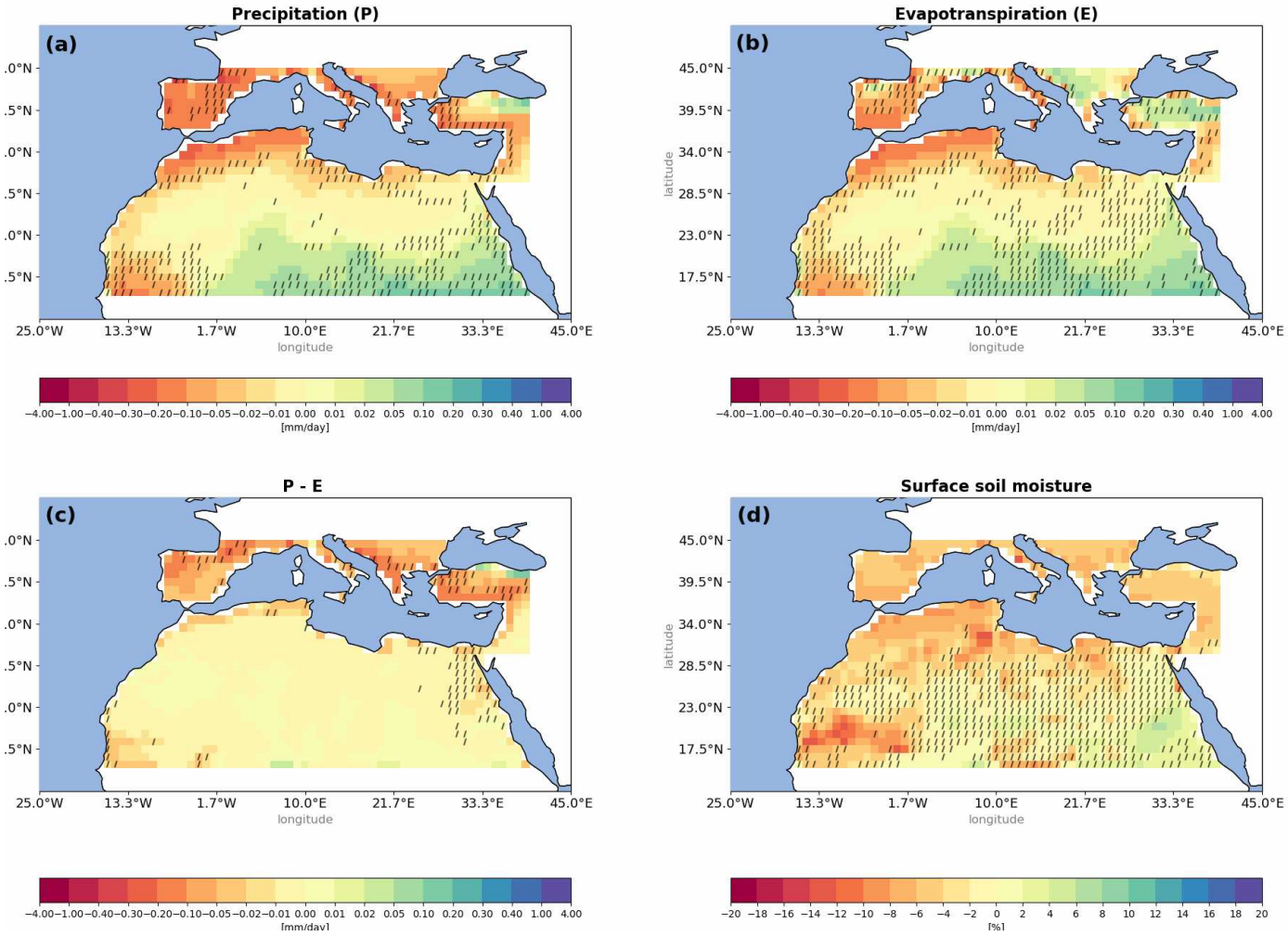

Figure 5.2: Same as Figure 5.1 but for the SSP2-4.5 scenario.

5.2.3.2 Seasonal aspects

Since the rainy season in the Mediterranean starts from October and extends to approximately April (Driouech (2010); Xoplaki (2002)), separate analyses are conducted for extended boreal winter (OND-JFMA) and summer (MJJAS) for the SSP5.8–5 scenario. The projected 21st-century precipitation decrease is especially intense for the N_MED in MJJAS and for S_MED in ONDJFMA. Increases in precipitation over SAH are twice more intense in summer than in winter (Figure 5.3.a, b). In the Iberian Peninsula, Turkey, and northwestern Maghreb, the precipitation reduction under SSP5-8.5 scenario (Figure 5.3.a, b) reaches -0.2 mm day^{-1} to -0.4 mm day^{-1} during wintertime. While summertime results point to -0.2 mm day^{-1} over Northern Maghreb, and exceed -4 mm day^{-1} in N_MED. This significant decrease in wet-season precipitation throughout the S_MEDsector is consistent with previous studies (Diffenbaugh and Giorgi (2012); Tuel and Eltahir (2020)). The increase in annual precipitation over SAH found in Section 3.1 is most pronounced during summer which concurs with the study of Almazroui et al. (2020). Summertime changes over SAH vary between +0.3 and + 4 mm day^{-1}. Summertime evapotranspiration signal (Figure 5.3.c, d) follows the precipitation behavior

with a projected decrease reaching -0.4 mm day^{-1} over MED and an increase of about +0.4 mm day^{-1} over South-Eastern Sahara. However, wintertime changes for S_MEDare about +0.2 mm day^{-1}, -0.2 mm day^{-1} in Northern Maghreb, and around +0.1 mm day^{-1} in Southern SAH. P–E (Figure 5.3.e, f) shows an opposite sign between summer and winter over almost the study area, with decreasing changes over the Mediterranean ($\sim$ -0.3 mm day^{-1}) and Southern Sahara ($\sim$ -0.1 mm day^{-1}) during winter, and increasing changes during summer ($\sim$ + 0.2 mm day^{-1}) over MED and Southern SAH. Surface SM (Figure 5.3.g, h) follows the same behavior to a large extent. The projected changes reach -16 (-8)% during the extended winter (respectively, summer) over Northern Africa, and -8 (-18)% over the IP, Italy, Greece, and Turkey. Changes across SAH vary from +10% during winter to +14% during summer.

Results from SSP2-4.5 are shown in Figure 6.20 in the supplement. Seasonal changes exhibit similar behavior mainly during summer, with reduced intensity, compared to the SSP5-8.5 during winter.

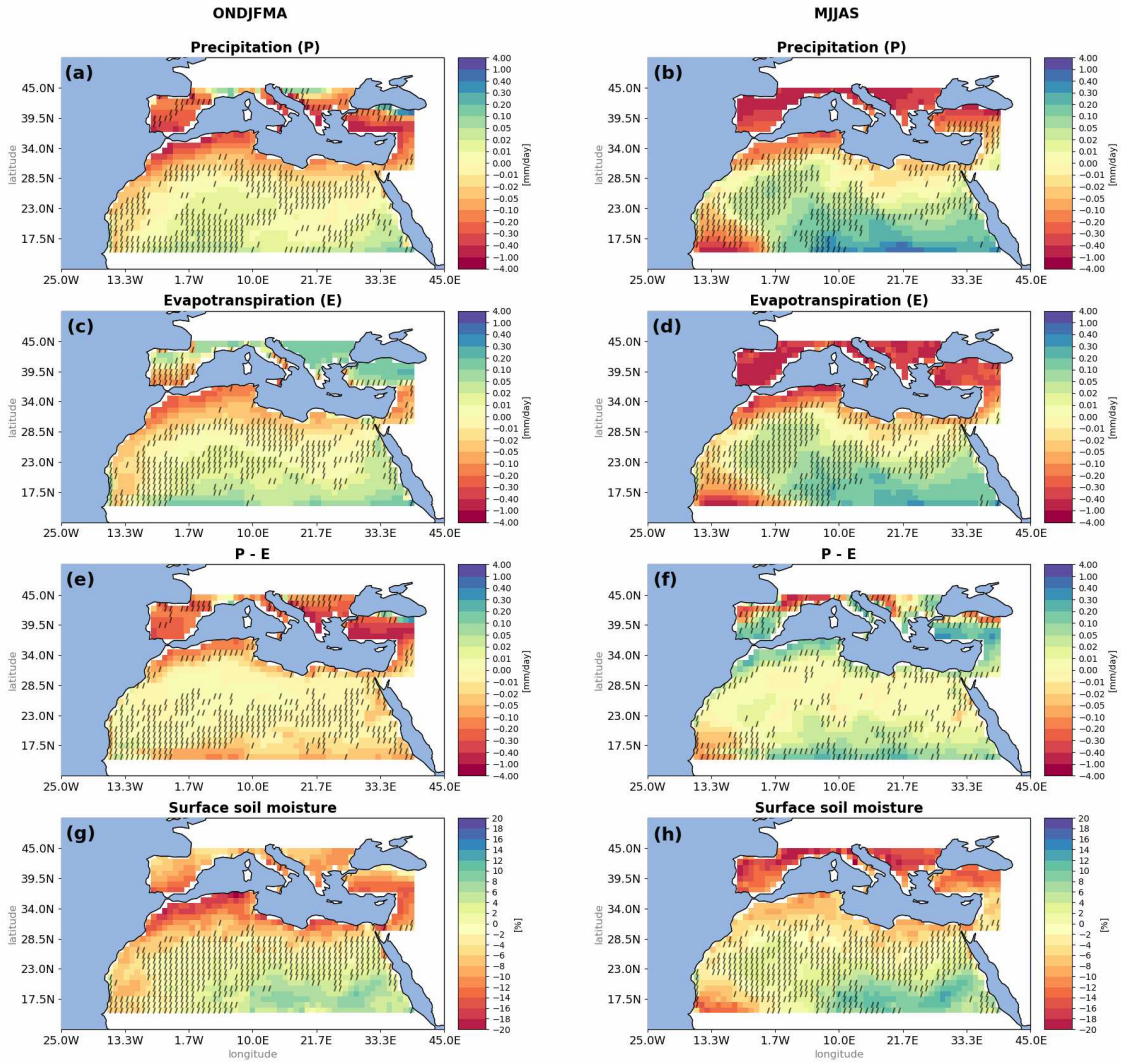

Figure 5.3: As Figure 5.1 but for the extended boreal winter (left panel) and summer (right panel) seasons under the SSP5-8.5 scenario.

5.2.3.3 Regional assessment and impact of spatial resolution

a. Time evolution by region

We now examine more in detail the time evolution of P, E, P–E, and SM, spatially averaged over the N_MED, S_MED, and SAH sectors for the extreme SSP5-8.5 scenario. Figure 5.4 shows the evolution of the mean annual anomalies and evidences the acceleration of the Mediterranean drying and saharan moistening from the 2020s. The amplitude of change is generally greater in N_MED than in S_MED, mainly due to the higher mean annual precipitation in the Mediterranean, which conditions the evaporation and P–E changes. Figure 5.4 also shows a gradual decrease in SM during the study period over the entire MED where projected anomalies are around -15% over both N_MED and S_MED, while the evolution over SAH shows a near-zero trend until the 2000s when a slight increase of +2.5% emerges.

b. Spatial resolution impact

Given the sharp topographic and land surface-type contrasts of the MED regions, regional-scale climate change projections in this region are expected to depend on the model resolution (Ashfaq et al. (2016)). We conduct a preliminary analysis by separating a $\sim$ 100 km resolution CMIP6 simulation ensemble from that with a $\sim$ 250 km resolution.
While the 250 km resolution and the 100 km resolution ensembles agree over the "historical" period (Figure 5.4), their future projections show statistically significant differences in precipitation, exceeding 0.1 mm day^{-1} over MED. The lower resolution generally yields more pronounced changes and intermodel variability over MED, while this behavior is less marked over SAH. For almost all the studied variables, the intermodel variability increases with time and decreases with resolution for both shores of the Mediterranean Sea. The differences between the high and low-resolution ensembles also increased toward the end of the century. Unlike MED, the lowest resolution exhibits less intermodel variability over SAH. SM signal shows that less intermodel spread characterizes the highest resolution for almost the entire area. A quite similar behavior is also shown in total SM (Figure 6.22), except for N_MED, where the 100 km ensemble intermodel variability exceeds that of 250 km. This can be explained by the higher magnitude of total SM which reaches $\sim$2000 kg m^{-2}, while it varies from 500 to 800 kg m^{-2} in the rest of the study area.

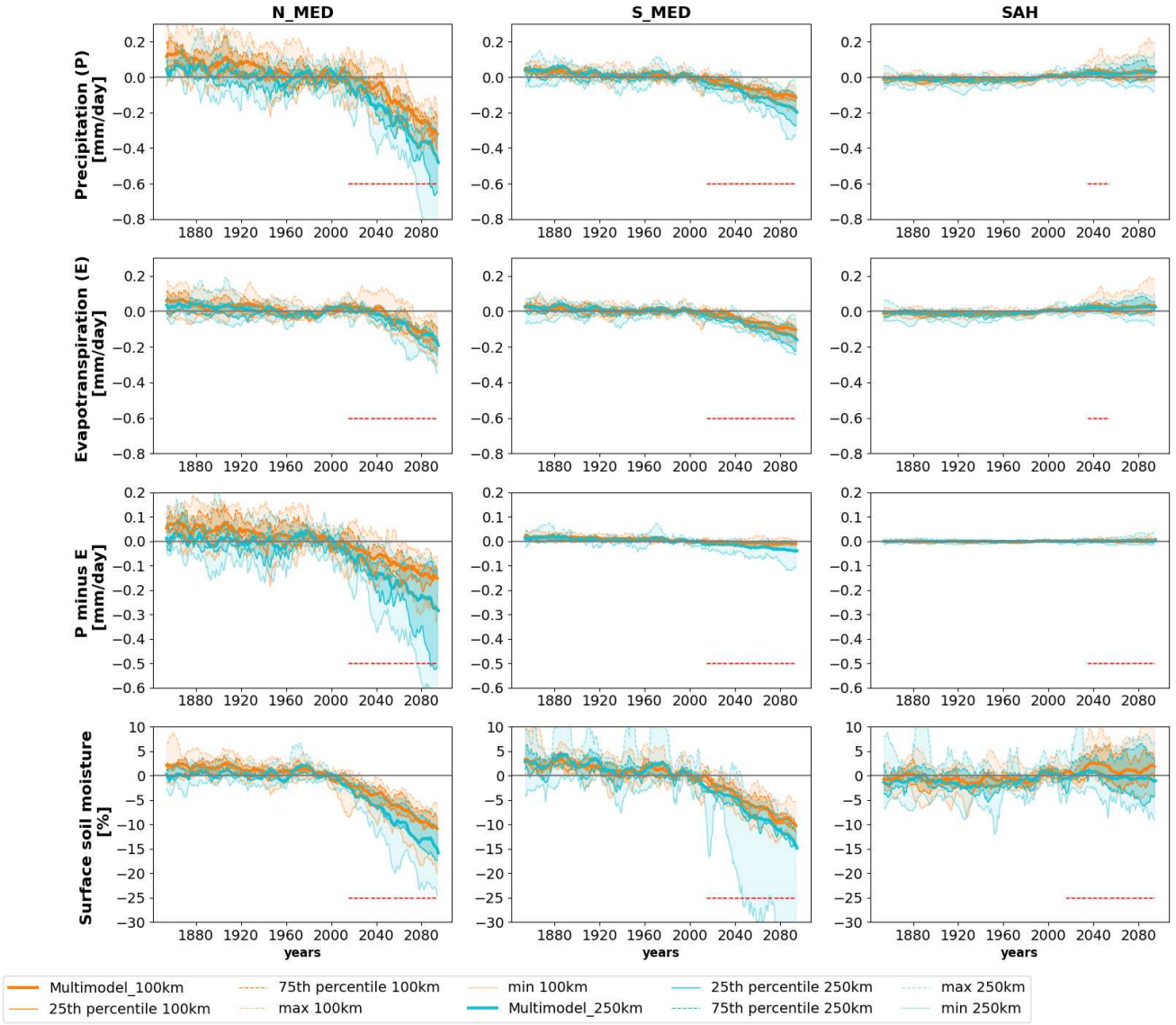

Figure 5.4: Spatially-averaged mean annual changes in precipitation (mm day^{-1}), evapotranspiration (mm day^{-1}), P–E (mm day^{-1}), and surface soil moisture (%) for the Northern and Southern Mediterranean (N_MED and S_MED) and Sahara (SAH) regions under the SSP5-8.5 scenario. Curves are constructed by subtracting, for each year in the period 1850–2100, the mean value for the baseline 1981–2010. Then, a 10-year running mean is applied to smooth the resulting time series. Bold curves represent the multi-ensemble mean anomaly of the 100 km (orange) and 250 km (blue) resolutions, color shadings show the envelope between the maximum and minimum values (light shading) and between the 25th and 90th percentiles (dark shading). In order to assess the significance of the discrepancies between the two different resolutions, we performed the Wilcoxon–Mann–Whitney test to compare 100- and 250 km ensemble time series by dividing the future period into four sub-periods. The horizontal dotted red curves indicate the sub-periods where the test is significant at a 95% threshold.

5.2.3.4 Temperature- versus scenario-dependent Mediterranean drying and Saharan moistening

Our results and previous studies project a strong drying trend over the Mediterranean region and a substantial moistening trend over the South-Eastern Sahara for the next decades. To what extent precipitation and evapotranspiration changes may be explained by circulation changes and/or by the direct response of the hydrological cycle to the increase in global temperature and how this will vary in time and space remain open questions. Tuel et al. (2021) show that CMIP5 GCMs project the development of a strong winter anticyclone centered on the Mediterranean Sea that results from a combination of large-scale shifts in winter planetary waves and to the reduced warming of the sea with respect to the surrounding lands. This anticyclonic anomaly and the associated dry advection effect over North Africa and S_MED may explain most of the decrease in precipitation in this region. Drobinski et al. (2020) also underlined that the aridification over the Sahara and IP cannot be solely explained by the increase in temperature and that the development of local circulations associated with the faster increase in temperature over land plays a significant role.

To explore the behavior of the CMIP6 simulations concerning this aspect, we compare the evolution of the surface water budget under a fastly-warming and a slowly-warming scenario for a given increment in mean global temperature. The increase in mean global temperature between the 2041–2070 period and the 1981–2010 period under the SSP5-8.5 in the CMIP6 model ensemble ($\sim$2.89 K) is very close to the increase in mean global land temperature between the 2075–2100 and 1981–2010 under the SSP2-4.5 scenario ($\sim$ 2.90 K). The future change by the mid-century (2041–2070 vs. 1981–2010) for the high-end scenario (left panels in Figure 5.5), compared to the end of the century (2071–2100 vs. 1981–2100) for the SSP2-4.5 scenario (right panels in Figure 5.5) is, therefore, assessed for P, E and the mean surface air temperature for the 100 km resolution ensemble. The overall near-surface temperature change over MED and SAH is very close between the two ensembles. Over SAH, both ensembles project a moistening, P and E do not significantly change and the two ensembles do not show statistically different results except in some parts in the southeast. This suggests that changes in E and P over SAH are slightly or not scenario-dependent and rather respond to the overall temperature increase. Regarding the Mediterranean basin, results show statistically different projections of P and E even if the geographical patterns are qualitatively alike. Changes in P and E are therefore scenario dependent and cannot be directly related to the net increment of global near-surface temperature. In line with Drobinski et al. (2020) and Tuel et al. (2021), CMIP6 models thus suggest local land heating differences—such as over Morocco (see Figure 5.5.a, b)—and changes in circulation likely superimpose on the overall temperature increase signal to explain the future Mediterranean drying. Further investigation into those physical and dynamical mechanisms is needed, considering for instance seasonal aspects (Brogli et al. (2019)) but it is beyond the scope of the present paper.

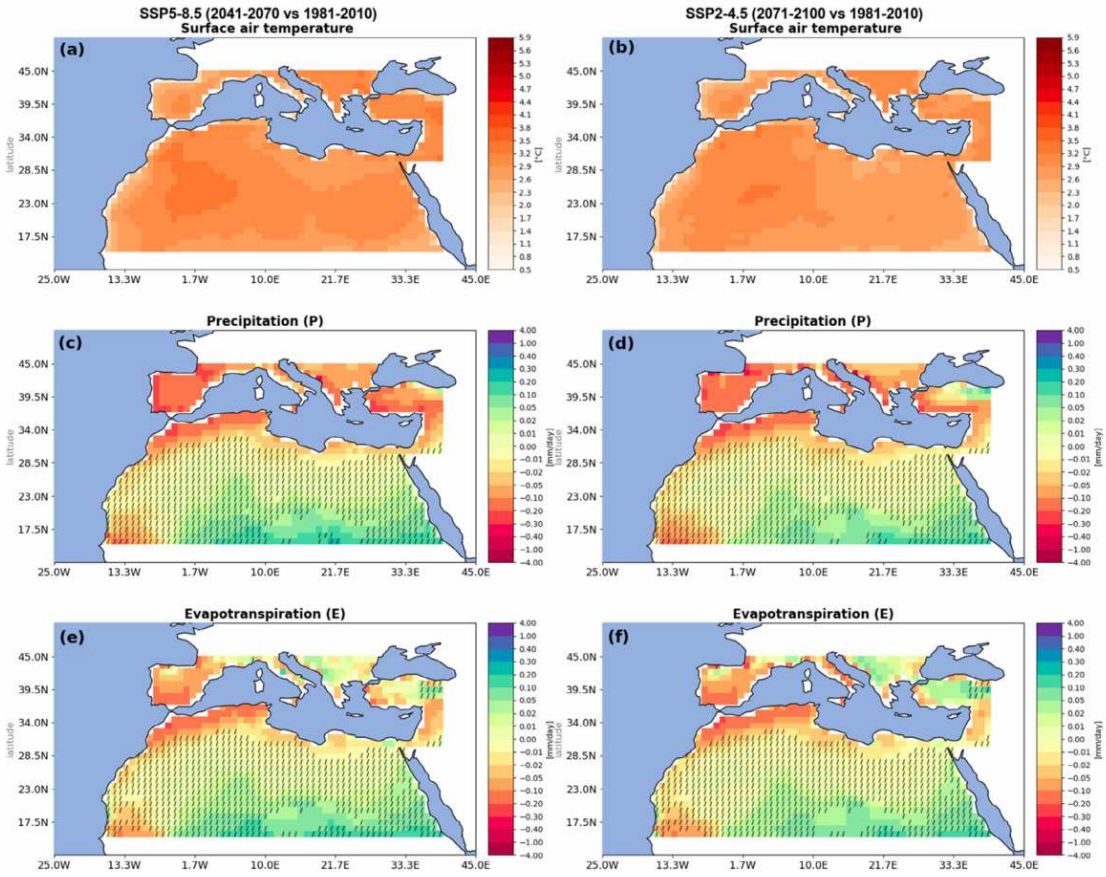

Figure 5.5: Mean future changes from the 100 km ensemble of annual surface air temperature (°C), precipitation (mm day^{-1}) and evapotranspiration (mm day^{-1}). Panels in the left column show the differences between the 2041–2070 and 1981–2010 periods for the SSP5-8.5 while those in the right column show the differences between the 2071–2100 and 1981–2010 periods for the SSP2-4.5. Hatches indicate grid boxes where the high-end and low-end changes are not statistically different based on the nonparametric Wilcoxon–Mann–Whitney with a 95% threshold.

5.2.3.5 Projected changes in CMIP6 compared to CMIP5

Prior to concluding this letter, it is worth examining to what extent our CMIP6-based results differ or concur with CMIP5 projections. We thus compare CMIP6 and CMIP5 results under high-end forcing over the MED and SAH regions, with a particular focus on precipitation. Figure 5.6.a shows CMIP6 and CMIP5 differences in future projected precipitation (CMIP6 minus CMIP5). Results show more intense changes than in CMIP5. This former shows less intense future precipitation increase over SAH with differences ranging to +0.3 mm day^{-1}. This concurs with Almazroui et al. (2020) who found intense mean annual precipitation in CMIP6 compared to CMIP5 over Sahara. Differences in precipitation extends up to -0.2 mm day^{-1} across the Northern parts of Morocco and Algeria, Mauritanian coasts, and N_MED. Indeed, Figure 5.6.b shows that CMIP6 and CMIP5 precipitation changes generally agree on the sign of the change. However, the projected drying is more intense in CMIP6 over western N_MED, Northern Morocco and Libya, and Atlantic coasts of Mauritanians, the Saharan moistening is also more intense in CMIP6. Similar results have also been found in previous

studies (e.g., Chen et al. (2020); Lee et al. (2021)). CMIP6 models project intense globally-averaged surface air temperature (GSAT) increase in comparison with CMIP5 (Lee et al. (2021))—in particular, due to a higher climate sensitivity of models (Meehl et al. (2020))—the change in several climate quantities such as large-scale precipitation scales with GSAT signal (Lee et al. (2021)).

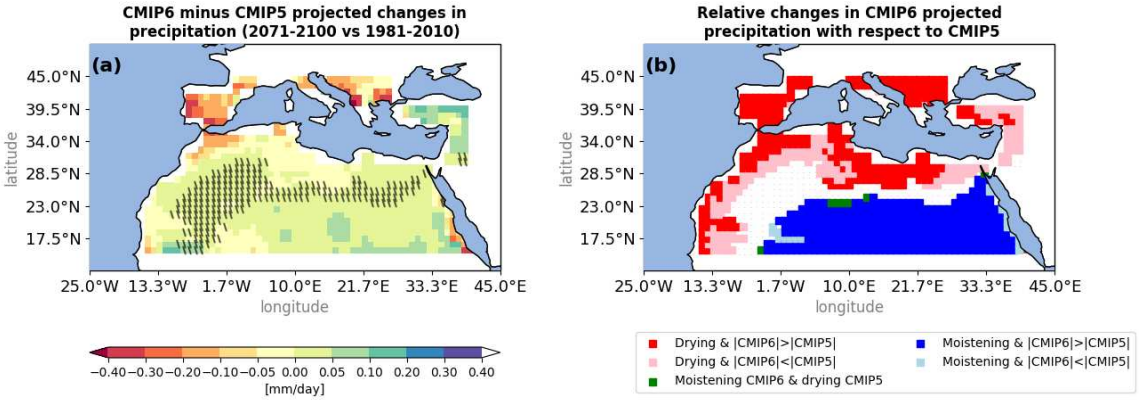

Figure 5.6: Panel (a): CMIP6 minus CMIP5 model ensemble projection of mean annual precipitation change between 2071–2100 and 1981–2010. Backslashes indicate the grid boxes corresponding to statistically insignificant differences based on the non-parametric Wilcoxon–Mann–Whitney with a 95% threshold. The color shading in panel (b) qualitatively shows how the changes of precipitation projected by CMIP6 models compare with those from CMIP5 models. Dark red (respectively, dark blue) regions are where CMIP5 models predict a decrease or drying (respectively, increase or moistening) and for which CMIP6 models predict an even stronger decrease (respectively, increase) by the end of the century. Light red (respectively, light blue) regions are where the CMIP5 models ensemble projects a decrease or drying (respectively, increase or moistening) and where the CMIP6 models ensemble projects a less intense decrease (respectively, increase). Green pixels are regions where CMIP5 models project a decrease or drying and where CMIP6 models project an increase.

5.2.4 Summary and conclusions

CMIP6 models project a robust decrease in precipitation over MED by the end of the century with larger uncertainty across Southern Morocco and Mauritania. An opposite behavior is projected in South-Eastern Sahara with a relative increase in precipitation in all models. Evapotranspiration behavior follows the precipitation pattern with weaker intensity over N_MED, resulting in a negative projected freshwater flux over this region and a near-zero projected P-E over S_MED and Sahara. The future negative freshwater flux over MED may exacerbate existing water scarcity issues, particularly in areas heavily reliant on agriculture (García-Ruiz et al. (2011)). These changes may also have implications in terms of wildfire which is already a significant risk in the Mediterranean region (Rovithakis et al. (2022); Turco et al. (2018)). Interestingly, the projected increase in precipitation over South-Eastern Sahara does not result in a climatological increase in P–E which means that the net surface water availability is not projected to increase. This may have important implications for the future of water resources in this region but this result should be interpreted with caution. In fact, the increase in evapotranspiration that balances precipitation does not necessarily translate into a net loss of water, it

may have the potential to support increased plant transpiration leading to a boost in vegetation growth in the region. The seasonal analysis also reveals a contrasted evolution with a relative increase in P–E in summer and a decrease in winter, the main rainy season, over North Africa. Such an evolution has potential implications regarding the adaptation to the future of the water resources in the region, for instance, rainwater harvesting, water storage facilities, and efficient water management and irrigation systems.

A preliminary analysis has revealed that the 100 km resolution models project less intense drying over MED with a less intermodel spread in comparison with the 250 km resolution models. However, those results should be interpreted with caution since the differences between the two ensembles are not only explained by the difference in resolution. Further work focusing on scenarios performed with one given model at various resolutions would help assess in a more robust way the effective sensitivity to resolution.

A brief complementary analysis suggests a higher scenario-dependency of the hydrological cycle changes over the Mediterranean than over the Sahara where changes seem more directly related to the overall global increase in temperature. Moreover, while the CMIP6 model ensemble qualitatively agrees with the CMIP5 ensemble in terms of precipitation projection, the magnitude of the projected changes is generally higher in CMIP6, with a more intense drying over MED and more intense moistening over the Sahara.

Our results allow us to identify robust signals in future model projections over the Mediterranean and North Africa even though on a regional scale, climate change depends on the ability of models to properly simulate the main atmospheric circulation patterns. Further studies making use of empirical bias-corrections methods (Krinner et al. (2020)) would make it possible to further strengthen the reliability of GCM-based regional projections over the MED and SAH regions. Future scenarios over North Africa would also benefit from fostering the development and evaluation of model parameterizations and configurations specifically adapted for Africa, as models are generally insufficiently developed and evaluated for this continent (James et al. (2018)).

Author contributions

***Khadija Arjdal**: Investigation; software; visualization; writing – original draft; writing – review and editing. **Fatima Driouech**: Conceptualization; methodology; project administration; supervision; writing – original draft; writing – review and editing. **Étienne Vignon**: Methodology; supervision; writing – original draft; writing – review and editing. **Frédérique Cheruy**: Conceptualization; writing – review and editing. **Rodrigo Manzanas**: Methodology; writing – original draft; writing – review and editing. Philippe Drobibski: Methodology; writing – review and editing. **Abdelghani Chehbouni**: Project administration; writing – review and editing. **Abderrahmane Idelkadi**: Software; writing – review and editing.*

Acknowldgements

We gratefully thank Frédéric Hourdin and Laurent Li for insightful discussions as well as Cécile Agosta for providing evaluation scripts to assess the reliability of large-scale circulation fields in CMIP6 simulations. This study was conducted using the ESPRI (Ensemble de Services Pour la Recherche l'IPSL) computing and data center (https://mesocentre.ipsl.fr) which is supported by CNRS, Sorbonne Université, École Polytechnique, and CNES and through national and international grants. We also thank the UM6P-X project for financing this work.

Funding information

This work was conducted in the context of Khadija Arjdal's doctoral program funded by Mohammed VI Polytechnic University (UM6P) in the framework of the UM6P and l'Institut Polytechnique de Paris (l'X) collaboration project on climate modeling.

Conflict of interest statement

The authors declare that they have no competing interests.

5.3 Changing climate in the Haouz plain as simulated by LMDZ-ORCHIDEE

The CMIP6 multimodel mean projects nearly -0.3 mm day^{-1} and +3K changes in annual precipitation and air temperature respectively, over the Haouz plain (Figures 5.1.a, 5.5.a) under SSP5-8.5 by the end of the century. The medium-end scenario (SSP2-4.5) suggests less intense changes, ranging to -0.2 mm day^{-1} and +2.9 K in precipitation and air temperature respectively (Figures 5.2.a, 5.5.b). In this section, we will refine these projections leveraging our LMDZ-ORCHIDEE model configuration zoomed around the plain to make future projections, with a focus on the surface climate.

5.3.1 Numerical design

To assess the future evolution of the near surface climate over the Haouz plain, we use the coupled LMDZ-ORCHIDEE model, described in chapter 3, with 64 (longitude) × 64 (latitude) grid points, 79 vertical levels, and an horizontal stretched grid refined over the Haouz plain that yields a grid point spacing of around 25km in the plain. This configuration makes it possible to carry out simulations at a relatively low computing cost while maintaining high horizontal resolution locally. Simulations are run with the adapted PFTs at each of the three stations grid cells (i.e Temperate Evergreen Broadleaf forests for Agdal and Agafay, and C3 crops for R3) and constant aerodynamic and thermal roughness heights (table 3.2). This choice has been made such that the climate simulated over those grid cells is - as much as possible - representative of the climate over the corresponding crops. Note also that in all the simulations that we will carry out, we will assume that the type of crop remain the same throughout the century i.e. we assume no local change in PFT. As irrigation practices may have a non-negligible impact on the local climate, we will assess the sensitivity to the activation of our simple irrigation parameterization presented in Section 4.3.

We carried out 4 LMDZ-ORCHIDEE simulations, the reference run for the early 21th century (2000-2011) is noted **PRSNT**, the second one for the same period but with irrigation parametrization is noted **PRSNT-Irr**. Simulations for the late 21th century (2080-2090) with and without the inclusion of irrigation are referred to as **FTR-Irr** and **FTR** respectively. The initial two years of each simulation -considered as spin-up time- are excluded from the analysis, limiting this latter to 10 years from 2002 to 2011 for PRSNT and PRSNT-Irr, and from 2082 to 2090 for FTR and FTR-Irr. Statistical significance of changes between PRSNT and FTR (respectively, between PRSNT-Irr and FTR-Irr) are tested with the non parametric Wilcoxon-Mann-Whitney test with a 95% threshold (i.e., the p-value of the Wilcoxon–Mann–Whitney test <= 0.05).

Following the simulations settings described in section 3.6, all the PRSNT(-Irr) and FTR(-Irr) simulations are run in a "nudged" mode, in which the large-scale meteorological fields (wind, temperature, and humidity) are relaxed towards a global model. For present time, as in Chapter 4, we use the ERA5 reanalysis. For the future simulations, we have to choose one or several CMIP6 scenarios. As CMIP6 models have various abilities to simulate the large-scale circulation patterns that drive the Moroccan climate (such as the circulation over the Atlantic ocean, see Balhane et al. (submitted)

for further details) a first approach could have been making a selection of global models based on climatic scores. Such a selection procedure is often performed to select forcings for Regional Climate Model simulations. A second approach, that we have chosen, consists in choosing one given global climate model and to run the so-called 'online biased-corrected simulations' which aims at removing systematic biases in ocean sea surface temperature and atmospheric circulation in the model. The method, proposed and established throughout a series of papers (e.g., Guldberg et al. (2005), Kharin and Scinocca (2012), Beaumet et al. (2019) and Krinner et al. (2019, 2020)) can be summarized as follows:
Firstly, a present-day global simulation is set up with the wind components (U,V) nudged towards ERA5 reanalysis at each model time step as follows:

$$\frac{\partial X}{\partial t} = F(X) - \frac{1}{\tau}(X - X^a) \tag{5.1}$$

With the time constant τ chosen equal to 1 day, and X^a is the equivalent reference field from reanalysis interpolated -at each model time-step- on the model grid. Then, the nudging tendencies $(-\frac{1}{\tau}(X - X^a))$ are saved at each nudging time-step (6h in our case) and then time-averaged to calculate a smooth running mean cycle as follows:

$$G = \frac{-1}{\tau}\overline{(X - X^a)} \tag{5.2}$$

Secondly, the future simulation is run with the correction terms G added at each model time-step to the operator F describing the prognostic evolution of the variable X, based on the hypothesis that the climate model biases are constant from the present to the future period (Kerkhoff et al. (2014); Krinner et al. (2020)) :

$$\frac{\partial X}{\partial t} = F(X) + G \tag{5.3}$$

Since we use a land-surface atmosphere model, the ocean boundary conditions (SST and SIC) are obtained by adding the bias of the simulated SST/SIC by the coupled IPSL-CM6 with respect to the climatological mean of its corresponding observations (Beaumet et al. (2019); Krinner et al. (2019)).

Bias correction approach improved climate metrics deemed important to represent the large scale drivers of the Moroccan climate (Balhane et al., (submitted)). Figure 5.7 illustrate the models ability to simulate the large-scale atmospheric circulation driving the climate over a region that encompasses Morocco. Bias corrected LMDZ-ORCHIDEE (*LMDZOR35kmMar.biasCor* in the Figure), the IPSL-CM model and a set of CMIP6 models are evaluated -with a set of variables characterizing the large-scale dynamics- by calculating the root mean squared error (RMSE) of the annual and wintertime averaged variables with respect to ERA5 reanalysis over the 20-50N, 40W-20E longitude-latitude box. A significant improvement is achieved with the bias-corrected LMDZ-ORCHIDEE in comparison to the IPSL-CM model, in particular for the T700 bias reduced by more than 2 levels.

In conducting our future simulations, careful attention was given to the quality and accuracy of the forcing data used. This critical component was meticulously prepared by Adriana Sima, Frédérique

Cheruy and Étienne Vignon, for whom we owe our gratitude.

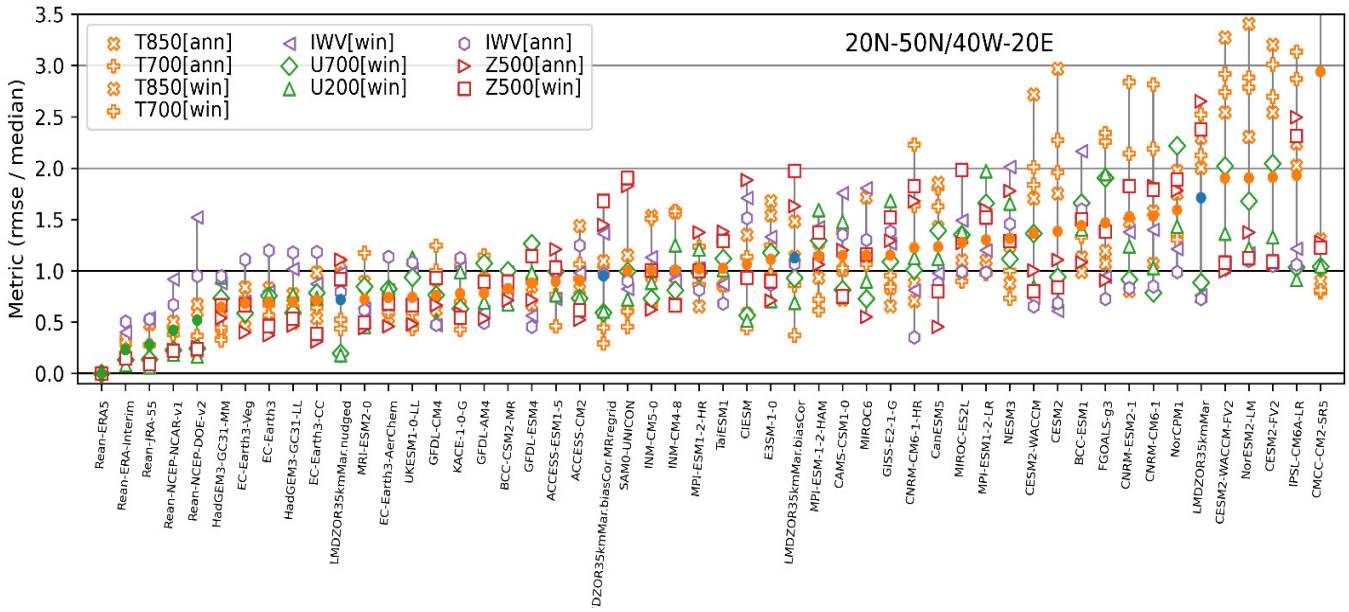

Figure 5.7: [Courtesy of F. Cheruy] Normalised RMSE with respect to ERA5 reanalysis of the following large scale metrics: 850 and 700 hPa air temperature (T850, T700), integrated water vapor (IWV), 700 and 200 hPa zonal wind (U700 and U200) and 500 hPa geopotential height (Z500) averaged annually (ann) or during winter (win) of CMIP6 models including IPSL-CM and the land-surface atmosphere LMDZ-ORCHIDEE. Results from ERA-Interim, JRA-55, NCEP-NCAR and NCEP-DOE reanalysis are also shown for comparison.

5.3.2 Projected near surface climate over the Haouz plain

Figure 5.8 shows time series of the annual averaged precipitation, maximum and minimum air temperature, and the surface soil moisture from the PRSNT and FTR simulations.

From 2002 to 2011, the annual precipitation average (panel 5.8.a) varies between 0.5 and 0.8 mm day^{-1} over Agdal and Agafay, equivalent of an annual total of 180 - 290 mm, and between 0.9 and 1.9 mm day^{-1} over R3 which is roughly twice the former. These differences can be explained by the proximity of R3 to the Atlas mountain and probable orographic effects. Projected changes in precipitation show a notable decrease over the targeted area; the FTR signal, with respect to the PRSNT, is projected to decrease by -0.16 mm day^{-1} (-40%), -0.23 mm day^{-1} (-50%), and -0.40 mm day^{-1} (-30%) over Agafay, Agdal and R3 respectively. These changes are consistent with the simulated results by CMIP6 models, Arjdal et al. (2023) reported an average decrease of -0.4 $\pm$ 0.1 mm day^{-1} by the end of the century. The seasonal cycle of precipitation in the Haouz plain (Figure 5.9.a) exhibits decreasing patterns throughout the year. During summer, the region experiences its minimal rainfall, with about 0.25 mm day^{-1} in the PRSNT, and almost no precipitation in the FTR. From the early autumn, precipitation gradually increases, transitioning to a relatively wet period, with up to 2.7 (respectively, 1.6) mm day^{-1} simulated in R3 and about 0.8 (respectively, 0.4) mm day^{-1} in Agdal and Agafay during winter according to PRSNT (respectively, FTR) signals. Then, the

seasonality of precipitation is projected to decrease with global warming over the Haouz plain, with a seasonal contrast of around 1.5 mm day^{-1} in FTR, in comparison with the PRSNT where it ranges to 2.5 mm day^{-1} primarily due to the reduction of winter rainfall. This pattern aligns with seasonal changes documented in Arjdal et al. (2023) (see Figure 5.3.a,b).

The annual average of air temperature in the Haouz plain varies between 19°C and 22°C from 2002 to 2011 (Figure 5.8.b) with higher values registered in R3 relative to Agdal and Agafay, mostly due to higher minimum temperature (Figure 5.8.c). A clear warming is projected over the three stations, with 4.4 ±0.5, 4.2 ±0.5 and 4.9 ±0.7 °C increase in air temperature expected by 2090 over Agdal, Agafay and R3 respectively, and both maximum and minimum temperatures are anticipated to experience a consistent increase throughout the study period ranging to up to +4.6 ±0.5 and +5.5 ±0.9°C increase projected in Tmin and Tmax respectively. The seasonal cycle of air temperature shown by Figure 5.9.b, corresponds to the typical cycle of the semi arid regions, with maximum values occurring during the summer months (> 35°C) and minimum temperatures during winter (around 10°C). Projected changes hold significant increase in air temperature, with an increment of about 4°C through the entire annual cycle. Accompanied with reductions in relative humidity (Figure 5.9.c) in FTR ranging to -10% during almost the annual cycle except during summer when it is expected to slightly increase.

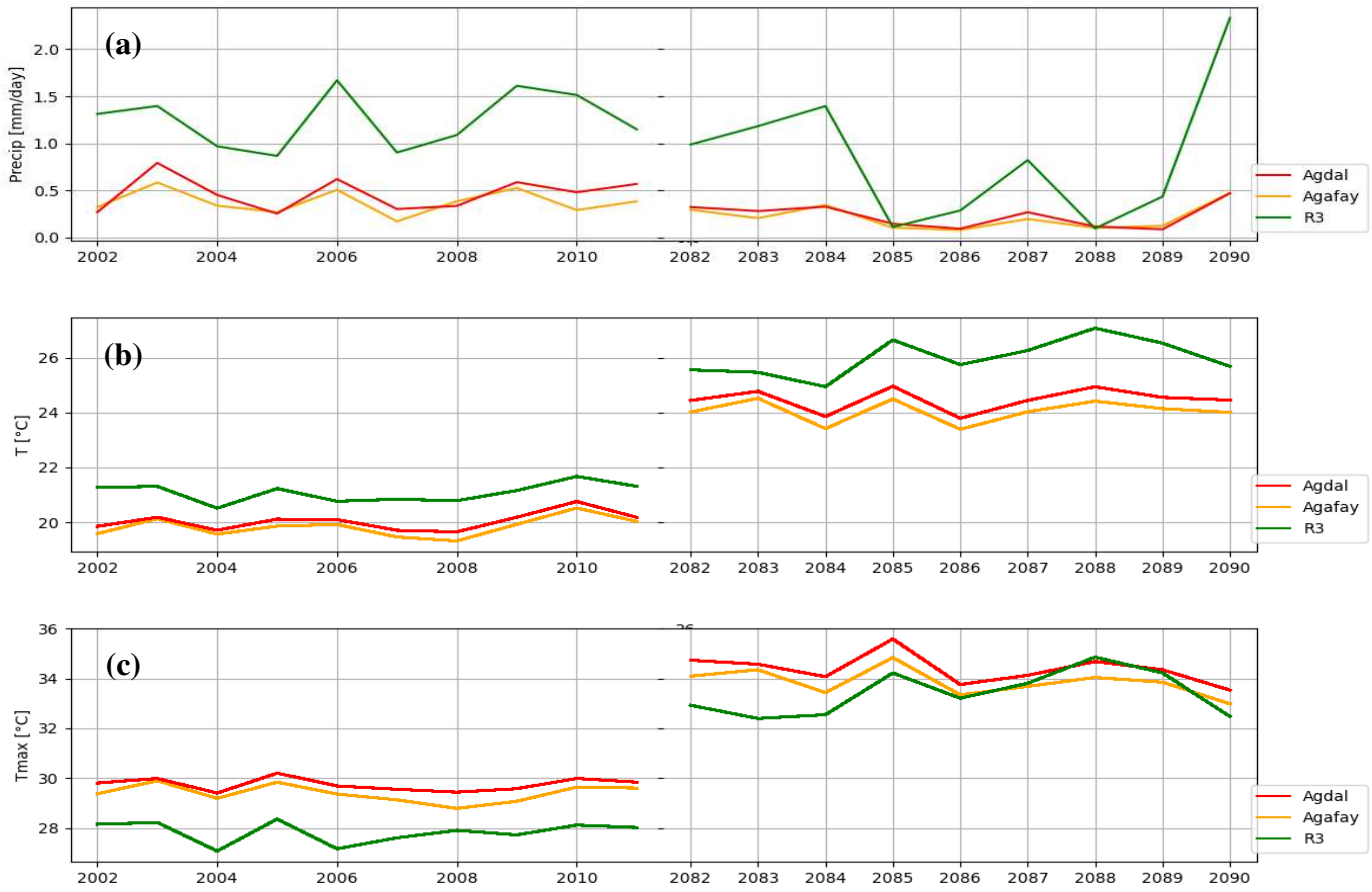

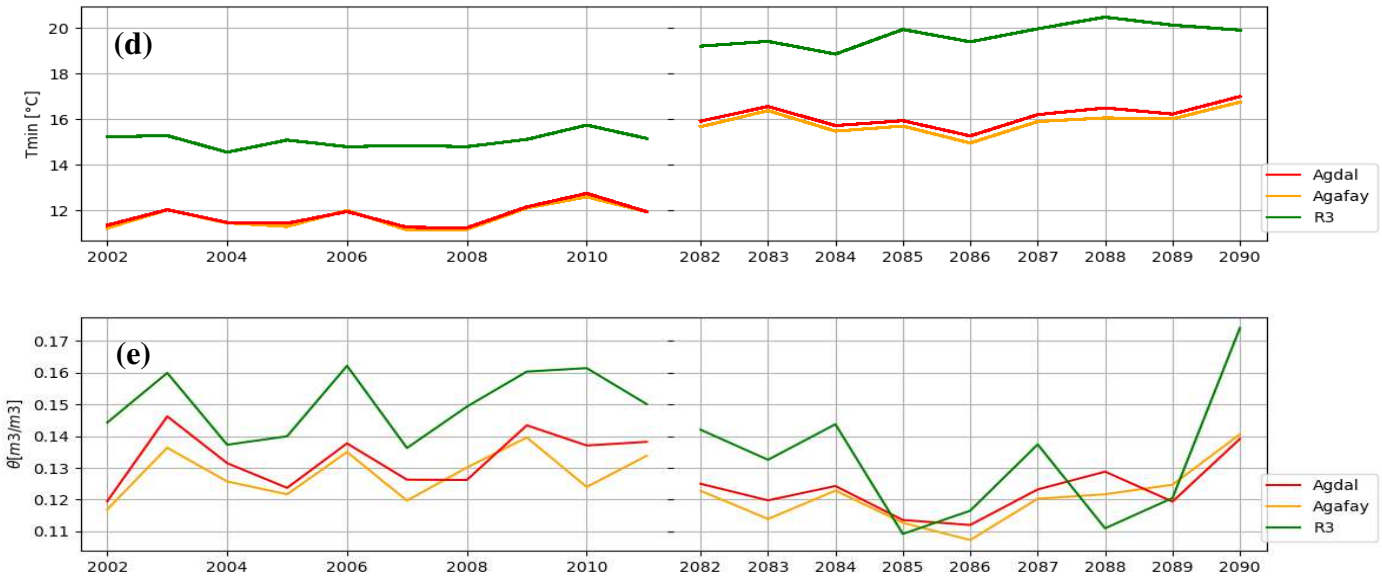

Figure 5.8: Annual average of precipitation (a), air temperature (b), maximum (c) and minimum (d) air temperature, and surface soil moisture (e) over Agdal (red curve), Agafay (orange) and R3 (green) during the PRSNT (2002-2011) and the FTR period (2082-2090)

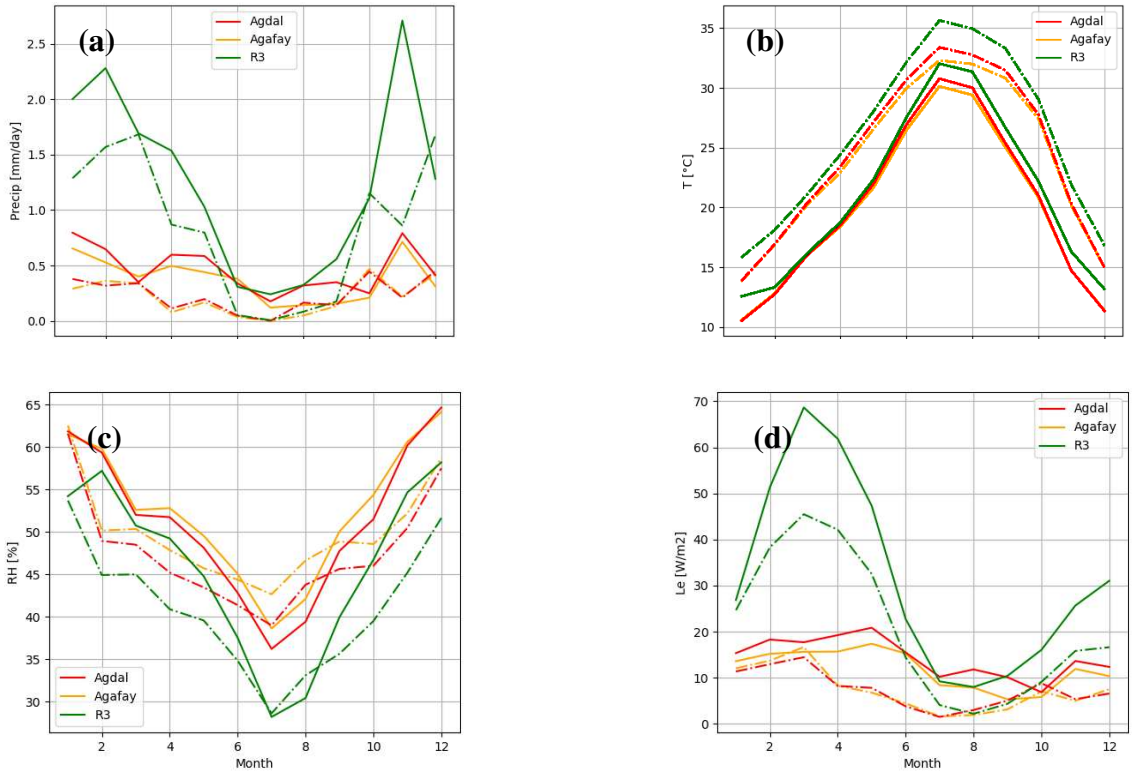

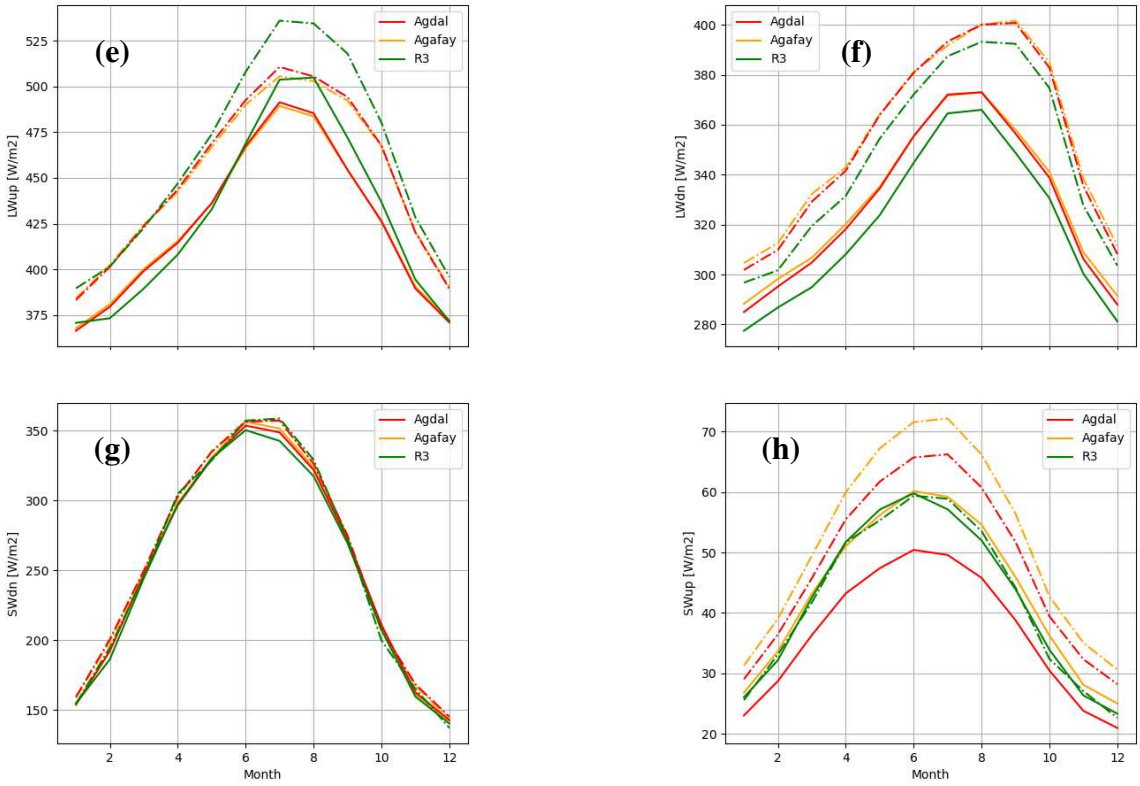

Figure 5.9: Seasonal cycle of average precipitation (panel a), air temperature (b), relative humidity (c) latent heat flux (d), upward (e) and downward (f) longwave radiation, downward (g) and upward (h) solar radiation, at the three sites Agdal (red), Agafay (orange) and R3 (green) during the present period 2002-2011 (solid lines) and the future period 2082-2090 (dotted-dashed lines)

In accordance with the precipitation decrease, the FTR shows a decreasing surface soil moisture by 2090 that ranges to -0.008 m^3 m^{-3} in Agafay and to -0.02 m^3 m^{-3} in Agdal and R3, equivalent of around -6% and -12% respectively (Figure 5.8.e) Similar results have also been reported by Arjdal et al. (2023). Nevertheless, the projected changes in the underlying soil layers are less significant (not shown) given that the top soil layer is more sensitive to the evaporative demand (Berg et al. (2016)). The projected decreasing soil moisture translates into decreasing annual averaged latent heat flux by -20 W m^{-2} (-30 to -40%) in the three stations, particularly during the growing season in R3 and almost during the entire year in Agdal and Agafay (Figure 5.9.d), latent heat flux changes are also greater during the day than night (Figure 5.10). Meanwhile, daytime surface sensible heat flux is enhanced in R3 and the differences in the monthly average does not show a substantial seasonal variation (not shown).

Correspondingly, the increased surface temperature by around 4°C due to climate change also projects to an increase in the upward longwave radiation ranging to +25 W m^{-2} at the three stations, counterbalanced by the reinforced downward longwave radiation which is particularly strong during summer (+40 W m^{-2}) resulting in a net LW increase in FTR (Figures 5.8.e,f). Projected downward solar radiation remains unchanged with respect to the PRSNT (Figure 5.8.g), except a slight decrease

(respectively, increase) of about -10 W m^{-2} (-3%) that emerges in summer over R3 (respectively, Agdal and Agafay), suggesting unchanged cloud cover despite the enhanced latent heat flux. In contrast, the decreased vegetation coverage due to climate change in the Evergreen Forests-covered stations increased surface albedo by +0.04 on annual average. Figure 5.11 shows the distribution of surface albedo as a function of LAI. In the future (stars), the average monthly LAI tends to decrease compared with the present period (dots) in Agdal and Agafay. At R3, the albedo does not substantially change between the present and future period (<-0.01). As a result, the upward shortwave radiation tends to be higher in the FTR over Agdal and Agafay by up to 15 W m^{-2}, during spring and summer, while it remains constant over R3 with a slight decrease (< 5 W m^{-2}) that emerges during spring followed by an increase in the same rate in summer.

Climate change over the Haouz plain warms the surface by more than 4K and reduces total precipitation by up to 0.4 mm day^{-1}, representing roughly 30% of the annual average. Therefore, the drying surface inhibit evaporative cooling and further dries and warms the lower atmosphere (Feldman et al. (2019)). These feedbacks could result in persistent drought and heatwaves, particularly in the absence of a moisture re-supply, such as irrigation (Feldman et al. (2019); Hirschi et al. (2011); Miralles et al. (2019); Roundy et al. (2013)).

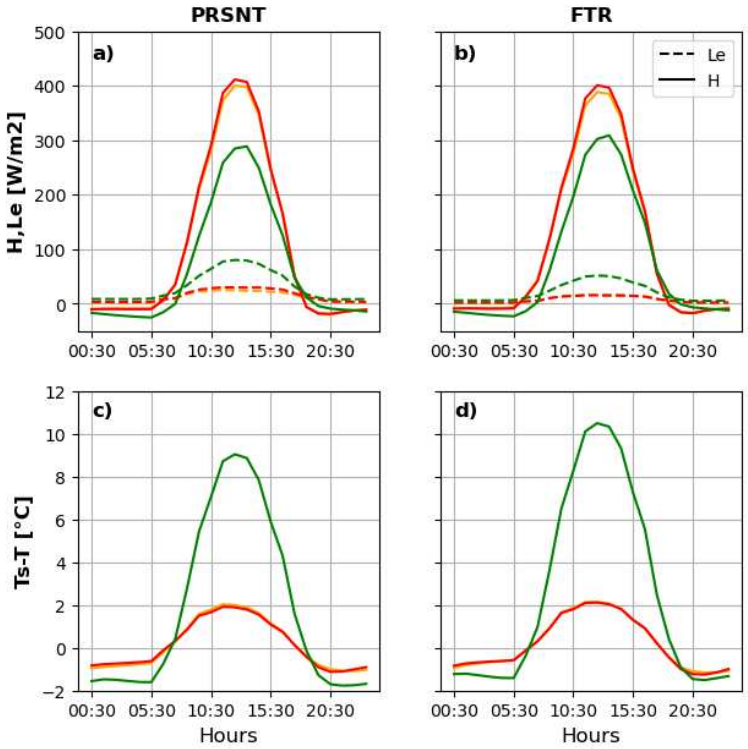

Figure 5.10: a,b): Average diurnal cycle of the sensible (H, solid lines) and latent heat fluxes (Le, dashed lines), (c,d) skin surface temperature minus air temperature (Ts-T) during the present period (left panel) and the future (right panel) over the three stations. Fluxes are defined negative towards the surface.

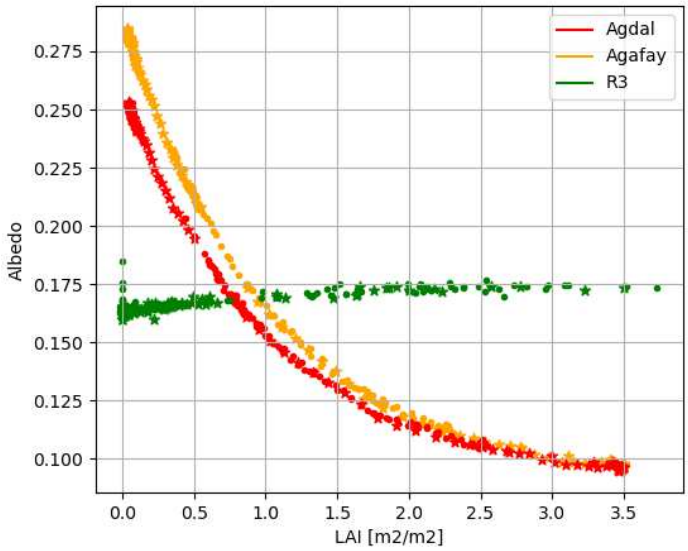

Figure 5.11: Monthly averaged Albedo against LAI during PRSNT (dottes) and FTR (stars) over Agdal (red), Agafay (orange) and R3 (green)

5.3.3 Influence of the irrigation parametrization on climate change projections

The activation of irrigation induces a strong increase of evapotranspiration rate (Figure 5.12.a), consistently with previous studies (Sherwood et al. (2018); Arboleda-Obando (2023)). Differences between FTR-Irr and FTR simulations exceed +1.2 mm day^{-1} over the plain, which represent twice the projected FTR rate in R3 and around four times the projected one in Agdal and Agafay. These differences may be partly explained by the increased LAI (see Figure 5.13), this latter is enhanced with irrigation since the extra water strengthen the plant transpiration (not shown). In the tree-covered stations (Agdal and Agafay), the simulated LAI increases throughout the year by +50% of the total average over the studied period, while its increase in R3 occurs only during the growing season and ranges to +26% (Table 5.2).

Soil moisture also increases with irrigation (Figure 5.12.b) but the effect is not as intense as for evapotranspiration. FTR-Irr shows a projected increase of +0.02 m^3 m^{-3} (+20%) in Agdal and Agafay and of +0.01 m^3 m^{-3} (+7%) in R3 with respect to FTR. Likewise, when comparing the projected FTR-Irr with its corresponding PRSNT-Irr simulation, the irrigation seems to reduce the amplitude of the projected soil moisture decline from -0.008 m^3 m^{-3} (-6%) in the reference simulation to -0.002 m^3 m^{-3} (-1%) in the irrigated configuration in Agdal and Agafay, but no significant difference was shown in R3. Despite the enhanced evapotranspiration and soil moisture rates, the precipitation rate doesn't show any response to irrigation in our study, at least locally (Figure 5.12.c).

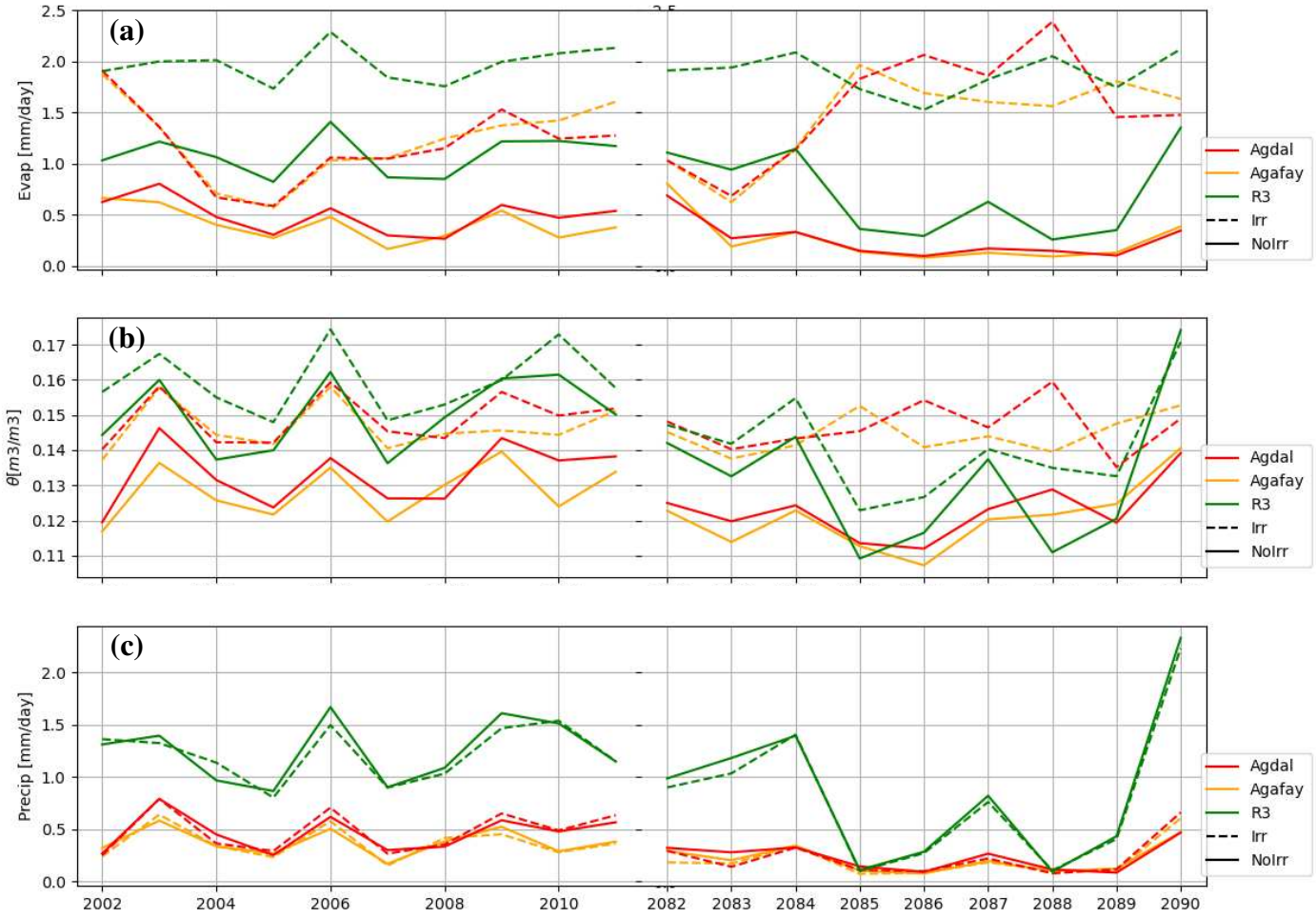

Figure 5.12: Annual average of evapotranspiration rate (a), volumetric soil moisture content at 6 cm (b) and precipitation rate (c) over Agdal (red), Agafay (orange) and R3 (green) during the present period (2002-2011) and the future period (2082-2090). Solid lines correspond to the PRSNT and FTR simulations, dashed lines correspond to their respective PRSNT-Irr and FTR-Irr simulations

Table 5.2: The simulated annual averaged Tsol, Tair, Tmax and Tmin [°C] in the PRSNT and FTR simulations, with their corresponding irrigated configurations in Agdal, Agafay and R3. Interquartile range in brackets.

Variable	Station	PRSNT	PRSNT-Irr	FTR	FTR-Irr
Tsol [°C]	Agdal	20.18 (0.49)	19.74 (0.73)	24.67 (0.39)	23.51 (0.75)
	Agafay	19.98 (0.52)	19.53 (0.85)	24.25 (0.37)	23.40 (0.63)
	R3	22.90 (0.27)	21.43 (0.49)	28.50 (1.62)	26.33 (0.66)
Tair [°C]	Agdal	20.04 (0.47)	19.63 (0.66)	24.46 (0.33)	23.45 (0.68)
	Agafay	19.82 (0.46)	19.45 (0.75)	24.04 (0.41)	23.32 (0.54)
	R3	21.08 (0.50)	20.38 (0.55)	25.99 (0.97)	24.97 (0.57)
Tmax [°C]	Agdal	29.75 (0.43)	29.09 (0.48)	34.38 (0.61)	33.11 (0.53)
	Agafay	29.39 (0.51)	28.75 (0.41)	33.85 (0.66)	32.92 (1.16)
	R3	27.83 (0.54)	26.95 (0.41)	33.41 (1.68)	32.38 (1.25)
Tmin [°C]	Agdal	11.76 (0.68)	11.71 (0.89)	16.15 (0.58)	15.54 (0.90)
	Agafay	11.70 (0.80)	11.77 (0.95)	15.88 (0.39)	15.57 (0.75)
	R3	15.06 (0.43)	14.22 (0.48)	16.69 (0.57)	18.34 (0.15)

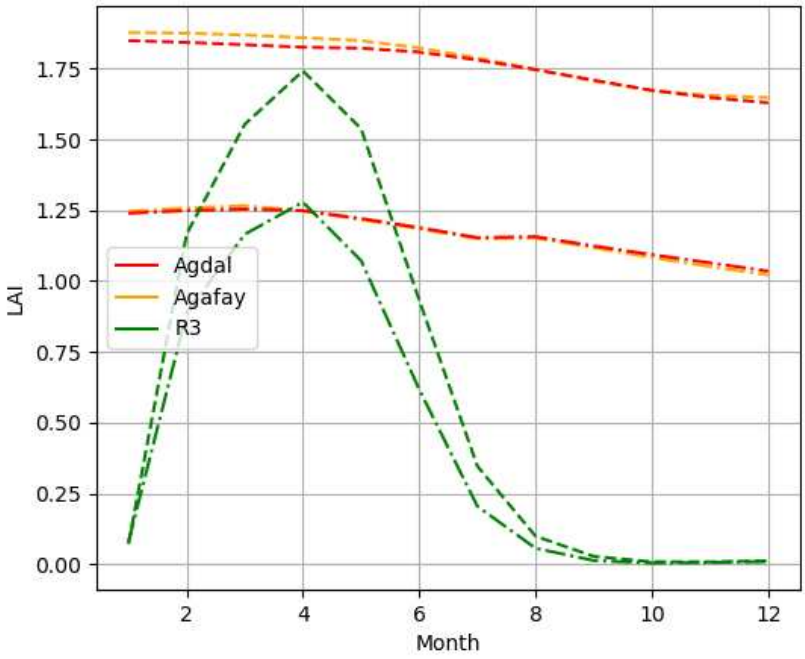

Figure 5.13: Seasonal cycle of averaged LAI as simulated by FTR (dashed lines) and FTR-Irr (dotted-dashed lines) at the three sites Agdal (red), Agafay (orange) and R3 (green)

Irrigation induces also substantial changes in surface and near-surface temperature (Table 5.2). From PRSNT to PRSNT-Irr, the annual mean of skin surface temperature is 0.4 °C (respectively,

1.5 °C) lower in Agdal and Agafay (respectively in R3), consistently, air temperature cooling varies between 0.3 and 0.7 °C. However, from FTR to FTR-Irr, the cooling effect is greater, mean air temperature is lower by more than 1°C over Agdal and R3, and +0.7 °C in Agafay when irrigation is activated. Surface temperature, being the most sensitive to irrigation impact, is projected to decrease by more than -2°C in R3 and by up to -1.2°C in Agdal and Agafay. The seasonal cycles at the three stations show that differences in the monthly mean surface and air temperature are particularly higher in summer than winter. Furthermore, the annual average change in Tmin varies between -0.3 and -0.6 °C in Agdal and Agafay while the registered Tmax changes are much greater (-0.9 to -1.2 °C). This suggests a stronger irrigation effect during the day than night, hence, a reduced diurnal temperature range. A similar pattern was also shown in previous studies (Sacks et al. (2009); Jiang et al. (2014)). In contrast, R3 shows a relatively higher Tmin difference between FTR and FTR-Irr ranging to -1.5 °C, together with decreasing nighttime Tsol.

The surface cooling effect induced by irrigation in the Haouz plain can be directly explained by the increased latent heat flux, partly at the expense of sensible heat flux, mainly during daytime. Figures 5.14 and 5.15 shows the diurnal cycle of averaged air and skin surface temperature, relative humidity, wind speed and the energy budget as simulated by the four studied simulations over R3 (5.14) and Agdal (5.15). Results from Agafay are not shown since they show similar results with Agdal. From FTR to FTR-Irr, Le increases by +50 to +75 W m^{-2} during daytime, and by +25 W m^{-2} during night, resulting in cooler temperatures and increased relative humidity by up to 10% over the three stations. While sensible heating decreases by -50 W m^{-2} during daytime, and shows near zero changes during night.

Wind speed (Figures 5.14.f, 5.15.f) is projected to increase with climate change by around +0.5 m s^{-1}, partly due to the reduced aerodynamic roughness height by 0.1 m in Agdal and Agafay, which may be attributed to the vegetation density decrease. When the irrigation is activated, z_{0m} increases by +0.15 (respectively, +0.02) m in Agdal, Agafay (respectively, R3). This translates into a systematic decreasing wind speed in FTR-Irr, less intense in R3.

Regarding the radiative fluxes, our results suggest two contrasting behaviours; in Agdal and Agafay, and consistently with previous studies (Kueppers et al. (2007); Sacks et al. (2009); Jiang et al. (2014)), irrigation reduces surface albedo by -0.05 (-40%) and decreases the reflected solar radiation by around -40 W ^{2} (-40%) (Figures 5.14.g,h, 5.15.g,h). In contrast, R3 exhibits an opposite, but negligible, surface albedo change from FTR to FTR-Irr (< +0.001).Solar radiation shows no change in all the implemented simulations and overall the studied stations, suggesting the absence of cloud cover response to irrigation despite the increased atmospheric water vapor. The emitted LW radiation (LWup) (Figures 5.14.j, 5.15.j) is reduced by around -20 W m^{-2} due to the cooler irrigated surfaces, combined with a negligible LWdn reduction, resulting in increased surface net longwave radiation.

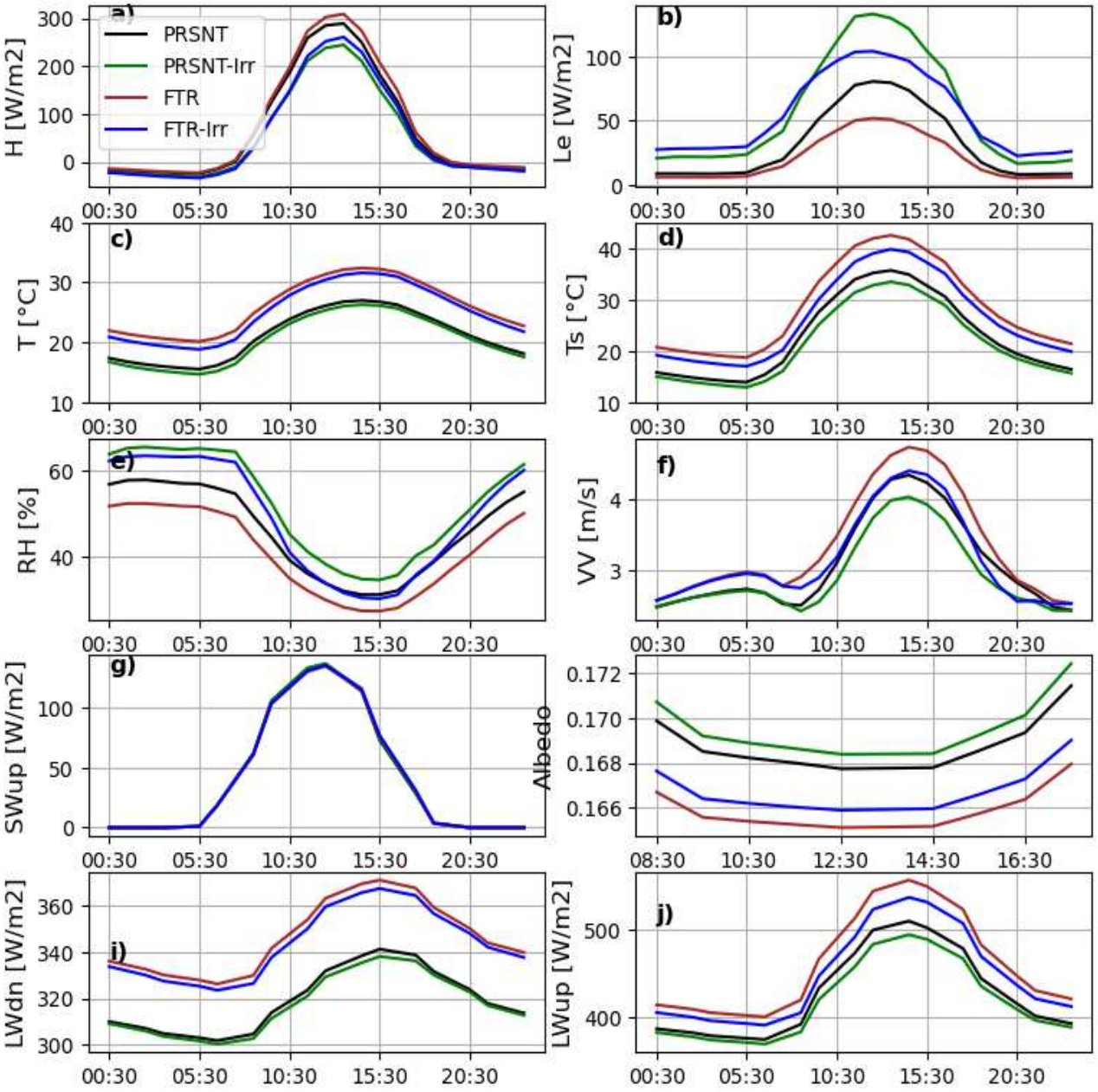

Figure 5.14: Diurnal cycle of air temperature, skin surface temperature, relative humidity, wind speed, sensible and latent heat fluxes, shortwave upward radiation, albedo and longwave downward and upward radiation simulated during the PRSNT (black curve), PRSNT-Irr (green), FTR (brown) and FTR-Irr (blue) over R3

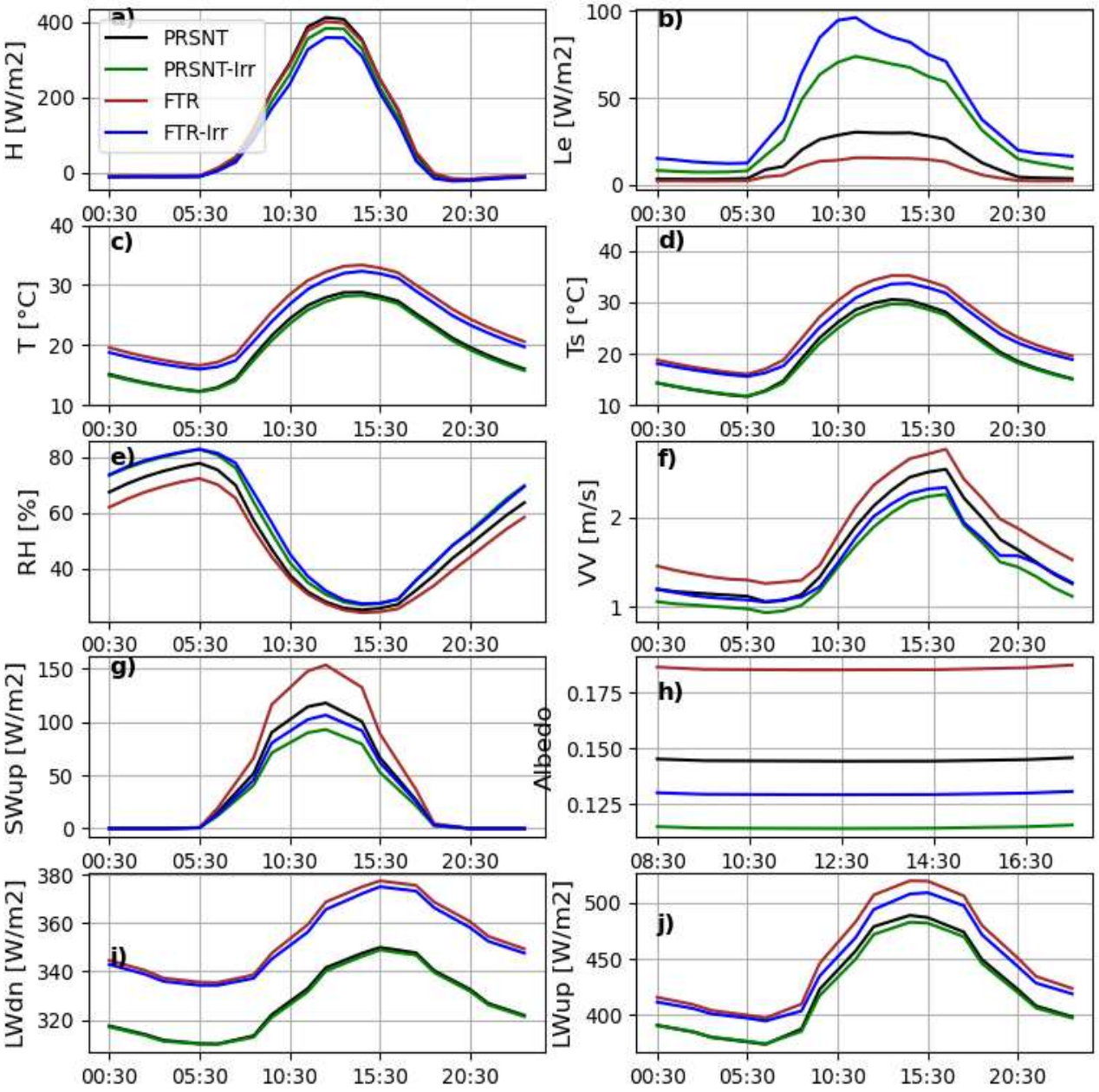

Figure 5.15: Similar as 5.14 but for Agdal

5.4 Chapter conclusions

This chapter aims to assess the future evolution of Moroccan climate as simulated by CMIP6 GCMs, and then to assess the LMDZ-ORCHIDEE projections over the Haouz plain.

In this chapter, we assessed and analyzed the projected changes in precipitation, evapotranspiration, net water supply, and surface soil moisture in the Mediterranean and Saharan regions using outputs from 17 CMIP6 models under SSP5-8.5 and SSP2-4.5 climate scenarios. Results evidenced a statistically robust drying across the entire Mediterranean region and coastal North Africa, where precipitation is projected to decrease by -0.4 $\pm$ 0.1 mm day^{-1} by the end of the 21st century under the SSP5-8.5 scenario, resulting in declining trends in both evapotranspiration and soil moisture. A contrasted behaviour is projected over the Sahara where an increase of up to +0.3 $\pm$ 0.1 mm day^{-1} in precipitation is foreseen, although, it is compensated by increasing evapotranspiration. It is worth noting that the CMIP6 and CMIP5 models yield qualitatively similar patterns of changes, but the CMIP6 models exhibit more pronounced changes over the Mediterranean basin and South-Eastern Sahara, especially during the winter season.

In order to refine the projections over the Moroccan plains, we assessed the projected changes in the Haouz plain, with a particular focus on the near surface climate. We analyzed the future evolution of the precipitation, temperature and the energy budget terms over the three stations Agdal, Agafay and R3 using the "zoomed" LMDZ-ORCHIDEE configuration, and nudging outside the plain towards a CMIP6 SSP5-8.5 scenario from a bias-corrected IPSL-CM6 simulation. Results show that air temperature is projected to increase by over 4K in the late 21th century (2082-2090) with respect to the reference period (2002-2011), as well as a -0.40 mm day^{-1} (-30%) decrease in precipitation resulting in up to -12% reduction of surface soil moisture and -20 W m^{-2} decrease in latent heat flux. With the changes being particularly intense during summer. Furthermore, LMDZ-ORCHIDEE projects an increase in the 10 m wind speed by around +0.5 m s^{-1}, particularly in the Evergreen forests-covered stations.

Given the extensive use of irrigation in Moroccan agricultural fields, and its effects which may extend beyond local processes, we introduced a first-order parameterization within ORCHIDEE to mimic the irrigation at the Haouz plain and we examined the potential changes in the plain's near surface climate. Our results indicate that temperature and the surface energy budget are sensitive to irrigation. Irrigation leads to a +50 to +75 W m^{-2} increase in the annual mean latent heat flux at the expense of decreasing sensible heating (-50 W m^{-2}), a decrease of -0.7 to -1K in air temperature, and a decrease of -1.2 to -2K in skin surface temperature. Furthermore, the surface soil moisture is also enhanced with irrigation, with +20% increase noticed in the tree-filled stations (Agdal and Agafay) and +7% in the C3 grasses-filled station (R3). Additionally, we find that the irrigation's cooling impact also leads to a decreased diurnal temperature range.

Irrigation in the Haouz plain mitigates the climate change-induced warming through the dominant evaporative cooling mechanism. When activating the irrigation, future changes of air temperature are reduced by 0.4 K, and skin surface temperature by 0.6 K over the three stations, but no major impact was observed in precipitation or the cloud cover. Nevertheless, Morocco faces increasing water

shortage risks and the groundwater, which could limit the access to irrigation in the coming years.

The results presented in the section 5.3 are a preliminary work carried out at the end of my thesis work. The next step is to set up a simulation with the moderate scenario SSP2-4.5, and to carry out a sensitivity study to the bias correction approach, the land cover evolution and also to the soil texture.

CHAPTER 6

Conclusions and prospects

Contents

6.1 General conclusions on the representation of land-surface atmosphere interaction in semi-arid agricultural plains in Morocco 115

6.2 Prospects 117

"The most beautiful experience we can have is the mysterious. It is the fundamental emotion that stands at the cradle of true art and true science."

-Albert Einstein

6.1 General conclusions on the representation of land-surface atmosphere interaction in semi-arid agricultural plains in Morocco

Morocco is among the most vulnerable climate change hotspots, characterized by rising temperatures, increasing atmospheric evaporative demand and decreasing rainfall. The warming and drying trends are strengthening in the future according to GCMs involved in the sixth IPCC report, generating subsequent impacts on socio-economic sectors, notably agriculture. This latter is the major contributor to the country's food security. Therefore, accurate simulation of hydrological cycle and surface climate in Moroccan agricultural areas is necessary, but it is still insufficiently investigated.

In this thesis, we contribute to the improvement of our knowledge of climate models capacity in representing the near surface climate in Moroccan agricultural plains. We use the CMIP6 GCMs to assess the future changes in land surface hydrology over Mediterranean and Sahara, then, we use the zoomed land-surface atmosphere component of IPSL-CM to investigate the processes driving the surface-atmosphere coupling at local scale, with a focus on the Haouz agricultural plain in Marrakech region, benefiting from precious in-situ measurements collected by the LMI TREMA. The thesis objectives were summarised in three questions that I tackled during my PhD:

- **Question 1**: What is the ability of climate models - and more particularly that of IPSL - to simulate the near surface climate over the Moroccan semi-arid agricultural plain ?

- **Question 2**: Which processes control the surface energy and water budgets and how their parameterization in models are efficient and sensitive?

In chapter 4 of this thesis, we firstly analyzed the CMIP6 version of LMDZ-ORCHIDEE land-surface atmosphere model, with its CMIP6 version of the physics, in representing the near surface climate over the Haouz plain. We leveraged the precious meteorological observations collected over the Haouz plain, as well as the "zoom" capability of LMDZ to perform a standard simulation refined over the plain and nudged outside of the zoom area. Although the monitoring stations are located in the middle of agricultural fields, since the sampling of these stations was not necessarily designed for the evaluation of GCMs, we have proposed an approach to perform more reliable model-observation comparisons. In each mesh, we set a full coverage with the PFT corresponding to the station's vegetation coverage. We also set up a series of sensitivity tests to identify the model's robust biases. Results showed that LMDZ-ORCHIDEE simulates the near surface climate over the Haouz plain reasonably well, but some biases persist. They can be synthesized in the following points:

- Overestimated 2m temperature attributed to higher solar radiation during daytime, and to surface-atmosphere decoupling during nighttime over tree-covered crops.
- Overly large aerodynamic roughness heights (z_0), leading to overly weak wind speeds, at the

stations with Evergreen Broadleaf forests when setting prescribed PFTs. The bias is slightly reduced when setting a constant value of z_0 corresponding to the mean observed value instead of the common and default LAI-dependent z_0 in the ORCHIDEE land surface model.

- The dry bias associated with underestimated evaporative flux and overestimated Bowen ratio, can partly be attributed to the lack of irrigation parametrization in the surface model ORCHIDEE.

At the very local scale in crops, the surface water budget depends strongly on irrigation. Therefore, to assess the impact of irrigation on the model performances, we implemented a first-order parametrization in ORCHIDEE to mimic the drip irrigation over the plain, which consists in nudging the surface soil moisture towards a saturated value when it is below a fraction of this latter. Analysis of the simulated present-day climate suggests, at the very local scale, substantial changes in the surface energy partitioning with important increase of latent heat flux and decrease of sensible heat flux. Accompanied with a decrease of warm biases by up to 2K in skin surface temperature and 1K in 2m temperature. Soil moisture biases are also reduced by about 8%. In contrast, precipitation and cloud cover remain almost unchanged with irrigation. An increase in leaf area index is also noticed, mainly in the tree-covered sites, as a direct response to the enhanced transpiration, leading to reduced surface albedo.

- **Question 3**: How surface climate over the Moroccan semi-arid agricultural plains will evolve in the future and what is the sensitivity of climate scenarios to the parameterization of local processes driving the surface-atmosphere exchanges of energy and water?

In chapter 5 of this thesis, we assessed the future climate simulated by the state of the art of climate models, from the sixth CMIP exercise, in simulating the future climate over Mediterranean and Saharan region under the high and medium-end scenarios. CMIP6 models project robust reduction in precipitation over the Mediterranean region with higher intermodel variability noticed in southern Morocco, these changes are mirrored in evapotranspiration that follows the precipitation pattern but with less intense signal. In Southeastern Sahara, a contrasting behaviour shows up, the models suggest increasing precipitation and evapotranspiration. Therefore, the net water supply (P-E) suggests no change overall the region except the northern part of the Mediterranean where the magnitude of precipitation changes surpasses that of evapotranspiration resulting in negative P-E change. We also made a preliminary comparative study to assess the impact of horizontal resolution on the models response. Results suggest that, compared to lower resolution models (250 km), models with 100 km resolution project a milder drying trend over the Mediterranean region, showing less intermodel variations. However, this result could not be solely attributable to the differences in horizontal resolution. A more reliable assessment of resolution sensitivity could be achieved by conducting additional research that specifically focuses on scenarios conducted with a single model at multiple resolutions. Besides, a brief comparative study demonstrates that CMIP5 models qualitatively agree with CMIP6 on the precipitation changes over the whole region, however, CMIP6 signal is generally intense, mainly during winter.

In the second part of this chapter, we leveraged the LMDZ-ORCHIDEE configuration developed in chapter 4. The simulation is nudged, outside of the Haouz plain, to a global bias-corrected CMIP6 SSP5-8.5 scenario simulation performed with the IPSL-CM model. Since the Haouz plain -as the majority of agricultural lands in Morocco- is extensively irrigated, we included the irrigation parametrization presented in chapter 4 in our future scenario. Then, we compared two coupled LMDZ-ORCHIDEE simulations with and without irrigation for the period 2080-2090. The conclusions suggest, in the case of non-irrigation, significant warming and drying signal over the three stations, as well as decreasing surface soil moisture. Indeed, results show significant changes ranging to 4K in air temperature and up to 4.9K in skin surface temperature. Accompanied with up to -0.4 mm day^{-1} (30%) decrease in precipitation. Including irrigation in our simulations helped reducing air temperature changes by 0.4K, and skin surface temperature changes by 0.6K over the three stations, with no effect on precipitation or cloud cover. Certainly, maintaining irrigation over the plain in the future is an obvious choice for food security, but the over-exploitation of water resources combined with the projected drying trends could induce a halt to irrigation activities.

6.2 Prospects

The present thesis is the first evaluation work of LMDZ-ORCHIDEE on the representation of surface processes in Morocco. The evaluation work was conducted using the Haouz plain in-situ dataset. Although the latter provides a wide range of meteorological and energy fluxes dataset, the representativeness aspect of the monitoring stations limits our conclusions. In addition, implementing radiosoundings or remote-sensing observational systems in the plain could make it possible to explore the boundary layer dynamics in this region, and then making possible a more comprehensive assessment of the model performances. Then, our findings open some perspectives we may recommend for future works, summarized in the following points:

- To overcome the representativeness issue when evaluating the model with in-situ data, we set a unique PFT for each station's grid-cell. In fact, the model's horizontal resolution over the Haouz plain is around 25km. A model grid-cell with this resolution encompasses a wide variety of land coverages: the agricultural fields where the instruments are installed as well as bare soil, deserts and even buildings. Although our work allowed us to draw conclusions about the representation of surface-atmosphere interactions over a single surface type, the question of how dealing with the surface heterogeneities in a mesh to compute the mesh-average surface atmosphere exchanges of energy, momentum and water but also local exchanges over each sub-surface has not been tackled. Note that investigating the uncertainty and representativeness of the land atmosphere exchanges over heterogeneous landscapes is one of the key issues tackled in the ongoing MOSAI[1] project (Lohou et al. (2022)).

- The model showed a robust bias in incident solar radiation over the three stations, with signif-

[1]Modèles et Observations pour les Interactions entre la Surface et l'Atmopshère. https://anr.fr/Projet-ANR-20-CE01-0018

icant effects on surface and near-surface temperatures. This aspect questions the representation of cloud cover in the model, but also, the representativity of the radiation measurement at the mesh scale stresses the crucial need to acquire remote sensing measurements (Radar/Lidar) for a thorough characterisation of the cloud cover dynamics over the plain.

- Our first order irrigation parametrization has been shown to reduce the modeling biases for the evaporative flux, the Bowen ratio and the near-surface temperature. However, a more rigorous scheme could take into consideration the water demand and supply as well as the irrigated area as documented in several studies (e.g., Sacks et al. (2009); Arboleda-Obando et al. (2023)), the timing of irrigation is not usually prescribed in such studies, it would be retrieved from irrigation dates provided in our in-situ data. While writing this thesis, I am collaborating with P. Tiengou to implement the irrigation module on my configuration. An in-depth evaluation will be then carried out after setting up an operational configuration.

- Our research offers valuable insights into the future of climate over the Mediterranean and North Africa. At the local scale, our "zoomed" and nudged LMDZ-ORCHIDEE towards a CMIP6 SSP5-8.5 scenario from a bias-corrected IPSL-CM6 simulation projects a temperature increase exceeding 4K in the late 21th century (2082-2090) with respect to the reference period (2002-2011), with a -0.40 mm day^{-1} (-30%) decrease in precipitation over the three stations. Therefore, an interesting perspective is setting up a future simulation with the moderate-end scenario (SSP2-4.5) for a better comparison of changes intensity. Besides, a sensitivity study of future projections to the use of bias-corrected IPSL-CM6 for nudging would make it possible to assess the contribution of empirical bias-corrections methods in improving the models uncertainties reported in Arjdal et al. (2023). Furthermore, our study suggests a higher model uncertainties in GCMs with lower horizontal resolution (250 km) in comparison to models with 100 km resolution. The challenge of comparing the impact of horizontal resolution on the models behaviour could also be addressed through the comparison of several resolutions of the same model.

-Finally, this thesis work focuses on the representation of land-surface atmosphere interactions in LMDZ-ORCHIDEE, however, other critical aspects for the water balance have not been addressed, such as the model performances in simulating the large scale circulation patterns driving Moroccan climate. This aspect is subject of an ongoing thesis work (Balhane (in prep.)). The representation of the deep convection, and associated rainfall is also critical, particularly during summer, the season during which precipitation events in the Haouz plain are mostly related to the development of deep wet convective systems over the High Atlas Mountains (thunderstorms or showers) that propagate over the plain (Bell et al. (2022); Born et al. (2010)). Therefore, the deep convection triggering by orography must be then parameterized. Furthermore, our model regional configuration is actually challenging for such study, since the horizontal resolution in the zoom area ($\approx$ 20 km) is considered as a “gray zone” for convection.

Appendix A: *Supporting information for "Modeling land-atmosphere interactions over semi-arid plains in Morocco: in-depth assessment of GCM stretched-grid simulations using in situ data"*

A. Introduction

This supplementary completes the section 4.2 of the chapter 4 with supplementary Figures. Figure 6.1 shows the studied in situ sites location within the agricultural fields. Figure 6.2 shows the irrigated longitude latitude box with respect to the three stations location. Figure 6.3 shows a simplified schematisation of the implemented nudging parameterization. Figures 6.4 and 6.5 show the average diurnal cycle of meteorological variables (T, RH and U) during winter (DJF) and summer (JJA) over Agdal and R3 stations respectively. Figure 6.6 shows the observed and simulated average diurnal cycles of the energy fluxes in the three studied regions. Figure 6.7 shows the averaged daily cumulative convective precipitation in summer season (JJA) over the Haouze Plain, and 6.8 compares the february 2003 evolution of soil moisture simulated by the model with and without the irrigation parametrization, the Figures 6.9 and 6.10 show their corresponding averaged diurnal cycles (T, Ts, H, Le, RH and SWdn) over Agafay and R3. Figure 6.11 shows the averaged diurnal cycles (T, RH and U) simulated by the CTRL and CTRL-Txt simulations in R3, and Figure 6.12 shows their corresponding averaged diurnal cycles of the energy fluxes. Figure 6.13 ompares the february 2003 evolution of soil moisture simulated by the model with and without the irrigation parametrization in the CTRL-Txt simulation.

The section C shows a further analysis of the model behavior at the location of two additional stations Graoua and Chichaoua.

B. Supplementary Figures

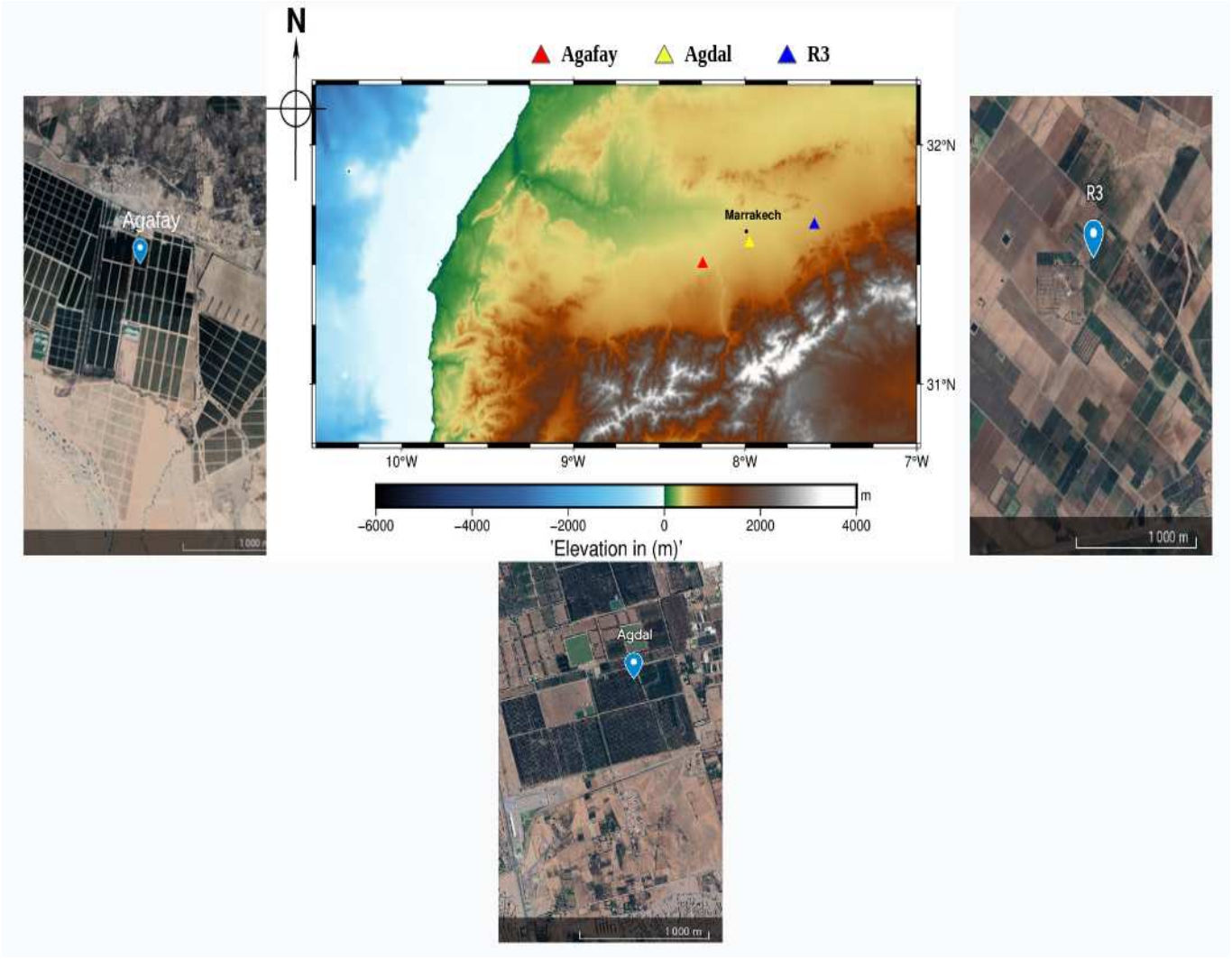

Figure 6.1: Overview of the studied in situ sites location with satellite maps showing their position with respect to the agricultural fields. (Satellite maps from Google Earth)

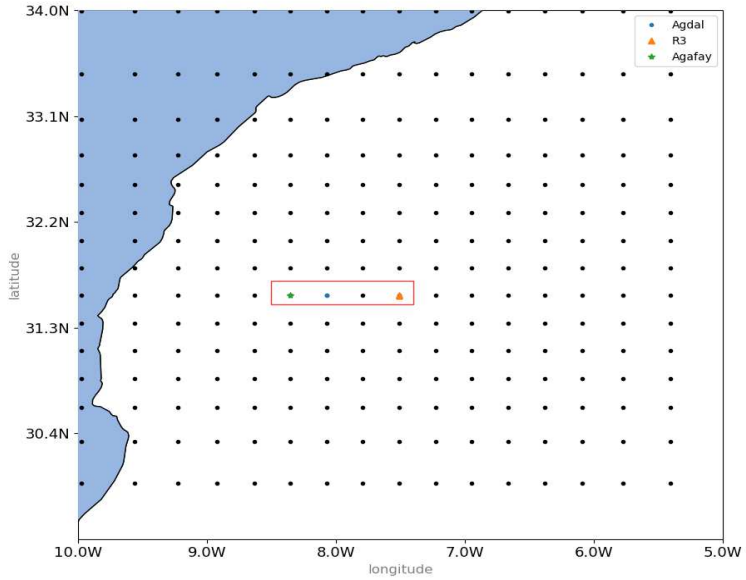

Figure 6.2: Overview of the irrigated longitude latitude box (red polygon), with the three stations location in colored symbols. Black points indicate the model grid.

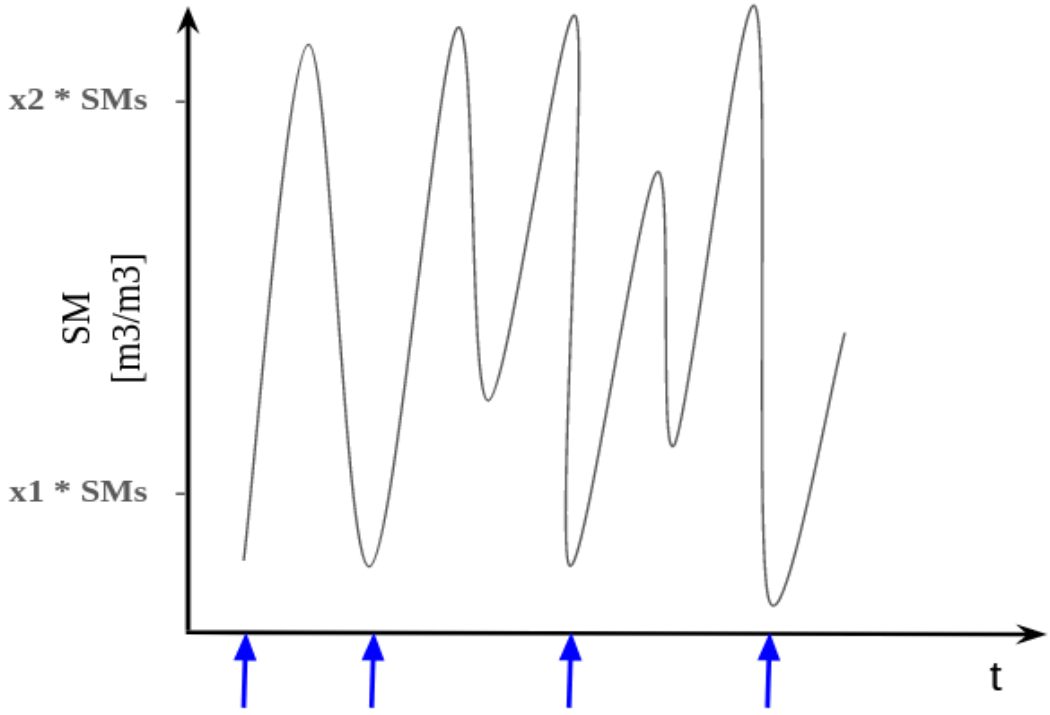

Figure 6.3: Simplified schematisation of the implemented nudging parameterization where soil moisture is forced to SMs (blue arrows) when it decreases below a fraction x_1 of SM_s

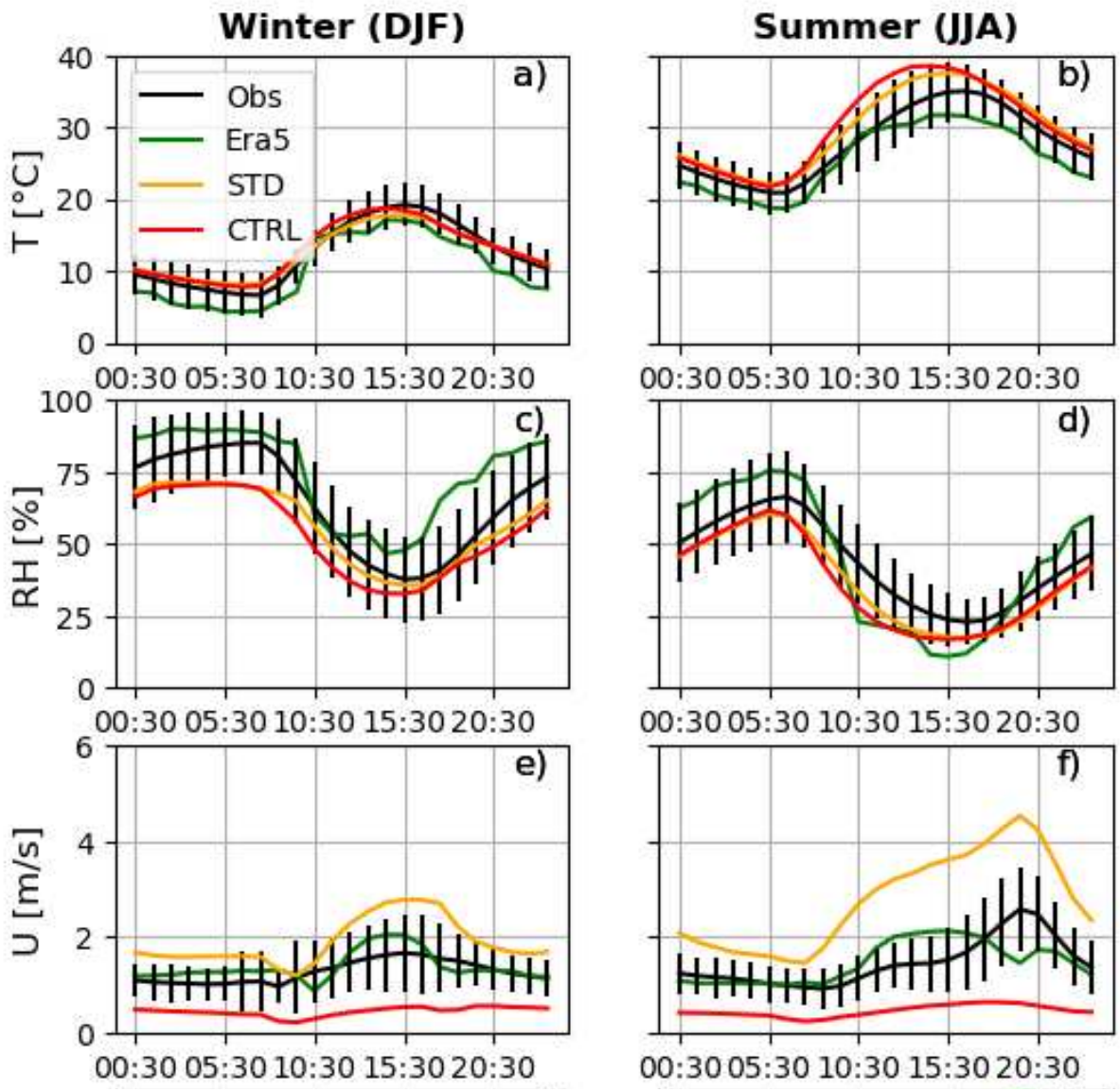

Figure 6.4: Average diurnal cycle of T, RH and U during winter (DJF) and summer (JJA) for 2002-2004 period at Agdal station. The black line shows observations, the orange line the standard simulation (STD), the red line the control simulation (CTRL) and the green one represents ERA5. Vertical bars denote the standard deviation around the observations' average value.

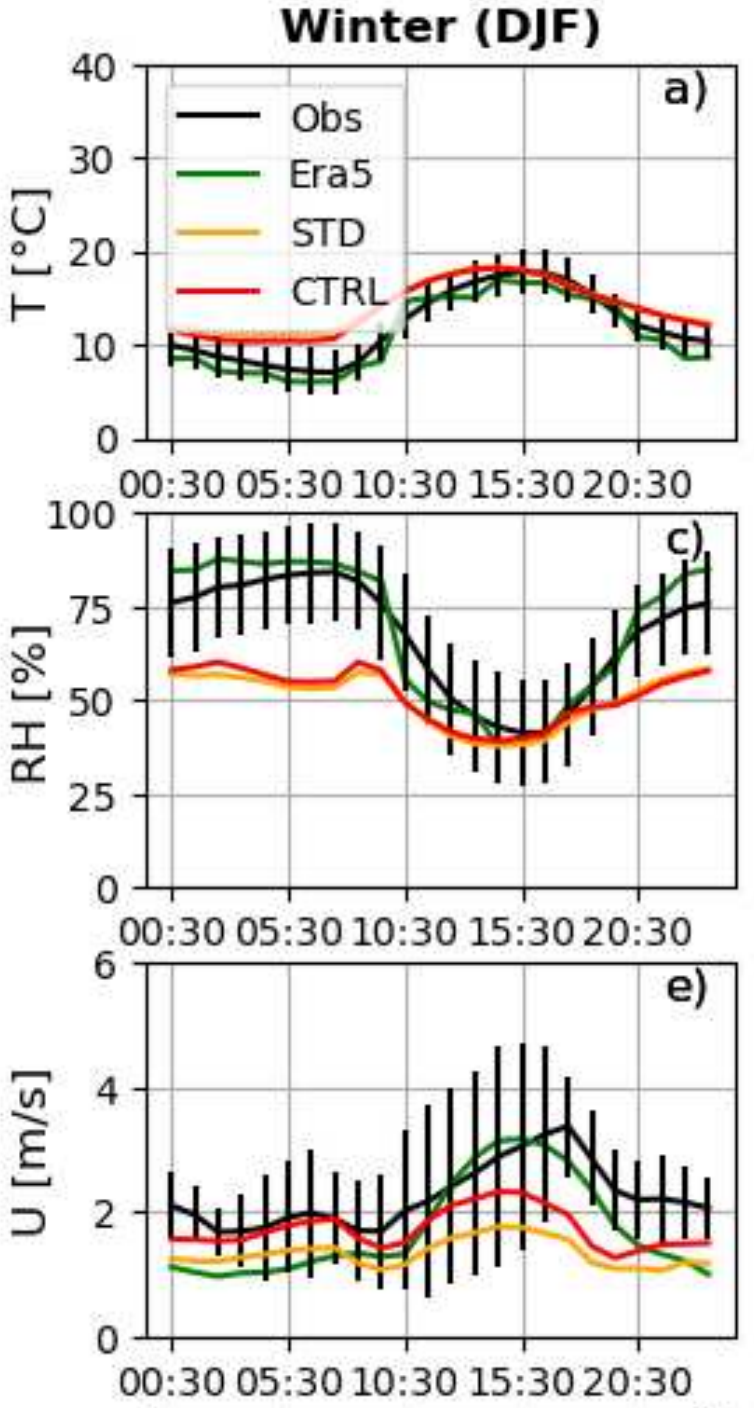

Figure 6.5: Same as Fig. 6.1 but with the control simulation CTRL set with updated land cover (red curves) in R3 station.

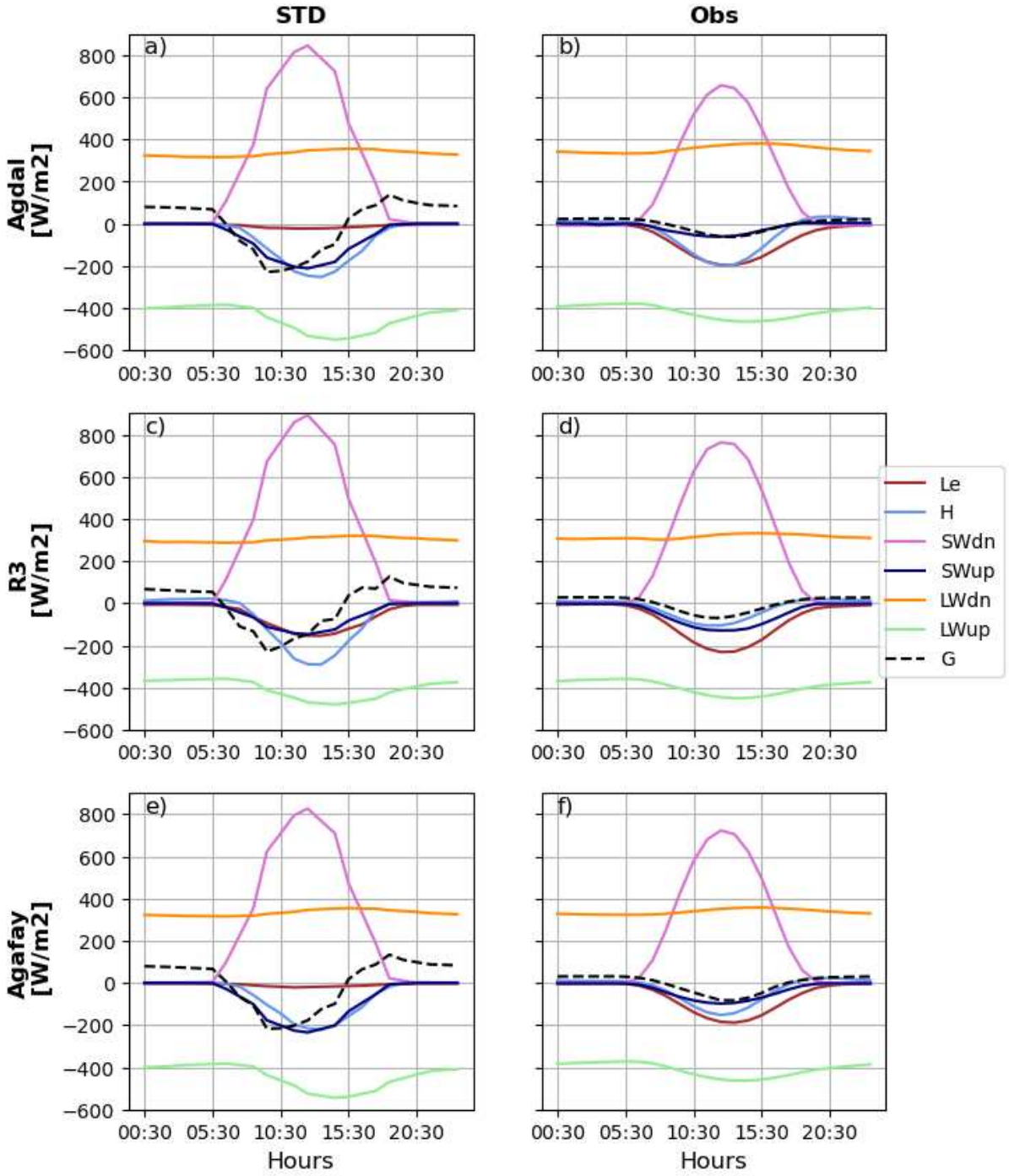

Figure 6.6: Average diurnal cycle of downward (SWdn) and upward (SWup) solar radiation, downward (LWdn) and upward (LWup) longwave radiation, the sensible (H) and latent heat fluxes (Le) and the ground heat flux (G) at Agdal (upper panel), R3 (middle panel) and Agafay (lower panel) stations. The left panel represents STD simulation and the right one represents observations. We decide that by convention, fluxes are positive towards the surface.

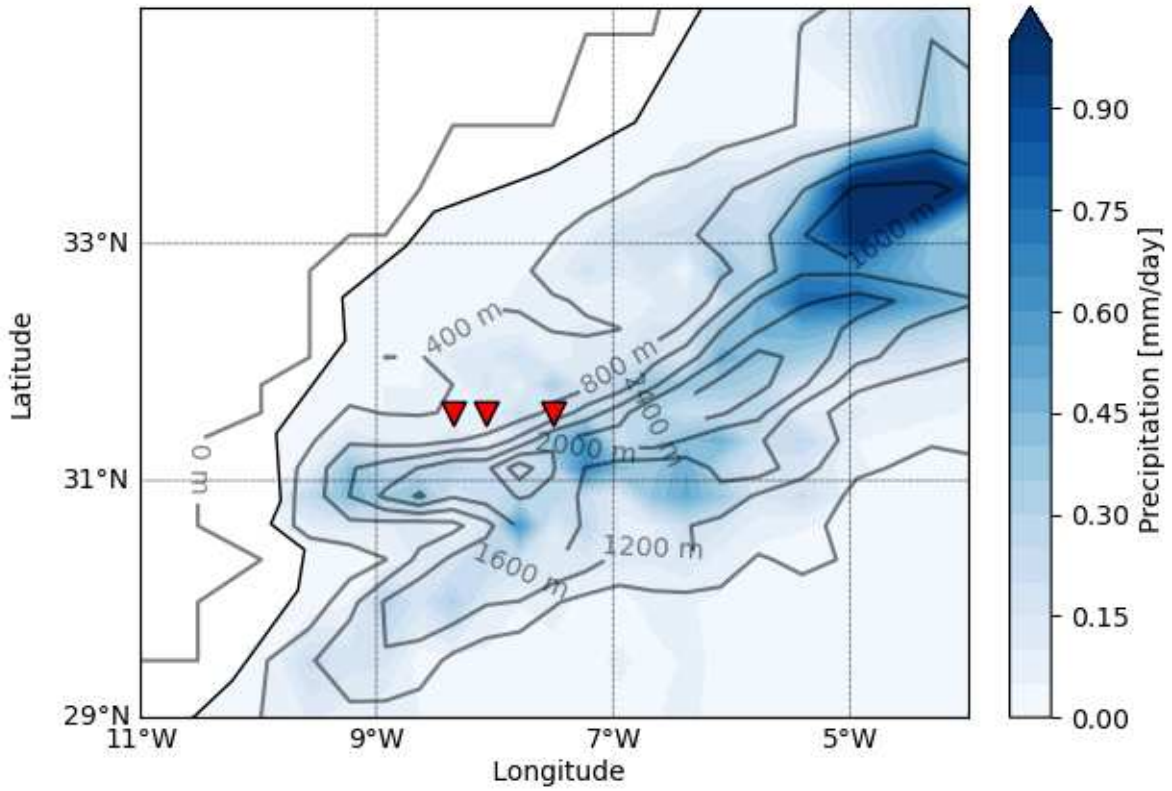

Figure 6.7: Averaged daily cumulative convective precipitation in summer season (JJA) over the Haouz Plain. Contours indicate the ground elevation (m) and the red arrows indicate the station's location; from left to right: Agafay, Agdal and R3.

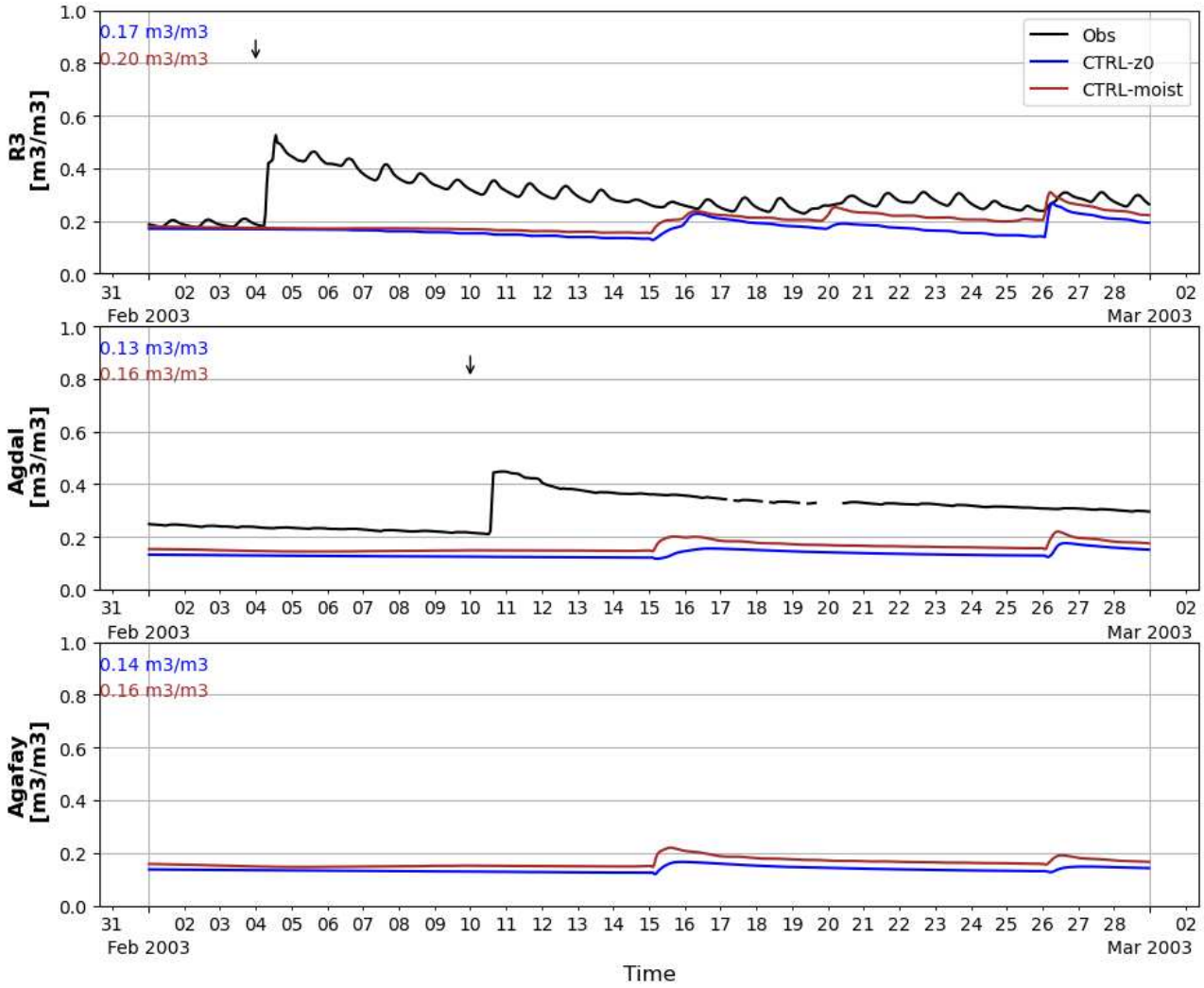

Figure 6.8: February 2003 evolution of soil moisture at 5cm depth in R3, Agdal and Agafay stations from model simulations (CTRL-z0 in blue and CTRL-moist in brown) and observations (black). The black arrow indicates the irrigated day. With the average soil moisture as simulated by both configurations (upper left). The observed soil moisture at Agafay station is not shown since the available dataset starts from 2006.

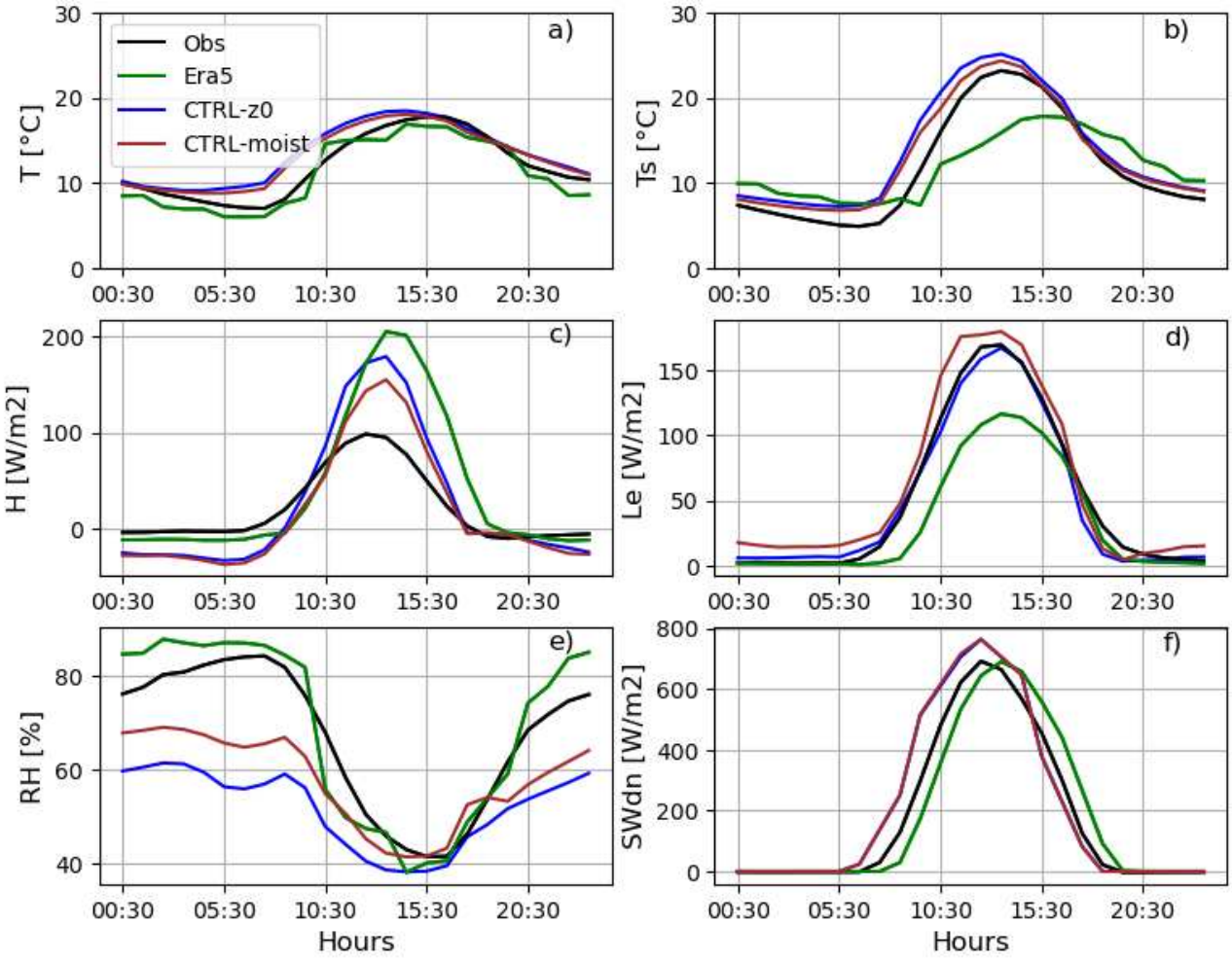

Figure 6.9: February 2003 evolution of Mean diurnal cycles of 2m temperature T, skin surface temperature Ts, Le, H, SWdn and RH in R3 station from model simulations (CTRL-z0 in blue and CTRL-moist in brown), ERA5 (green) and observations (black).

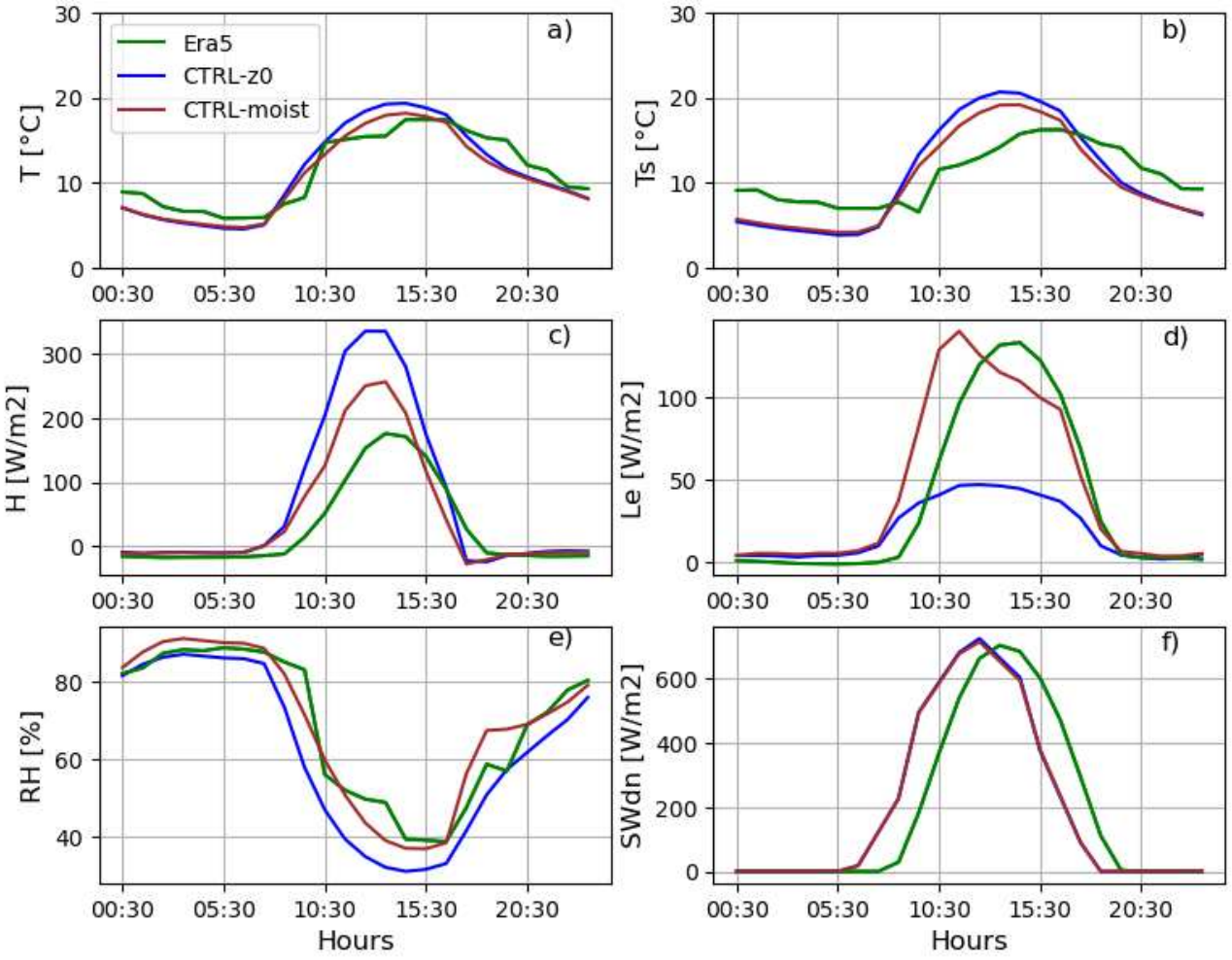

Figure 6.10: February 2003 evolution of Mean diurnal cycles of 2m temperature T, skin surface temperature Ts, Le, H, SWdn and RH in Agafay station from model simulations (CTRL-z0 in blue and CTRL-moist in brown), ERA5 (green). Observations are not shown since the available dataset starts from 2006.

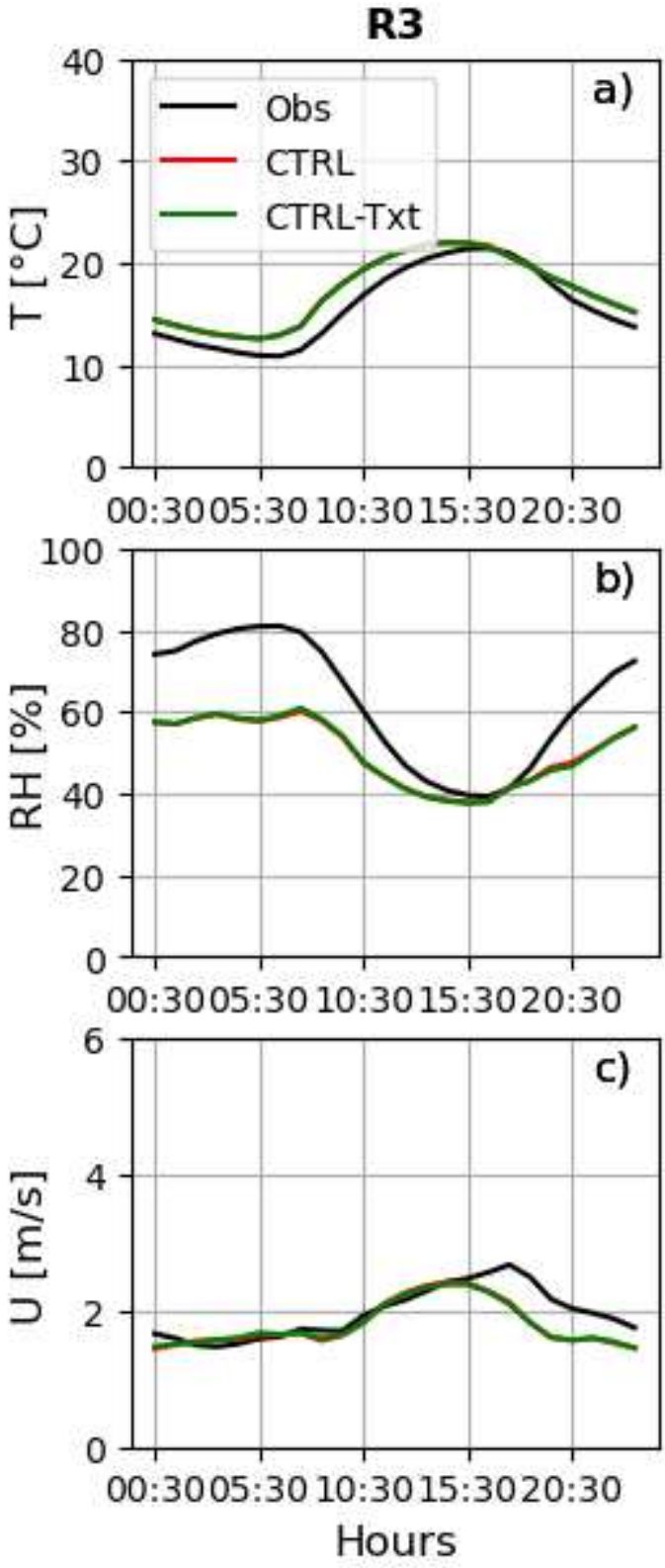

Figure 6.11: Average diurnal cycle of air temperature (T), relative humidity (RH) and wind speed (U) at R3 from model simulations (CTRL in red, CTRL-Txt in green).

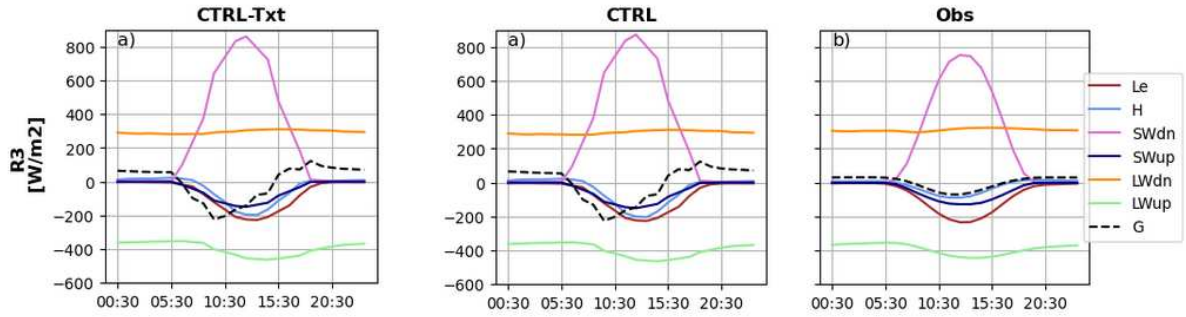

Figure 6.12: Average diurnal cycle of downward (SWdn) and upward (SWup) shortwave radiative fluxes, downward (LWdn) and upward (LWup) longwave radiation, the sensible (H) and latent heat fluxes (Le) and the ground heat flux (G) at R3. The left and the middle panels represent CTRL-Txt and CTRL simulation respectively and the right one represents observations. Fluxes are defined positive towards the surface.

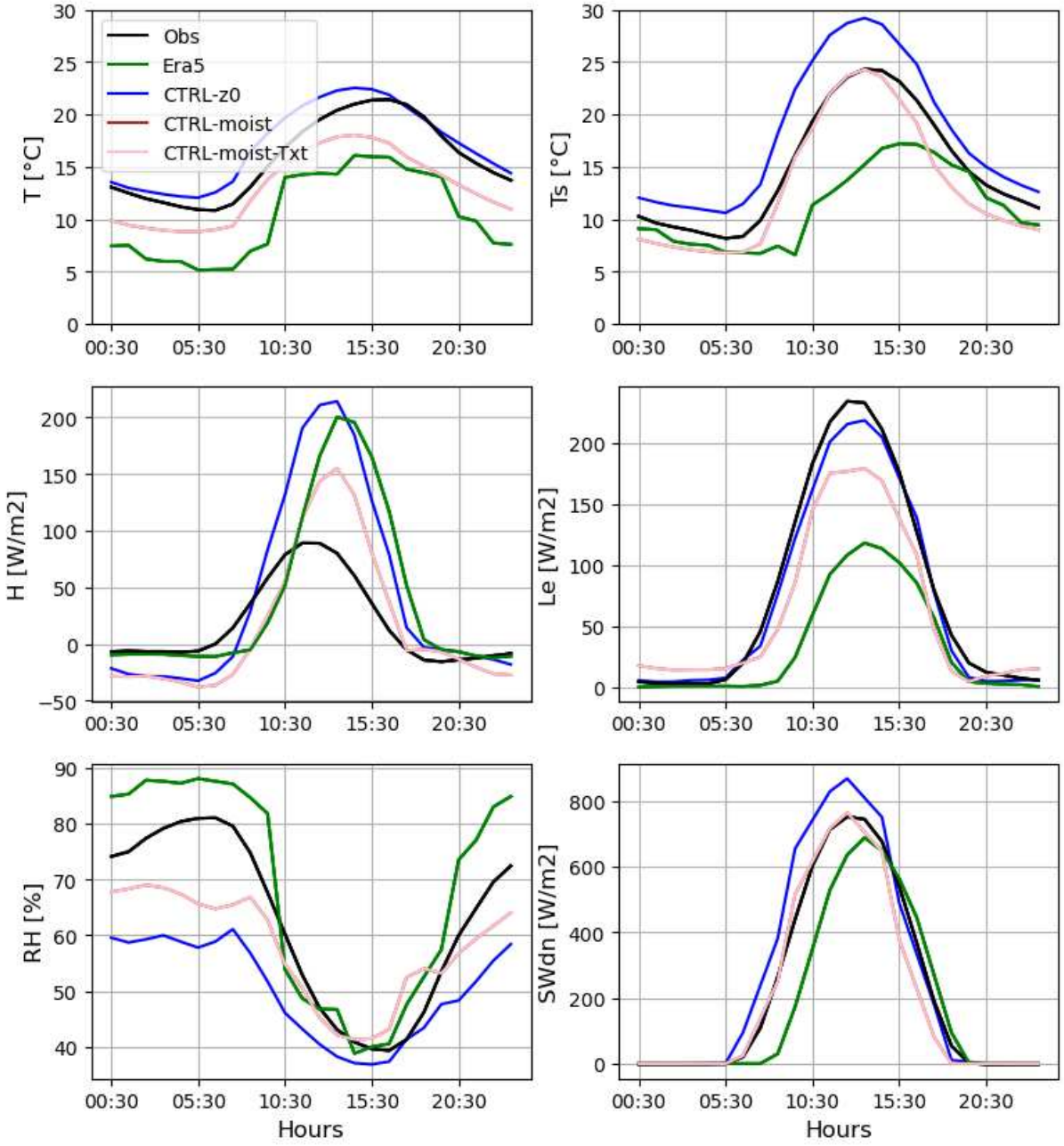

Figure 6.13: February 2003 evolution of Mean diurnal cycles of 2m temperature T, skin surface temperature Ts, Le, H, SWdn and RH in R3 station from model simulations (CTRL-z0 in blue, CTRL-moist in brown, CTRL-moist-Txt in pink), ERA5 (green) and observations (black). Note that the brown and pink lines are superimposed

C. Model evaluation at Graoua and Chichaoua stations

We leveraged the LMI-TREMA dataset to make a further analysis of the model behavior at the location of two additional stations Graoua (7.91°W;31.58) located 10km southern Marrakech, and Chichaoua (8.65°W;31.42°N) located 70 km western Marrakech city (see purple crosses in Fig. 4.1 of the main manuscript). Graoua and Chichaoua have been set-up in the middle of wheat crops (Fig. 6.14).

Then, we compared the model to the stations Graoua and Chichaoua (Fig. 6.15); the model shows a pronounced warm nocturnal bias in Graoua and Chichaoua reaching +2K to +3K. Daytime temperature is relatively well simulated, which leads to an underestimated diurnal temperature range, particularly in Chichaoua. Similarly to Agdal, Agafay and R3, the relative humidity signal reflects that of the temperature and LMDZ-ORCHIDEE exhibits a pronounced low bias during night-time. Differences with observations reach up to -20%, and are more intense during the night. Results show also that STD simulation overestimates wind speed during day and night with positive differences varying from 0.5 to 1.75 m s^{-1}. Daytime differences are the strongest in Graoua.

Figure 6.14: Overview of the instrumented stations Graoua and Chichaoua (Figures from http://trema.ucam.ac.ma/ObsTREMA)

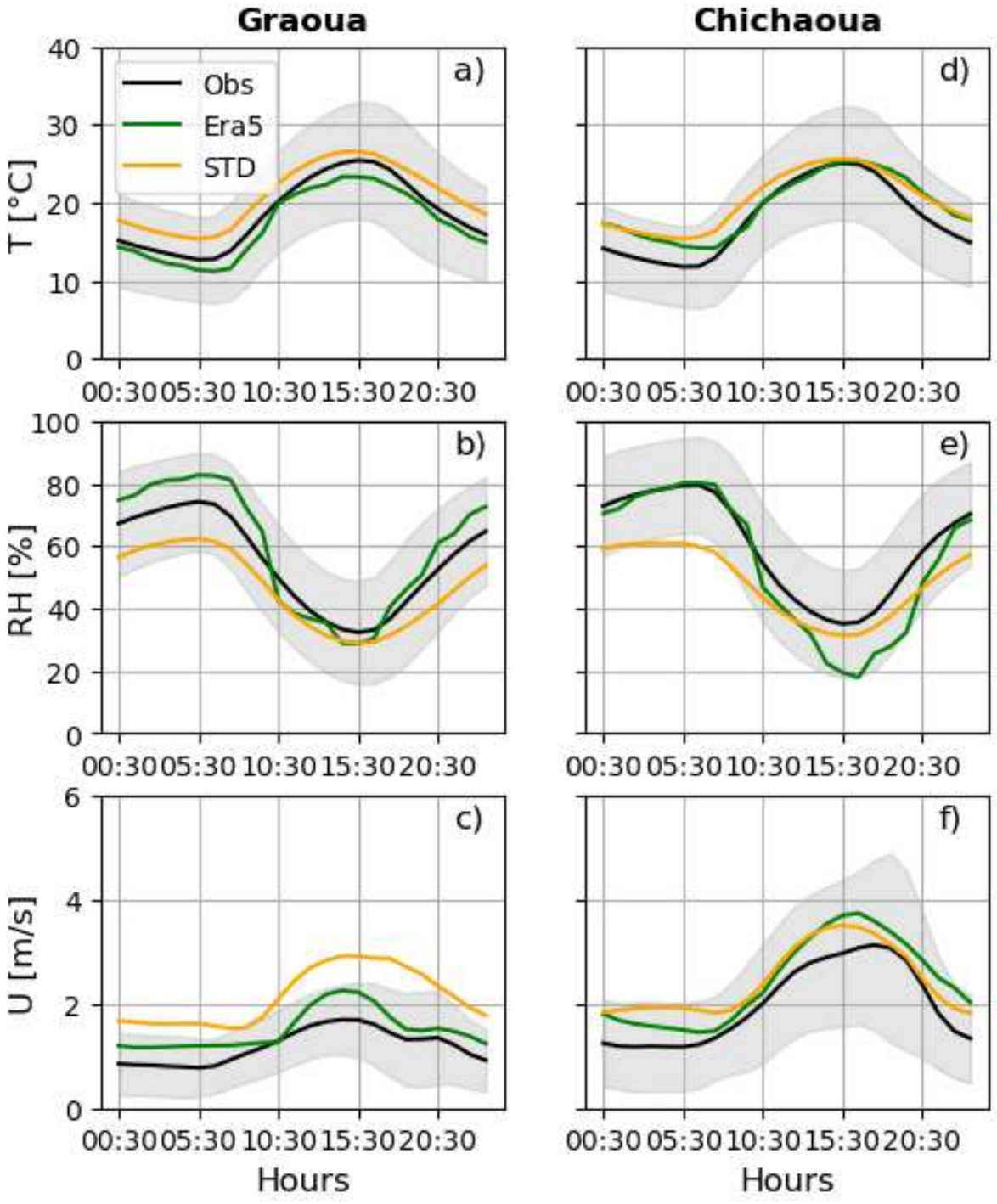

Figure 6.15: Mean diurnal cycle of T, RH and U over Graoua and Chichaoua stations. The black line shows observations, the orange line the standard simulation (STD) and the green one represents ERA5.

Appendix B: *Supporting information for "Future of land surface water availability over the Mediterranean basin and North Africa: analysis and synthesis from the CMIP6 exercise"*

A. Introduction

This supplementary completes the section 5.2 in chapter 5. The section B shows the supplementary Figures and tables, in which Table 6.1 lists the selected CMIP6 models and their corresponding CMIP5 versions used in the comparative study detailed in section 5.2.3.5. Figure 6.16 shows the future changes in the 100 km and 250 km annual total soil moisture (%) over the study region under the SSP5-8.5 and SSP2-4.5. Figures 6.17 show the future changes of precipitation, evapotranspiration, P-E surface and total soil moisture as simulated by the CMIP6 individual models. Models with 250km nominal resolution are marked with (*). Figure 6.18 shows future changes in the 100 km ensemble-mean during winter and summer under the scenario the SSP2-4.5. Figures 6.19 and 6.20 show the spatially-averaged mean annual changes under the SSP2-4.5 for P, E, P-E and surface soil moisture. And both SSP2-4.5 and SSP5-8.5 for total soil moisture. Figure 6.21 displays the studied region with the grid cells retained after the filtering procedure (more than 90% of the mesh is covered by land). Figure 6.22 shows an example of averaged spatial evapotranspiration flux over the study region when the mixed meshes are not filtered.

The section B explains the model selection procedure that consists of assessing the performances of the models in representing the large-scale atmospheric circulation.

B. Supplementary tables and figures

Table 6.1: List of CMIP6 and CMIP5 climate models used in the comparative study for each variable with their respective horizontal resolutions. A unique multimodel mean is calculated for each CMIP group independently of the models native resolutions.

CMIP6	Original horizontal resolution	CMIP5	Original horizontal resolution
CMCC-CM2-SR5	0.9° x 1.2°	CMCC-CM	0.75° x 0.75°
MPI-ESM1-2-HR	0.9° x 0.9°	MPI-ESM-MR	1.8° x 1.8°
MRI-ESM2-0	1.1° x 1.1°	MRI-ESM1	1° x 0.5°
NorESM2-MM	1.2° x 0.9°	NorESM1-M	2.5° x 1.9°
CNRM-CM6-1	1.4° x 1.4°	CNRM-CM5	1.4° x 1.4°
GISS-E2-1-G	2° x 2.5°	GISS-E2-R	2° x 2.5°
IPSL-CM6A-LR	2.5° x 1.3°	IPSL-CM5A-LR	2.5° x 1.3°
MIROC6	1.4° x 1.4°	MIROC5	1.4° x 1.4 °
MPI-ESM1-2-LR	1.9° x 1.9°	MPI-ESM-LR	1.8° x 1.8°

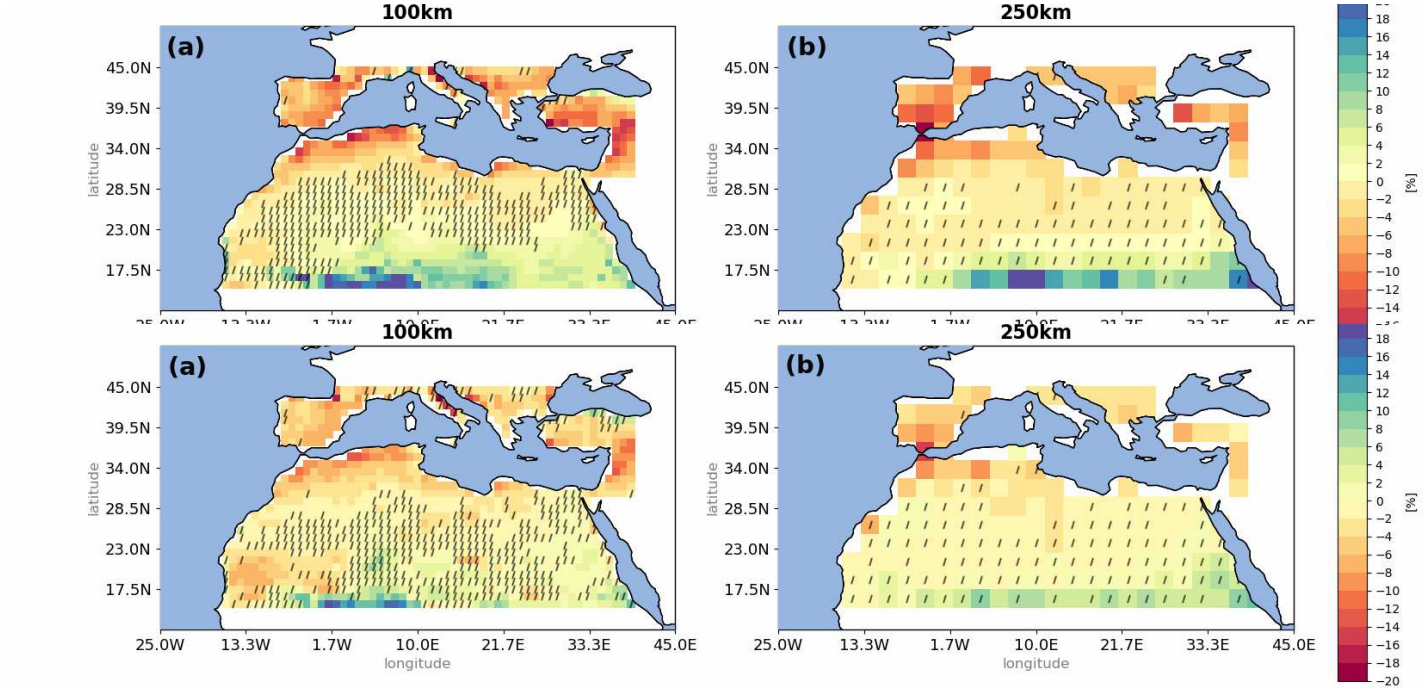

Figure 6.16: Figure S1: Similar as Fig. 1 but for the total soil moisture under SSP5-8.5 (top panels) and SSP2-4.5 (bottom) for both 100km (a) and 250km (b) resolution ensembles.

Figure 6.17: Individual models' future changes for P, E, P-E, surface and total soil moisture respectively from top to bottom, under the high-end emission scenario, 250km resolution models are marked with (*)

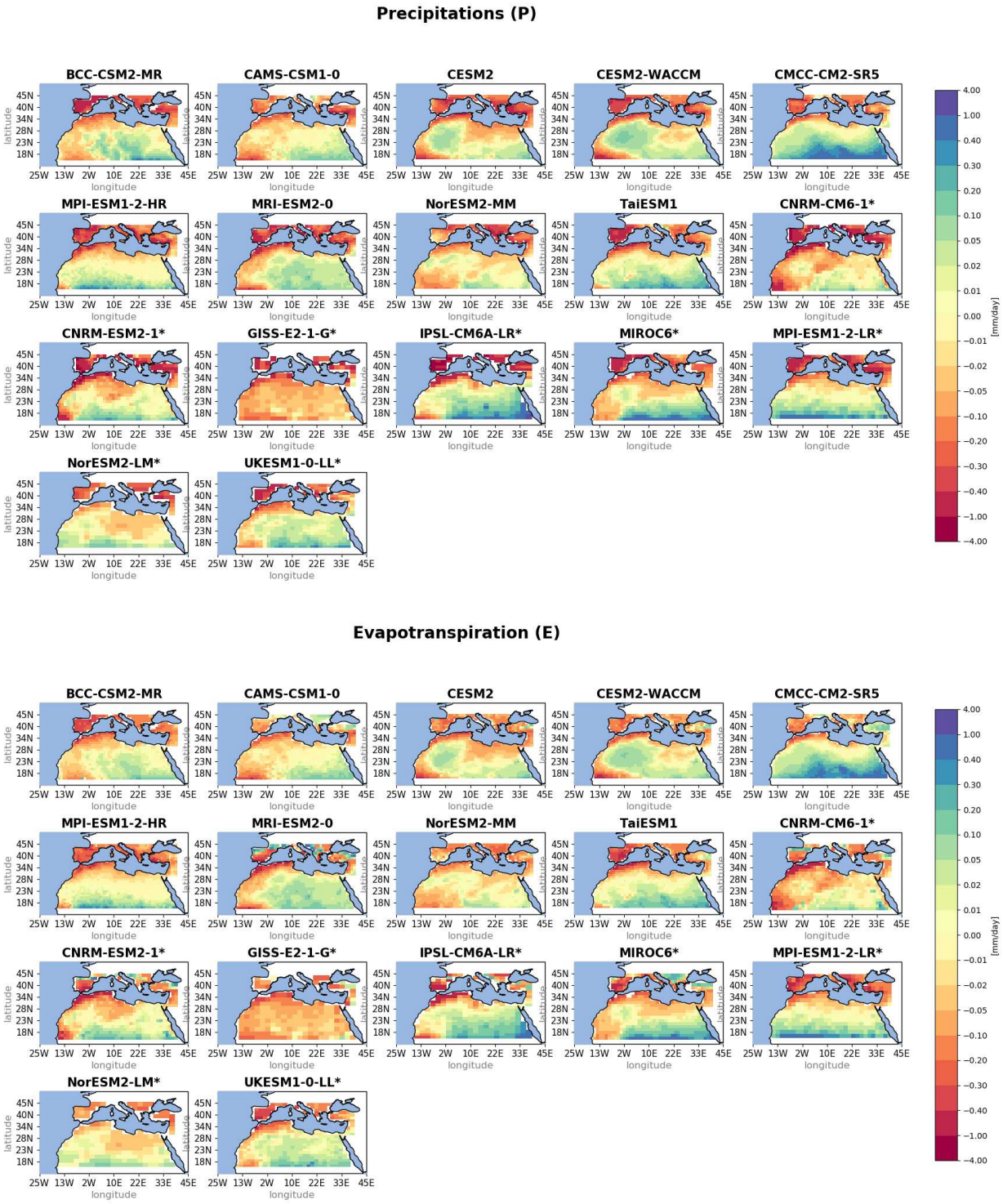

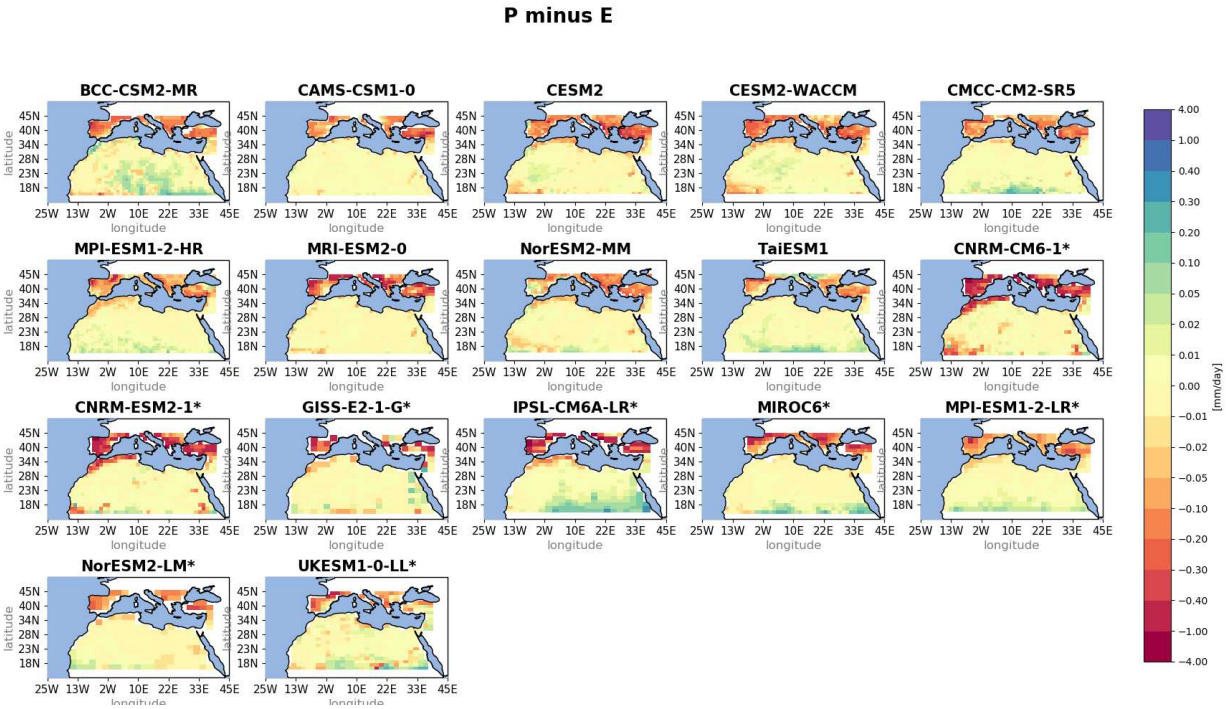
P minus E
BCC-CSM2-MR
CAMS-CSM1-0
CESM2
CESM2-WACCM
CMCC-CM2-SR5
MPI-ESM1-2-HR
MRI-ESM2-0
NorESM2-MM
TaiESM1
CNRM-CM6-1*
CNRM-ESM2-1*
GISS-E2-1-G*
IPSL-CM6A-LR*
MIROC6*
MPI-ESM1-2-LR*
NorESM2-LM*
UKESM1-0-LL*
latitude
longitude
45N 40N 34N 28N 23N 18N
25W 13W 2W 10E 22E 33E 45E
4.00 1.00 0.40 0.30 0.20 0.10 0.05 0.02 0.01 0.00 −0.01 −0.02 −0.05 −0.10 −0.20 −0.30 −0.40 −1.00 −4.00
[mm/day]

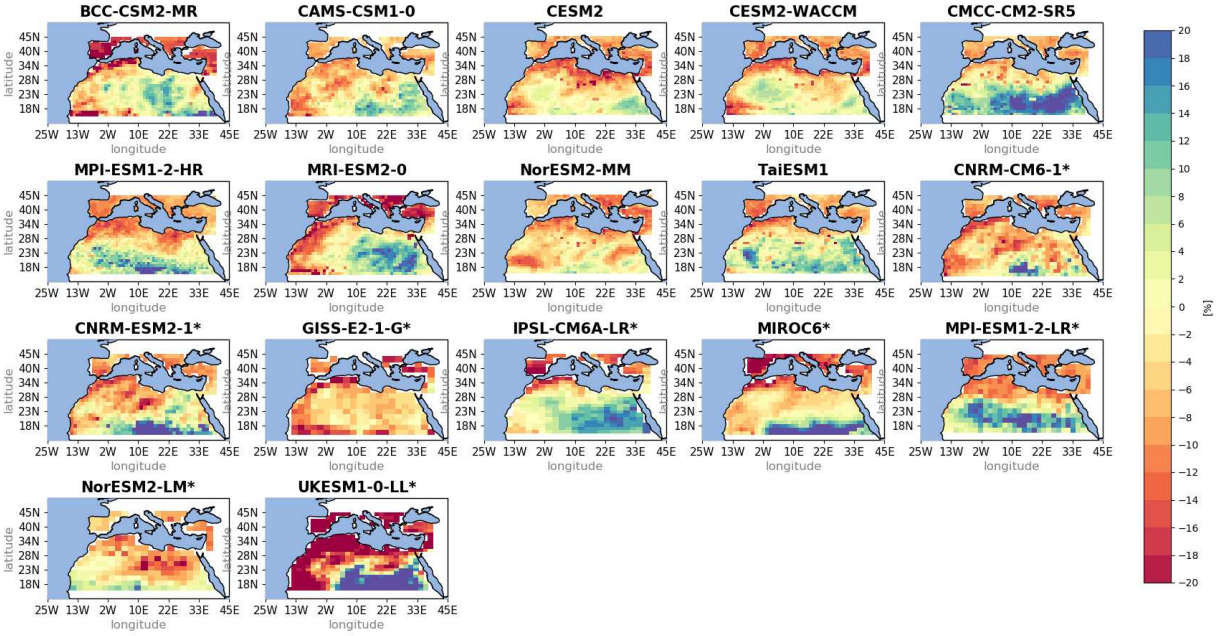
Surface soil moisture
BCC-CSM2-MR
CAMS-CSM1-0
CESM2
CESM2-WACCM
CMCC-CM2-SR5
MPI-ESM1-2-HR
MRI-ESM2-0
NorESM2-MM
TaiESM1
CNRM-CM6-1*
CNRM-ESM2-1*
GISS-E2-1-G*
IPSL-CM6A-LR*
MIROC6*
MPI-ESM1-2-LR*
NorESM2-LM*
UKESM1-0-LL*
latitude
longitude
45N 40N 34N 28N 23N 18N
25W 13W 2W 10E 22E 33E 45E
20 18 16 14 12 10 8 6 4 2 0 −2 −4 −6 −8 −10 −12 −14 −16 −18 −20
[%]

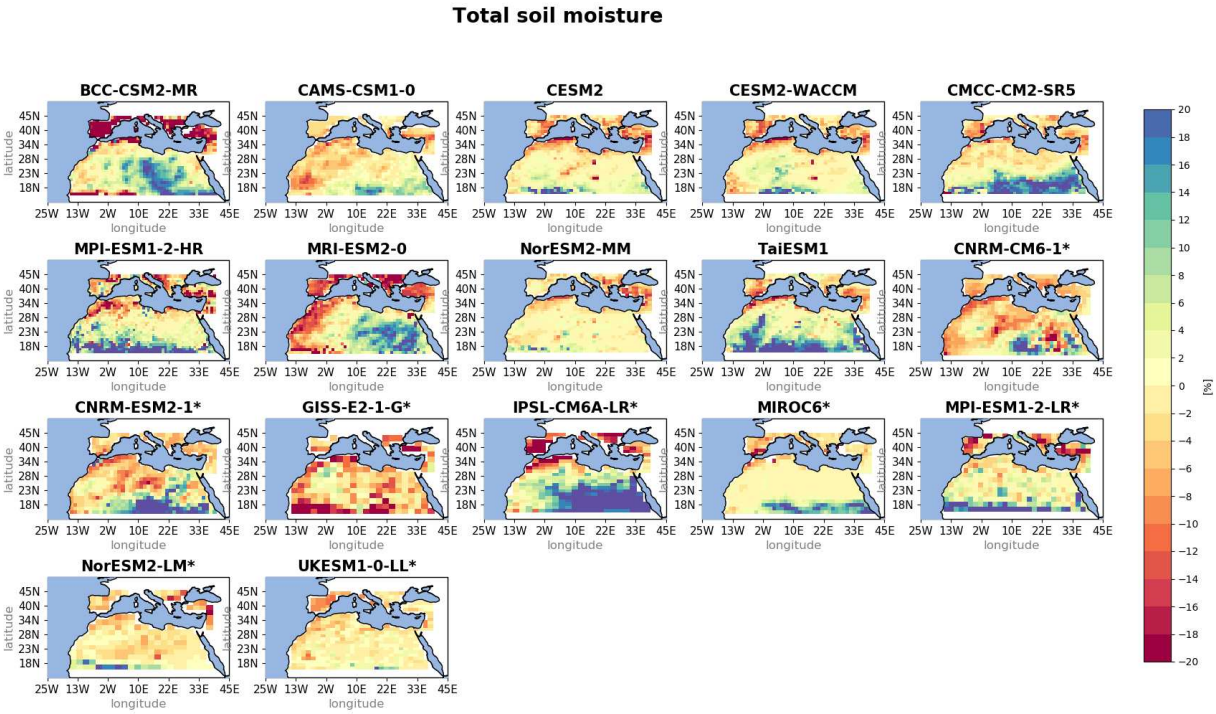
Total soil moisture
BCC-CSM2-MR
CAMS-CSM1-0
CESM2
CESM2-WACCM
CMCC-CM2-SR5
MPI-ESM1-2-HR
MRI-ESM2-0
NorESM2-MM
TaiESM1
CNRM-CM6-1*
CNRM-ESM2-1*
GISS-E2-1-G*
IPSL-CM6A-LR*
MIROC6*
MPI-ESM1-2-LR*
NorESM2-LM*
UKESM1-0-LL*
latitude
longitude
45N
40N
34N
28N
23N
18N
25W 13W 2W 10E 22E 33E 45E
20
18
16
14
12
10
8
6
4
2
0
−2
−4
−6
−8
−10
−12
−14
−16
−18
−20
[%]

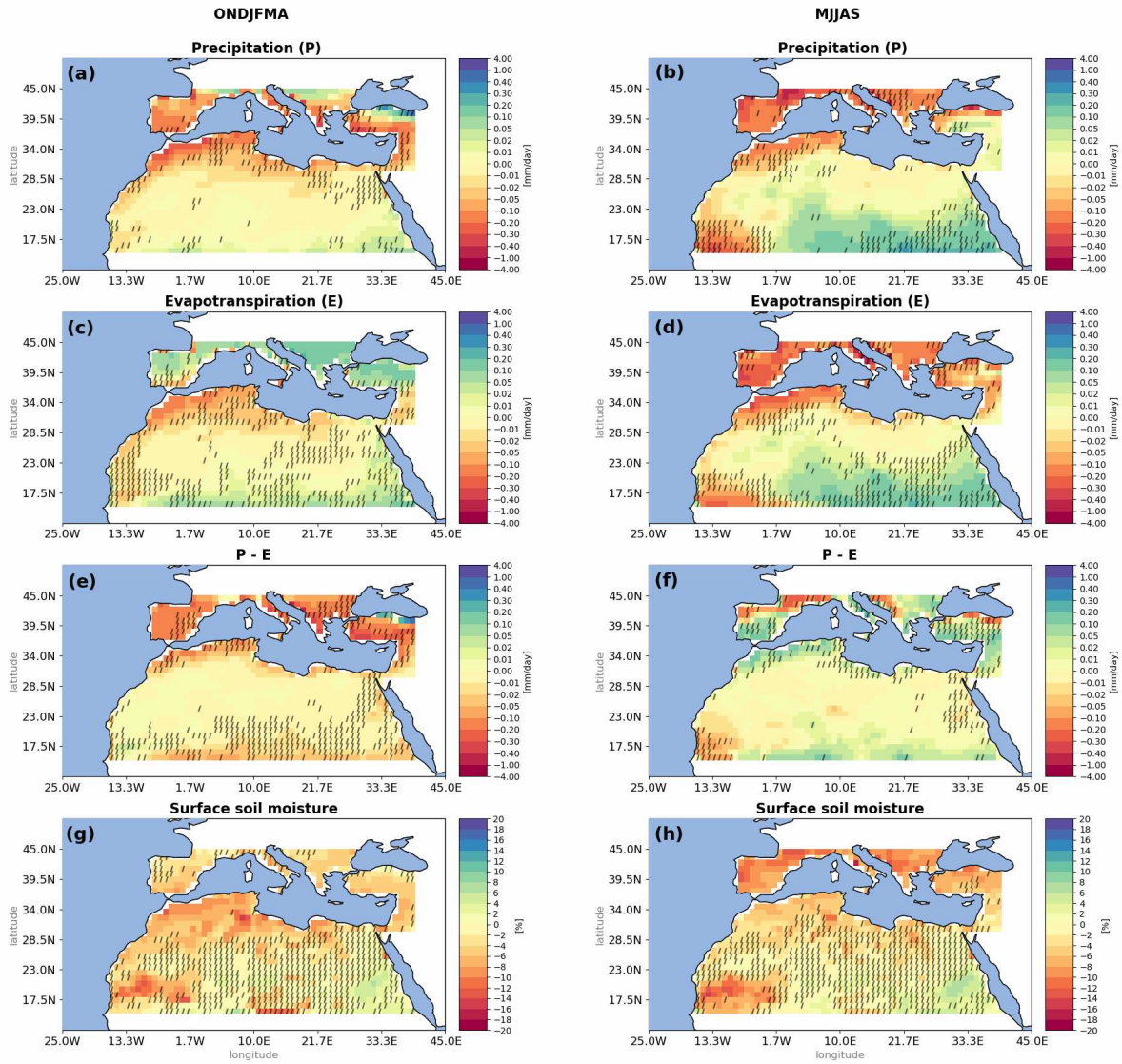

Figure 6.18: Future changes in the 100 km ensemble-mean during winter (left panel) and summer (right panel) of precipitation (mm day^{-1}), evapotranspiration (mm day^{-1}), P-E (mm day^{-1}) and surface soil moisture (%) over the Mediterranean basin and the Sahara under the SSP2-4.5 scenario for 2071–2100 with respect to 1981–2010. The slashes correspond to grid boxes exhibiting non robust changes based on the non-parametric Wilcoxon-Mann-Whitney test with a 95% threshold.

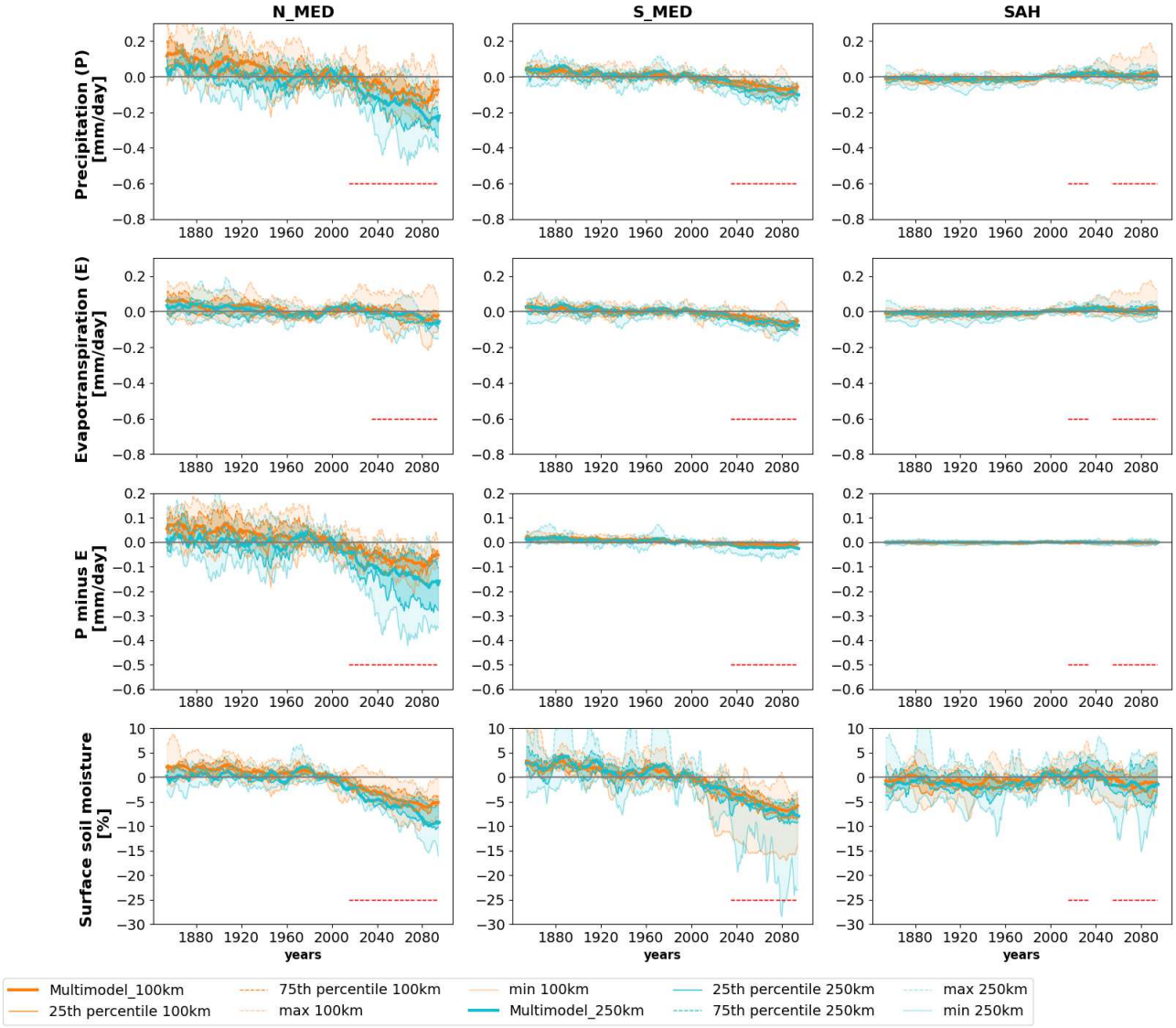

Figure 6.19: Spatially-averaged mean annual changes in precipitation (mm day^{-1}), evapotranspiration (mm day^{-1}), P-E (mm day^{-1}) and surface soil moisture (%) for the northern and southern Mediterranean (N_MED and S_MED) and Sahara (SAH) regions under the SSP2-4.5 scenario. Curves are constructed by subtracting, for each year in the period 1850 to 2100, the mean value for the baseline 1981-2010. Then, a 10-year running mean is applied to smooth the resulting time-series. Bold curves represent the MEM anomaly of the 100km (orange) and 250km (blue) resolutions, colour shadings show the envelope between the maximum and minimum values (light shading) and between the 25th and 90th percentiles (dark shading). In order to assess the significance of the discrepancies between the two different resolutions, we performed the Wilcoxon-Mann-Whitney to compare 100 and 250 km ensemble time series by dividing the future period into four sub-periods. The horizontal dotted red curves indicate the sub-periods where the test is significant at a 95% threshold.

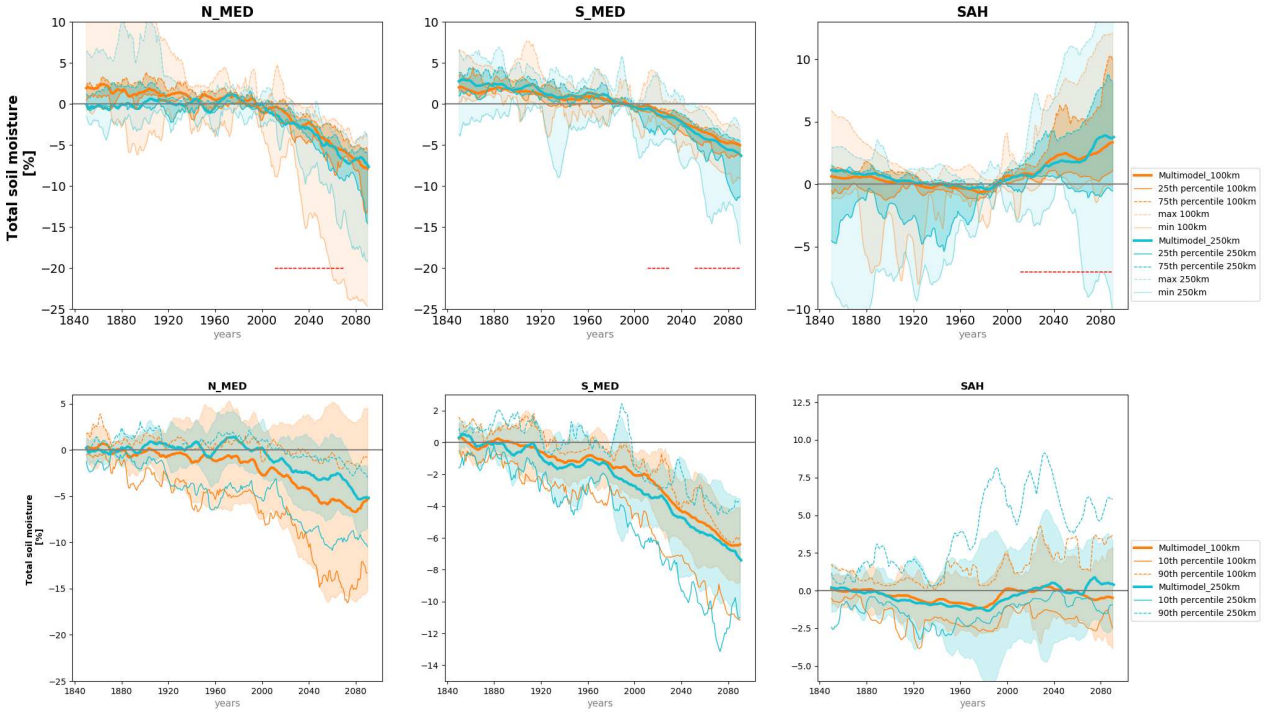

Figure 6.20: Same as Fig. S4 but for total soil moisture under the SSP5-8.5 (upper panel) and SSP2-4.5 (bottom).

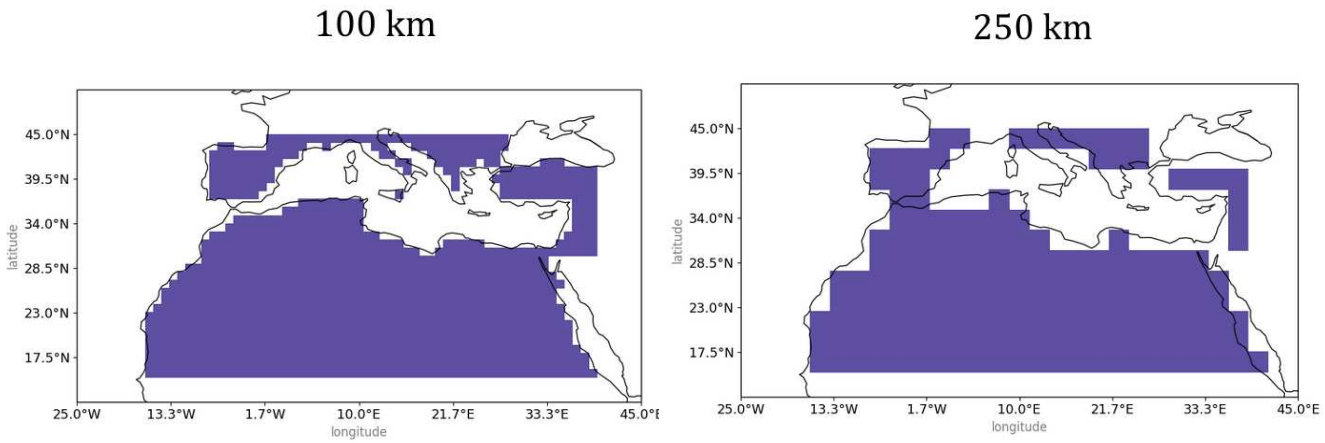

Figure 6.21: Map of the studied region showing the grid cells retained after the filtering procedure (more than 90% of the mesh is covered by land). Left panel shows the map for 100 km resolution models, right panel shows the map for 250 km (right panel) resolution models.

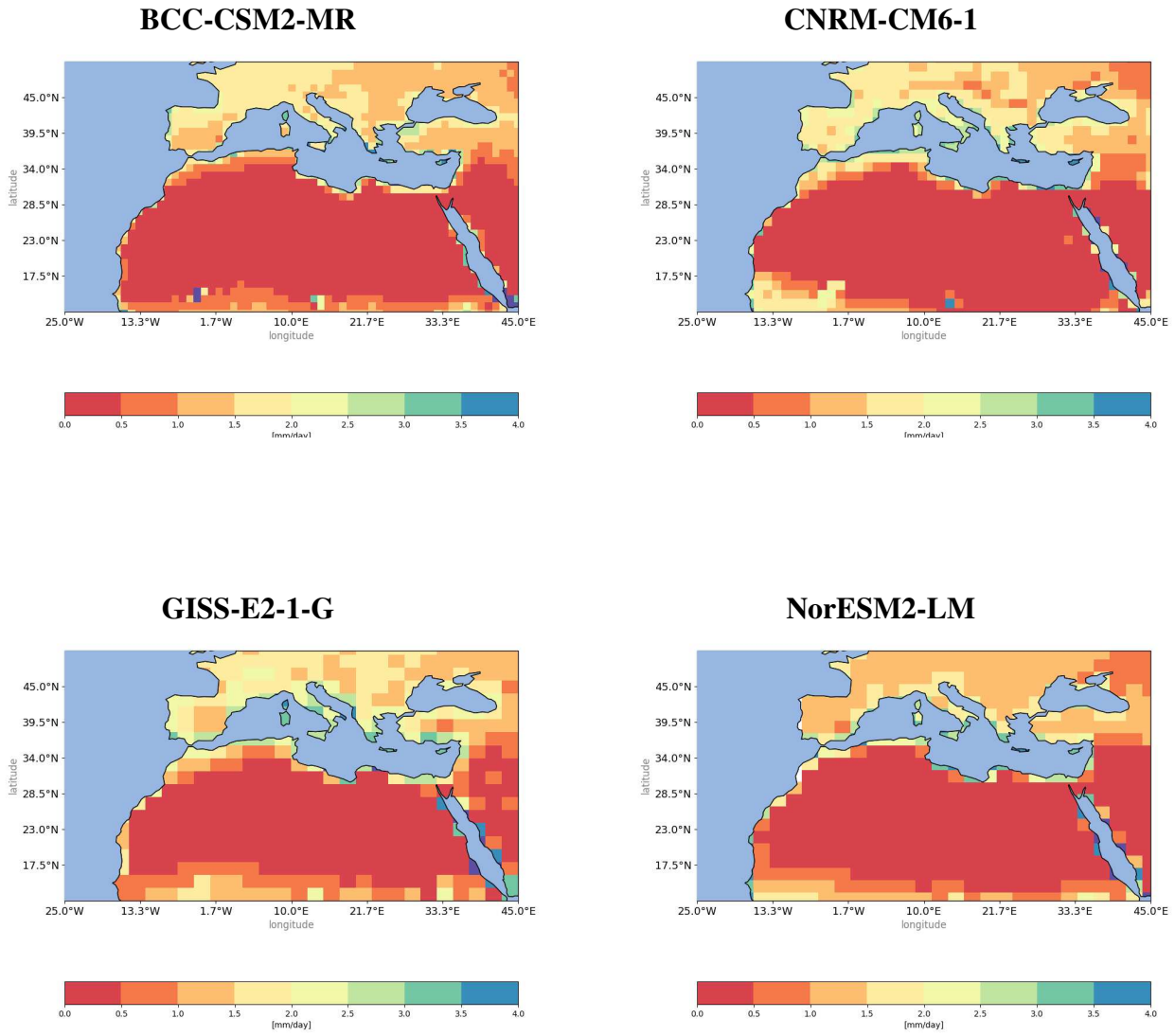

Figure 6.22: Averaged evapotranspiration flux (mm day^{-1}) during the historical period (1850-2014) for the models BCC-CSM2-MR, CNRM-CM6, GISS-E2-1-G and NorESM2-LM.

C. Model selection procedure

Following Agosta et al. (2015), we have assessed the ability of models to simulate the large-scale atmospheric circulation driving the climate over our region of interest using set of variables character-

izing the large-scale atmospheric circulation: 850 hPa air temperature (T850), 200 hPa and 700 hPa zonal wind (U200 and U700), 500 hPa geopotential height (Z500), sea surface temperature (SST) and sea level pressure (SLP). For each individual model, we have calculated the root mean squared error (RMSE) of the annual averaged variables during the historical period with respect to ERA5 reanalysis and normalised each metric by the median value over the 20-50N, 40W-20E longitude-latitude box which encompasses both SAH and MED regions.

The x-axis of the Figure lists the different models being compared, blue bars show the 100 km resolution models while the red bars represent the 250km resolution models. Additionally, results from ERA-Interim, JRA-55, NCEP-NCAR, and NCEP-DOE are also shown for comparison. The y-axis shows the normalized RMSE values for each of the variables being compared. Overall, results suggest that none of the models considered here outperforms or lies outside the others. Nonetheless the 100km resolution models generally perform better than the 250km resolution models, with lower normalized RMSE values for most of the variables.

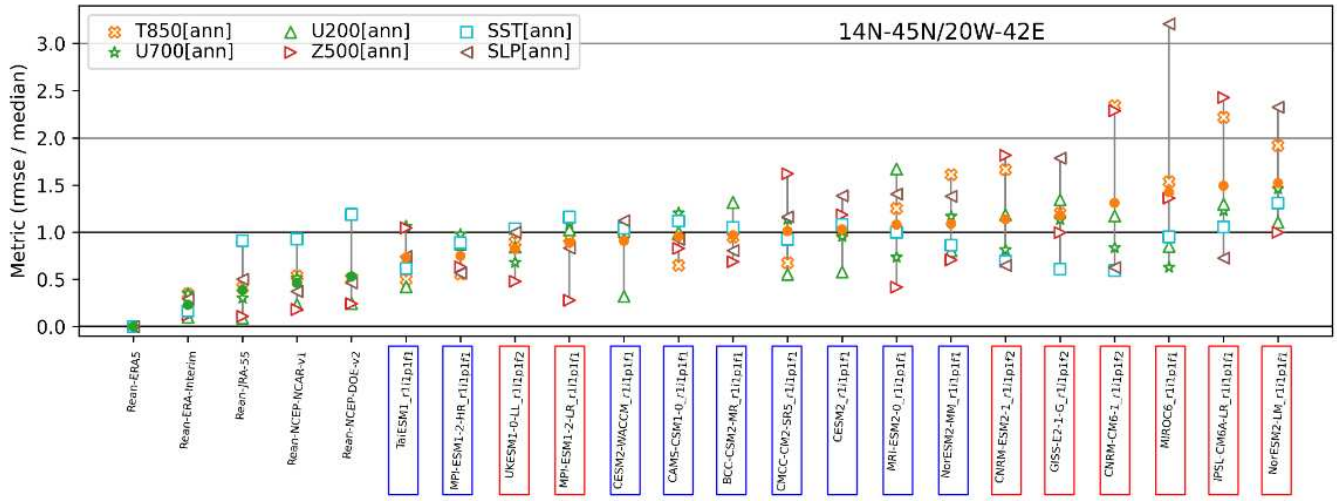

Figure 6.23: Normalised RMSE with respect to ERA5 reanalysis of the following large scale metrics: 850 hPa air temperature (T850), 200 hPa and 700 hPa zonal wind (U200 and U700), 500 hPa geopotential height (Z500), sea surface temperature (SST) and sea level pressure (SLP) of the studied models. 100km resolution models are outlined in blue colour and 250km in red colour. Results from ERA-Interim, JRA-55, NCEP-NCAR and NCEP-DOE reanalysis are also shown for comparison.

List of Figures

1.1 Figure Atlas 11 in IPCC (2021). Observed linear trends of signals in annual mean surface air temperature in the Berkeley Earth (**a**) and CRU TS dataset (**b**). Trends (°C per decade) correspond to 1961–2015 mean with respect to climatological period. Regions with non-significant trends (at a 0.1 significance level) are marked with crosses. The black outlines delimit the reference regions defined in Atlas.1. 12

1.2 Moroccan climate types according to the Koeppen-Geiger classification based on in-situ parameters covering the period 1981-2010. As the name of cities is barely visible, we indicate the location of Marrakech, Casablanca, Rabat, Agadir and Laayoune with the letters M, C, R, A and L respectively. (Adapted from D.G.M (2023)) 13

1.3 **a)** Spatially distributed average annual rainfall totals during the period 1991-2020. Time evolution of observed annual temperature (**b**) and precipitation (**c**) in Morocco. The red line represents the 1981-2010 average. (Adapted from D.G.M (2023))) . . . 14

1.4 Variations in annual rainfall (blue curve), snowfall (grey) and total (black) measured at the Oukaimden station (3239m altitude) in the High Atlas between 1988 and 2008. (Figure adapted from Boudhar (2010)). 15

1.5 Projected warming in the Mediterranean basin over land. Projected changes in annual temperature relative to the recent past reference period (1980-1999), based on the EURO-CORDEX 0.11° ensemble mean, **A**: simulations for pathways RCP2.6 and RCP8.5, **B**: warming at the end of the 21st century (2080-2099) for RCP2.6, **C**: idem for RCP8.5. (Figure SPM.2 in MedECC (2020)) 18

1.6 Schematic of land surface-atmosphere interactions. Blue arrows indicate a positive feedback that leads to an increase of the recipient variable, and red arrows indicate a negative one (Ochsner et al. (2013)) 20

1.7 Overview of the Root zone with the saturated and unsaturated soil layers (Seneviratne et al. (2010)) 21

2.1 Topography of the Haouz plain (the red border) within Tensift basin (black border) with piezometer, rain gauge and tower fluxes superimposed together with a map showing the groundwater decrease between 1972 and 2008 calculated from piezometic levels. (Figure from Le Page et al. (2012)) 25
2.2 Land use and land cover map of the Haouz Plain on 2011 issued from Landsat-5 TM satellite image (Figure from Ait El Mekki and Laftouhi (2016)) 25
2.3 Overview of the studied in situ sites location with satellite maps showing their position with respect to the agricultural fields. (Satellite maps from Google Earth) 27
2.4 Photograph of the sonic anemometer in Agafay **(a,b)**, R3 **(c)** and Agdal site **(d,e)** with an example of the the Time Domain Reflectometry instrument **(g)** planted at different soil depths **(f)** over the three sites (Copyright: LMI-TREMA). 28
2.5 Location and footprint of the EC system installed at Agdal station (corresponding to 95% of the sensible heat flux), with irrigation orientation. (Figure adapted from Ezzahar et al. (2007)) 29
2.6 Annual rainfall distribution in the catchments of Tensift basin between 1972 and 2000 (adapted from Boudhar (2010)) 31
2.7 Overview of the instrumented stations Chichawa (a), Aremd (b) and Grawa (c) (Figures from http://trema.ucam.ac.ma/Obs_TREMA) 32
2.8 Seasonal cycles of mean temperatures (curves) and cumulative rainfall (bars) at Chichaoua, Graoua, Aremd and Agafay stations between 2004 and 2020 33

3.1 The sub-surfaces treatment in LMDZ. (Figure from Vignon (2017)) 37
3.2 **a)**: Overview of the three soil tiles of the ORCHIDEE land surface model; 1: bare soil, 2: forests and 3: crops, the blue arrows indicate the main water balance fluxes in the surface. **b)**: the vertical discretization of the 2m soil into 11 layers with geometric distance between layers (from De Rosnay et al. (2002)) 41
3.3 Overview of the implemented LMDZ grid with 64x64 horizontal resolution and the grid refinement over the Haouz plain (right panel) 44

4.1 Map of the topography with a focus on the Haouz plain and the Atlas mountain range (inset). The black dots indicate the center of the model meshes. Black crosses show the location of the three main stations considered in this study, their corresponding model meshes are marked with red crosses. The location of the two additional stations Chichaoua and Graoua is indicated with purple crosses. 50
4.2 From left to right: Agafay, Agdal and R3 monitoring stations (Copyright: LMI-TREMA) 51
4.3 Overview of the ORCHIDEE default grid cell land cover (a) and the updated one consisting of 100% of Forest in Agdal and Agafay and Crops in R3. The percentage of each type of land cover in each station grid cell is listed in the table (b) as simulated by the model (left panel) and the adapted one (right panel). 55

4.4 Mean diurnal cycle of T, RH and U over Agdal, R3 and Agafay stations. The black line shows observations, the orange line the standard simulation (STD), the red line the control simulation (CTRL) and the green one represents ERA5. Shadings denote the variability over the measurement period for each station ($\pm\sigma$). Note that the mean and standard deviation are calculated for each hour over the full measurement period for each station. 58
4.5 Mean diurnal cycle of T, RH and U during winter (DJF) and summer (JJA) for 2006-2009 period at Agafay station. The black line shows observations, the orange line the standard simulation (STD), the red line the control simulation (CTRL) and the green one represents ERA5. Shadings denote the variability over the measurement period for each station ($\pm\sigma$). Note that the mean and standard deviation are calculated for each hour over the full measurement period for each station. 59
4.6 Wind speed distribution in observations (black hatches), STD (orange) and CTRL (red) simulations over Agdal (a), R3 (b) and Agafay (c) stations. 60
4.7 Average diurnal cycle of downward (SWdn) and upward (SWup) shortwave radiative fluxes, downward (LWdn) and upward (LWup) longwave radiation, the sensible (H) and latent heat fluxes (Le) and the ground heat flux (G) at Agdal (upper panel), R3 (middle panel) and Agafay (lower panel) stations. The left panel represents CTRL simulation and the right one represents observations. Fluxes are defined positive towards the surface. 61
4.8 Observed (black curves) and simulated (red curves) skin surface temperature (solid lines) in Agdal, R3 and Agafay stations. Shadings denote the variability over the measurement period for each station ($\pm\sigma$). Note that the mean and standard deviation are calculated for each hour over the full measurement period for each station. 62
4.9 Mean diurnal cycle of T (panel a), RH (b) and U (c), with near-surface vertical profiles of temperature over Agafay station at 01:30 LT (d). The black line shows observations, the red line the control simulation (CTRL), the blue line the simulation with prescribed z_0 (CTRL-z0) and the green one shows ERA5. 64
4.10 Soil moisture at 5 cm depth in R3 and Agafay stations grid cells for observations (black), ERA5 (green), CTRL (red) and CTRL-z0 (blue) simulation. The black arrows indicate the days with effective irrigation. 66
4.11 February 2003 evolution of Mean diurnal cycles of 2m temperature T, skin surface temperature Ts, Le, H, SWdn and RH in Agdal station from model simulations (CTRL-z0 in blue and CTRL-moist in brown), ERA5 (green) and observations (black). Note that the time in the Figures is in UTC time zone 67
4.12 Simplified schematisation of the implemented nudging parameterization where soil moisture is forced to SMs (blue arrows) when it decreases below a fraction x_1 of SM_s 71
4.13 Overview of the irrigated longitude latitude box (red polygon), with the three stations location in colored symbols. Black points indicate the model grid. 71

4.14 2006-2009 diurnal cycle composite of (panel **a**): latent (Le) and sensible (H) heat fluxes, **b**): mean diurnal cycles of 2m temperature (T), skin surface temperature (Ts), **c**): relative humidity (RH), **d**): downward (SWdn) and upward solar radiation (SWup), **e**): downward (LWdn) and upward longwave radiation (LWup), **f**): albedo, **g**): surface net radiation (Rn) and the ground heat flux (G) in Agafay station from model simulations (PRSNT in orange and PRSNT-Irr in blue) and observations (black). 74
4.15 Similar as Figure 4.14 but for Agdal station during the study period 2002-2004 . . . 75
4.16 Similar as Figure 4.14 but for R3 station during the study period 01/2003 - 05/2003 . 76
4.17 Soil moisture at 5 cm depth at R3, Agdal and Agafay stations grid cells for observations (black), PRSNT (blue) and PRSNT-Irr (orange) simulations. The average of each time series are shown at the top left of the Figure. 77
4.18 Monthly averaged transpiration (mm day^{-1}) over Agdal (red color), Agafay (orange) and R3 (green) during the 10-year simulaion 2002-2011. Solid lines correspond to the PRSNT configuration, dashed lines correspond to the PRSN-Irr. 77
4.19 Observed and simulated (PRSNT and PRSNT-Irr) monthly surface and air temperature, relative humidity and precipitation rate during the period 2006-2009 over Agafay 79
4.20 Monthly averaged precipitation rates (mm day^{-1}) over Agdal (red color), Agafay (orange) and R3 (green) during the 10-year simulaion 2002-2011. Solid lines correspond to the PRSNT configuration, dashed lines correspond to the PRSN-Irr. 80

5.1 Future changes in the 100 km ensemble-mean annual precipitation (mm day^{-1}), evapotranspiration (mm day^{-1}), P–E (mm day^{-1}), and surface soil moisture (%) over the Mediterranean basin and the Sahara under the SSP5-8.5 scenario for 2071–2100 with respect to 1981–2010. The slashes correspond to grid boxes exhibiting nonrobust changes based on the nonparametric Wilcoxon–Mann–Whitney test with a 95% threshold. 88
5.2 Same as Figure 5.1 but for the SSP2-4.5 scenario. 90
5.3 As Figure 5.1 but for the extended boreal winter (left panel) and summer (right panel) seasons under the SSP5-8.5 scenario. 91

5.4 Spatially-averaged mean annual changes in precipitation (mm day^{-1}), evapotranspiration (mm day^{-1}), P–E (mm day^{-1}), and surface soil moisture (%) for the Northern and Southern Mediterranean (N_MED and S_MED) and Sahara (SAH) regions under the SSP5-8.5 scenario. Curves are constructed by subtracting, for each year in the period 1850–2100, the mean value for the baseline 1981–2010. Then, a 10-year running mean is applied to smooth the resulting time series. Bold curves represent the multi-ensemble mean anomaly of the 100 km (orange) and 250 km (blue) resolutions, color shadings show the envelope between the maximum and minimum values (light shading) and between the 25th and 90th percentiles (dark shading). In order to assess the significance of the discrepancies between the two different resolutions, we performed the Wilcoxon–Mann–Whitney test to compare 100- and 250 km ensemble time series by dividing the future period into four sub-periods. The horizontal dotted red curves indicate the sub-periods where the test is significant at a 95% threshold. . 93

5.5 Mean future changes from the 100 km ensemble of annual surface air temperature (°C), precipitation (mm day^{-1}) and evapotranspiration (mm day^{-1}). Panels in the left column show the differences between the 2041–2070 and 1981–2010 periods for the SSP5-8.5 while those in the right column show the differences between the 2071–2100 and 1981–2010 periods for the SSP2-4.5. Hatches indicate grid boxes where the high-end and low-end changes are not statistically different based on the nonparametric Wilcoxon–Mann–Whitney with a 95% threshold. 95

5.6 Panel (a): CMIP6 minus CMIP5 model ensemble projection of mean annual precipitation change between 2071–2100 and 1981–2010. Backslashes indicate the grid boxes corresponding to statistically insignificant differences based on the non-parametric Wilcoxon–Mann–Whitney with a 95% threshold. The color shading in panel (b) qualitatively shows how the changes of precipitation projected by CMIP6 models compare with those from CMIP5 models. Dark red (respectively, dark blue) regions are where CMIP5 models predict a decrease or drying (respectively, increase or moistening) and for which CMIP6 models predict an even stronger decrease (respectively, increase) by the end of the century. Light red (respectively, light blue) regions are where the CMIP5 models ensemble projects a decrease or drying (respectively, increase or moistening) and where the CMIP6 models ensemble projects a less intense decrease (respectively, increase). Green pixels are regions where CMIP5 models project a decrease or drying and where CMIP6 models project an increase. 96

5.7 [Courtesy of F. Cheruy] Normalised RMSE with respect to ERA5 reanalysis of the following large scale metrics: 850 and 700 hPa air temperature (T850, T700), integrated water vapor (IWV), 700 and 200 hPa zonal wind (U700 and U200) and 500 hPa geopotential height (Z500) averaged annually (ann) or during winter (win) of CMIP6 models including IPSL-CM and the land-surface atmosphere LMDZ-ORCHIDEE. Results from ERA-Interim, JRA-55, NCEP-NCAR and NCEP-DOE reanalysis are also shown for comparison. 101

5.8 Annual average of precipitation (a), air temperature (b), maximum (c) and minimum (d) air temperature, and surface soil moisture (e) over Agdal (red curve), Agafay (orange) and R3 (green) during the PRSNT (2002-2011) and the FTR period (2082-2090) 103
5.9 Seasonal cycle of average precipitation (panel a), air temperature (b), relative humidity (c) latent heat flux (d), upward (e) and downward (f) longwave radiation, downward (g) and upward (h) solar radiation, at the three sites Agdal (red), Agafay (orange) and R3 (green) during the present period 2002-2011 (solid lines) and the future period 2082-2090 (dotted-dashed lines) 104
5.10 a,b): Average diurnal cycle of the sensible (H, solid lines) and latent heat fluxes (Le, dashed lines), (c,d) skin surface temperature minus air temperature (Ts-T) during the present period (left panel) and the future (right panel) over the three stations. Fluxes are defined negative towards the surface. 105
5.11 Monthly averaged Albedo against LAI during PRSNT (dottes) and FTR (stars) over Agdal (red), Agafay (orange) and R3 (green) 106
5.12 Annual average of evapotranspiration rate (a), volumetric soil moisture content at 6 cm (b) and precipitation rate (c) over Agdal (red), Agafay (orange) and R3 (green) during the present period (2002-2011) and the future period (2082-2090). Solid lines correspond to the PRSNT and FTR simulations, dashed lines correspond to their respective PRSNT-Irr and FTR-Irr simulations 107
5.13 Seasonal cycle of averaged LAI as simulated by FTR (dashed lines) and FTR-Irr (dotted-dashed lines) at the three sites Agdal (red), Agafay (orange) and R3 (green) . 108
5.14 Diurnal cycle of air temperature, skin surface temperature, relative humidity, wind speed, sensible and latent heat fluxes, shortwave upward radiation, albedo and longwave downward and upward radiation simulated during the PRSNT (black curve), PRSNT-Irr (green), FTR (brown) and FTR-Irr (blue) over R3 110
5.15 Similar as 5.14 but for Agdal 111

6.1 Overview of the studied in situ sites location with satellite maps showing their position with respect to the agricultural fields. (Satellite maps from Google Earth) 120
6.2 Overview of the irrigated longitude latitude box (red polygon), with the three stations location in colored symbols. Black points indicate the model grid. 121
6.3 Simplified schematisation of the implemented nudging parameterization where soil moisture is forced to SMs (blue arrows) when it decreases below a fraction x_1 of SM_s 121
6.4 Average diurnal cycle of T, RH and U during winter (DJF) and summer (JJA) for 2002-2004 period at Agdal station. The black line shows observations, the orange line the standard simulation (STD), the red line the control simulation (CTRL) and the green one represents ERA5. Vertical bars denote the standard deviation around the observations' average value. 122
6.5 Same as Fig. 6.1 but with the control simulation CTRL set with updated land cover (red curves) in R3 station. 123

6.6 Average diurnal cycle of downward (SWdn) and upward (SWup) solar radiation, downward (LWdn) and upward (LWup) longwave radiation, the sensible (H) and latent heat fluxes (Le) and the ground heat flux (G) at Agdal (upper panel), R3 (middle panel) and Agafay (lower panel) stations. The left panel represents STD simulation and the right one represents observations. We decide that by convention, fluxes are positive towards the surface. 124
6.7 Averaged daily cumulative convective precipitation in summer season (JJA) over the Haouz Plain. Contours indicate the ground elevation (m) and the red arrows indicate the station's location; from left to right: Agafay, Agdal and R3. 125
6.8 February 2003 evolution of soil moisture at 5cm depth in R3, Agdal and Agafay stations from model simulations (CTRL-z0 in blue and CTRL-moist in brown) and observations (black). The black arrow indicates the irrigated day. With the average soil moisture as simulated by both configurations (upper left). The observed soil moisture at Agafay station is not shown since the available dataset starts from 2006. . 126
6.9 February 2003 evolution of Mean diurnal cycles of 2m temperature T, skin surface temperature Ts, Le, H, SWdn and RH in R3 station from model simulations (CTRL-z0 in blue and CTRL-moist in brown), ERA5 (green) and observations (black). 127
6.10 February 2003 evolution of Mean diurnal cycles of 2m temperature T, skin surface temperature Ts, Le, H, SWdn and RH in Agafay station from model simulations (CTRL-z0 in blue and CTRL-moist in brown), ERA5 (green). Observations are not shown since the available dataset starts from 2006. 128
6.11 Average diurnal cycle of air temperature (T), relative humidity (RH) and wind speed (U) at R3 from model simulations (CTRL in red, CTRL-Txt in green). 129
6.12 Average diurnal cycle of downward (SWdn) and upward (SWup) shortwave radiative fluxes, downward (LWdn) and upward (LWup) longwave radiation, the sensible (H) and latent heat fluxes (Le) and the ground heat flux (G) at R3. The left and the middle panels represent CTRL-Txt and CTRL simulation respectively and the right one represents observations. Fluxes are defined positive towards the surface. 130
6.13 February 2003 evolution of Mean diurnal cycles of 2m temperature T, skin surface temperature Ts, Le, H, SWdn and RH in R3 station from model simulations (CTRL-z0 in blue, CTRL-moist in brown, CTRL-moist-Txt in pink), ERA5 (green) and observations (black). Note that the brown and pink lines are superimposed 131
6.14 Overview of the instrumented stations Graoua and Chichaoua (Figures from http://trema.ucam.ac.ma/Obs
6.15 Mean diurnal cycle of T, RH and U over Graoua and Chichaoua stations. The black line shows observations, the orange line the standard simulation (STD) and the green one represents ERA5. 133
6.16 Figure S1: Similar as Fig. 1 but for the total soil moisture under SSP5-8.5 (top panels) and SSP2-4.5 (bottom) for both 100km (a) and 250km (b) resolution ensembles. . . . 135

6.17 Individual models' future changes for P, E, P-E, surface and total soil moisture respectively from top to bottom, under the high-end emission scenario, 250km resolution models are marked with (*) 136
6.18 Future changes in the 100 km ensemble-mean during winter (left panel) and summer (right panel) of precipitation (mm day^{-1}), evapotranspiration (mm day^{-1}), P-E (mm day^{-1}) and surface soil moisture (%) over the Mediterranean basin and the Sahara under the SSP2-4.5 scenario for 2071–2100 with respect to 1981–2010. The slashes correspond to grid boxes exhibiting non robust changes based on the non-parametric Wilcoxon-Mann-Whitney test with a 95% threshold. 139
6.19 Spatially-averaged mean annual changes in precipitation (mm day^{-1}), evapotranspiration (mm day^{-1}), P-E (mm day^{-1}) and surface soil moisture (%) for the northern and southern Mediterranean (N_MED and S_MED) and Sahara (SAH) regions under the SSP2-4.5 scenario. Curves are constructed by subtracting, for each year in the period 1850 to 2100, the mean value for the baseline 1981-2010. Then, a 10-year running mean is applied to smooth the resulting time-series. Bold curves represent the MEM anomaly of the 100km (orange) and 250km (blue) resolutions, colour shadings show the envelope between the maximum and minimum values (light shading) and between the 25th and 90th percentiles (dark shading). In order to assess the significance of the discrepancies between the two different resolutions, we performed the Wilcoxon-Mann-Whitney to compare 100 and 250 km ensemble time series by dividing the future period into four sub-periods. The horizontal dotted red curves indicate the sub-periods where the test is significant at a 95% threshold. 140
6.20 Same as Fig. S4 but for total soil moisture under the SSP5-8.5 (upper panel) and SSP2-4.5 (bottom). 141
6.21 Map of the studied region showing the grid cells retained after the filtering procedure (more than 90% of the mesh is covered by land). Left panel shows the map for 100 km resolution models, right panel shows the map for 250 km (right panel) resolution models. 141
6.22 Averaged evapotranspiration flux (mm day^{-1}) during the historical period (1850-2014) for the models BCC-CSM2-MR, CNRM-CM6, GISS-E2-1-G and NorESM2-LM. . . 142
6.23 Normalised RMSE with respect to ERA5 reanalysis of the following large scale metrics: 850 hPa air temperature (T850), 200 hPa and 700 hPa zonal wind (U200 and U700), 500 hPa geopotential height (Z500), sea surface temperature (SST) and sea level pressure (SLP) of the studied models. 100km resolution models are outlined in blue colour and 250km in red colour. Results from ERA-Interim, JRA-55, NCEP-NCAR and NCEP-DOE reanalysis are also shown for comparison. 143

List of Tables

2.1 Characteristics of the in situ measurements in the three sites Agdal, Agafay and R3 . 30

3.1 List of the CMIP6 and CMIP5 models used in our study with the nominal resolution . 36
3.2 Prescribed roughness lengths for momentum and for heat per PFT 42

4.1 Characteristics of the in situ measurements in the three stations Agdal, Agafay and R3 51
4.2 Observed and simulated albedo and roughness height (median value and interquartile range in brackets). As z_{0m} spans several orders of magnitude, the median of z_{0m} is calculated as the median of the distribution of the logarithmic values i.e. the exponential of the median of $\log(z_{0m})$. 60
4.3 Median and interquartile values of thermal roughness length and sensible heat flux at 01:30 LT as simulated by STD, CTRL and CTRL-z0 configurations in Agafay station. As z_{0m} and z_{0h} span several orders of magnitude, their median is calculated as the median of the distribution of the logarithmic values i.e. the exponential of the median of $\log(z_{0m})$. 63
4.4 Observed and simulated annual and seasonal averaged precipitation at the three stations during the study periods. Note that no measurements for the JJA period are available at R3. 66

5.1 List and characteristics of CMIP6 models used in this study. 87
5.2 The simulated annual averaged Tsol, Tair, Tmax and Tmin [°C] in the PRSNT and FTR simulations, with their corresponding irrigated configurations in Agdal, Agafay and R3. Interquartile range in brackets. 108

6.1 List of CMIP6 and CMIP5 climate models used in the comparative study for each variable with their respective horizontal resolutions. A unique multimodel mean is calculated for each CMIP group independently of the models native resolutions. . . . 134

List of abbreviations

A
ABL: Atmospheric Boundary Layer.
AR5: Fifth Assessment Report from the IPCC.
AR6: Sixth Assessment Report from the IPCC.

C
CMIP5: Coupled Model Intercomparison Project Phase 5.
CMIP6: Coupled Model Intercomparison Project Phase 6.

D
DJF: Boreal winter.

E
E: Evapotranspiration.
ECMWF: European Centre for Medium-Range Weather Forecasts.
ERA5 ECMWF Reanalysis version 5.
ESM: Earth System Model.

G
GCM: General Circulation Model

H
H: Sensible heat flux.

I
IPSL: Institut de Pierre Simon Laplace, https://www.ipsl.fr/
IPCC: Intergovernmental Panel on Climate Change

ITCZ: Intertropical Convergence Zone.

J
JJA: Boreal summer.

L
LAI: Leaf Area Index.
Le: Latent heat flux.
LMD: Laboratoire de Météorologie Dynamique, http://www.lmd.jussieu.fr.
LMDZ: Laboratoire de Météorologie Dynamique-Zoom GCM, http://lmdz.lmd.jussieu.fr.
LMI-TREMA: Laboratoire Mixte International de Télédetection et Ressources en Eau en Méditerrannée semi Aride.
LW: Longwave Radiarion

M
MJJAS: Extended boreal summer (March-September).
MO: Monin-Obukhov

O
ORCHIDEE: ORganizing Carbon and Hydrology In Dynamics EcosystEm
ONDJFMA: Extended boreal winter (October-April)

R
Rn: Net Radiaion

S
ScenarioMIP: Scenario Model Intercomparison Project
SECHIBA: Schématisation des Echanges Hydriques à l'interface entre la Biosphère et l'Atmosphère.
SIC: Sea Ice Content.
SM: Soil Moisture.
SSP: Shared Socioeconomic Pathways.
SST: Sea Surface Temperature.
STOMATE: Saclay Toulouse Orsay Model for Analysis of Terrestrial Ecosytems.
SW: Shortwave Radiation

T
T: Air temperature.
Ts: Skin surface temperature

Bibliography

Abourida, A., Simonneaux, V., Sadik, E., Brahim, B., and Fathallah, S. (2009). Estimation des volumes d'eau pompés dans la nappe pour l'irrigation (plaine du Haouz, Marrakech, Maroc). Comparaison d'une méthode statistique et d'une méthode basée sur l'utilisation de la télédétection. *Revue des sciences de l'eau*, 22(1):1–13.

Agosta, C., Fettweis, X., and Datta, R. (2015). Evaluation of the CMIP5 models in the aim of regional modelling of the Antarctic surface mass balance. *The Cryosphere*, 9(6):2311–2321.

Agoumi, A. and DEBBARH, A. (2006). Ressources en eau et bassins versants du Maroc . 50 ans de développement (1955-2005). Technical report.

Ait El Mekki, O. and Laftouhi, N.-E. (2016). Combination of a geographical information system and remote sensing data to map groundwater recharge potential in arid to semi-arid areas: the Haouz Plain, Morocco. *Earth Science Informatics*, 9(4):465–479.

Ait Hssaine, B. (2019). *Spatialisation des flux d'énergie et d'eau : combinaison de la modélisation des échanges de surface-atmosphère et de la télédétection optique, thermique et micro-ondes*. PhD thesis, Université Toulouse 3 - Paul Sabatier; Université Cadi Ayyad Marrakech.

Ali, E., Cramer, W., Carnicer, J., Georgopoulou, E., Hilmi, N., Le Cozannet, G., and Lionello, P. (2022). Cross-Chapter Paper 4: Mediterranean Region. In: Climate Change 2022: Impacts, Adaptation and Vulnerability. Contribution of Working Group II to the Sixth Assessment Report of the Intergovernmental Panel on Climate Change [H.-O. Pörtner, D.C. Roberts, M. Tignor, E.S. Poloczanska, K. Mintenbeck, A. Alegría, M. Craig, S. Langsdorf, S. Löschke, V. Möller, A. Okem, B. Rama (eds.)]. Technical report, Cambridge 632 University Press, Cambridge, UK and New York, NY, USA.

Almazroui, M., Saeed, F., Saeed, S., Nazrul Islam, M., Ismail, M., Klutse, N. A. B., and Siddiqui, M. H. (2020). Projected Change in Temperature and Precipitation Over Africa from CMIP6. *Earth Systems and Environment*, 4(3):455–475.

Ameur, F., Kuper, M., Lejars, C., and Dugué, P. (2017). Prosper, survive or exit: Contrasted fortunes of farmers in the groundwater economy in the Saiss plain (Morocco). *Agricultural Water Management*, 191:207–217.

Arboleda-Obando, P. F. (2023). *Feedback from groundwater and irrigation on past and future climate simulated by the IPSL climate model*. Hydrology, Sorbonne Université.

Arboleda-Obando, P. F., Ducharne, A., Yin, Z., and Ciais, P. (2023). Validation of a new global irrigation scheme in the land surface model ORCHIDEE v2.2. preprint, Hydrology.

Arjdal, K., Driouech, F., Vignon, , Chéruy, F., Manzanas, R., Drobinski, P., Chehbouni, A., and Idelkadi, A. (2023). Future of land surface water availability over the Mediterranean basin and North Africa: Analysis and synthesis from the CMIP6 exercise. *Atmospheric Science Letters*, page e1180.

Ashfaq, M., Rastogi, D., Mei, R., Kao, S.-C., Gangrade, S., Naz, B. S., and Touma, D. (2016). High-resolution ensemble projections of near-term regional climate over the continental United States: CLIMATE PROJECTIONS OVER THE U.S. *Journal of Geophysical Research: Atmospheres*, 121(17):9943–9963.

Avissar, R. and Liu, Y. (1996). Three-dimensional numerical study of shallow convective clouds and precipitation induced by land surface forcing. *Journal of Geophysical Research: Atmospheres*, 101(D3):7499–7518.

Aït-Mesbah, S., Dufresne, J. L., Cheruy, F., and Hourdin, F. (2015). The role of thermal inertia in the representation of mean and diurnal range of surface temperature in semiarid and arid regions. *Geophysical Research Letters*, 42(18):7572–7580.

Babaousmail, H., Hou, R., Ayugi, B., Ojara, M., Ngoma, H., Karim, R., Rajasekar, A., and Ongoma, V. (2021). Evaluation of the Performance of CMIP6 Models in Reproducing Rainfall Patterns over North Africa. *Atmosphere*, 12(4):475.

Bahir, M., Ouhamdouch, S., Ouazar, D., and El Moçayd, N. (2020). Climate change effect on groundwater characteristics within semi-arid zones from western Morocco. *Groundwater for Sustainable Development*, 11:100380.

Balhane, S., Driouech, F., Chafki, O., Manzanas, R., Chehbouni, A., and Moufouma-Okia, W. (2021). Changes in mean and extreme temperature and precipitation events from different weighted multi-model ensembles over the northern half of Morocco. *Climate Dynamics*.

Bayram, H. and Öztürk, A. (2014). Global Climate Change, Desertification, and Its Consequences in Turkey and the Middle East. In *Pinkerton, K.E., Rom, W.N. (eds) Climate Change and Global Public Health*, Respiratory Medicine. Humana, Cham.

Bağçaci, S. , Yucel, I., Duzenli, E., and Yilmaz, M. T. (2021). Intercomparison of the expected change in the temperature and the precipitation retrieved from CMIP6 and CMIP5 climate projections: A Mediterranean hot spot case, Turkey. *Atmospheric Research*, 256:105576.

Beaumet, J., Krinner, G., Déqué, M., Haarsma, R., and Li, L. (2019). Assessing bias corrections of oceanic surface conditions for atmospheric models. *Geoscientific Model Development*, 12(1):321–342. Publisher: Copernicus GmbH.

Behnassi, M., Barjees Baig, M., El Haiba, M., and Reed, M. R., editors (2021). *Emerging Challenges to Food Production and Security in Asia, Middle East, and Africa: Climate Risks and Resource Scarcity*. Springer International Publishing, Cham.

Bell, B. A., Hughes, P. D., Fletcher, W. J., Cornelissen, H. L., Rhoujjati, A., Hanich, L., and Braithwaite, R. J. (2022). Climate of the Marrakech High Atlas, Morocco: Temperature lapse rates and precipitation gradient from piedmont to summits. *Arctic, Antarctic, and Alpine Research*, 54(1):78–95.

Berg, A., Findell, K., Lintner, B., Giannini, A., Seneviratne, S. I., Van Den Hurk, B., Lorenz, R., Pitman, A., Hagemann, S., Meier, A., Cheruy, F., Ducharne, A., Malyshev, S., and Milly, P. C. D. (2016). Land–atmosphere feedbacks amplify aridity increase over land under global warming. *Nature Climate Change*, 6(9):869–874.

Berg, A. and Sheffield, J. (2019). Historic and Projected Changes in Coupling Between Soil Moisture and Evapotranspiration (ET) in CMIP5 Models Confounded by the Role of Different ET Components. *Journal of Geophysical Research: Atmospheres*, 124(11):5791–5806.

Betts, A. K. (2007). Coupling of water vapor convergence, clouds, precipitation, and land-surface processes: LAND-SURFACE-CLOUD PROCESSES. *Journal of Geophysical Research: Atmospheres*, 112(D10).

Betts, A. K., Ball, J. H., Beljaars, A. C. M., Miller, M. J., and Viterbo, P. A. (1996). The land surface-atmosphere interaction: A review based on observational and global modeling perspectives. *Journal of Geophysical Research: Atmospheres*, 101(D3):7209–7225.

Born, K., Fink, A. H., and Knippertz, P. (2010). I-5.2 Meteorological processes influencing the weather and climate of Morocco. page 15.

Born, K., Fink, A. H., and Paeth, H. (2008). Dry and wet periods in the northwestern Maghreb for present day and future climate conditions. *Meteorologische Zeitschrift*, 17(5):533–551.

Botta, A., Viovy, N., Ciais, P., Friedlingstein, P., and Monfray, P. (2000). A global prognostic scheme of leaf onset using satellite data: GLOBAL PROGNOSTIC SCHEME OF LEAF ONSET. *Global Change Biology*, 6(7):709–725.

Boucher, O., Myhre, G., and Myhre, A. (2004). Direct human influence of irrigation on atmospheric water vapour and climate. *Climate Dynamics*, 22(6-7):597–603.

Boucher, O., Servonnat, J., Albright, A. L., Aumont, O., Balkanski, Y., Bastrikov, V., Bekki, S., Bonnet, R., Bony, S., Bopp, L., Braconnot, P., Brockmann, P., Cadule, P., Caubel, A., Cheruy, F., Codron, F., Cozic, A., Cugnet, D., D'Andrea, F., Davini, P., de Lavergne, C., Denvil, S., Deshayes, J., Devilliers, M., Ducharne, A., Dufresne, J.-L., Dupont, E., Éthé, C., Fairhead, L., Falletti, L., Flavoni, S., Foujols, M.-A., Gardoll, S., Gastineau, G., Ghattas, J., Grandpeix, J.-Y., Guenet, B., Guez, Lionel, E., Guilyardi, E., Guimberteau, M., Hauglustaine, D., Hourdin, F., Idelkadi, A., Joussaume, S., Kageyama, M., Khodri, M., Krinner, G., Lebas, N., Levavasseur, G., Lévy, C., Li, L., Lott, F., Lurton, T., Luyssaert, S., Madec, G., Madeleine, J.-B., Maignan, F., Marchand, M., Marti, O., Mellul, L., Meurdesoif, Y., Mignot, J., Musat, I., Ottlé, C., Peylin, P., Planton, Y., Polcher, J., Rio, C., Rochetin, N., Rousset, C., Sepulchre, P., Sima, A., Swingedouw, D., Thiéblemont, R., Traore, A. K., Vancoppenolle, M., Vial, J., Vialard, J., Viovy, N., and Vuichard, N. (2020). Presentation and Evaluation of the IPSL-CM6A-LR Climate Model. *Journal of Advances in Modeling Earth Systems*, 12(7):e2019MS002010. _eprint: https://onlinelibrary.wiley.com/doi/pdf/10.1029/2019MS002010.

Boudhar, A. (2010). *Long-term analysis of snow-covered area in the Moroccan High-Atlas through remote sensing*. PhD thesis.

Boudhar, A., Duchemin, B., Hanich, L., Jarlan, L., Chaponnière, A., Maisongrande, P., Boulet, G., and Chehbouni, A. (2010). Long-term analysis of snow-covered area in the Moroccan High-Atlas through remote sensing. *International Journal of Applied Earth Observation and Geoinformation*, 12:S109–S115.

Bouramdane, A.-A. (2022). Assessment of CMIP6 Multi-Model Projections Worldwide: Which Regions Are Getting Warmer and Are Going through a Drought in Africa and Morocco? What Changes from CMIP5 to CMIP6? *Sustainability*, 15(1):690.

Brogli, R., Sørland, S. L., Kröner, N., and Schär, C. (2019). Causes of future Mediterranean precipitation decline depend on the season. *Environmental Research Letters*, 14(11):114017.

Byrne, M. P. and O'Gorman, P. A. (2015). The Response of Precipitation Minus Evapotranspiration to Climate Warming: Why the "Wet-Get-Wetter, Dry-Get-Drier" Scaling Does Not Hold over Land*. *Journal of Climate*, 28(20):8078–8092.

Campoy, A., Ducharne, A., Cheruy, F., Hourdin, F., Polcher, J., and Dupont, J. C. (2013). Response of land surface fluxes and precipitation to different soil bottom hydrological conditions in a general circulation model: BOTTOM HYDROLOGICAL CONDITIONS IN A GCM. *Journal of Geophysical Research: Atmospheres*, 118(19):10,725–10,739.

Casado-Lopez, A. and Li, L. (2009). Heat fluxes at the Mediterranean sea surface and the relation to the atmospheric large-scale dynamics with a regional coupled model. *9th EMS Annual Meeting, 9th European Conference on Applications of Meteorology (ECAM) Abstracts*.

Cavicchia, L., Scoccimarro, E., Gualdi, S., Marson, P., Ahrens, B., Berthou, S., Conte, D., Dell'Aquila, A., Drobinski, P., Djurdjevic, V., Dubois, C., Gallardo, C., Li, L., Oddo, P., Sanna, A., and Torma, C. (2018). Mediterranean extreme precipitation: a multi-model assessment. *Climate Dynamics*, 51(3):901–913.

CESE (2014). Conseil Economique, Social et Environnemental (CESE). Rapport annuel de 2014. Retrieved from: www.cese.ma. Technical report.

CESE (2021). Conseil Economique, Social et Environnemental (CESE). Rapport annuel de 2021. Retrieved from: www.cese.ma. Technical report.

Chehbouni, A., Escadafal, R., Dedieu, G., Errouane, S., Boulet, G., Duchemin, B., Mougenot, B., Sminonneaux, V., Seghieri, J., and Timouk, F. (2003). A multidisciplinary program for assessing the sustainability of water resources in semi-arid basin in Morocco: SUDMED. page 14229. Conference Name: EGS - AGU - EUG Joint Assembly ADS Bibcode: 2003EAEJA....14229C.

Chehbouni, A., Escadafal, R., Duchemin, B., Boulet, G., Simonneaux, V., Dedieu, G., Mougenot, B., Khabba, S., Kharrou, H., Maisongrande, P., Merlin, O., Chaponnière, A., Ezzahar, J., Er-Raki, S., Hoedjes, J., Hadria, R., Abourida, A., Cheggour, A., Raibi, F., Boudhar, A., Benhadj, I., Hanich, L., Benkaddour, A., Guemouria, N., Chehbouni, A. H., Lahrouni, A., Olioso, A., Jacob, F., Williams, D. G., and Sobrino, J. A. (2008). An integrated modelling and remote sensing approach for hydrological study in arid and semi-arid regions: the SUDMED Programme. *International Journal of Remote Sensing*, 29(17-18):5161–5181.

Chen, H., Sun, J., Lin, W., and Xu, H. (2020). Comparison of CMIP6 and CMIP5 models in simulating climate extremes. *Science Bulletin*, 65(17):1415–1418.

Cherchi, A., Fogli, P. G., Lovato, T., Peano, D., Iovino, D., Gualdi, S., Masina, S., Scoccimarro, E., Materia, S., Bellucci, A., and Navarra, A. (2019). Global Mean Climate and Main Patterns of Variability in the CMCC-CM2 Coupled Model. *Journal of Advances in Modeling Earth Systems*, 11(1):185–209. _eprint: https://onlinelibrary.wiley.com/doi/pdf/10.1029/2018MS001369.

Cherif, S., Doblas-Miranda, E., Lionello, P., Borrego, C., Giorgi, F., Iglesias, A., Jebari, S., Moriondo, M., Pringault, O., Rilov, G., Somot, S., Tsikliras, A., Vilà, M., and Zittis, G. (2020). Drivers of Change. Technical report.

Cheruy, F. (2018). Etude par modélisation des interactions surface-atmosphère à l'échelle globale.

Cheruy, F., Campoy, A., Dupont, J.-C., Ducharne, A., Hourdin, F., Haeffelin, M., Chiriaco, M., and Idelkadi, A. (2013). Combined influence of atmospheric physics and soil hydrology on the simulated meteorology at the SIRTA atmospheric observatory. *Climate Dynamics*, 40(9-10):2251–2269.

Cheruy, F., Ducharne, A., Hourdin, F., Musat, I., Vignon, , Gastineau, G., Bastrikov, V., Vuichard, N., Diallo, B., Dufresne, J., Ghattas, J., Grandpeix, J., Idelkadi, A., Mellul, L., Maignan, F.,

Ménégoz, M., Ottlé, C., Peylin, P., Servonnat, J., Wang, F., and Zhao, Y. (2020). Improved Near-Surface Continental Climate in IPSL-CM6A-LR by Combined Evolutions of Atmospheric and Land Surface Physics. *Journal of Advances in Modeling Earth Systems*, 12(10).

Cheruy, F., Dufresne, J. L., Aït Mesbah, S., Grandpeix, J. Y., and Wang, F. (2017). Role of Soil Thermal Inertia in Surface Temperature and Soil Moisture-Temperature Feedback: SOIL MOISTURE TEMPERATURE FEEDBACK. *Journal of Advances in Modeling Earth Systems*, 9(8):2906–2919.

Choukri, F., Raclot, D., Naimi, M., Chikhaoui, M., Nunes, J. P., Huard, F., Hérivaux, C., Sabir, M., and Pépin, Y. (2020). Distinct and combined impacts of climate and land use scenarios on water availability and sediment loads for a water supply reservoir in northern Morocco. *International Soil and Water Conservation Research*, 8(2):141–153.

Chéruy, F. and Aires, F. (2009). Cluster Analysis of Cloud Properties over the Southern European Mediterranean Area in Observations and a Model. *Monthly Weather Review*, 137(10):3161–3176. Publisher: American Meteorological Society Section: Monthly Weather Review.

Coindreau, O., Hourdin, F., Haeffelin, M., Mathieu, A., and Rio, C. (2007). Assessment of Physical Parameterizations Using a Global Climate Model with Stretchable Grid and Nudging. *Monthly Weather Review*, 135(4):1474–1489.

Cook, B. I., Mankin, J. S., Marvel, K., Williams, A. P., Smerdon, J. E., and Anchukaitis, K. J. (2020). Twenty-First Century Drought Projections in the CMIP6 Forcing Scenarios. *Earth's Future*, 8(6).

Cook, B. I., Shukla, S. P., Puma, M. J., and Nazarenko, L. S. (2015). Irrigation as an historical climate forcing. *Climate Dynamics*, 44(5-6):1715–1730.

Cornes, R. C., Van Der Schrier, G., Van Den Besselaar, E. J. M., and Jones, P. D. (2018). An Ensemble Version of the E-OBS Temperature and Precipitation Data Sets. *Journal of Geophysical Research: Atmospheres*, 123(17):9391–9409.

Dai, A. (2013). Increasing drought under global warming in observations and models. *Nature Climate Change*, 3(1):52–58.

De Rosnay, P., Polcher, J., Bruen, M., and Laval, K. (2002). Impact of a physically based soil water flow and soil-plant interaction representation for modeling large-scale land surface processes: PHYSICALLY BASED SOIL HYDROLOGY IN GCM. *Journal of Geophysical Research: Atmospheres*, 107(D11):ACL 3–1–ACL 3–19.

DeAngelis, A., Dominguez, F., Fan, Y., Robock, A., Kustu, M. D., and Robinson, D. (2010). Evidence of enhanced precipitation due to irrigation over the Great Plains of the United States. *Journal of Geophysical Research*, 115(D15):D15115.

D.G.M (2023). MAROC Etat du Climat en 2022. Direction Génarale de Météorologie. https://www.marocmeteo.ma/sites/default/files/climat_report/pdfs/Maroc_etat_climat_2022.pdf. Technical report.

Diallo, F. B., Hourdin, F., Rio, C., Traore, A.-K., Mellul, L., Guichard, F., and Kergoat, L. (2017). The Surface Energy Budget Computed at the Grid-Scale of a Climate Model Challenged by Station Data in West Africa: GCM FACING WEST AFRICA IN-SITU DATA. *Journal of Advances in Modeling Earth Systems*, 9(7):2710–2738.

Diarra, A. (2017). *Suivi de l'évapotranspiration des cultures irriguées du Sud de la Méditerranée par télédétection multi-capteurs et modélisation globale*. Sciences de la Terre, Université Pierre et Marie Curie - Paris VI; Université Cadi Ayyad.

Diffenbaugh, N. S. and Giorgi, F. (2012). Climate change hotspots in the CMIP5 global climate model ensemble. *Climatic Change*, 114(3-4):813–822.

Dirmeyer, P. A. (2011). A History and Review of the Global Soil Wetness Project (GSWP). *Journal of Hydrometeorology*, 12(5):729–749.

Dirmeyer, P. A., Chen, L., Wu, J., Shin, C.-S., Huang, B., Cash, B. A., Bosilovich, M. G., Mahanama, S., Koster, R. D., Santanello, J. A., Ek, M. B., Balsamo, G., Dutra, E., and Lawrence, D. M. (2018). Verification of Land–Atmosphere Coupling in Forecast Models, Reanalyses, and Land Surface Models Using Flux Site Observations. *Journal of Hydrometeorology*, 19(2):375–392.

Donat, M. G., Peterson, T. C., Brunet, M., King, A. D., Almazroui, M., Kolli, R. K., Boucherf, D., Al-Mulla, A. Y., Nour, A. Y., Aly, A. A., Nada, T. A. A., Semawi, M. M., Al Dashti, H. A., Salhab, T. G., El Fadli, K. I., Muftah, M. K., Dah Eida, S., Badi, W., Driouech, F., El Rhaz, K., Abubaker, M. J. Y., Ghulam, A. S., Erayah, A. S., Mansour, M. B., Alabdouli, W. O., Al Dhanhani, J. S., and Al Shekaili, M. N. (2014). Changes in extreme temperature and precipitation in the Arab region: long-term trends and variability related to ENSO and NAO: Extreme temperature and precipitation in the Arab region. *International Journal of Climatology*, 34(3):581–592.

Donnelly, C., Greuell, W., Andersson, J., Gerten, D., Pisacane, G., Roudier, P., and Ludwig, F. (2017). Impacts of climate change on European hydrology at 1.5, 2 and 3 degrees mean global warming above preindustrial level. *Climatic Change*, 143(1-2):13–26.

Douville, H. and John, A. (2021). Fast adjustment versus slow SST-mediated response of daily precipitation statistics to abrupt 4xCO2. *Climate Dynamics*, 56(3-4):1083–1104.

Driouech, F. (2010). *Distribution des précipitations hivernales sur le Maroc dans le cadre d'un changement climatique : descente d'échelle et incertitudes*. PhD thesis.

Driouech, F., Déqué, M., and Mokssit, A. (2009). Numerical simulation of the probability distribution function of precipitation over Morocco. *Climate Dynamics*, 32(7-8):1055–1063.

Driouech, F. and ElRhaz, K. (2017). ALADIN-Climate projections for the Arab region. Arab Climate change assessment report, United Nations Economic and Social Commission for Western Asia ESCWA). Technical report, E/ESCWA/SDPD/2017/RICCAR/Report.

Driouech, F., ElRhaz, K., Moufouma-Okia, W., Arjdal, K., and Balhane, S. (2020). Assessing Future Changes of Climate Extreme Events in the CORDEX-MENA Region Using Regional Climate Model ALADIN-Climate. *Earth Systems and Environment*, 4(3):477–492.

Driouech, F., Mahé, G., Déqué, M., Dieulin, C., Heirech, T. E., Milano, M., Benabdelfadel, A., and Rouche, N. (2010). Evaluation d'impacts potentiels de changements climatiques sur l'hydrologie du bassin versant de la Moulouya au Maroc. page 8.

Driouech, F., Stafi, H., Khouakhi, A., Moutia, S., Badi, W., ElRhaz, K., and Chehbouni, A. (2021). Recent observed country-wide climate trends in Morocco. *International Journal of Climatology*, 41(S1).

Drobinski, P., Da Silva, N., Bastin, S., Mailler, S., Muller, C., Ahrens, B., Christensen, O. B., and Lionello, P. (2020). How warmer and drier will the Mediterranean region be at the end of the twenty-first century? *Regional Environmental Change*, 20(3):78.

Drobinski, P., Silva, N. D., Panthou, G., Bastin, S., Muller, C., Ahrens, B., Borga, M., Conte, D., Fosser, G., Giorgi, F., Güttler, I., Kotroni, V., Li, L., Morin, E., Önol, B., Quintana-Segui, P., Romera, R., and Torma, C. Z. (2016). Scaling precipitation extremes with temperature in the Mediterranean: past climate assessment and projection in anthropogenic scenarios. *Climate Dynamics*, 51(3):1237–1257.

Duchemin, B., Hadria, R., Erraki, S., Boulet, G., Maisongrande, P., Chehbouni, A., Escadafal, R., Ezzahar, J., Hoedjes, J. C. B., Kharrou, M. H., Khabba, S., Mougenot, B., Olioso, A., Rodriguez, J. C., and Simonneaux, V. (2006). Monitoring wheat phenology and irrigation in Central Morocco: On the use of relationships between evapotranspiration, crops coefficients, leaf area index and remotely-sensed vegetation indices. *Agricultural Water Management*, 79(1):1–27.

Ducoudré, N. I., Laval, K., and Perrier, A. (1993). SECHIBA, a New Set of Parameterizations of the Hydrologic Exchanges at the Land-Atmosphere Interface within the LMD Atmospheric General Circulation Model. *Journal of Climate*, 6(2):248–273.

Dufresne, J.-L. and Ghattas, J. (2009). Description du sch ema de la couche limite turbulente et l'interface avec la surface planetaire dans LMDZ. Technical note of the Laboratoire de Météorologie Dynamique, Paris, France.

Déqué, M. and Piedelievre, J. P. (1995). High resolution climate simulation over Europe.

Ek, M. and Mahrt, L. (1994). Daytime evolution of relative humidity at the boundary-layer top. *Mon. Wea. Rev.*, pages 2709–2721.

Er-Raki, S., Chehbouni, A., Guemouria, N., Duchemin, B., Ezzahar, J., and Hadria, R. (2007). Combining FAO-56 model and ground-based remote sensing to estimate water consumptions of wheat crops in a semi-arid region. *Agricultural Water Management*, 87(1):41–54.

Er-Raki, S., Chehbouni, A., Khabba, S., Simonneaux, V., Jarlan, L., Ouldbba, A., Rodriguez, J., and Allen, R. (2010). Assessment of reference evapotranspiration methods in semi-arid regions: Can weather forecast data be used as alternate of ground meteorological parameters? *Journal of Arid Environments*, 74(12):1587–1596.

Er-Raki, S., Ezzahar, J., Merlin, O., Amazirh, A., Hssaine, B. A., Kharrou, M., Khabba, S., and Chehbouni, A. (2021). Performance of the HYDRUS-1D model for water balance components assessment of irrigated winter wheat under different water managements in semi-arid region of Morocco. *Agricultural Water Management*, 244:106546.

Eyring, V., Bony, S., Meehl, G. A., Senior, C. A., Stevens, B., Stouffer, R. J., and Taylor, K. E. (2016). Overview of the Coupled Model Intercomparison Project Phase 6 (CMIP6) experimental design and organization. *Geoscientific Model Development*, 9(5):1937–1958.

Ezzahar, J., Chehbouni, A., Hoedjes, J., Er-Raki, S., Chehbouni, A., Boulet, G., Bonnefond, J.-M., and De Bruin, H. (2007). The use of the scintillation technique for monitoring seasonal water consumption of olive orchards in a semi-arid region. *Agricultural Water Management*, 89(3):173–184.

Feldman, A. F., Short Gianotti, D. J., Trigo, I. F., Salvucci, G. D., and Entekhabi, D. (2019). Satellite-Based Assessment of Land Surface Energy Partitioning–Soil Moisture Relationships and Effects of Confounding Variables. *Water Resources Research*, 55(12):10657–10677.

Ferguson, I. M. and Maxwell, R. M. (2012). Human impacts on terrestrial hydrology: climate change versus pumping and irrigation. *Environmental Research Letters*, 7(4):044022.

Fesquet, C., Drobinski, P., Barthlott, C., and Dubos, T. (2009). Impact of terrain heterogeneity on near-surface turbulence structure. *Atmospheric Research*, 94(2):254–269.

Filahi, S., Tanarhte, M., Mouhir, L., El Morhit, M., and Tramblay, Y. (2016). Trends in indices of daily temperature and precipitations extremes in Morocco. *Theoretical and Applied Climatology*, 124(3-4):959–972.

Filahi, S., Tramblay, Y., Mouhir, L., and Diaconescu, E. P. (2017). Projected changes in temperature and precipitation indices in Morocco from high-resolution regional climate models: CLIMATE CHANGE. *International Journal of Climatology*, 37(14):4846–4863.

Fink, A., Christoph, M., and Born, K. (2010). Climate. In: Speth, P., Christoph, M., Diekkrüger, B. (Eds.), Impacts of Global Change on the Hydrological Cycle in West and Northwest Africa. Technical report, Springer, Heidelberg.

Fita, L. (2013). LMDZ physical schemes. A brief description for the LMDZ-B configuration. Technical report, Laboratorie de Météorologie Dynamique, IPSL, UPMC, CNRS, Tw. 45-55 3rd fl., B99, Jussieu, 75005, Paris, France.

Foken, T. (2008). *Micrometeorology*. Springer, Berlin. OCLC: ocn178312172.

Forster, P., Storelvmo, T., Armour, K., Collins, W., Dufresne, J.-L., Frame, D., Lunt, D., Mauritsen, T., Palmer, M., Watanabe, M., Wild, M., and Zhang, H. (2021). The Earth's Energy Budget, Climate Feedbacks, and Climate Sensitivity. In Climate Change 2021: The Physical Science Basis. Contribution of Working Group I to the Sixth Assessment Report of the Intergovernmental Panel on Climate Change [Masson-Delmotte, V., P. Zhai, A. Pirani, S.L. Connors, C. Péan, S. Berger, N. Caud, Y. Chen, L. Goldfarb, M.I. Gomis, M. Huang, K. Leitzell, E. Lonnoy, J.B.R. Matthews, T.K. Maycock, T. Waterfield, O. Yelekçi, R. Yu, and B. Zhou (eds.)]. Technical report, Cambridge University Press, Cambridge, United Kingdom and New York, NY, USA.

Gao, J., Masson-Delmotte, V., Yao, T., Tian, L., Risi, C., and Hoffmann, G. (2011). Precipitation Water Stable Isotopes in the South Tibetan Plateau: Observations and Modeling*. *Journal of Climate*, 24(13):3161–3178.

García-Ruiz, J. M., López-Moreno, J. I., Vicente-Serrano, S. M., Lasanta–Martínez, T., and Beguería, S. (2011). Mediterranean water resources in a global change scenario. *Earth-Science Reviews*, 105(3-4):121–139.

Garratt, J. R. and Hicks, B. B. (1973). Momentum, heat and water vapour transfer to and from natural and artificial surfaces. *Quarterly Journal of the Royal Meteorological Society*, 99(422):680–687.

Gerken, T., Ruddell, B. L., Yu, R., Stoy, P. C., and Drewry, D. T. (2019). Robust observations of land-to-atmosphere feedbacks using the information flows of FLUXNET. *npj Climate and Atmospheric Science*, 2(1):37.

Gillett, N. P., Shiogama, H., Funke, B., Hegerl, G., Knutti, R., Matthes, K., Santer, B. D., Stone, D., and Tebaldi, C. (2016). Detection and Attribution Model Intercomparison Project (DAMIP). preprint, Climate and Earth System Modeling.

Giorgi, F. and Mearns, L. O. (1991). Approaches to the simulation of regional climate change: A review. *Reviews of Geophysics*, 29(2):191.

Goubanova, K. and Li, L. (2007). Extremes in temperature and precipitation around the Mediterranean basin in an ensemble of future climate scenario simulations. *Global and Planetary Change*, 57(1-2):27–42.

Gueye, B. M. (2015). *Modélisation des couplages entre les aérosols désertiques et le climat ouest-africain*. PhD thesis, Université Pierre et Marie Curie - Paris VI; Université Cheikh Anta Diop de Dakar. Faculté des sciences.

Guldberg, A., Kaas, E., Déqué, M., Yang, S., and Thorsen, S. V. (2005). Reduction of systematic errors by empirical model correction: impact on seasonal prediction skill. *Tellus A: Dynamic Meteorology and Oceanography*, 57(4):575.

Gutiérrez, J., Jones, R., Narisma, G., Alves, L., Amjad, M., Gorodetskaya, I., Grose, M., Klutse, N., Krakovska, J., Martínez-Castro, D., Mearns, L., Mernild, S., Ngo-Duc, T., van den Hurk, B., and Yoon, J.-H. (2021). Atlas. In Climate Change 2021: The Physical Science Basis. Contribution of Working Group I to the Sixth Assessment Report of the Intergovernmental Panel on Climate Change [Masson-Delmotte, V., P. Zhai, A. Pirani, S.L. Connors, C. Péan, S. Berger, N. Caud, Y. Chen, L. Goldfarb, M.I. Gomis, M. Huang, K. Leitzell, E. Lonnoy, J.B.R. Matthews, T.K. Maycock, T. Waterfield, O. Yelekçi, R. Yu, and B. Zhou (eds.)]. Technical report, Cambridge University Press, Cambridge, United Kingdom and New York, NY, USA.

Gutjahr, O., Putrasahan, D., Lohmann, K., Jungclaus, J. H., von Storch, J.-S., Brüggemann, N., Haak, H., and Stössel, A. (2019). Max Planck Institute Earth System Model (MPI-ESM1.2) for the High-Resolution Model Intercomparison Project (HighResMIP). *Geoscientific Model Development*, 12(7):3241–3281. Publisher: Copernicus GmbH.

HAJHOUJI, Y. (2018). *Modélisation hydrologique du bassin versant de l'oued Rheraya et sa contribution à la recharge de la nappe du Haouz (bassin du Tensift, Maroc)*. PhD thesis, Université Toulouse 3 - Paul Sabatier; Université Cadi Ayyad de Marrakech.

Hanel, M., Rakovec, O., Markonis, Y., Máca, P., Samaniego, L., Kyselý, J., and Kumar, R. (2018). Revisiting the recent European droughts from a long-term perspective. *Scientific Reports*, 8(1):9499.

Harbouze, R., Pellissier, J. P., Rolland, J. P., and Khechimi, W. (2019). Rapport de synthèse sur l'agriculture au Maroc. Recherche.

Harding, K. J. and Snyder, P. K. (2012). Modeling the Atmospheric Response to Irrigation in the Great Plains. Part I: General Impacts on Precipitation and the Energy Budget. *Journal of Hydrometeorology*, 13(6):1667–1686.

Hersbach, H., Bell, B., Berrisford, P., Hirahara, S., Horányi, A., Muñoz-Sabater, J., Nicolas, J., Peubey, C., Radu, R., Schepers, D., Simmons, A., Soci, C., Abdalla, S., Abellan, X., Balsamo, G., Bechtold, P., Biavati, G., Bidlot, J., Bonavita, M., De Chiara, G., Dahlgren, P., Dee, D., Diamantakis, M., Dragani, R., Flemming, J., Forbes, R., Fuentes, M., Geer, A., Haimberger, L., Healy, S., Hogan, R. J., Hólm, E., Janisková, M., Keeley, S., Laloyaux, P., Lopez, P., Lupu, C., Radnoti, G., De Rosnay, P., Rozum, I., Vamborg, F., Villaume, S., and Thépaut, J. (2020). The ERA5 global reanalysis. *Quarterly Journal of the Royal Meteorological Society*, 146(730):1999–2049.

Hirschi, M., Seneviratne, S. I., Alexandrov, V., Boberg, F., Boroneant, C., Christensen, O. B., Formayer, H., Orlowsky, B., and Stepanek, P. (2011). Observational evidence for soil-moisture impact on hot extremes in southeastern Europe. *Nature Geoscience*, 4(1):17–21.

Hourdin, F., Couvreux, F., and Menut, L. (2002). Parameterization of the Dry Convective Boundary Layer Based on a Mass Flux Representation of Thermals. *Journal of the Atmospheric Sciences*, 59(6):1105–1123.

Hourdin, F., Foujols, M.-A., Codron, F., Guemas, V., Dufresne, J.-L., Bony, S., Denvil, S., Guez, L., Lott, F., Ghattas, J., Braconnot, P., Marti, O., Meurdesoif, Y., and Bopp, L. (2013). Impact of the LMDZ atmospheric grid configuration on the climate and sensitivity of the IPSL-CM5A coupled model. *Climate Dynamics*, 40(9-10):2167–2192.

Hourdin, F., Gueye, M., Diallo, B., Dufresne, J.-L., Escribano, J., Menut, L., Marticoréna, B., Siour, G., and Guichard, F. (2015). Parameterization of convective transport in the boundary layer and its impact on the representation of the diurnal cycle of wind and dust emissions. *Atmospheric Chemistry and Physics*, 15(12):6775–6788.

Hourdin, F., Gueye, M., Diallo, B., Dufresne, J.-L., Menut, L., Marticoréna, B., Siour, G., and Guichard, F. (2014). Parametrization of convective transport in the boundary layer and its impact on the representation of diurnal cycle of wind and dust emissions. preprint, Aerosols/Atmospheric Modelling/Troposphere/Physics (physical properties and processes).

Hourdin, F. and Guillemot, H. (2021). MODÉLISATION DU CLIMAT. Technical report.

Hourdin, F., Jam, A., Rio, C., Couvreux, F., Sandu, I., Lefebvre, M., Brient, F., and Idelkadi, A. (2019). Unified Parameterization of Convective Boundary Layer Transport and Clouds With the Thermal Plume Model. *Journal of Advances in Modeling Earth Systems*, 11(9):2910–2933.

Hourdin, F., Rio, C., Grandpeix, J., Madeleine, J., Cheruy, F., Rochetin, N., Jam, A., Musat, I., Idelkadi, A., Fairhead, L., Foujols, M., Mellul, L., Traore, A., Dufresne, J., Boucher, O., Lefebvre, M., Millour, E., Vignon, E., Jouhaud, J., Diallo, F. B., Lott, F., Gastineau, G., Caubel, A., Meurdesoif, Y., and Ghattas, J. (2020a). LMDZ6A: The Atmospheric Component of the IPSL Climate Model With Improved and Better Tuned Physics. *Journal of Advances in Modeling Earth Systems*, 12(7).

Hourdin, F., Rio, C., Jam, A., Traore, A., and Musat, I. (2020b). Convective Boundary Layer Control of the Sea Surface Temperature in the Tropics. *Journal of Advances in Modeling Earth Systems*, 12(6).

Hurrell, J. W. and Van Loon, H. (1997). Decadal Variations in Climate Associated with the North Atlantic Oscillation. *Climatic Change at High Elevation Sites*, pages 69–94.

IPCC (2021). Climate Change 2021: The Physical Science Basis. Contribution of Working Group I to the Sixth Assessment Report of the Intergovernmental Panel on Climate Change [Masson-Delmotte, V., P. Zhai, A. Pirani, S.L. Connors, C. Péan, S. Berger, N. Caud, Y. Chen, L. Goldfarb, M.I. Gomis, M. Huang, K. Leitzell, E. Lonnoy, J.B.R. Matthews, T.K. Maycock, T. Waterfield, O. Yelekçi, R. Yu, and B. Zhou (eds.)]. Technical report, Cambridge University Press, Cambridge, United Kingdom and New York, NY, USA.

IPCC (2022). Climate Change 2022: Impacts, Adaptation and Vulnerability. Contribution of Working Group II to the Sixth Assessment Report of the Intergovernmental Panel on Climate Change [H.-O. Pörtner, D.C. Roberts, M. Tignor, E.S. Poloczanska, K. Mintenbeck, A. Alegría, M. Craig,

S. Langsdorf, S. Löschke, V. Möller, A. Okem, B. Rama (eds.)]. Technical report, Cambridge University Press. Cambridge University Press, Cambridge, UK and New York, NY, USA.

Iturbide, M., Gutiérrez, J. M., Alves, L. M., Bedia, J., Cimadevilla, E., Cofiño, A. S., Cerezo-Mota, R., Di Luca, A., Faria, S. H., Gorodetskaya, I., Hauser, M., Herrera, S., Hewitt, H. T., Hennessy, K. J., Jones, R. G., Krakovska, S., Manzanas, R., Marínez-Castro, D., Narisma, G. T., Nurhati, I. S., Pinto, I., Seneviratne, S. I., van den Hurk, B., and Vera, C. S. (2020). An update of IPCC climate reference regions for subcontinental analysis of climate model data: Definition and aggregated datasets. preprint, Data, Algorithms, and Models.

Jacobs, C. and De Bruin, H. (1992). The sensitivity of regional transpiration to land- Surface characteristics: significance of feedback. *J. clim.*, pages 683–698.

Jam, A., Hourdin, F., Rio, C., and Couvreux, F. (2013). Resolved Versus Parametrized Boundary-Layer Plumes. Part III: Derivation of a Statistical Scheme for Cumulus Clouds. *Boundary-Layer Meteorology*, 147(3):421–441.

James, R., Washington, R., Abiodun, B., Kay, G., Mutemi, J., Pokam, W., Hart, N., Artan, G., and Senior, C. (2018). Evaluating Climate Models with an African Lens. *Bulletin of the American Meteorological Society*, 99(2):313–336.

Jarlan, L., Khabba, S., Er-Raki, S., Le Page, M., Hanich, L., Fakir, Y., Merlin, O., Mangiarotti, S., Gascoin, S., Ezzahar, J., Kharrou, M., Berjamy, B., Saaïdi, A., Boudhar, A., Benkaddour, A., Laftouhi, N., Abaoui, J., Tavernier, A., Boulet, G., Simonneaux, V., Driouech, F., El Adnani, M., El Fazziki, A., Amenzou, N., Raibi, F., El Mandour, A., Ibouh, H., Le Dantec, V., Habets, F., Tramblay, Y., Mougenot, B., Leblanc, M., El Faïz, M., Drapeau, L., Coudert, B., Hagolle, O., Filali, N., Belaqziz, S., Marchane, A., Szczypta, C., Toumi, J., Diarra, A., Aouade, G., Hajhouji, Y., Nassah, H., Bigeard, G., Chirouze, J., Boukhari, K., Abourida, A., Richard, B., Fanise, P., Kasbani, M., Chakir, A., Zribi, M., Marah, H., Naimi, A., Mokssit, A., Kerr, Y., and Escadafal, R. (2015). Remote Sensing of Water Resources in Semi-Arid Mediterranean Areas: the joint international laboratory TREMA. *International Journal of Remote Sensing*, 36(19-20):4879–4917.

Jiang, L., Ma, E., and Deng, X. (2014). Impacts of Irrigation on the Heat Fluxes and Near-Surface Temperature in an Inland Irrigation Area of Northern China. *Energies*, 7(3):1300–1317.

Jimenez, P. A., De Arellano, J. V.-G., Navarro, J., and Gonzalez-Rouco, J. F. (2014). Understanding Land–Atmosphere Interactions across a Range of Spatial and Temporal Scales. *Bulletin of the American Meteorological Society*, 95(1):ES14–ES17.

Kabbaj, A., Zeryouhi, I., and Pointet, T. (1979). Alimentation en eau de la ville de Marrakech: projet à court, moyen et long terme. Influences sur la nappe. Effects of Urbanization and Industraialization on the Hydrological Regime and on Water Quality. Technical report, IAHS, Amsterdam.

Kanamaru, H. and Kanamitsu, M. (2008). Model Diagnosis of Nighttime Minimum Temperature Warming during Summer due to Irrigation in the California Central Valley. *Journal of Hydrometeorology*, 9(5):1061–1072.

Kantha, L. H. and Clayson, C. A. (2000). *Small Scale Processes in Geophysical Fluid Flows*. Elsevier. Google-Books-ID: c9BsNjRd9oYC.

Kelley, M., Schmidt, G. A., Nazarenko, L. S., Bauer, S. E., Ruedy, R., Russell, G. L., Ackerman, A. S., Aleinov, I., Bauer, M., Bleck, R., Canuto, V., Cesana, G., Cheng, Y., Clune, T. L., Cook, B. I., Cruz, C. A., Del Genio, A. D., Elsaesser, G. S., Faluvegi, G., Kiang, N. Y., Kim, D., Lacis, A. A., Leboissetier, A., LeGrande, A. N., Lo, K. K., Marshall, J., Matthews, E. E., McDermid, S., Mezuman, K., Miller, R. L., Murray, L. T., Oinas, V., Orbe, C., García-Pando, C. P., Perlwitz, J. P., Puma, M. J., Rind, D., Romanou, A., Shindell, D. T., Sun, S., Tausnev, N., Tsigaridis, K., Tselioudis, G., Weng, E., Wu, J., and Yao, M.-S. (2020). GISS-E2.1: Configurations and Climatology. *Journal of Advances in Modeling Earth Systems*, 12(8):e2019MS002025. _eprint: https://onlinelibrary.wiley.com/doi/pdf/10.1029/2019MS002025.

Kerkhoff, C., Künsch, H. R., and Schär, C. (2014). Assessment of Bias Assumptions for Climate Models. *Journal of Climate*, 27(17):6799–6818.

Khabba, S., Jarlan, L., Er-Raki, S., Le Page, M., Ezzahar, J., Boulet, G., Simonneaux, V., Kharrou, M., Hanich, L., and Chehbouni, G. (2013). The SudMed Program and the Joint International Laboratory TREMA: A Decade of Water Transfer Study in the Soil-plant-atmosphere System over Irrigated Crops in Semi-arid Area. *Procedia Environmental Sciences*, 19:524–533.

Kharin, V. V. and Scinocca, J. F. (2012). The impact of model fidelity on seasonal predictive skill: IMPACT OF FIDELITY ON SKILL. *Geophysical Research Letters*, 39(18).

Kharrou, M. H., Er-Raki, S., Chehbouni, A., Duchemin, B., Simonneaux, V., LePage, M., Ouzine, L., and Jarlan, L. (2011). Water use efficiency and yield of winter wheat under different irrigation regimes in a semi-arid region. *Agricultural Sciences*, 02(03):273–282.

King, J. C., Connolley, W. M., and Derbyshire, S. H. (2001). Sensitivity of modelled Antarctic climate to surface and boundary-layer flux parametrizations. *Quarterly Journal of the Royal Meteorological Society*, 127(573):779–794.

Knippertz, P. (2004). A Simple Identification Scheme for Upper-Level Troughs and Its Application to Winter Precipitation Variability in Northwest Africa. *Journal of Climate*, 17(6):1411–1418.

Knippertz, P., Christoph, M., and Speth, P. (2002). Long-term precipitation variability in Morocco and the link to the large-scale circulation in recent and future climates. *Meteorology and Atmospheric Physics*, 83(1-2):67–88.

Knippertz, P., Ulbrich, U., Marques, F., and Corte-Real, J. (2003). Decadal changes in the link between El Niño and springtime North Atlantic oscillation and European-North African rainfall: EL

NIÑO, NAO, EUROPEAN-NORTH AFRICAN RAINFALL. *International Journal of Climatology*, 23(11):1293–1311.

Koster, R. D., Suarez, M. J., Liu, P., Jambor, U., Berg, A., Kistler, M., Reichle, R., Rodell, M., and Famiglietti, J. (2004). Realistic Initialization of Land Surface States: Impacts on Subseasonal Forecast Skill. *Journal of Hydrometeorology*, 5(6):1049–1063.

Krinner, G., Beaumet, J., Favier, V., Déqué, M., and Brutel-Vuilmet, C. (2019). Empirical Run-Time Bias Correction for Antarctic Regional Climate Projections With a Stretched-Grid AGCM. *Journal of Advances in Modeling Earth Systems*, 11(1):64–82.

Krinner, G., Genthon, C., Li, Z.-X., and Le Van, P. (1997). Studies of the Antarctic climate with a stretched-grid general circulation model. *Journal of Geophysical Research: Atmospheres*, 102(D12):13731–13745.

Krinner, G., Kharin, V., Roehrig, R., Scinocca, J., and Codron, F. (2020). Historically-based run-time bias corrections substantially improve model projections of 100 years of future climate change. *Communications Earth & Environment*, 1(1):29.

Krinner, G., Viovy, N., De Noblet-Ducoudré, N., Ogée, J., Polcher, J., Friedlingstein, P., Ciais, P., Sitch, S., and Prentice, I. C. (2005). A dynamic global vegetation model for studies of the coupled atmosphere-biosphere system: DVGM FOR COUPLED CLIMATE STUDIES. *Global Biogeochemical Cycles*, 19(1).

Kueppers, L. M., Snyder, M. A., and Sloan, L. C. (2007). Irrigation cooling effect: Regional climate forcing by land-use change. *Geophysical Research Letters*, 34(3):L03703.

Lamb, P. J. and Peppier, R. A. (1987). North Atlantic Oscillation: Concept and an Application. *Climate and Meteorology Section*, pages 1218–1225.

Lauritzen, P. H., Nair, R. D., Herrington, A. R., Callaghan, P., Goldhaber, S., Dennis, J. M., Bacmeister, J. T., Eaton, B. E., Zarzycki, C. M., Taylor, M. A., Ullrich, P. A., Dubos, T., Gettelman, A., Neale, R. B., Dobbins, B., Reed, K. A., Hannay, C., Medeiros, B., Benedict, J. J., and Tribbia, J. J. (2018). NCAR Release of CAM-SE in CESM2.0: A Reformulation of the Spectral Element Dynamical Core in Dry-Mass Vertical Coordinates With Comprehensive Treatment of Condensates and Energy. *Journal of Advances in Modeling Earth Systems*, 10(7):1537–1570.

Le Page, M., Berjamy, B., Fakir, Y., Bourgin, F., Jarlan, L., Abourida, A., Benrhanem, M., Jacob, G., Huber, M., Sghrer, F., Simonneaux, V., and Chehbouni, G. (2012). An Integrated DSS for Groundwater Management Based on Remote Sensing. The Case of a Semi-arid Aquifer in Morocco. *Water Resources Management*, 26(11):3209–3230.

Lee, J.-E., Risi, C., Fung, I., Worden, J., Scheepmaker, R. A., Lintner, B., and Frankenberg, C. (2012). Asian monsoon hydrometeorology from TES and SCIAMACHY water vapor isotope measurements and LMDZ simulations: Implications for speleothem climate

record interpretation. *Journal of Geophysical Research: Atmospheres*, 117(D15). _eprint: https://onlinelibrary.wiley.com/doi/pdf/10.1029/2011JD017133.

Lee, J.-Y., Marotzke, J., Bala, J., Cao, L., Corti, S., Dunne, J., Engelbrecht, F., Fischer, E., Fyfe, J., Jones, C., Maycock, A., Mutemi, J., Ndiaye, O., Panickal, S., and Zhou, T. (2021). *Climate Change 2021 – The Physical Science Basis: Working Group I Contribution to the Sixth Assessment Report of the Intergovernmental Panel on Climate Change*. Cambridge University Press, 1 edition.

Lee, W.-L., Wang, Y.-C., Shiu, C.-J., Tsai, I.-c., Tu, C.-Y., Lan, Y.-Y., Chen, J.-P., Pan, H.-L., and Hsu, H.-H. (2020). Taiwan Earth System Model Version 1: description and evaluation of mean state. *Geoscientific Model Development*, 13(9):3887–3904.

Lelieveld, J., Proestos, Y., Hadjinicolaou, P., Tanarhte, M., Tyrlis, E., and Zittis, G. (2016). Strongly increasing heat extremes in the Middle East and North Africa (MENA) in the 21st century. *Climatic Change*, 137(1-2):245–260.

Li, L. (2019). CAS FGOALS-g3 model output prepared for CMIP6 ScenarioMIP ssp370 (Version 20191026). *Earth System Grid Fed*.

Li, S.-Y., Miao, L.-J., Jiang, Z.-H., Wang, G.-J., Gnyawali, K. R., Zhang, J., Zhang, H., Fang, K., He, Y., and Li, C. (2020). Projected drought conditions in Northwest China with CMIP6 models under combined SSPs and RCPs for 2015–2099. *Advances in Climate Change Research*, 11(3):210–217.

Lionello, P. and Scarascia, L. (2018). The relation between climate change in the Mediterranean region and global warming. *Regional Environmental Change*, 18(5):1481–1493.

Lo, M. and Famiglietti, J. S. (2013). Irrigation in California's Central Valley strengthens the southwestern U.S. water cycle. *Geophysical Research Letters*, 40(2):301–306.

Lohou, F., Lothon, M., Bastin, S., Brut, A., Canut, G., Cheruy, F., Couvreux, F., Cohard, J.-M., Darrozes, J., Dupont, J.-C., Lafont, S., Roehrig, R., and Román-Cascón, C. (2022). Model and Observation for Surface Atmosphere Interactions (MOSAI) project. Technical Report EGU22-8797, Copernicus Meetings. Conference Name: EGU22.

Louis, J., Tiedtke, M., and Geleyn, J.-F. (1982). A short history of the operational pbl parametrization at ECMWF.

Lurton, T., Balkanski, Y., Bastrikov, V., Bekki, S., Bopp, L., Braconnot, P., Brockmann, P., Cadule, P., Contoux, C., Cozic, A., Cugnet, D., Dufresne, J., Éthé, C., Foujols, M., Ghattas, J., Hauglustaine, D., Hu, R., Kageyama, M., Khodri, M., Lebas, N., Levavasseur, G., Marchand, M., Ottlé, C., Peylin, P., Sima, A., Szopa, S., Thiéblemont, R., Vuichard, N., and Boucher, O. (2020). Implementation of the CMIP6 Forcing Data in the IPSL-CM6A-LR Model. *Journal of Advances in Modeling Earth Systems*, 12(4).

Mamalakis, A., Randerson, J. T., Yu, J.-Y., Pritchard, M. S., Magnusdottir, G., Smyth, P., Levine, P. A., Yu, S., and Foufoula-Georgiou, E. (2021). Zonally opposing shifts of the intertropical convergence zone in response to climate change. page 45.

Marcella, M. P. and Eltahir, E. A. B. (2014). Introducing an Irrigation Scheme to a Regional Climate Model: A Case Study over West Africa. *Journal of Climate*, 27(15):5708–5723.

Marchane, A., Tramblay, Y., Hanich, L., Ruelland, D., and Jarlan, L. (2017). Climate change impacts on surface water resources in the Rheraya catchment (High Atlas, Morocco). *Hydrological Sciences Journal*, 62(6):979–995.

Mariotti, A., Pan, Y., Zeng, N., and Alessandri, A. (2015). Long-term climate change in the Mediterranean region in the midst of decadal variability. *Climate Dynamics*, 44(5-6):1437–1456.

Massman, W. J. (1999). A model study of kBH1 for vegetated surfaces using 'localized near- field' Lagrangian theory. *Journal of Hydrology*.

Mauritsen, T., Bader, J., Becker, T., Behrens, J., Bittner, M., Brokopf, R., Brovkin, V., Claussen, M., Crueger, T., Esch, M., Fast, I., Fiedler, S., Fläschner, D., Gayler, V., Giorgetta, M., Goll, D. S., Haak, H., Hagemann, S., Hedemann, C., Hohenegger, C., Ilyina, T., Jahns, T., Jimenéz-de-la-Cuesta, D., Jungclaus, J., Kleinen, T., Kloster, S., Kracher, D., Kinne, S., Kleberg, D., Lasslop, G., Kornblueh, L., Marotzke, J., Matei, D., Meraner, K., Mikolajewicz, U., Modali, K., Möbis, B., Müller, W. A., Nabel, J. E. M. S., Nam, C. C. W., Notz, D., Nyawira, S., Paulsen, H., Peters, K., Pincus, R., Pohlmann, H., Pongratz, J., Popp, M., Raddatz, T. J., Rast, S., Redler, R., Reick, C. H., Rohrschneider, T., Schemann, V., Schmidt, H., Schnur, R., Schulzweida, U., Six, K. D., Stein, L., Stemmler, I., Stevens, B., Storch, J., Tian, F., Voigt, A., Vrese, P., Wieners, K., Wilkenskjeld, S., Winkler, A., and Roeckner, E. (2019). Developments in the MPI-M Earth System Model version 1.2 (MPI-ESM1.2) and Its Response to Increasing CO $_2$. *Journal of Advances in Modeling Earth Systems*, 11(4):998–1038.

McSweeney, C. F., Jones, R. G., Lee, R. W., and Rowell, D. P. (2015). Selecting CMIP5 GCMs for downscaling over multiple regions. *Climate Dynamics*, 44(11-12):3237–3260.

Meddi, M. M., Assani, A. A., and Meddi, H. (2010). Temporal Variability of Annual Rainfall in the Macta and Tafna Catchments, Northwestern Algeria. *Water Resources Management*, 24(14):3817–3833.

MedECC (2020). Climate and Environmental Change in the Mediterranean Basin – Current Situation and Risks for the Future. First Mediterranean Assessment Report. Technical report, Zenodo. ISBN: 9782957741618 Version Number: 1.

Meehl, G. A., Senior, C. A., Eyring, V., Flato, G., Lamarque, J.-F., Stouffer, R. J., Taylor, K. E., and Schlund, M. (2020). Context for interpreting equilibrium climate sensitivity and transient climate response from the CMIP6 Earth system models. *Science Advances*, 6(26):eaba1981.

Michael J Iacono (2011). Application of Improved Radiation Modeling to General Circulation Models. Technical Report DOE/ER61549-1, 1010861.

Miralles, D. G., Gentine, P., Seneviratne, S. I., and Teuling, A. J. (2019). Land–atmospheric feedbacks during droughts and heatwaves: state of the science and current challenges. *Annals of the New York Academy of Sciences*, 1436(1):19–35.

Miralles, D. G., Teuling, A. J., Van Heerwaarden, C. C., and Vilà-Guerau De Arellano, J. (2014). Mega-heatwave temperatures due to combined soil desiccation and atmospheric heat accumulation. *Nature Geoscience*, 7(5):345–349.

Mizuochi, H., Ducharne, A., Cheruy, F., Ghattas, J., Al-Yaari, A., Wigneron, J.-P., Bastrikov, V., Peylin, P., Maignan, F., and Vuichard, N. (2021). Multivariable evaluation of land surface processes in forced and coupled modes reveals new error sources to the simulated water cycle in the IPSL (Institute Pierre Simon Laplace) climate model. *Hydrology and Earth System Sciences*, 25(4):2199–2221.

Mlawer, E. J., Taubman, S. J., Brown, P. D., Iacono, M. J., and Clough, S. A. (1997). Radiative transfer for inhomogeneous atmospheres: RRTM, a validated correlated-k model for the longwave. *Journal of Geophysical Research: Atmospheres*, 102(D14):16663–16682.

Mohamed, N. A. H., Bannari, A., Mohamed Fadul, H., and Zakieldeen, S. (2016). Ecological Zones Degradation Analysis in Central Sudan during a Half Century Using Remote Sensing and GIS. *Advances in Remote Sensing*, 05(04):355–371.

Monin, A. and Obukhov, A. (1954). Basic laws of turbulent mixing in the atmosphere near the ground. *Trudy Geofiz Inst*, pages 163–187.

Monsi, M. and Saeki, T. (1953). Uber den Lichtfaktor in den Pflanzengesellschaften und seine Bedeutung für die Stoffproduktion. pages 22–52.

Nassah, H., Er-Raki, S., Khabba, S., Fakir, Y., Raibi, F., Merlin, O., and Mougenot, B. (2018). Evaluation and analysis of deep percolation losses of drip irrigated citrus crops under non-saline and saline conditions in a semi-arid area. *Biosystems Engineering*, 165:10–24.

Nicholson, S. E. and Kim, J. (1997). THE RELATIONSHIP OF THE EL NIÑO–SOUTHERN OSCILLATION TO AFRICAN RAINFALL. *International Journal of Climatology*, 17(2):117–135.

Ochsner, T. E., Cosh, M. H., Cuenca, R. H., Dorigo, W. A., Draper, C. S., Hagimoto, Y., Kerr, Y. H., Larson, K. M., Njoku, E. G., Small, E. E., and Zreda, M. (2013). State of the Art in Large-Scale Soil Moisture Monitoring. *Soil Science Society of America Journal*, 77(6):1888–1919.

O'Neill, B. C., Tebaldi, C., van Vuuren, D. P., Eyring, V., Friedlingstein, P., Hurtt, G., Knutti, R., Kriegler, E., Lamarque, J.-F., Lowe, J., Meehl, G. A., Moss, R., Riahi, K., and Sanderson, B. M.

(2016). The Scenario Model Intercomparison Project (ScenarioMIP) for CMIP6. *Geoscientific Model Development*, 9(9):3461–3482.

Orlowsky, B. and Seneviratne, S. I. (2013). Elusive drought: uncertainty in observed trends and short- and long-term CMIP5 projections. *Hydrology and Earth System Sciences*, 17(5):1765–1781.

Ozturk, T., Turp, M. T., Türkeş, M., and Kurnaz, M. L. (2017). Projected changes in temperature and precipitation climatology of Central Asia CORDEX Region 8 by using RegCM4.3.5. *Atmospheric Research*, 183:296–307.

PaiMazumder, D. and Done, J. M. (2016). Potential predictability sources of the 2012 U.S. drought in observations and a regional model ensemble. *Journal of Geophysical Research: Atmospheres*, 121(21):12,581–12,592.

Panthou, G., Vrac, M., Drobinski, P., Bastin, S., and Li, L. (2018). Impact of model resolution and Mediterranean sea coupling on hydrometeorological extremes in RCMs in the frame of HyMeX and MED-CORDEX. *Climate Dynamics*, 51(3):915–932.

Pokhrel, Y., Hanasaki, N., Koirala, S., Cho, J., Yeh, P. J.-F., Kim, H., Kanae, S., and Oki, T. (2012). Incorporating Anthropogenic Water Regulation Modules into a Land Surface Model. *Journal of Hydrometeorology*, 13(1):255–269.

Polcher, J., McAvaney, B., Viterbo, P., Gaertner, M.-A., Hahmann, A., Mahfouf, J.-F., Noilhan, J., Phillips, T., Pitman, A., Schlosser, C., Schulz, J.-P., Timbal, B., Verseghy, D., and Xue, Y. (1998). A proposal for a general interface between land surface schemes and general circulation models. *Global and Planetary Change*, 19(1-4):261–276.

Prudhomme, C., Giuntoli, I., Robinson, E. L., Clark, D. B., Arnell, N. W., Dankers, R., Fekete, B. M., Franssen, W., Gerten, D., Gosling, S. N., Hagemann, S., Hannah, D. M., Kim, H., Masaki, Y., Satoh, Y., Stacke, T., Wada, Y., and Wisser, D. (2014). Hydrological droughts in the 21st century, hotspots and uncertainties from a global multimodel ensemble experiment. *Proceedings of the National Academy of Sciences*, 111(9):3262–3267.

Puma, M. J. and Cook, B. I. (2010). Effects of irrigation on global climate during the 20th century. *Journal of Geophysical Research*, 115(D16):D16120.

Raymond, F., Drobinski, P., Ullmann, A., and Camberlin, P. (2018). Extreme dry spells over the Mediterranean Basin during the wet season: Assessment of HyMeX/Med-CORDEX regional climate simulations (1979-2009). *International Journal of Climatology*, 38(7):3090–3105.

Raymond, F., Ullmann, A., Camberlin, P., Drobinski, P., and Smith, C. C. (2016). Extreme dry spell detection and climatology over the Mediterranean Basin during the wet season: DRY SPELL OVER THE MEDITERRANEAN BASIN. *Geophysical Research Letters*, 43(13):7196–7204.

Raymond, F., Ullmann, A., Tramblay, Y., Drobinski, P., and Camberlin, P. (2019). Evolution of Mediterranean extreme dry spells during the wet season under climate change. *Regional Environmental Change*, 19(8):2339–2351.

Rio, C., Grandpeix, J.-Y., Hourdin, F., Guichard, F., Couvreux, F., Lafore, J.-P., Fridlind, A., Mrowiec, A., Roehrig, R., Rochetin, N., Lefebvre, M.-P., and Idelkadi, A. (2013). Control of deep convection by sub-cloud lifting processes: the ALP closure in the LMDZ5B general circulation model. *Climate Dynamics*, 40(9-10):2271–2292.

Rio, C., Hourdin, F., Couvreux, F., and Jam, A. (2010). Resolved Versus Parametrized Boundary-Layer Plumes. Part II: Continuous Formulations of Mixing Rates for Mass-Flux Schemes. *Boundary-Layer Meteorology*, 135(3):469–483.

Rochdane, S., Elgettafi, M., El Mandour, A., Himi, M., Casas, A., Daafi, Y., Karroum, M., and Chouikri, I. (2022). Contribution of electrical resistivity tomography in the study of aquifer geometry and groundwater salinization of Eastern Haouz and upstream Tassaout domain, Morocco. *Environmental Earth Sciences*, 81(4):122.

Rochdane, S., Reichert, B., Messouli, M., Babqiqi, A., and Khebiza, M. Y. (2012). Climate Change Impacts on Water Supply and Demand in Rheraya Watershed (Morocco), with Potential Adaptation Strategies. *Water*, 4(1):28–44.

Rochetin, N., Grandpeix, J.-Y., Rio, C., and Couvreux, F. (2014). Deep Convection Triggering by Boundary Layer Thermals. Part II: Stochastic Triggering Parameterization for the LMDZ GCM. *Journal of the Atmospheric Sciences*, 71(2):515–538.

Rong, X.-Y., LI, J., CHEN, H.-M., XIN, Y.-F., SU, J.-Z., HUA, L.-J., and ZHANG, Z.-Q. (2019). Introduction of CAMS-CSM model and its participation in CMIP6. *Climate Change Research*, 15(5):540.

Roundy, J. K., Ferguson, C. R., and Wood, E. F. (2013). Temporal Variability of Land–Atmosphere Coupling and Its Implications for Drought over the Southeast United States. *Journal of Hydrometeorology*, 14(2):622–635.

Roundy, J. K., Ferguson, C. R., and Wood, E. F. (2014). Impact of land-atmospheric coupling in CFSv2 on drought prediction. *Climate Dynamics*, 43(1-2):421–434.

Rovithakis, A., Grillakis, M. G., Seiradakis, K. D., Giannakopoulos, C., Karali, A., Field, R., Lazaridis, M., and Voulgarakis, A. (2022). Future climate change impact on wildfire danger over the Mediterranean: the case of Greece. *Environmental Research Letters*, 17(4):045022.

Roy, S. B. and Avissar, R. (2002). Impact of land use/land cover change on regional hydrometeorology in Amazonia.

Ruosteenoja, K., Markkanen, T., Venäläinen, A., Räisänen, P., and Peltola, H. (2018). Seasonal soil moisture and drought occurrence in Europe in CMIP5 projections for the 21st century. *Climate Dynamics*, 50(3-4):1177–1192.

Sacks, W. J., Cook, B. I., Buenning, N., Levis, S., and Helkowski, J. H. (2009). Effects of global irrigation on the near-surface climate. *Climate Dynamics*, 33(2-3):159–175.

Sadourny, R. and Laval, K. (1984). January and July performance of the LMD general circulation model. *New perspectives in climate modeling*, pages 173–197.

Saidi, A. and Diouri, M. (2017). Food self-sufficiency under the Green-Morocco Plan. *Journal of Experimental Biology and Agricultural Sciences*, 5(Spl-1- SAFSAW):33–40.

Sandu, I., Beljaars, A., Balsamo, G., and Ghelli, A. (2012). Revision of the surface roughness length table. *ECMWF newsletter*, pages 8–9.

Santanello, J. A., Dirmeyer, P. A., Ferguson, C. R., Findell, K. L., Tawfik, A. B., Berg, A., Ek, M., Gentine, P., Guillod, B. P., van Heerwaarden, C., Roundy, J., and Wulfmeyer, V. (2018). Land–Atmosphere Interactions: The LoCo Perspective. *Bulletin of the American Meteorological Society*, 99(6):1253–1272.

Saouabe, T., Naceur, K. A., El Khalki, E. M., Hadri, A., and Saidi, M. E. (2022). GPM-IMERG product: a new way to assess the climate change impact on water resources in a Moroccan semi-arid basin. *Journal of Water and Climate Change*, 13(7):2559–2576.

Schilling, J., Freier, K. P., Hertig, E., and Scheffran, J. (2012). Climate change, vulnerability and adaptation in North Africa with focus on Morocco. *Agriculture, Ecosystems & Environment*, 156:12–26.

Schilling, J., Hertig, E., Tramblay, Y., and Scheffran, J. (2020). Climate change vulnerability, water resources and social implications in North Africa. *Regional Environmental Change*, 20(1):15.

Schleussner, C.-F., Donges, J. F., Donner, R. V., and Schellnhuber, H. J. (2016). Armed-conflict risks enhanced by climate-related disasters in ethnically fractionalized countries. *Proceedings of the National Academy of Sciences*, 113(33):9216–9221.

Schwilch, G., Liniger, H. P., and Hurni, H. (2014). Sustainable Land Management (SLM) Practices in Drylands: How Do They Address Desertification Threats? *Environmental Management*, 54(5):983–1004.

Schär, C., Lüthi, D., Beyerle, U., and Heise, E. (1999). The Soil–Precipitation Feedback: A Process Study with a Regional Climate Model. *Journal of Climate*, 12(3):722–741.

Segal, M. and rritt, R. W. (1992). onclassical mesoscale circulations caused by surface sensible heat-flux gradients. *Bull. Am. Meteorol. Soc.*, pages 1593–1604.

Seker, M. and Gumus, V. (2022). Projection of temperature and precipitation in the Mediterranean region through multi-model ensemble from CMIP6. *Atmospheric Research*, 280:106440.

Seland, , Bentsen, M., Seland Graff, L., Olivié, D., Toniazzo, T., Gjermundsen, A., Debernard, J. B., Gupta, A. K., He, Y., Kirkevåg, A., Schwinger, J., Tjiputra, J., Schancke Aas, K., Bethke, I., Fan, Y., Griesfeller, J., Grini, A., Guo, C., Ilicak, M., Hafsahl Karset, I. H., Landgren, O., Liakka, J., Onsum Moseid, K., Nummelin, A., Spensberger, C., Tang, H., Zhang, Z., Heinze, C., Iverson, T., and Schulz, M. (2020). The Norwegian Earth System Model, NorESM2 – Evaluation of theCMIP6 DECK and historical simulations. preprint, Climate and Earth System Modeling.

Sellar, A. A., Jones, C. G., Mulcahy, J. P., Tang, Y., Yool, A., Wiltshire, A., O'Connor, F. M., Stringer, M., Hill, R., Palmieri, J., Woodward, S., de Mora, L., Kuhlbrodt, T., Rumbold, S. T., Kelley, D. I., Ellis, R., Johnson, C. E., Walton, J., Abraham, N. L., Andrews, M. B., Andrews, T., Archibald, A. T., Berthou, S., Burke, E., Blockley, E., Carslaw, K., Dalvi, M., Edwards, J., Folberth, G. A., Gedney, N., Griffiths, P. T., Harper, A. B., Hendry, M. A., Hewitt, A. J., Johnson, B., Jones, A., Jones, C. D., Keeble, J., Liddicoat, S., Morgenstern, O., Parker, R. J., Predoi, V., Robertson, E., Siahaan, A., Smith, R. S., Swaminathan, R., Woodhouse, M. T., Zeng, G., and Zerroukat, M. (2019). UKESM1: Description and Evaluation of the U.K. Earth System Model. *Journal of Advances in Modeling Earth Systems*, 11(12):4513–4558. _eprint: https://onlinelibrary.wiley.com/doi/pdf/10.1029/2019MS001739.

Sen, Z. (2008). *Wadi hydrology. Crc Press.*

Seneviratne, S., Zhang, X., Adnan, M., Badi, W., Dereczynski, C., and Di Luca, A. (2021). In: Masson-Delmotte, V., Zhai, P., Pirani, A., Connors, S.L., Péan, C., Berger, S. et al. (Eds.) Weather and Climate Extreme Events in a Changing Climate. In: Climate Change 2021: The Physical Science Basis. Contribution of Working Group I to the Sixth Assessment Report of the Intergovernmental Panel on Climate Change. Technical report, Cambridge University Press. In Press.

Seneviratne, S. I., Corti, T., Davin, E. L., Hirschi, M., Jaeger, E. B., Lehner, I., Orlowsky, B., and Teuling, A. J. (2010). Investigating soil moisture–climate interactions in a changing climate: A review. *Earth-Science Reviews*, 99(3-4):125–161.

Sherwood, S. C., Dixit, V., and Salomez, C. (2018). The global warming potential of near-surface emitted water vapour. *Environmental Research Letters*, 13(10):104006.

Sillmann, J., Kharin, V. V., Zwiers, F. W., Zhang, X., and Bronaugh, D. (2013). Climate extremes indices in the CMIP5 multimodel ensemble: Part 2. Future climate projections. *Journal of Geophysical Research: Atmospheres*, 118(6):2473–2493.

Simonneaux, V., Duchemin, B., Helson, D., Er-Raki, S., Olioso, A., and Chehbouni, A. G. (2008). The use of high-resolution image time series for crop classification and evapotranspiration estimate over an irrigated area in central Morocco. *International Journal of Remote Sensing*, 29(1):95–116.

Srairi, M. T. (2017). *MOROCCO ENVIRONMENTAL, SOCIAL AND ECONOMIC ISSUES OF THE 21ST CENTURY*. Nova Science Publishers, Inc. † New York.

Su, Z., Schmugge, T., Kustas, W. P., and Massman, W. J. (2001). An Evaluation of Two Models for Estimation of the Roughness Height for Heat Transfer between the Land Surface and the Atmosphere. *Journal of Applied Meteorology*, 40(11):1933–1951.

Séférian, R., Nabat, P., Michou, M., Saint-Martin, D., Voldoire, A., Colin, J., Decharme, B., Delire, C., Berthet, S., Chevallier, M., Sénési, S., Franchisteguy, L., Vial, J., Mallet, M., Joetzjer, E., Geoffroy, O., Guérémy, J.-F., Moine, M.-P., Msadek, R., Ribes, A., Rocher, M., Roehrig, R., Salas-y Mélia, D., Sanchez, E., Terray, L., Valcke, S., Waldman, R., Aumont, O., Bopp, L., Deshayes, J., Éthé, C., and Madec, G. (2019). Evaluation of CNRM Earth System Model, CNRM-ESM2-1: Role of Earth System Processes in Present-Day and Future Climate. *Journal of Advances in Modeling Earth Systems*, 11(12):4182–4227. _eprint: https://onlinelibrary.wiley.com/doi/pdf/10.1029/2019MS001791.

Tang, Q., Oki, T., Kanae, S., and Hu, H. (2007). The Influence of Precipitation Variability and Partial Irrigation within Grid Cells on a Hydrological Simulation. *Journal of Hydrometeorology*, 8(3):499–512.

Tang, S., Vlug, A., Piao, S., Li, F., Wang, T., Krinner, G., Li, L. Z. X., Wang, X., Wu, G., Li, Y., Zhang, Y., Lian, X., and Yao, T. (2023). Regional and tele-connected impacts of the Tibetan Plateau surface darkening. *Nature Communications*, 14(1):32.

Tatebe, H., Ogura, T., Nitta, T., Komuro, Y., Ogochi, K., Takemura, T., Sudo, K., Sekiguchi, M., Abe, M., Saito, F., Chikira, M., Watanabe, S., Mori, M., Hirota, N., Kawatani, Y., Mochizuki, T., Yoshimura, K., Takata, K., O'ishi, R., Yamazaki, D., Suzuki, T., Kurogi, M., Kataoka, T., Watanabe, M., and Kimoto, M. (2019). Description and basic evaluation of simulated mean state, internal variability, and climate sensitivity in MIROC6. *Geoscientific Model Development*, 12(7):2727–2765. Publisher: Copernicus GmbH.

Tebaldi, C., Smith, R. L., Nychka, D., and Mearns, L. O. (2005). Quantifying Uncertainty in Projections of Regional Climate Change: A Bayesian Approach to the Analysis of Multimodel Ensembles. *Journal of Climate*, 18(10):1524–1540.

Tramblay, Y., Badi, W., Driouech, F., El Adlouni, S., Neppel, L., and Servat, E. (2012). Climate change impacts on extreme precipitation in Morocco. *Global and Planetary Change*, 82-83:104–114.

Tramblay, Y., Jarlan, L., Hanich, L., and Somot, S. (2018). Future Scenarios of Surface Water Resources Availability in North African Dams. *Water Resources Management*, 32(4):1291–1306.

Tramblay, Y., Ruelland, D., Somot, S., Bouaicha, R., and Servat, E. (2013). High-resolution Med-CORDEX regional climate model simulations for hydrological impact studies: a first evaluation of the ALADIN-Climate model in Morocco. *Hydrology and Earth System Sciences*, 17(10):3721–3739.

Tuel, A. and Eltahir, E. A. B. (2020). Why Is the Mediterranean a Climate Change Hot Spot? *JOURNAL OF CLIMATE*, 33:15.

Tuel, A., Kang, S., and Eltahir, E. A. B. (2021). Understanding climate change over the southwestern Mediterranean using high-resolution simulations. *Climate Dynamics*, 56(3-4):985–1001.

Turco, M., Rosa-Cánovas, J. J., Bedia, J., Jerez, S., Montávez, J. P., Llasat, M. C., and Provenzale, A. (2018). Exacerbated fires in Mediterranean Europe due to anthropogenic warming projected with non-stationary climate-fire models. *Nature Communications*, 9(1):3821.

Vafeidis, A., Abdulla, A., Bondeau, A., Brotons, L., Ludwig, R., Portman, M., Reimann, L., Vousdoukas, M., and Xoplaki, E. (2020). Managing future risks and building socio-ecological resilience in the Mediterranean. In: Climate and Environmental Change in the Mediterranean Basin – Current Situation and Risks for the Future. First Mediterranean Assessment Report [Cramer W, Guiot J, Marini K (eds.)]. Technical report, Marseille, France.

Vicente-Serrano, S. M., Lopez-Moreno, J.-I., Beguería, S., Lorenzo-Lacruz, J., Sanchez-Lorenzo, A., García-Ruiz, J. M., Azorin-Molina, C., Morán-Tejeda, E., Revuelto, J., Trigo, R., Coelho, F., and Espejo, F. (2014). Evidence of increasing drought severity caused by temperature rise in southern Europe. *Environmental Research Letters*, 9(4):044001.

Vignon, E., Hourdin, F., Genthon, C., Gallée, H., Bazile, E., Lefebvre, M.-P., Madeleine, J.-B., and Van de Wiel, B. J. H. (2017). Antarctic boundary layer parametrization in a general circulation model: 1-D simulations facing summer observations at Dome C: ANTARCTIC ABL PARAMETRIZATION IN A GCM. *Journal of Geophysical Research: Atmospheres*, 122(13):6818–6843.

Vignon, E., Hourdin, F., Genthon, C., Van de Wiel, B. J. H., Gallée, H., Madeleine, J., and Beaumet, J. (2018). Modeling the Dynamics of the Atmospheric Boundary Layer Over the Antarctic Plateau With a General Circulation Model. *Journal of Advances in Modeling Earth Systems*, 10(1):98–125.

Vignon, (2017). *La couche limite extrême du Plateau Antarctique et sa représentation dans les modèles de climat*. PhD thesis, Université de Grenoble Alpes.

Voldoire, A., Saint-Martin, D., Sénési, S., Decharme, B., Alias, A., Chevallier, M., Colin, J., Guérémy, J.-F., Michou, M., Moine, M.-P., Nabat, P., Roehrig, R., Salas y Mélia, D., Séférian, R., Valcke, S., Beau, I., Belamari, S., Berthet, S., Cassou, C., Cattiaux, J., Deshayes, J., Douville, H., Ethé, C., Franchistéguy, L., Geoffroy, O., Lévy, C., Madec, G., Meurdesoif, Y., Msadek, R., Ribes, A., Sanchez-Gomez, E., Terray, L., and Waldman, R. (2019). Evaluation of CMIP6 DECK Experiments With CNRM-CM6-1. *Journal of Advances in Modeling Earth Systems*, 11(7):2177–2213. _eprint: https://onlinelibrary.wiley.com/doi/pdf/10.1029/2019MS001683.

Waha, K., Krummenauer, L., Adams, S., Aich, V., Baarsch, F., Coumou, D., Fader, M., Hoff, H., Jobbins, G., Marcus, R., Mengel, M., Otto, I. M., Perrette, M., Rocha, M., Robinson, A., and

Schleussner, C.-F. (2017). Climate change impacts in the Middle East and Northern Africa (MENA) region and their implications for vulnerable population groups. *Regional Environmental Change*, 17(6):1623–1638.

Wang, F., Ducharne, A., Cheruy, F., Lo, M.-H., and Grandpeix, J.-Y. (2018). Impact of a shallow groundwater table on the global water cycle in the IPSL land–atmosphere coupled model. *Climate Dynamics*, 50(9-10):3505–3522.

Wang, S. S., Santanello, J., Wang, H., Barandiaran, D., Pinker, R. T., Schubert, S., Gillies, R. R., Oglesby, R., Hilburn, K., Kilic, A., and Houser, P. (2015). An intensified seasonal transition in the Central U.S. that enhances summer drought. *Journal of Geophysical Research: Atmospheres*, 120(17):8804–8816.

Wang, W., Liu, G., Wei, J., Chen, Z., Ding, Y., and Zheng, J. (2021). The climatic effects of irrigation over the middle and lower reaches of the Yangtze River, China. *Agricultural and Forest Meteorology*, 308-309:108550.

Ward, M. N., Lamb, P. J., Portis, D. H., El Hamly, M., and Sebbari, R. (1999). Climate Variability in Northern Africa: Understanding Droughts in the Sahel and the Maghreb. In Navarra, A., editor, *Beyond El Niño*, pages 119–140. Springer Berlin Heidelberg, Berlin, Heidelberg.

Wu, T., Lu, Y., Fang, Y., Xin, X., Li, L., Li, W., Jie, W., Zhang, J., Liu, Y., Zhang, L., Zhang, F., Zhang, Y., Wu, F., Li, J., Chu, M., Wang, Z., Shi, X., Liu, X., Wei, M., Huang, A., Zhang, Y., and Liu, X. (2019). The Beijing Climate Center Climate System Model (BCC-CSM): the main progress from CMIP5 to CMIP6. *Geoscientific Model Development*, 12(4):1573–1600.

Xin, X., Li, Z., Yu, R., and Zhou, T. (2008). Impacts of upper tropospheric cooling upon the late spring drought in East Asia simulated by a regional climate model. *Advances in Atmospheric Sciences*, 25(4):555–562.

Xoplaki, E. (2002). *Climate variability over the Mediterranean*. Ph.D. thesis, Universität Bern, Switzerland.

Yamada, T. (1983). Simulations of nocturnal drainage flows by a q2l turbulence closure model. *Journal of the Atmospheric Sciences*.

Yang, H., Jiang, Z., and Li, L. (2016). Biases and improvements in three dynamical downscaling climate simulations over China. *Climate Dynamics*, 47(9-10):3235–3251.

Yukimoto, S., Kawai, H., Koshiro, T., Oshima, N., Yoshida, K., Urakawa, S., Tsujino, H., Deushi, M., Tanaka, T., Hosaka, M., Yabu, S., Yoshimura, H., Shindo, E., Mizuta, R., Obata, A., Adachi, Y., and Ishii, M. (2019). The Meteorological Research Institute Earth System Model Version 2.0, MRI-ESM2.0: Description and Basic Evaluation of the Physical Component. *Journal of the Meteorological Society of Japan. Ser. II*, 97(5):931–965.

Zhang, X., Xiong, Z., and Tang, Q. (2017). Modeled effects of irrigation on surface climate in the Heihe River Basin, Northwest China. *Journal of Geophysical Research: Atmospheres*, 122(15):7881–7895.

Zkhiri, W., Tramblay, Y., Hanich, L., Jarlan, L., and Ruelland, D. (2019). Spatiotemporal characterization of current and future droughts in the High Atlas basins (Morocco). *Theoretical and Applied Climatology*, 135(1-2):593–605.

Zobler, L. (1986). A World Soil File for Global Climate Modeling: National Aeronautics and Space Administration, Goddard Space Flight Center. *Institute for Space Studies*.

INSTITUT POLYTECHNIQUE DE PARIS

Titre : Modélisation des couplages surface-atmosphère dans les plaines semi-arides marocaines dans un contexte de changement climatique

Mots clés : Modèle de circulation générale, Intéractions surface-atmosphère, Maroc, Changement Climatique, Irrigation, Données In Situ.

Résumé : Les plaines Marocaines jouent un rôle majeur dans la production agricole du pays, représentant ainsi un tiers des terres agricoles et deux tiers des zones irriguées du pays. Cependant, la fréquence croissante des sécheresses constitue un défi majeur pour la gestion durable des ressources en eau, en particulier, dans ces régions vulnérables. Correctement représenter le climat de surface au Maroc dans les modèles de climat est fondamental pour prédire les effets du changement climatique sur les ressources en eau dans cette région.

L'objectif de cette thèse consiste en deux volets: i) évaluer et améliorer la représentation des processus physiques qui gouvernent le climat de surface et le bilan d'eau et d'énergie dans la plaine du Haouz, située à la région de Marrakech. ii) Mettre en place des projections futures fiables dans l'Afrique du Nord et plus particulièrement dans les plaines Marocaines. Ainsi, nous utilisons la composante LMDZ-ORCHIDEE du Modèle Couplé de l'Institut Pierre Simon Laplace (IPSL-CM), dont le modèle atmosphérique LMDZ est couplé au modèle de surface continentale ORCHIDEE. Une configuration originale a été mise en place, en bénéficiant de la "capacité du zoom" du LMDZ, avec une grille globale raffinée autour de la plaine du Haouz, et la dynamique à grande échelle forcée à suivre les réanalyses à l'extérieur de la zone zoomée. La première partie de ce travail est consacrée à la mise en place d'une évaluation approfondie du modèle LMDZ-ORCHIDEE dans la représentation des interactions surface-atmosphère en utilisant des mesures sur site collectées dans la plaine du Haouz. Des expériences de sensibilité sont menées avec un couvert végétal adapté afin de permettre une comparaison modèle-observation plus robuste et concluante. Les résultats montrent que le modèle -avec sa physique standard du CMIP6- représente raisonnablement bien le climat de la surface dans la plaine. Cependant, un biais chaud de température nocturne, associé à une sous-estimation de la chaleur sensible et de la vitesse du vent a été identifié et partiellement corrigé en prescrivant des hauteurs de rugosité plus réalistes. Une sous-estimation de l'évapotranspiration et de l'humidité du sol, accompagnée des biais chauds de la température diurne ont été également identifiés dans nos simulations. Ainsi, une paramétrisation du premier ordre, visant à imiter l'irrigation dans la plaine, est développée en ORCHIDEE. Les résultats montrent une réduction des biais de l'évapotranspiration et de la température diurne. Par conséquent, cette étude de sensibilité souligne le rôle majeur qu'occupe l'irrigation dans la régulation du climat local dans les champs agricoles. Dans la deuxième partie, nous avons étudié la réponse de l'hydrologie de surface au changement climatique dans le bassin Méditerranéen et l'Afrique du nord. Une analyse approfondie des modèles CMIP6 montre un assèchement intense à la Méditerranée et une augmentation des précipitations au Sahara, cependant, celles-ci sont compensées par l'augmentation de l'évapotranspiration. Une étude de comparaison à CMIP5 montre des résultats qualitativement similaires avec des changements moins intenses qu'en CMIP6, en particulier pendant l'hiver. Pour raffiner les projections sur les plaines agricoles Marocaines, nous avons mis en place une configuration LMDZ-ORCHIDEE zoomée sur la plaine du Haouz, dont les champs de vent et de température sont guidés à l'extérieur du Maroc vers une simulation globale CMIP6 bien choisie suivant un scénario SSP5-8.5. Les projections montrent un réchauffement de 4K sur la plaine, ainsi qu'une diminution de l'humidité du sol et du flux latent suite à une diminution des précipitations par 30%. L'irrigation atténue le réchauffement induit par le changement climatique et réduit le rapport de Bowen suite à l'augmentation de l'humidité du sol, soulignant ainsi l'importance de la prise en compte de l'irrigation dans les simulations climatiques sur les zones agricoles Marocaines.

ECOLE DOCTORALE

Title : Modeling the surface-atmosphere coupling in the Moroccan semi-arid plains in the context of climate change

Keywords : General Circulation Model, Land-atmosphere interactions, Morocco, Climate Change, Irrigation, In Situ Data.

Abstract : Moroccan plains play a major role in the agricultural production of the country, accounting for a third of utilized agricultural land and two thirds of the irrigated areas of the country. However, the increasing droughts and water shortage risks raise a real challenge for sustainable water management in such vulnerable regions. An accurate modeling of the near surface climate is critical to understand and anticipate the climate change in the plains and their potential impacts on the region's water cycle and resources.

The aim of this thesis is two fold: i) to evaluate and improve the modeling of the physical processes governing the surface climate and the water and energy budgets over the Moroccan agricultural plains,and ii) to conduct a critical assessment of future climate projections over the North African region and more particularly over the Moroccan plains. To this purpose, we use the LMDZ-ORCHIDEE model,the atmosphere-land surface component of IPSL-CM (The Institut de Pierre Simon Laplace CoupledModel). An original configuration has been set-up - leveraging the 'zooming capability' of LMDZ -with a global grid locally refined over the Haouz plain in Marrakech region and with the large-scale dynamics nudged to follow reanalysis outside of the zoomed area.

The first part of this work consists of performing a thorough evaluation of LMDZ-ORCHIDEEin representing the surface-atmosphere interactions using in situ measurements collected over theHaouz plain. Sensitivity experiments are performed with adapted land cover to make more robust model-observation comparison. Results show that LMDZ-ORCHIDEE - with the CMIP6 version of its physics - reasonably represents the plain's near surface climate. However, a nocturnal warm bias as-sociated with underestimated sensible heating and wind speed has been identified and partly corrected by prescribing more realistic roughness heights. An underestimation of the evapotranspiration and soil moisture along with overly warm diurnal temperatures remain in our simulations. A first-order irrigation parameterisation has then been implemented in ORCHIDEE to mimic the drip irrigation process extensively used in the plain. Comparison with observations show that the evapotranspiration flux and the daytime temperature biases are reduced, suggesting that irrigation plays a significant role in determining the local climate in the agricultural fields.

In the second part, we assessed the response of the different terms of the surface water budget to climate change over the Mediterranean basin and North-Africa. An in-depth analysis using selectedCMIP6 models is carried out, and suggests a statistically robust amplification of the drying over the Mediterranean and an increasing precipitation pattern over Sahara, counterbalanced by increasing evaporative flux. Compared to the CMIP5 exercise, CMIP6 models show qualitatively similar patterns but generally predict more intense changes in precipitation and evapotranspiration over the Mediter-ranean basin and South-Eastern Sahara, especially during winter. To refine the projections over theMoroccan agricultural plains, we then run a new simulation with LMDZ-ORCHIDEE configuration- with a "zoom" over the Haouz plain - in which wind and temperature fields outside Morocco are nudged towards a CMIP6 SSP5-8.5 Shared Socioeconomic Pathway. This simulation shows a warm-ing of 4K by the end of the century over the plain with the high-end scenario, as well as a decrease in soil moisture and latent heat flux following the decrease in precipitation by 30%. Sensitivity studies suggest that irrigation can potentially mitigate by 1K the climate change-induced warming and reduce the Bowen ratio as a result of enhanced soil moisture, emphasizing the importance of accounting forthe irrigation in climate projections over the Moroccan agricultural areas.

Institut Polytechnique de Paris
91120 Palaiseau, France